STUDIES OF THE IMF AND DAYSIDE RECONNECTION-DRIVEN CONVECTION SEEN BY POLARDARN

A Thesis Submitted to the College of
Graduate Studies and Research
In Partial Fulfillment of the Requirements
For the Degree of Master of Science
In the Department of Physics and Engineering Physics
University of Saskatchewan
Saskatoon

By

Xi Yan

PERMISSION TO USE

In presenting this thesis in partial fulfilment of the requirements for a Postgraduate degree from the University of Saskatchewan, I agree that the Libraries of this University may make it freely available for inspection. I further agree that permission for copying of this thesis in any manner, in whole or in part, for scholarly purposes may be granted by the professor or professors who supervised my thesis work or, in their absence, by the Head of the Department or the Dean of the College in which my thesis work was done. It is understood that any copying or publication or use of this thesis or parts thereof for financial gain shall not be allowed without my written permission. It is also understood that due recognition shall be given to me and to the University of Saskatchewan in any scholarly use which may be made of any material in my thesis.

Requests for permission to copy or to make other use of material in this thesis in whole or part should be addressed to:

Head of the Department of Physics and Engineering Physics

University of Saskatchewan

Saskatoon, Saskatchewan

Canada S7N 5E2

ABSTRACT

The original objectives of this thesis were to use the new PolarDARN radars to study the convection patterns at high latitudes and to attempt to explain them in terms of reconnection. Because the IMF is important in reconnection, studies of the Interplanetary Magnetic Field (IMF) components Bx, By and Bz were done. The study showed that <|Bz|> was lower by 21.5% than <|By|> from Jan. 2006 to Dec. 2008, so By was expected to play an important role in reconnection. The IMF, spiral angle, and the amount of warping of the solar magnetic field in interplanetary space decreased slightly during this 36-month period. The decrease in IMF was a more sensitive indicator of the solar minimum than the decrease in the 10.7 cm solar microwave flux.

A solar magnetic sector boundary study from the Jan 1, 2007 – Dec 31, 2008 interval showed the occurrence of four or two sectors in a synodic solar rotation cycle. A sector boundary crossing frequently takes place in less than 3 hours. The transition from four sectors to two sectors is surprisingly smooth, in that no interruption in the 27-day synodic period occurs. A superposed epoch analysis of solar wind speed near sector boundary crossings showed a speed minimum about half a day before the crossing, and a maximum about two days after the crossing. The standard deviation reached a minimum at about the same time as the velocity. The sector boundary study also showed that, since Dec. 2007, there were six roughly 27-day synodic solar rotation cycles near spring equinox when “away” field dominated, and that the following seven 27-day cycles close to the autumnal equinox were dominated by “toward” field. This is consistent with the quasi-sinusoidal annual magnetic sector polarity oscillations that occur for about three years during solar minimum. These oscillations are due to the mainly dipolar magnetic field which is roughly aligned with the Sun’s axis, tilted 7.25° from the normal to the ecliptic plane. The three-year oscillation for the present minimum between Solar Cycles 23 and 24 appeared to begin in Dec. 2007. For the past four solar minima, an El Nino event has occurred during the last of the three oscillations, and the El Nino and sinusoidal

magnetic oscillation ended together. The new solar cycle began about 6 months before that.

During the past eight years, a new 3D topological “null-separator” formulation of magnetic reconnection and its effect on convection has been led by Dr. M. Watanabe in ISAS at the University of Saskatchewan. This formulation includes two types of interchange reconnection (Russell and Tanaka) as well as the traditional Dungey reconnection. For conditions when the IMF clock angle was within 30° of a Bz+ dominant convection, the new reconnection model shows that the convection can be driven strictly by the two types of interchange reconnection. The model predicts the existence of a “reciprocal cell” on closed field lines and an “interchange merging cell” surrounding an interior lobe cell. The construction of the PolarDARN radars at Rankin Inlet and Inuvik, completed in December, 2007, allowed polar cap convection to be measured for predominantly Bz+ conditions. The existence of the two predicted features was confirmed. This also required that satellite data be analyzed to determine the location of the open-closed-field-line-boundary (OCFLB). Several PolarDARN studies are represented to show convection for different IMF clock angles and seasons.

ACKNOWLEDGEMENTS

I would like to thank my supervisor Dr. George Sofko for his guidance and support during my graduate career. He is a patient teacher who helped me understand theories, a good supervisor who provided me ideas and suggestions for performing the research, and also an excellent advisor who told me to open my mind as essential preparation to becoming a good scientist.

I would like to thank my co-supervisor Dr. Kathryn McWilliams for her kind help in programming and her suggestions and encouragement for my thesis.

I am very grateful for the great help I received from the members of ISAS and also the Department of Physics and Engineering Physics from University of Saskatchewan. Thanks to Dr. M. Watanabe for explaining the reconnection theory to me and for helping me with my research. Thanks to Dr. D. Andre for his help in programming. Thanks to Jan Wiid for providing me the information about the wire TTFD antenna. Thanks to Dr. G. Hussey, Dr. A. Bourassa, Dr. J.-P. St. Maurice and Dr. S. Koustov for all their valuable comments and suggestions. Thanks to Dr. C. Xiao and Dr. C. Rangacharyulu for their help and encouragement. Finally, thanks to my fellow graduate students, G. Perry, H. Liu, R. Gillies, M. Gillies, and R. Drayton for their constant support.

I would also like to acknowledge the Canadian Space Agency, the National Science and Engineering Research Council (NSERC) and all the international funding agencies which support financially the PolarDARN/SuperDARN program and the Department of Physics and Engineering Physics, University of Saskatchewan for awarding me scholarship funding. Thanks to all the people and institutes who provided the DMSP, POES, METOP and ACE satellite data used in this thesis.

Finally, I would like to thank my parents for their support and love, and my landlady Ms. Beth Murphy for her understanding.

TABLE OF CONTENTS

LIST OF TABLES

LIST OF FIGURES

LIST OF ABBREVIATIONS

3D	three-Dimensional
A	Away
Aa	a daily average level for geomagnetic activity
AACGM	Altitude Adjusted Corrected GeoMagnetic
ACE	Advanced Composition Explorer
ACF	AutoCorrelation Function
AMISR	Advanced Modular Incoherent Scatter Radar
AU	Astronomical Unit
CME	Coronal Mass Ejection
CS	Current Sheet
CWSE	ClockWiSE
C-CWSE	CounterClockWiSE
DMSP	Defense Meteorological Satellite Program
EM	ElectroMagnetic
EMP	ElectroMagnetic Pulse
ENSO	El Niño-Southern Oscillation
ESA	European Space Agency
ESR	European Incoherent Scatter (EISCAT) Svalbard Radar
GA	Geomagnetic Activity
GCR	Galactic Cosmic Ray
GST	Global Surface Temperature
HCS	Heliospheric Current Sheet
HF	High Frequency (3-30MHz)
HPS	Heliospheric Plasma Sheet
I	In phase
IMF	Interplanetary Magnetic Field
ISR	Incoherent Scatter Radar
ISUAL	Imager of Sprites and and Upper Atmospheric Lightning
LOS	Line-Of-Sight
LPF	Low Pass Filter
Kp	a measure of the global average geomagnetic potential
MEPED	Medium Energy Proton and Electron Detector
MHD	MagnetoHydroDynamic
ML and MLAT	Magnetic Latitude
MLT	Magnetic Local Time
MSP	geographic Meridian at the Sub-solar Point
NASA	National Aeronautics and Space Administration
NGP	North Geographic Pole

NMP	AACGM North Magnetic Pole
NOAA	National Oceanic and Atmospheric Administration
OCFLB	Open-Closed Field Line Boundary
OLS	low-light-level imager
PFISR	Poker Flat Advanced Modular Incoherent Scatter Radar
POES	Polar Orbiting Environmental Satellites
PolarDARN	Polar Dual Auroral Radar Network
PSS	Phenomenological Solar Signatures
Q	Quadrature
QS	Quiet Sun
SEM-2	Space Environment Monitor-2
SOI	Southern Oscillation Index
SP	IMF Sector Polarity
SSC	Storm Sudden Commencement
SSIES	thermal plasma monitor
SSJ/3 and SSJ/4	precipitating particle spectrometers
SSM	flux-gate magnetometer
SuperDARN	Super Dual Auroral Radar Network
SVD	Singular Value Decomposition
SWICS	Solar Wind Ion Composition Spectrometer
T	Toward
TED	Total Energy Detector
TLE	Transient Luminous Event
TSI	Total Solar Irradiance
TTFD	Twin-Terminated Folded Dipole
UT	Universal Time

1. INTRODUCTION

1.1 Objectives of the Thesis

The new PolarDARN radars [*Watanabe et al.*, 2009; *Koustov et al.*, 2009; *Hososkawa et al.*, 2009] are unique in examining the polar cap region of "open" field lines in which the Earth's field is connected (by the process of merging or reconnection) to the IMF carried by the solar wind.

Clearly, the solar wind conditions and especially the reconnection between IMF and Earth's field are critical elements of the study. However, this study has been made much more interesting because the initial period of the operation of PolarDARN has taken place during one of the deepest solar minima of the past century. Consequently, a study of the solar magnetic sector structure in the IMF has been important not only for the polar cap measurements but for its relationship to solar activity.

There are three main objectives for this thesis: (1) to study measured convection and electric fields in the polar cap; (2) to study a new formulation of reconnection that can explain all the observed types of convection; (3) to study the Sun, the solar cycle (which is in a deep minimum), and the solar wind, particularly its associated interplanetary magnetic field (IMF) and magnetic sector structure that are critical in determining the types of reconnection that can occur. We now expand on each of these three objectives, relating them to the relevant chapters in this thesis.

(1) First of all, we have studied measured convection and electric fields by PolarDARN radars in the polar cap. The study involves a description of the PolarDARN radars and the supporting satellite data (DMSP and NOAA POES satellites) in Chapter 2. In particular the extraction of the Doppler shift frequency from the ACF technique is, for the first time, described completely in mathematical terms, and this has been relegated to Appendix 1. Also, one of the new features of the PolarDARN radars is the wire antenna system, which uses TTFD (twin-terminated folded dipole) antennas. This also is described in Chapter 2, as part of the description of PolarDARN. The convection events are studied in detail in Chapter 4, in particularly for IMF conditions characterized by a northward magnetic field (Bz+). The convection cells driven by the "interchange" types of reconnection are stressed, especially the reciprocal cell whose streamlines occur completely on closed magnetic field lines in the ionosphere.

(2) The second goal is to study a new complete formulation of the four types of reconnection. The explanation of the complex polar cap convection particularly in Bz+ IMF, was not adequately addressed by previous reconnection theories. During the past six years, a new comprehensive three-dimensional (3D) topological formulation of steady-state reconnection has been undertaken at the University of Saskatchewan in

concert with the PolarDARN development. The historical theory of reconnection and the new 3D topological formulation are discussed in the Introductory Chapter (Chapter 1), and then are used in Chapter 4 to explain specific patterns measured by PolarDARN.

(3) Finally, we have studied the Sun and the solar cycle under the present deep solar minimum conditions, with emphasis upon the magnetic sector structure in the IMF. It is the solar wind and the IMF it carries that determine the types of reconnection and the resulting convection patterns. Therefore, the study of the IMF itself through the magnetic sector structure between the Sun and the Earth is a key to understanding the reconnection. The sector structure is the focus of Chapter 3 of the thesis. In addition, the magnetic sector structure is found not only to be a major influence on the high altitude "space weather" in the coupled Magnetosphere-Ionosphere system, but also appears to play a role in influencing meteorological weather near the Earth's surface (troposphere, stratosphere). Since the solar wind and IMF are intimately related to conditions on the Sun and to the solar cycle, relevant aspects of the Sun and solar cycle are first discussed in Chapter 1.

1.2 The Sun

1.2.1 Description

The Sun has a radius of 696,000 km. The distance from the Sun to the Earth (1 AU) is 150×10^6 km. The effective blackbody temperature of the Sun is 5785 K.

As shown in Figure 1.1, its interior consists of the core, radiative zone and convection zone. The core is the zone where fusion reactions occur and generate energy, much of which is gamma-rays. The temperature of the core is about 1.5×10^7 K. The gamma-rays diffuse outward into the radiative zone, where they encounter the free electrons and undergo numerous Compton scatterings, at each of which the wavelength increases and the effective temperature falls. The photons eventually pass through the radiative zone in 10 million years. The temperature drops from 8×10^6 K at the bottom to 5×10^5 K at the top of the radiative zone. Above it is the convection zone, whose name derives from the convection that results from the rapid drop in temperature and the associated large adiabatic lapse rate. The temperature drops to 6600 K at top of the convection zone, which is also the bottom of the photosphere. The photosphere is a thin layer which is only about 500 km thick and throughout which the temperature falls to about 4300 K, after which the temperature rises in the chromosphere.

The Sun's atmosphere has four layers: the photosphere, chromosphere, transition zone and the corona. The photosphere is the visible surface of the Sun, where sunspots are seen. The temperature of its upper boundary is 4300 K, which is also the base of the chromosphere. In the chromosphere, the temperature increases to about 20,000 K at a height of about 2500 km. There is then a thin transition zone of only about 200 – 300 km width in which the temperature rises rapidly to about 500,000 K. Finally, the outer region is the corona, in which the temperature further rises to about 2 x 10^6 K. Because of its

high temperature, the outward pressure in the corona exceeds the inward gravitational pull, so the corona inflates into space in the form of the solar wind [*Parker*, 1957a].

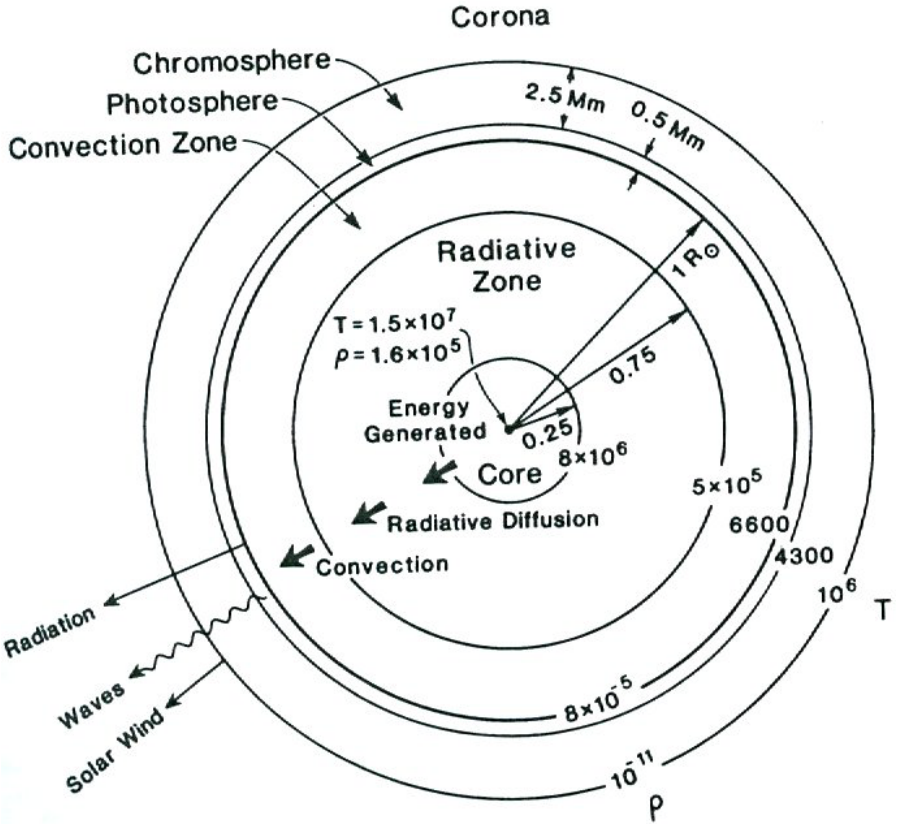

Figure 1.1. The structure of the Sun, including the interior: core, radiative zone and convection zone and atmosphere: the photosphere, chromosphere and the corona (taken from *Kivelson and Russell* [1995]).

1.2.2 Solar sunspot cycle, solar activity

The solar magnetic activity has roughly an 11-year cycle, and a 22-year solar magnetic cycle called the Hale cycle [*Hale et al.*, 1919]. Figure 1.2 shows the 11-year sunspot cycle. We are currently in the minimum between Solar Cycles 23 and 24. Figure 1.2 shows that four of the strongest cycles (18, 19, 21 and 22) have occurred in the past 60 years.

As shown in Figure 1.3, during the period from 1645 – 1715 which includes about six sunspot cycles, there was a minimum period in which there were few sunspots or northern lights, called the Maunder Minimum. Prior to the Maunder Minimum, the Spörer Minimum took place from about 1460 to 1550, lasting about eight solar cycles.

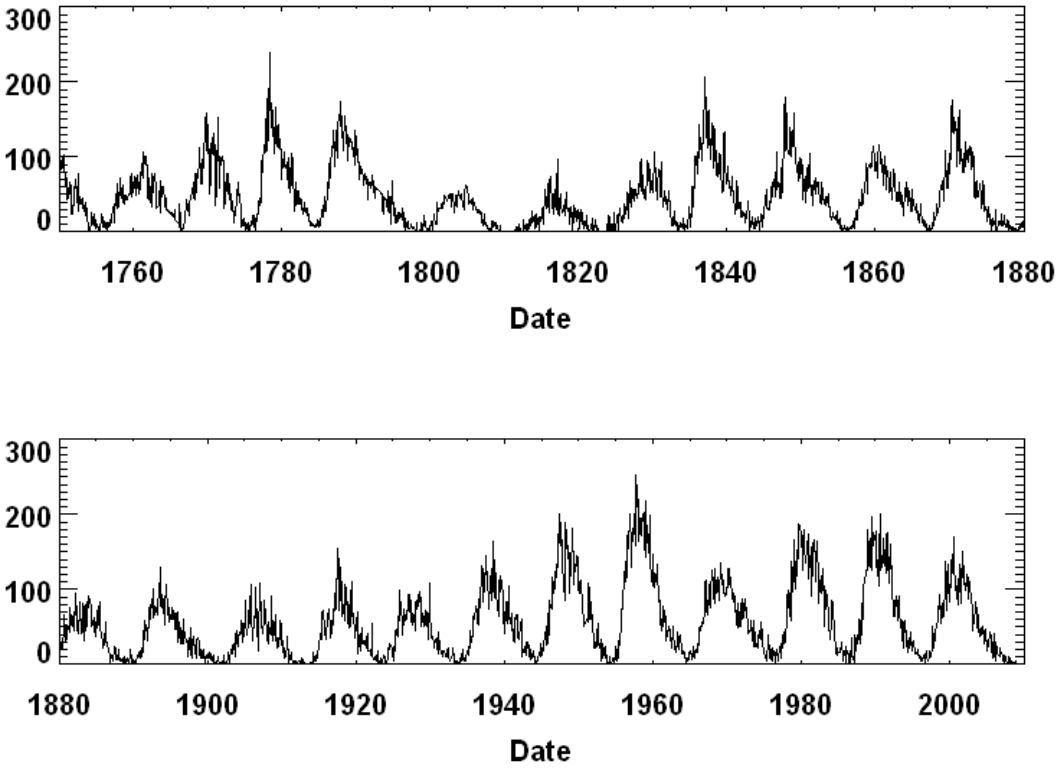

Figure 1.2. A plot showing the sunspot numbers since 1750.

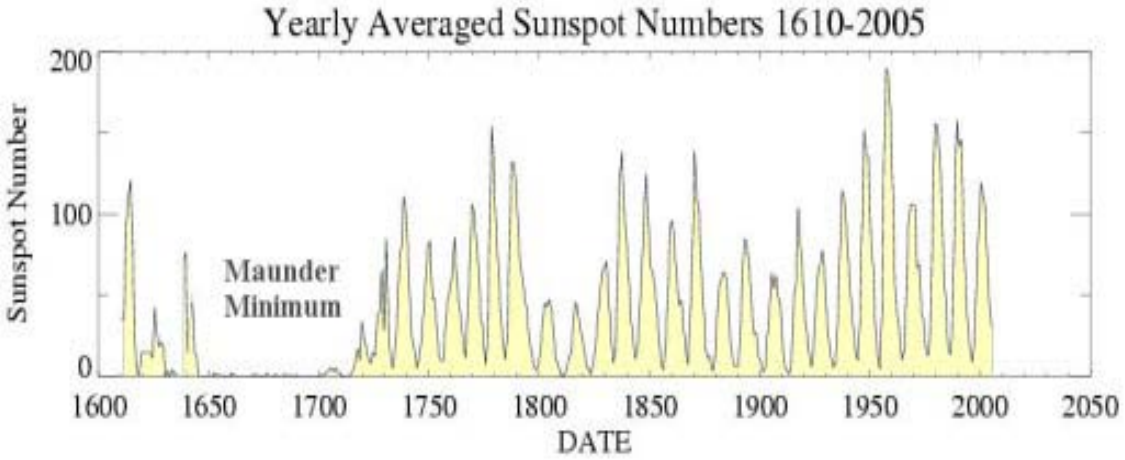

Figure 1.3. A sunspot cycle plot which shows the Maunder Minimum from 1645 – 1715 when there were few sunspots.

The sunspots have a bipolar structure in which there is a “leading” spot and a “following” spot. The line joining the centers of the leading and following spots is not usually quite

aligned along a constant latitude, but is slightly tilted on average by about 12°, such that the leading spot is closer to the equator. Figure 1.4 shows a sunspot group in Solar Cycle 23 in the northern hemisphere. The major leading sunspot is on the right with north (N) magnetic polarity, and the major following sunspot is on the left with south (S) polarity. For the bipolar sunspots in the southern hemisphere, the polarities are opposite to those in the northern hemisphere.

The sunspots consist of a central dark portion called the umbra, in which the magnetic field is about normal to the surface. The magnetic field is normally very strong in the umbra, in the range ~0.15 to 0.35 T. The umbra is surrounded by a lighter portion called the penumbra, in which the magnetic field is roughly parallel to the surface [*Solanki*, 2003].

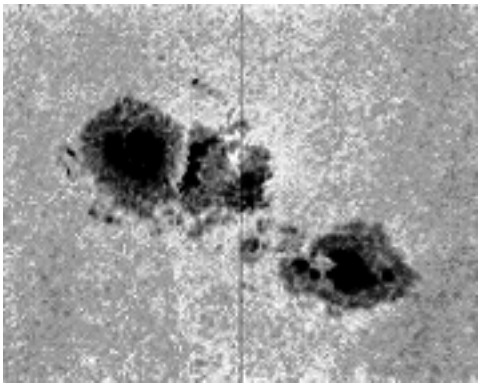

Figure 1.4. A sunspot group in Solar Cycle 23 in the northern hemisphere.

Solar flares are large explosions in the corona. Figure 1.5 shows the development of a flare. In the flare, magnetic reconnection occurs between antiparallel magnetic fields in the "open" field line region above the top of the closed magnetic loops. The reconnection region is labelled "flare origin" in Fig. 1.5. Electrons accelerated by the conversion of magnetic to particle kinetic energy travel down to the chromosphere, and heat the footpoints, producing two Hα emission ribbons. The reconnection site moves upward, causing the accelerated electrons to go downward along the more separated field lines, resulting in two bright separated Hα ribbons that move away from each other. Other particles go outward, resulting in radio bursts. Also, the energy release heats the flare site to tens of millions of degrees and causes extensive x-ray emission.

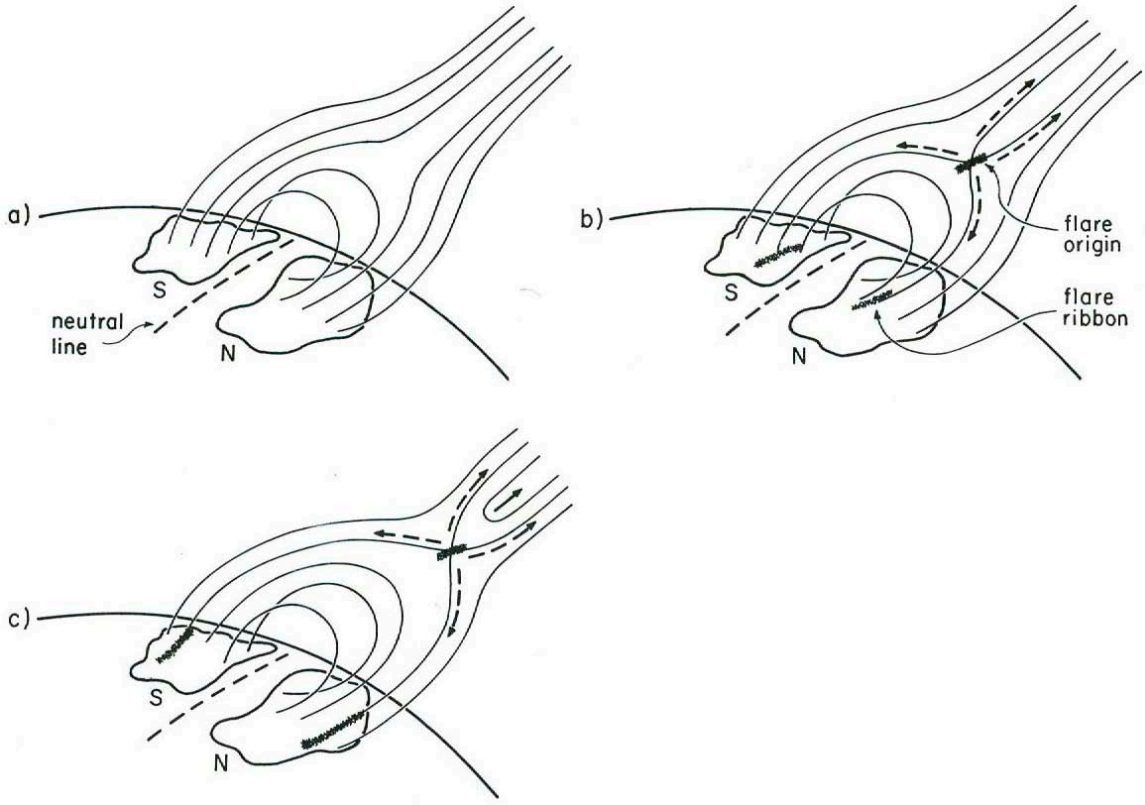

Figure 1.5. Sketches of development of a flare. (a) The pre-flare structure includes magnetic loops connecting north and south poles, and separated by a neutral line. (b) The onset of a flare when reconnection takes place between the oppositely directed field lines above the loop. Magnetic energy is released, accelerates elections and ions to high speeds, and also heats the flare site to tens of millions of degrees producing x-rays. Some of the electrons go down along the field lines to the chromospheres/photosphere, and heat the footpoints, producing two Hα emission ribbons shown cross-hatched. Other particles go outward, resulting in radio bursts. (c) Later, the reconnection site moves upward, and the electrons go down along more separated field lines, causing the Hα ribbons to move away from each other (taken from *Noyes* [1982]).

The solar flares have significant effects on the Earth. As shown in Figure 1.6, these effects can be divided into simultaneous effects and delayed effects. The "simultaneous" effects involve the electromagnetic radiation generated by the flare, while the delayed effects result from the accelerated particles from the flare, both in cosmic ray production and in the electrons and ions that flow in the enhanced solar wind. On the Earth, magnetic storms and auroral displays follow large solar flares after a delay of a day or two. When sunspots are absent, there are no solar flares, and also few auroras. For example, there were few auroras reported during the Maunder Minimum [*Noyes*, 1982].

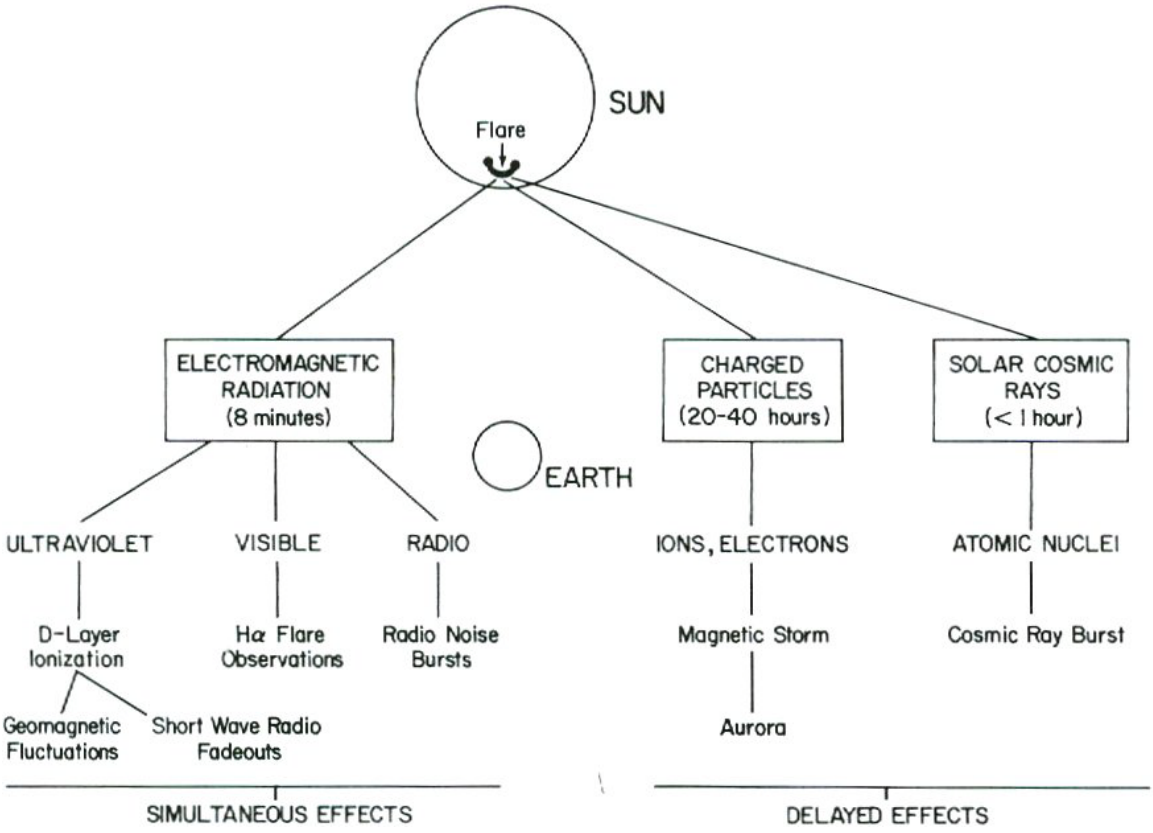

Figure 1.6. The main effects of solar flares on the Earth (taken from *Noyes* [1982]).

1.2.3 Solar wind, IMF and sector structure

In this thesis work, we have studied the solar wind, its IMF and sector structure, and these are discussed in detail in Chapter 3.

1.3 The Current Deep Sunspot Minimum

We are now in an unusual period during the deep solar minimum between Solar Cycles 23 and 24. The current solar minimum is unusually long. There have been 750 days without sunspots through Nov. 10, 2009, compared with 485 days without sunspots in a typical solar minimum. The solar wind is in a uniquely low energy state [*Fisk and Zhao*, 2009]. As a result, the normal location of the auroral zone has shifted to higher latitudes, where the recently built PolarDARN radars are fortunately in optimum locations to study the poleward portion of the auroral oval and the polar cap during such solar minimum conditions.

As shown in Figure 1.7, there were 266 spotless days (73%) in 2008, the year of the second most spotless days of the past century. The year 2009 had 260 spotless days

(71%), slightly less than the 266 spotless days in 2008, both being less than the 311 spotless days (85%) in 1913.

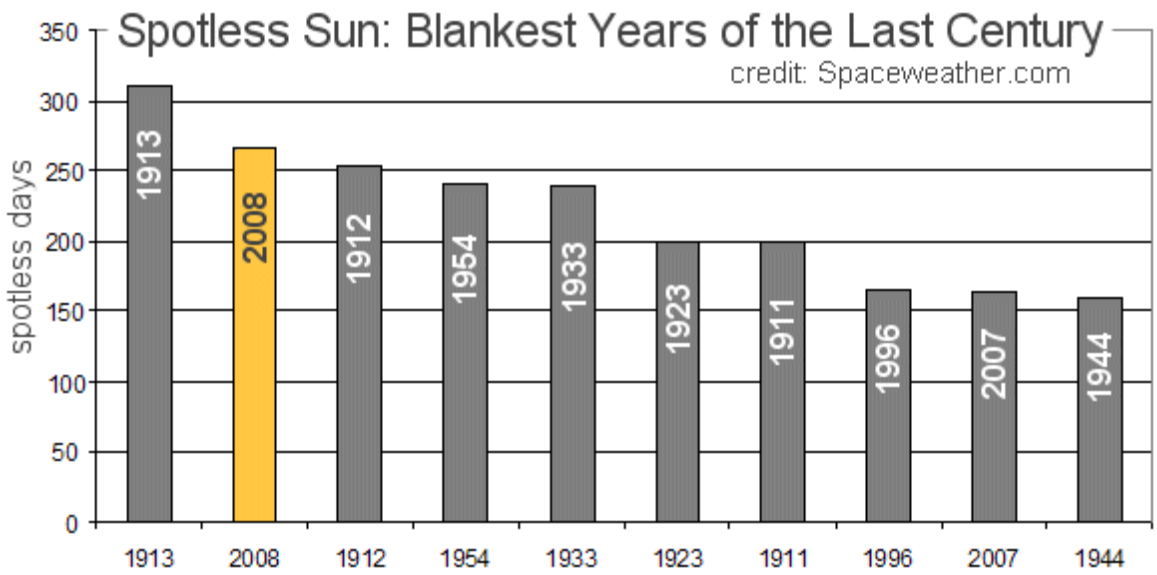

Figure 1.7. The top ten years of most spotless days since last century (taken from spaceweather.com).

As measured at Kitt Peak, Arizona, by the high-resolution solar telescope and an attached infrared spectrometer measuring the Zeeman splitting of the Fe I 1564.8 nm line, there has been a progressive decrease in the umbral magnetic field strength and the area of the sunspots since 1992, showing that the sunspot activity has greatly decreased [*Penn and Livingston*, 2006; *Livingston and Penn*, 2009]. Figure 1.8 (b) shows that the maximum sunspot field strength has decreased with time independent of the solar cycle. The sunspots exist when the magnetic field strength is greater than about 1500 Gauss. A linear fit of the data suggests that we may experience a dearth of bipolar sunspots by 2015. The question is now whether we are approaching a period like the Maunder Minimum from 1645 to 1715 when the Sun was in a period of low activity with few sunspots. Most of the recent sunspots have not been bipolar spot groups but have been tiny single "pores" consisting of a small umbra and lacking a penumbra.

Figure 1.8 (a) shows the relationship of the umbral magnetic field strength and infrared intensity. Both Figure 1.8 (a) and (b) show data for the same spots. The sunspot field strength, measured by using the Zeeman splitting of the Fe I 1564.8 nm line, is weaker now as shown in Figure 1.8 (b), whereas the infrared intensity has been increasing with time [*Livingston and Penn*, 2009].

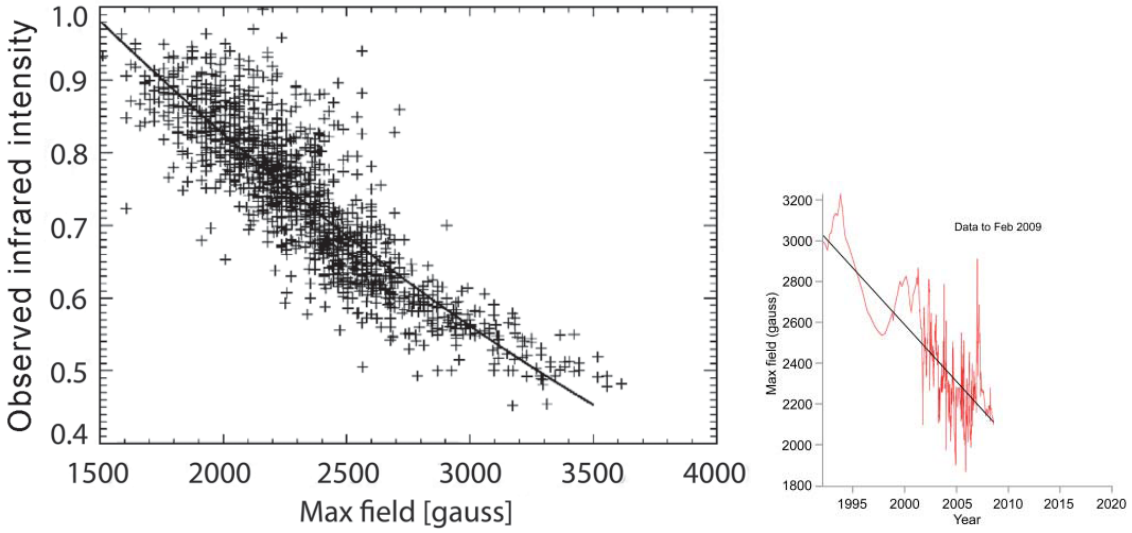

(a) (b)

Figure 1.8. (a) The observed infrared intensity in the darkest place of the umbrae as a function of the magnetic field strength for 1392 sunspots during the time period 1992 to February 2009. The black line shows the quadratic fit to the data (taken from *Livingston and Penn* [2009]). (b) The maximum sunspot field as a function of time in the interval 1992 to February 2009. The red line shows a-12 point running average. Its linear fit line is shown in black (taken from *Livingston and Penn* [2009]).

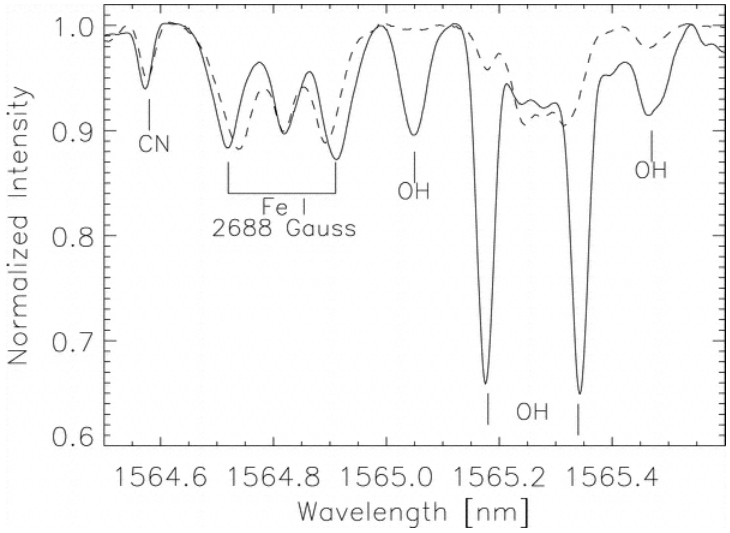

Figure 1.9. The solid line shows the sunspot umbral spectrum on September 18, 1998, while the dashed line shows the sunspot umbral spectrum on December 27, 2005. The two spectra are normalized to the same continuum intensity. The reduction with time of the Zeeman splitting of the Fe I 1564.8 nm line is clearly seen. Also shown are absorption lines of CN at 1564.6 nm, and OH at 1565.2, 1565.4 nm, 1565.1 and 1565.5 nm (taken from *Penn and Livingston* [2006]).

Figure 1.9 compares spectra taken near 1565 nm 1998 and 2005. The solid line shows the sunspot umbral spectrum typical of the period around September 18, 1998. The Zeeman splitting is seen for Fe I 1564.8 nm absorption line, indicating the magnetic field strength to be 2688 G. To the blue side of it, a weak CN 1564.6 nm absorption line is seen [*Wallace and Livingston*, 1992]. Two very strong OH absorption lines are seen at 1565.2 and 1565.4 nm, mixing with a Fe I 1565.3 nm line, and two weaker OH absorption lines are seen at 1565.1 and 1565.5 nm. In Figure 1.9, the dashed line shows a sunspot umbral spectrum typical of the period around December 27, 2005. The splitting of Fe I 1564.8 nm line indicates that the magnetic field strength is only 2180 G. The OH absorption lines are much weaker because of the increased in temperature in the umbral region. The CN 1564.6 nm absorption line is about the same. The changes indicate that the umbral regions in 2005 have a higher temperature [*Penn et al.*, 2003] and a weaker magnetic field strength [*Penn and Livingston*, 2006]. *Penn and Livingston* [2006] report that in the period 1998 – 2005, the mean magnetic field strength in the umbral regions has been decreasing at 52 G per year, while the umbral temperatures have been increasing about 73 K per year. As reported in EOS on July 28, 2009, *Livingston and Penn* [2009] assert that the earlier trend has continued from 2005 – 2009.

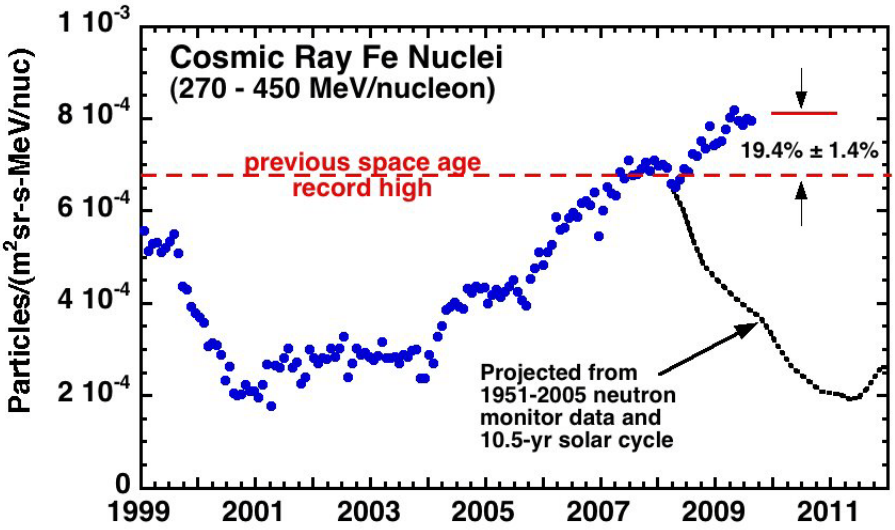

Figure 1.10. In 2009, the cosmic ray flux was higher by 19% than the previous space age record, in terms of Cosmic Ray Fe Nuclei measured by Cosmic Ray Isotope Spectrometer on NASA's ACE satellite (taken from *Phillips* [2009]).

Galactic cosmic rays (GCRs) are very energetic subatomic particles composed of protons and some heavy nuclei. They enter the solar system from outside, and are shielded by the heliosphere because the heliospheric magnetic field deflects the cosmic rays. As a result, the cosmic ray level increases (this is known as a Forbush increase) when the solar activity decreases. Due to the current deep solar minimum, the cosmic ray intensities are higher by 19% in 2009 than the previous space age record, as shown in Figure 1.10.

The cosmic ray flux in the past can be estimated by the record of the radioactive isotope of beryllium, $^{10}B_e$, which is produced when the cosmic rays enter the atmosphere and which is subsequently preserved in the polar ice. The ice record shows that the cosmic ray levels were sometimes at least 200% - 300% higher in the past few hundred years than the Space Age record of the past fifty years.

In the current solar minimum, three features have contributed to the rise of cosmic ray intensities [*Phillips*, 2009].

1. The solar wind IMF (Interplanetary Magnetic Field) has decreased. It is down to about 4nT, compared with the average IMF of 6-8nT. As a result, the heliospheric magnetic field is lower (and the size of the heliosphere is also smaller). There is therefore a Forbush increase in cosmic ray intensities.

2. The solar wind has become weak. The lowest solar wind pressure in the past 50 years causes the heliosphere, namely the magnetic bubble containing the solar wind, to become smaller. As a result, the path of the cosmic rays in the heliosphere to the Earth is shorter. In the heliosphere, the solar wind flows away from the Sun while the cosmic rays enter from outside the heliosphere and on the average are going toward the Sun. The cosmic rays thus go upstream in the solar wind. Since the solar wind speed has dropped, it is easier for the cosmic rays to penetrate deeper into the heliosphere.

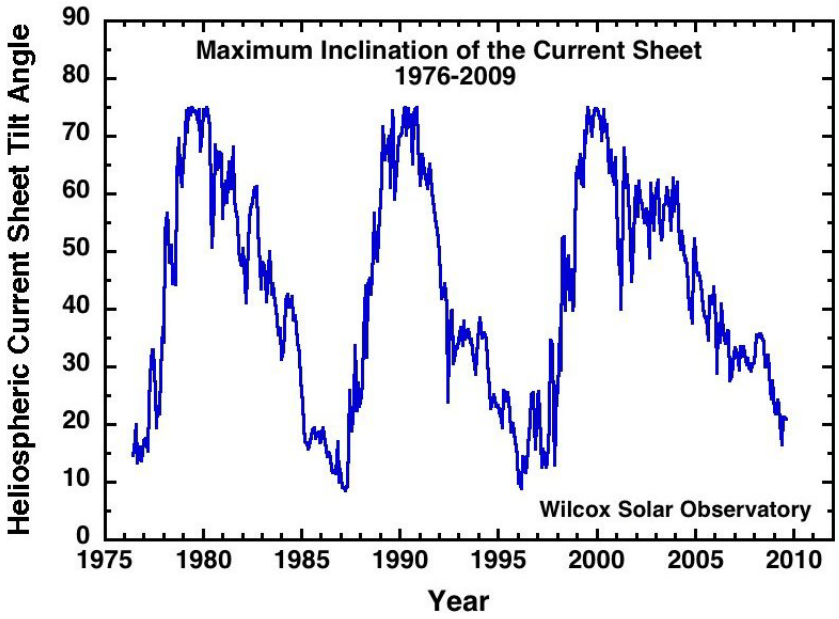

Figure 1.11. The maximum inclination of the current sheet in the interval 1976 (taken from *Phillips* [2009]).

3. The heliospheric current sheet becomes less warped. As shown in Figure 1.11, the maximum inclination of the heliospheric current sheet (HCS) has an 11-year cycle corresponding to the solar cycle, and reaches the minimum values in the solar minimum

periods. The cosmic rays tend to follow the undulations of the heliospheric current sheet, and since these undulations are flattening out, the cosmic rays reach the Earth more directly.

If the current sheet tilt angle keeps decreasing, the cosmic ray intensities may reach values higher by 30% than the Space Age record [*Phillips*, 2009].

1.4 Relationship between space weather and normal meteorological weather

Two kinds of energy from the Sun reach the Earth. One is the radiant or EM energy which is roughly that from a blackbody at 5785 K. This effective blackbody has an output power of 3.86×10^{26} W, or an irradiance over its surface (a sphere of radius 6.96×10^{8} m) of 663.5 MW m^{-2}. At the distance of Earth, this irradiance becomes 1366 W m^{-2}, often referred to as the solar constant, or the Total Solar Irradiance (TSI). The word "constant" above is not actually the case, as the TSI is believed to vary during a sunspot cycle, but the variation is small, about 0.1 %, or roughly 100 TW. On the other hand, it is also the case that the irradiance at the shortest wavelengths can vary by several percent, reaching a minimum at the solar cycle minimum. The other energy output is carried by solar wind in two forms: the kinetic energy of fast-moving (~400 – 2000 km/s) charged particles (mostly H+, He++ and electrons e-), which is estimated to be 10 TW, and the magnetic field energy in the Interplanetary Magnetic Field (IMF), which is small (about 1% of the kinetic energy). The energy in the solar wind is much more variable over the solar cycle and is very bursty during intense solar activity, such as that during the occurrence of strong magnetic regions, sunspots and solar flares, as was illustrated in Figure 1.6. There can even be solar cosmic radiation and some nuclear energy release from the solar flare activity.

Both types of solar energy, the TSI and the solar wind, influence the weather. It is most obvious that the EM energy plays a role, as solar heating is important to warm the Earth and produce the high and low pressure systems. However, there is increasing recognition of the effect on the climate of the changing solar wind conditions that result from the strong solar variability during the solar cycles. It should be noted, however, that there is considerable controversy about the contribution of sunspot-cycle-related solar variability to the climate, and that is largely because the physical processes by which that variability is transferred from space to the atmosphere have not been identified definitively. One obvious mechanism is the effect of GCRs on the global electric circuit [*Feynman et al.*, 1964] because these cosmic rays produce "air showers" of secondary charged particles which not only directly increase the conductivity of the circuit but which can provide enhanced nucleation centers for clouds, and clouds (particularly thunderclouds) are the batteries that drive the current in the global electric circuit [*Tinsley*, 2008; *Ram et al.*, 2009]. *Girish and Eapen* [2008] have also shown that the lightning occurrence rate at the magnetic dip equator near Trivandrum, India, has an inverse relationship with sunspot number.

Direct solar observations have been made since 1610 when Galileo invented the telescope and were made routinely following the opening of observatories, such as the Paris

observatory in 1845. A more formal measure in the form of the sunspot number arose from the work of Heinrich Schwabe [1843] and Rudolf Wolf after 1843. Aside from the direct telescope observations, tree rings contain valuable information because of the presence of ^{14}C resulting from GCR. Because the tree rings are thin in the cold years when growth is slow, scientists have studied tree rings to examine the relationship between the solar activity and the weather, and to estimate the historical solar activity. A significant 22-year cycle in tree rings [*Stockton and Meko*, 1975] is closely in phase with the solar cycle [*Mitchell et al.*, 1979].

When the cosmic rays enter the atmosphere, they interact with molecules such as CO_2 to produce the radio-carbon isotope ^{14}C. The effect of the solar activity on the cosmic rays is similar to that of ^{10}Be mentioned above, so the ^{14}C level in the tree rings is as an effective indicator of the solar activity.

Although there is no obvious evidence of the short-term 11-year cycle in ^{14}C in the tree rings, long term effects are studied to explore the solar history [*Eddy*, 1976]. Three significant periods have been noted when changes in the $^{14}C/^{12}C$ ratio are likely to be related with the solar activity: a low ^{14}C period in about AD 1200 implying high solar activity, and two high ^{14}C periods in about AD 1500 and AD 1700 implying low solar activity. These increases of ^{14}C are called "DeVries Effects", first found in 1958 [*de Vries*, 1958].

The low ^{14}C period is called the Grand Maximum (1100 - 1250), when there were more sunspots and northern lights. The two periods of "DeVries Effects" are called the Maunder Minimum (1645-1715) [*Eddy*, 1976] and Spörer Minimum (1460-1550), when there were few sunspots or northern lights [*Eddy*, 1977b].

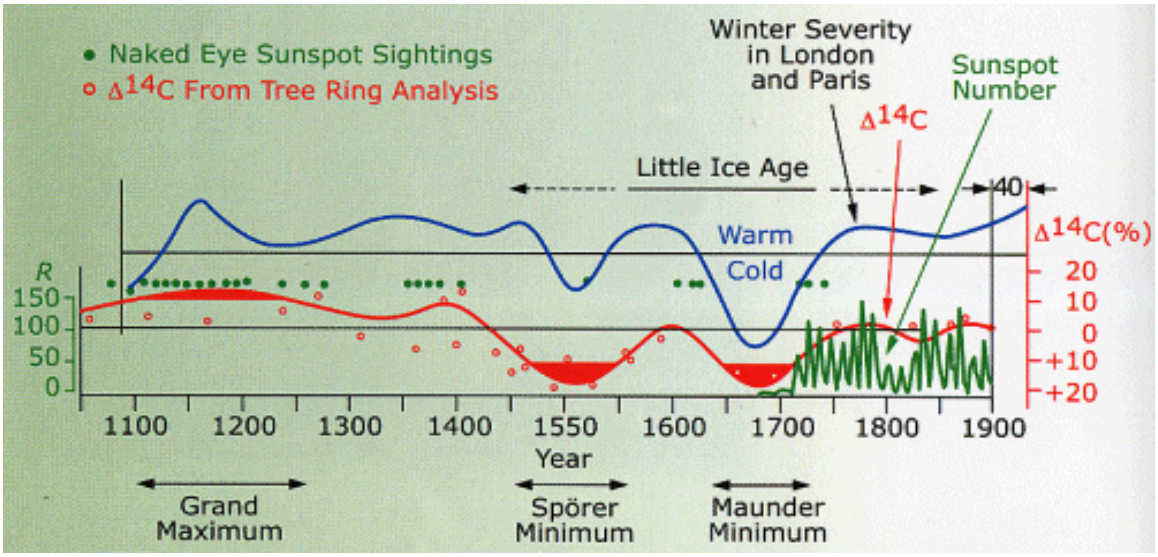

Figure 1.12. The blue line shows the global temperature in the past 800 years. The red line shows the ^{14}C from the tree ring analysis (note that the red scale on the left of the ^{14}C is inverted, with positive values downward, and that the minus signs are missing from the top values of -20 and -10). The green line shows the sunspot number. Also shown are the Grand Maximum, the Spörer Minimum and the Maunder Minimum.

These long-term changes in solar activity appear to have influenced the global climate [*Eddy*, 1977a]. The Maunder and Spörer Minima are amongst the two coldest periods of the past 1000 years, and their combination is simultaneous with "The Little Ice Age" [*Gates and Mintz*, 1975]. The modern distinctively high solar activity may be one of the reasons for the present period of global warming [*Eddy*, 1978].

Figure 1.12 shows the relationship between the solar activity and Earth's weather. During the Grand Maximum (1100 - 1250), the global temperature reached a maximum and less ^{14}C was in the tree rings, while during the Spörer and Maunder Minimum, the global temperature reached a minimum and more ^{14}C was in the tree rings.

It is worthwhile to mention an important recent statistical study of the global short-term (less than the 11-year solar cycle period) average temperature variation on the Earth. It was found by *Scafetta and West* [2008] that the short-term temperatures follow a Lévy distribution $P(t) \approx A/t^{\alpha}$, where t is the time between successive events and A is a normalization constant. It is well-known in statistical physics that if two quasi-related processes are found that both have Levy distributions, which are unusual non-equilibrium distributions to begin with, and if they both have similar values of the index α, then it is virtually certain that the two processes are closely related physically. When *Scafetta and West* [2008] began looking for another process that had a Levy distribution, they found that solar flare events had such distributions. Furthermore, the index α is 2.14 for the solar flares and 2.11 for the global short-term air temperatures. These nearly equal indices α are a measure of the complexity matching effect [*Allegrini et al.*, 2007; *Aquino et al.*, 2007], and indicate that the global short-term temperature variation appears to respond to the Sun's variability as reflected in the incidence of solar flares during solar cycles. This is perhaps not too surprising because, as noted by *Noyes* [1982], the total flare energy released in EM radiation and particle energy is about 10^{25} J, which is the energy that would be consumed by the US in 100,000 years, if it were consumed at the 1980 consumption rate. On the basis of this finding, *Scafetta and West* [2008] came to a conclusion which led to considerable criticism of their work (there are five letters of criticism in the "letters" section of the October, 2008, issue of Physics Today), namely that their results showed a relationship to the TSI. However, from the right side of Figure 1.6, it is clear that solar flares result in a large amount of energy being fed to particles and hence to stronger solar wind and its accompanying effects such as stronger IMF and magnetic storms. Although the energy in the solar wind is about 10^4 times less than the TSI, reconnection can act as a trigger for magnetic storms and/or substorms which release large amounts of energy stored in magnetospheric particles and the distorted geomagnetic field. As stated by *Noyes* [1982], "It may be that geomagnetic interactions with the magnetized solar wind somehow trigger much more energetic processes that do have the capability to affect weather or climate." If *Scafetta and West* [2008] would have related the short-term temperature fluctuations on the Earth to the solar wind/IMF solar cycle variability and reconnection rather than to TSI variability, their work might have been subjected to much less criticism.

Two phenomenological solar signatures (PSS) of climate are reconstructed based on the inclusion of the short-term temperature statistics into the long-term temperature records [*Scafetta and West*, 2007]. In Figure 1.13, from 1950 to 2010, the 11-year and 22-year

cycles are shown in the smoothed global temperature, consistent with 11-year and 22-year cycles in the PSS. We should note that since 2002, Figure 1.13 shows that the global temperature is decreasing instead of increasing, which may partly be due to the decreased solar activity between the solar maximum year of 2001 and the solar minimum conditions of ~2007. Firgure 1.13 shows that the effect of solar variability can account for as much as 69% (red curve) or as little as 25% (blue curve) of the increase of the global average temperature [*Scafetta and West*, 2007]. The effect of global warming might be diminished if the solar activity continues to decrease in the next decades as some solar scientists predict [*Scafetta and West*, 2008; *Penn and Livingston*, 2006; *Phillips*, 2009].

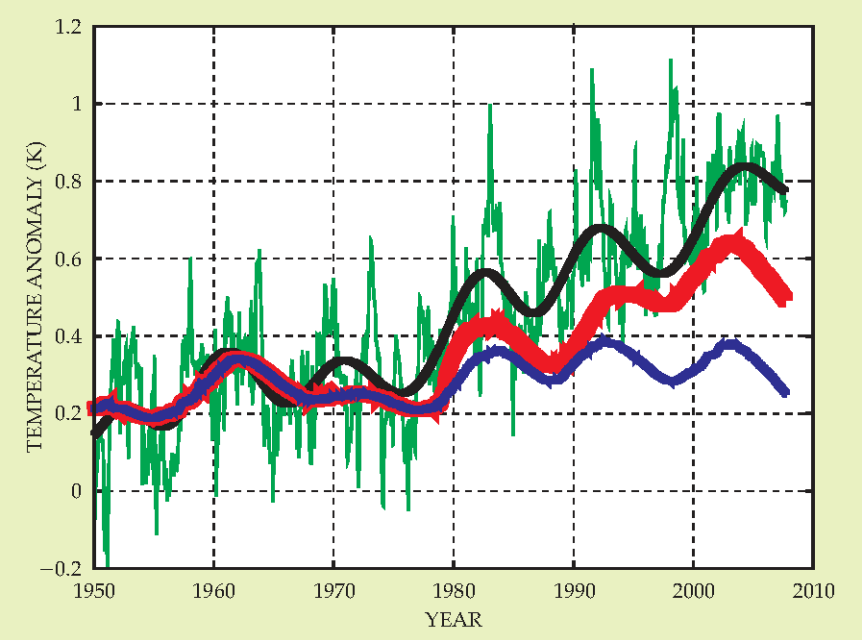

Figure 1.13. The green line represents the measured global surface temperature (GST) subtracting the averaged GST from 1890 to 1910; it stresses the observed global warming since 1900. The GST anomaly data are low-pass filtered to eliminate volcanic signals. The smoothed data as a black line shows 11-year period. Red and blue lines represent two new PSS constructions incorporating the short-term temperature statistics into models which had not contained them, namely a data series taken from http://www.cru.uea.ac.uk and http://www.acrim.com for the red line and another from http://www.pmodwrc.ch for the blue line (taken from *Scafetta and West* [2008]).

In Figure 1.14, the global temperature record from the Climate research Unit of the University of East Anglia shows that the temperature had risen since 1970 until the last 4 years, when there has been a decrease. However, 2008 is still the 10th warmest year on record.

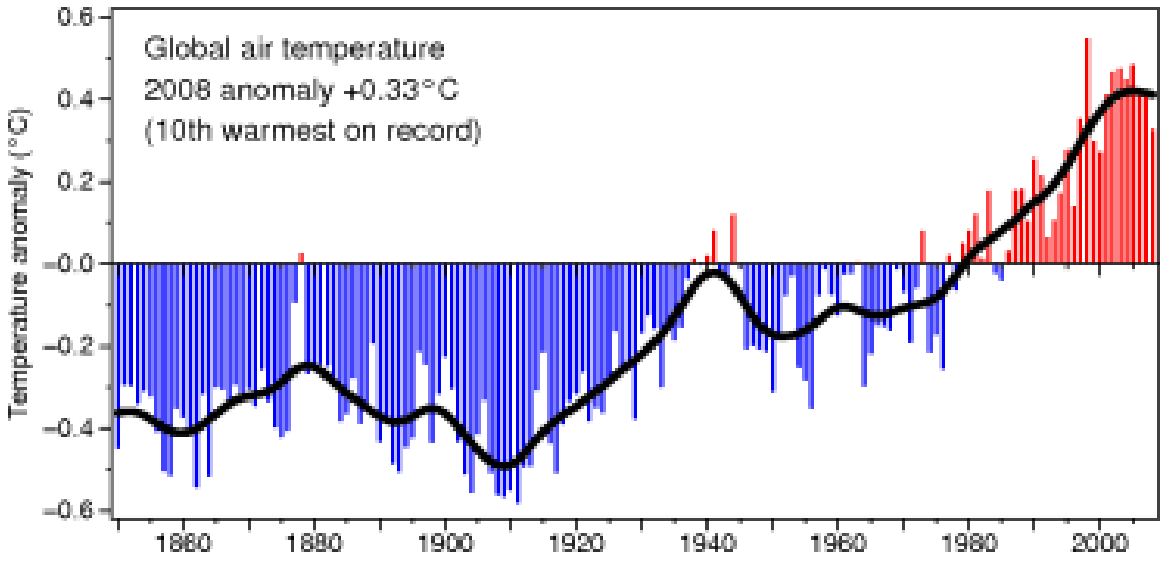

Figure 1.14. Annual average of HadCRUT3v [*Brohan et al.*, 2006] temperature in the interval 1850 to 2008.

During the recent decades, the global temperature variation appears to be affected by two about equal factors: the anthropogenic factor (pollution by greenhouse gases) and the solar variability factor. The greenhouse gases heat the Earth, but the weak solar activity during this solar minimum period may be exerting a cooling influence, the result being a stoppage of the global temperature rise since about 2004, as shown in Figure 1.15. The next solar cycles 24 and particularly 25 are predicted to be weak, which could either prevent the global temperature from rising as rapidly as during the decade before 2002 or even lead to a cooling.

Recently, *Khachikjan et al.* [2009] studied the correlation between Storm Sudden Commencement (SSC) occurrence, IMF sector polarity and ENSO climate cycles, and discovered a further relationship between solar activity and the Earth climate, in particular the El Nino cycles. This work will be discussed in Section 3.1.4 and shown in Figure 3.22 in chapter 3.

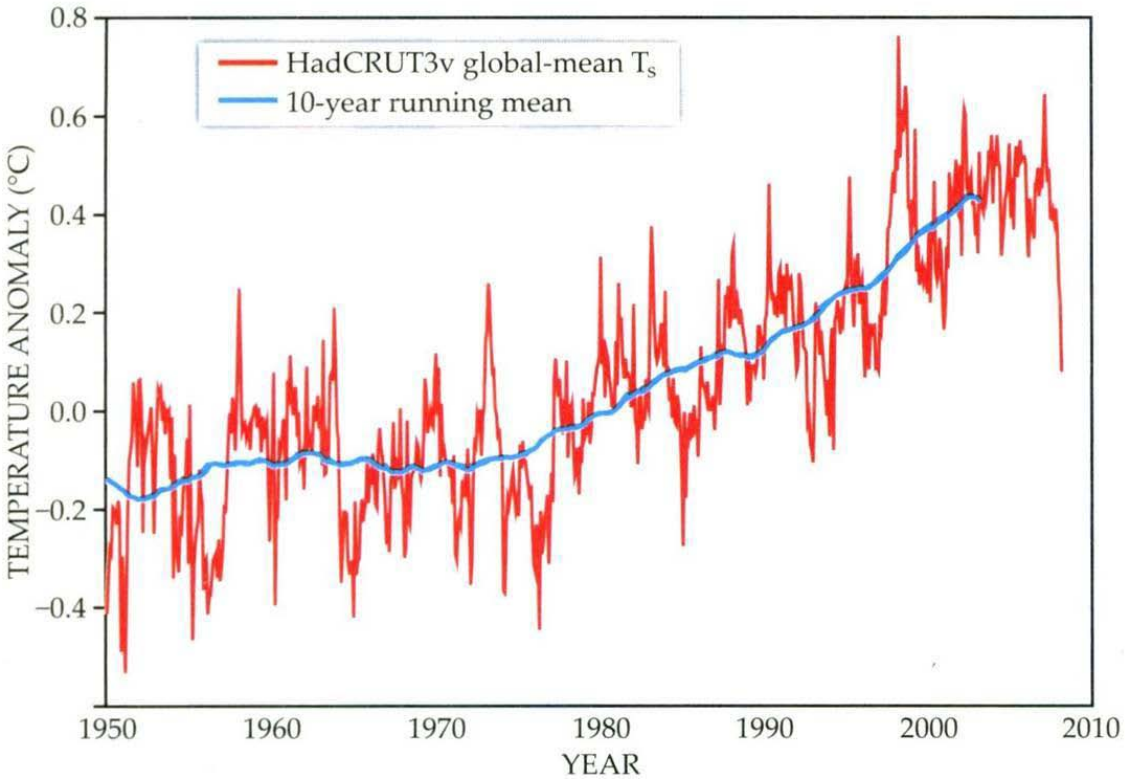

Figure 1.15. The measured monthly global temperature anomalies. The red line shows the HadCRUT3v data of global average near surface temperature, whose 10-year running mean is shown as the blue line. The data are from the Climate Research Unit, University of East Anglia, UK (taken from *Duffy et al.*, [2009]).

1.5 Reconnection

1.5.1 Reconnection and its historical basis

Reconnection is one of the most important processes by which magnetic energy is transformed to particle energy.

Early solar observations [*Giovanelli*, 1947; *Hoyle*, 1949] suggested that solar flares took place near the magnetic neutral line associated with the acceleration of particles. *Dungey* [1953, 1958] introduced the idea of magnetic reconnection in the solar flares. He suggested that the diffusion of the magnetic field in a thin current sheet between antiparallel magnetic field regions resulted in the field lines forming an "X-line" and reconnecting with each other, causing the release of magnetic energy to heat and accelerate the particles. Dungey suggested later that this same type of reconnection also happened between the southward IMF and the northward field lines on the dayside of the Earth's magnetosphere. *Sweet* [1958] also was aware that two oppositely directed magnetic field could press together in a plane sheet current to make a reconnection configuration. *Sweet* [1958] and *Parker* [1957] proposed the first reconnection theory but

it had the disadvantage that the reconnection rate was too slow. The Sweet-Parker theory was followed by a nonlinear magnetohydrodynamic (MHD) theory by Petschek in which the reconnection was much faster and enabled a large energy transformation in a short time [*Petschek*, 1964, 1966].

Dungey [1961] introduced two types of reconnection in the Earth's magnetosphere: the reconnection between southward IMF and closed field lines on the dayside and North and South lobe lines on the nightside, which drove two convection cells in the magnetosphere. *Russell* [1972] then proposed reconnection between northward IMF and lobe (north lobe or south lobe) magnetic field lines, which drove lobe cells. It was not until 1999 that Tanaka proposed the fourth type of reconnection, namely reconnection between lobe (north lobe or south lobe) lines and closed field lines [*Tanaka*, 1999]. At the University of Saskatchewan, Watanabe has developed a three-dimensional (3D) steady-state reconnection topology which includes all four types of reconnection in the null-separator model [*Watanabe et al.*, 2007; *Watanabe and Sofko*, 2008]. We will discuss these theories in more detail below.

1.5.2 Sweet-Parker (slow) and Petschek (fast) Reconnection

Two oppositely directed magnetic fields pressing together across a plane central current sheet constitutes the reconnection configuration [*Sweet*, 1958]. When the plasma pressure in the dotted current sheet region in Figure 1.16 (c) (called the diffusion zone) is not strong enough to separate the two opposite fields, the fluid is squeezed from in between, and the two fields move toward each other. The gradient of the magnetic field steepens, and the current density becomes very large, resulting in strong resistive dissipation. The dissipation in the thin layer between the opposite fields breaks the magnetic lines of force, which diffuse across the resistive layer and reconnect. The fluid is accelerated away and parallel to the plane of the resistive layer by the Maxwell stresses in the new field configuration. New plasma and magnetic flux move forward to recruit the vacancy and reconnect [*Kennel*, 1995].

Sweet [1958] and *Parker* [1957] used an MHD model to propose the first reconnection theory, which applied a simplification of a two-dimensional, steady state reconnection and incompressible plasma. As shown in Figure 1.16 (a), they suggested the reconnection took place in a current sheet with the global length L_e of the reconnecting magnetic field. The plasma entered the current sheet at a speed about

$$v_e = v_{Ae} S^{-\frac{1}{2}} \tag{1.1}$$

in which $S = \mu_0 L_e v_{Ae} / \eta$ is the Lundquist number, the ratio of the time scales of Alfvén waves to the resistive diffusion. The permeability of free space is μ_0, η is electric resistivity, L_e is the global magnitude length of the current sheet, and $v_{Ae} = B_e / \sqrt{\mu_0 \rho_e}$ is the Alfvén speed in the inflow area. The magnetic field is B_e, and ρ_e is the plasma mass density. The plasma flows out from the current sheet at the Alfven speed v_{Ae}. The electric field E, which is perpendicular to the plane of Figure 1.16 (a), is proportional to the reconnection rate, and determines the rate at which the magnetic flux flows to another topological region [*Vasyliunas*, 1975]. Thus the Alfvén Mach number, $M_{Ae} =$

$v_e/v_{Ae} = E/(v_{Ae}B_e)$, effectively represents the reconnection rate normalized by the "characteristic field" $v_{Ae}B_e$. The Sweet-Parker reconnection rate is thus $M_{Ae} = S^{-\frac{1}{2}}$. However, S is huge ($S \gg 10^6$) in solar and space plasmas, with the result that the reconnection rate is too slow to explain the rapid and extensive release of energy in solar flares.

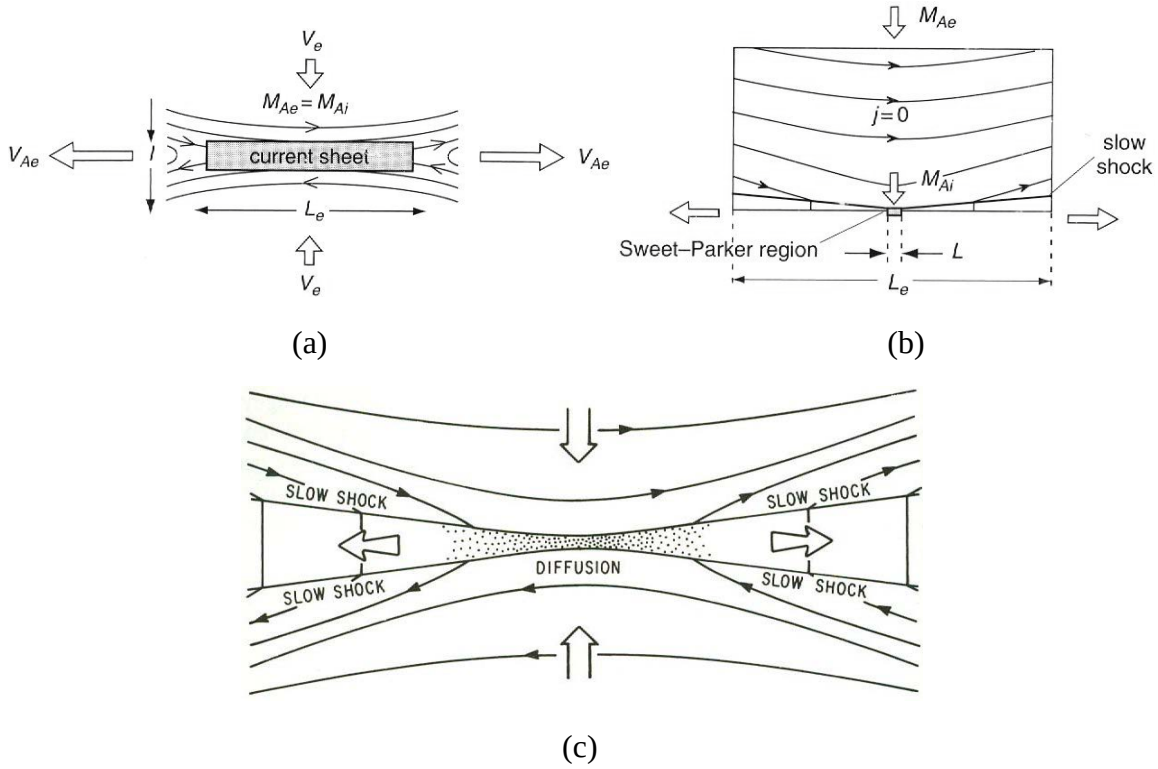

Figure 1.16. (a) The Sweet-Parker reconnection. The plasma enters the current sheet with a length L_e from above and below at a speed v_e, and flows out from the current sheet through the tips of the sheet width l at a speed v_{Ae}. The magnetic field is considered to be uniform in the inflow area, so the external Alfvén Mach number, M_{Ae}, at large scale and the internal Alfvén Mach number, M_{Ai}, at the midpoint edge of the current sheet, are equal (taken from *Forbes* [2007]). (b) Petschek reconnection (*Petschek* [1964]). The panel (b) (taken from *Forbes* [2007]) shows the simplest Petscheck MHD reconnection configuration, namely antiparallel magnetic fields on each side of the reconnection current sheet that becomes the "diffusion layer". The length of the current sheet L is much smaller than the global length Sweet-Parker region L_e. (c) Nonlinear behavior of Petschek reconnection (taken from *Petschek* [1964]). Two pairs of standing slow shocks emanate from the current sheet. The magnetic field in the inflow area decreases as the plasma inflow approaches the current sheet. The inflow plasmas then enter the diffusion layer where the magnetic fields disappear and the magnetic energy is converted to kinetic energy in the form of heating and outflowing particle kinetic energy (the reconnection jets). The plasma escapes and is accelerated by the magnetic tension across the slow shocks to approximately the Alfven speed.

As shown in Figure 1.16(b), *Petschek* [1964, 1966] introduced a new model in which the length L of the current sheet was much shorter than the Sweet-Parker model. This short current sheet L is put into the field of global magnitude length L_e. Two pairs of standing slow shock waves emanate from the end of the current sheet, and it is mainly these shocks which heat and accelerate the plasma to produce two reconnection jets.

Based on his assumption that the magnetic field in the inflow area is current free, that no large field sources exist on the large scale, and that the resultant shape of the inflow area is trapezoidal, Petschek concluded the magnetic field magnitude decreased logarithmically as it approached the current sheet. Petschek showed that the Mach number of the maximum reconnection rate was

$$M_{Ae[Max]} = \pi/(8lnS) \quad . \tag{1.2}$$

As a result of the logarithmic dependence on S, the Petschek reconnection rate was greater by several orders of magnitude than the Sweet-Parker reconnection rate. The value of M_{Ae} is about 10^{-1} to 10^{-2} for most cases, fast enough to allow the large and fast energy transformation in solar flares [*Forbes*, 2007].

1.5.3 Dungey and Interchange Types of Reconnection

The original idea for reconnection-driven convection was proposed by *Dungey* [1961]. Dungey had in 1953 introduced the X-line idea for explaining reconnection in the Sun. Dungey realized in the early 1960s that reconnection could be used to explain how the magnetosphere could develop large-scale two-cell convection, with dusk-side and dawn-side cells. These cells are attached to magnetic flux tubes which flow sunward at auroral latitudes, undergo reconnection as they cross the open-closed field line boundary (OCFLB) near noon into the open field line region, then flow antisunward on open field lines until reaching the nightside OCFLB near midnight. There they again take part in reconnection prior to reaching the auroral zone, where the flux tubes turn sunward and the cycle begins again. There are thus two reconnection regions, one on the dayside (equation 1 below) and one on the nightside (equation 2 below). The two equations are the basis of the "Dungey cycle" of flux transport, which requires that the lobe lines originally generated by reconnection on the dayside must travel antisunward over the polar cap to the nightside before reconnecting. The resulting closed field line can then travel sunward to the dayside, where it in effect replaces the original closed line that was lost in the initial reconnection. Figure 1.17 shows the Dungey cycle by means of the sequence of numbered field lines.

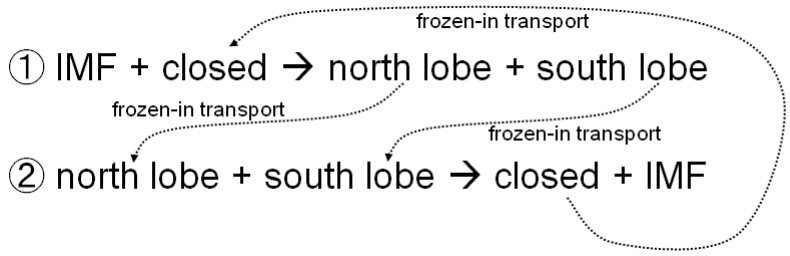

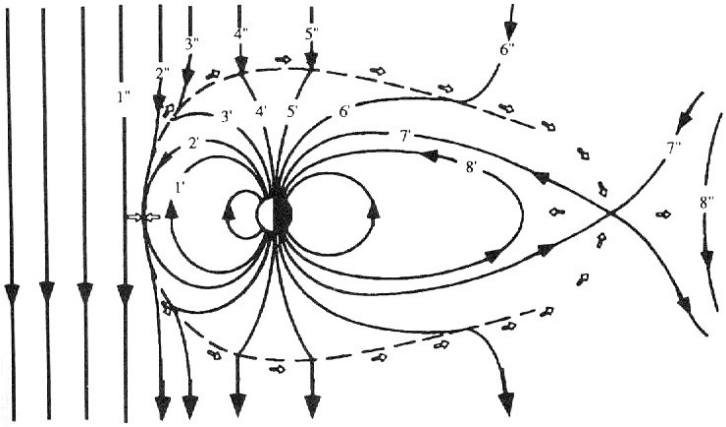

Figure 1.17. The Dungey cycle. Shown is the noon-midnight meridian plane, looking from dusk side. Solar wind comes from the left side. The field line portions marked 1", 2", … , are connected to the IMF in the solar wind, and the field line portions marked 1', 2', … , are connected to the Earth. At time 1, the closed field line 1' is flowing towards the magnetopause, and the IMF line 1" is coming from the Sun to the Earth. The dayside reconnection is between lines 2' and 2", producing north and south lobe lines which flow antisunward over the polar cap (3'-3", 4'-4", 5'-5", 6'-6"). The north lobe and the south lobe reconnect a second time (7'-7"), producing a closed field line and an IMF line. The closed line 8' flows sunward to 1', and a new cycle begins (taken from *Kennel* [1995]; based on *Dungey* [1961]).

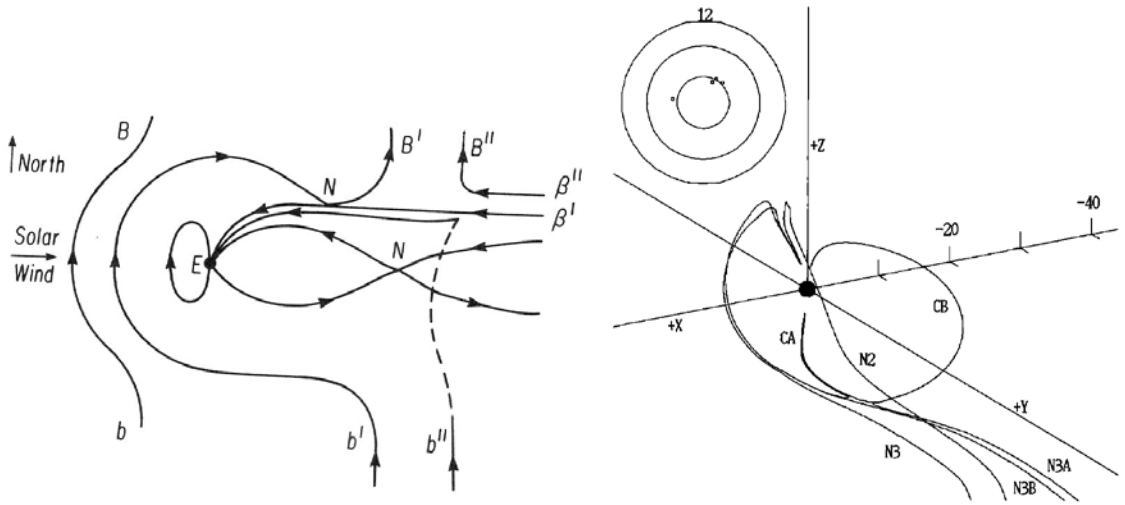

(a) (b)

Figure 1.18. (a) The solar wind comes from left as "B-b", and reconnects with the north lobe line "β^{I}" as "B^{I}-b^{I}", producing IMF line as "B^{II}-β^{II}" and north lobe line as "b^{II}" (taken from *Russel* [1972]). (b) A view showing north lobe to closed line reconnection. N3B and N3A are north lobe lines before and after the nightside reconnection. CB and CA are the closed field lines before and after reconnection (taken from *Tanaka* [1999]).

There are two other types of reconnection, which are known as interchange types of reconnection [*Crooker et al.*, 2002; *Watanabe and Sofko*, 2009a, 2009b]. *Russell* [1972] suggested that reconnection between northward IMF and lobe field lines (north lobe or south lobe) produces new lobe lines and IMF, as shown in Figure 1.18(a). This type of reconnection results in lobe cells which are inside the OCFLB in the ionosphere. *Tanaka* [1999] used a MHD simulation to show the fourth type of reconnection. Lobe (north lobe or south lobe) lines and closed field lines reconnect to produce new lobe and closed field lines, as shown in Figure 1.18(b).

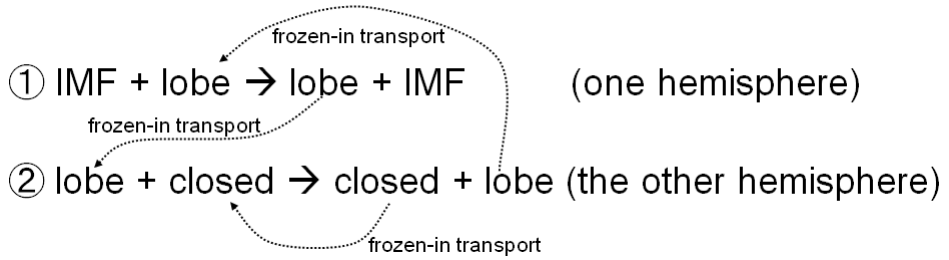

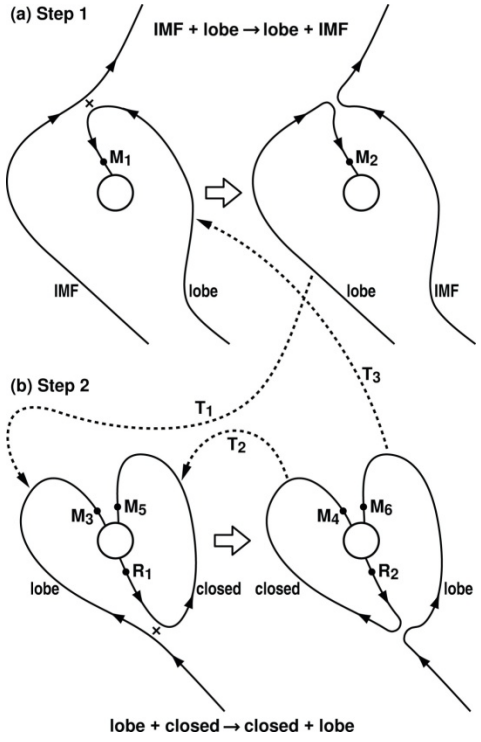

Figure 1.19. Shown is the interchange cycle, namely northward IMF to lobe (Russell-type interchange) in (a), followed by lobe to closed field line reconnection (Tanaka-type interchange) in (b). Solid lines show the magnetic field lines. Dashed lines show frozen-in transport of field lines during intervals between the reconnection events (taken from *Watanabe and Sofko* [2009c]).

Figure 1.19 shows how, for northward IMF, the interchange types of reconnection result in a new convection cycle that is naturally called "the interchange cycle". Step 1 involves the merging of northward IMF with lobe field lines in one hemisphere, producing new IMF lines and lobe draped-over lines. The latter take part in frozen-in transport and, in Step 2, merge with closed lines in the other hemisphere. The new closed lines undergo frozen-in transport to replace the original closed lines Step 2, while the new lobe lines engage in frozen-in transport to replace the lobe lines in Step 1.

Reconnection driven convection is associated with three types of convection cells: merging cells in which any streamline crosses the OCFLB twice, lobe cells which are driven by the IMF-lobe type of reconnection and result in convection cells completely in the region of open magnetic field lines, and reciprocal cells which are driven by the interchange closed line-lobe line type of reconnection equatorward of the polar cap and result in convection completely within the region of closed field lines.

1.5.4 Topological Representation of All Four Types of Reconnection in the Null-Separator Model

The three dimensional reconnection with guide field (along the x-axis) is shown in Figure 1.20. The figure shows the 3D picture of reconnection but, to reduce it to a 2D view which agrees with the more traditional "X-line" picture, panels a2 and b2 show the view of the reconnection as seen by an observer looking in the negative x-direction. In that view of the projection onto the yz plane, the X-line is obvious. Essentially, the two original magnetic field lines are antiparallel along the z-axis in the yz plane, with line 4-3 in the +z direction and line 1-2 in the –z direction. To maintain such an antiparallel field line geometry, there must be a current sheet which lies in the xz plane through the origin and for which the current points in the –x-direction. Because of some type of disturbance in the plasma, the field lines are forced together in the X-line region. The current is intense along the x-axis, and the non-ideal plasma in this so-called "diffusion zone" is such that the field lines essentially lose their identity. The final result of the interaction is shown 2D in panel b2, which shows that after reconnection, line 1 has joined to line 4, and line 3 to line 2. In the 3D model, the guide field lines are parallel along the x-axis in the diffusion region. In this configuration, the current, which is in the –x-direction, is antiparallel to the guide field, as indicated in panels a2 and b2. One essential point is that the reconnection electric field is always in the same direction as the current. This ensures that the inequality $\vec{J} \cdot \vec{E} > 0$ (in which the current density is $\vec{J}$ and the electric field is $\vec{E}$) applies to the reconnection process, which states that electromagnetic energy is being consumed or destroyed. Of course, by conservation of energy, the lost EM energy reappears as kinetic energy in two forms, first in thermal energy (heating) of the plasma and secondly in the bulk flow of the reconnection jets. As a result of the reconnection, the original field lines 1-2 (shown by a dashed line) and 3-4 (shown by a solid line) are transformed to new field lines 1-4 (shown by a dashed line) and 2-3 (shown by a solid line).

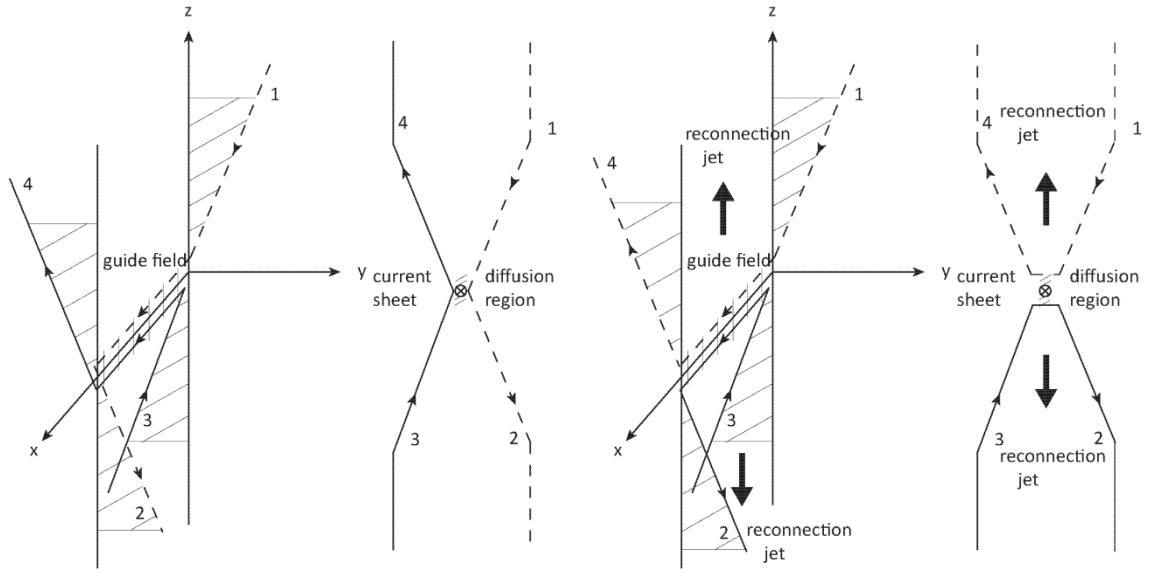

(a1) (a2) (b1) (b2)

Figure 1.20. Three dimensional reconnection with guide field (along x-axis). (a1) is a 3D view before reconnection, while (a2) is a view before reconnection in the yz plane. (b1) is a 3D view after reconnection, while (b2) is a view after reconnection in the yz plane.

In the null separator topology, the magnetosphere consists of the superposition of a dipole field (approximating the Earth's field) and a uniform field in a vacuum (approximating the IMF carried by the solar wind) [*Dungey*, 1963; *Cowley*, 1973; *Lau and Finn*, 1990]. Figure 1.21 shows separatrix surfaces of the topology for the superposition model of the magnetic field in a vacuum. The open field line region and closed field line region are separated by a surface topologically equivalent to a torus, which encompasses the Earth. The open field line region and IMF region are separated by a surface topologically equivalent to a cylinder, which is tangent to the torus along the Euclidean circle centered at the Earth's center. The circle consists of two opposite-sense magnetic field lines, separator l_1 and separator l_2, which connect the null points M and N on the circle, and hence the name "null-separator model". The torus surface above (below) the separator circle is called Separatrix β (α), while the cylinder surface above (below) the separator circle is called Separatrix γ (δ). All the field lines associated with Null M converge to Null M and are on Separatrix α and Separatrix γ, except for two singular lines, s_1 on Separatrix β and s_3 on Separatrix δ, which diverge from Null M and are perpendicular to Separatrix α and Separatrix γ near Null M. All the field lines associated with Null N diverge from Null N and are on Separatrix β and on Separatrix δ, except for two singular lines, s_2 on Separatrix α and s_4 on Separatrix γ, which converge to Null N and are perpendicular to Separatrix β and on Separatrix δ near Null N [e.g., *Cowley*, 1973]. The singular lines s_1 and s_2 connect the null points and the ionosphere, and are called stemlines [*Siscoe et al.*, 2001b]. The vacuum superposition topology in Figure 1.21 also applies to MHD models for dipole tilt and various IMF orientations [*Crooker et al.*, 1998;

White et al., 1998; *Siscoe et al.*, 2001a, 2001b; *Watanabe et al.*, 2005; *Dorelli et al.*, 2007], and characterizes this magnetospheric model, namely “the null-separator model”.

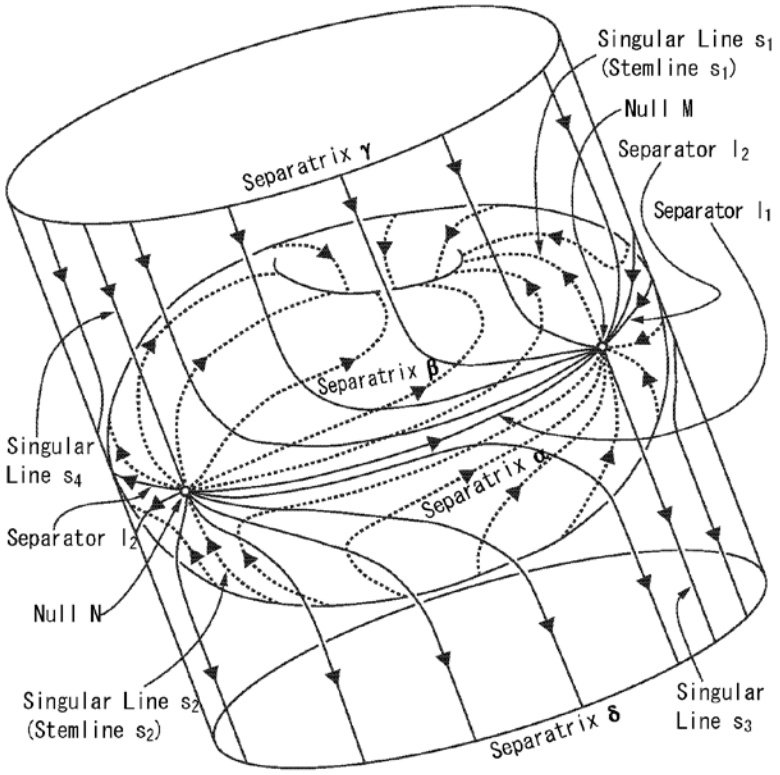

Figure 1.21. The separatrix surfaces are topologically shown as a torus and a cylinder, resulting from superposition of a dipole field and a uniform IMF in a vacuum. The arrowed lines represent magnetic field lines on the separatrix surfaces, as dashed lines on the torus surface and solid lines on the cylinder surface (taken from Figure 1 of *Watanabe and Sofko* [2008]).

Figure 1.22 shows topologically the eight types of reconnection associated with Null M, which can be divided into four groups by the location of merging, type A merging on separator l_1 shown in Figure 1.22(a), type C merging on the Separatrix γ shown in Figure 1.22(b), type E merging on the Separatrix α shown in Figure 1.22(c) and type G merging on Separator l_2 shown in Figure 1.22(d). There are two types of reconnection in each group, which are the inverses of each other. The magnetic field lines are not only on the separatrix surfaces, but in their immediate neighborhood. The diffusion region shown as the hatched area occupies a finite space around “center-of -merging” line, so Figure 1.22 is not a vacuum model. In the diffusion zone, the magnetic field is approximately parallel to the current, called a guide field, and the electric field is in the same direction as the current. At each merging location, the two types of merging are labeled plus (minus) if the electric field is toward (away from) the Null M. In Figure 1.22(a-d), the plus types of

merging are from left panel to right panel, and the minus types of merging are from right panel to left panel.

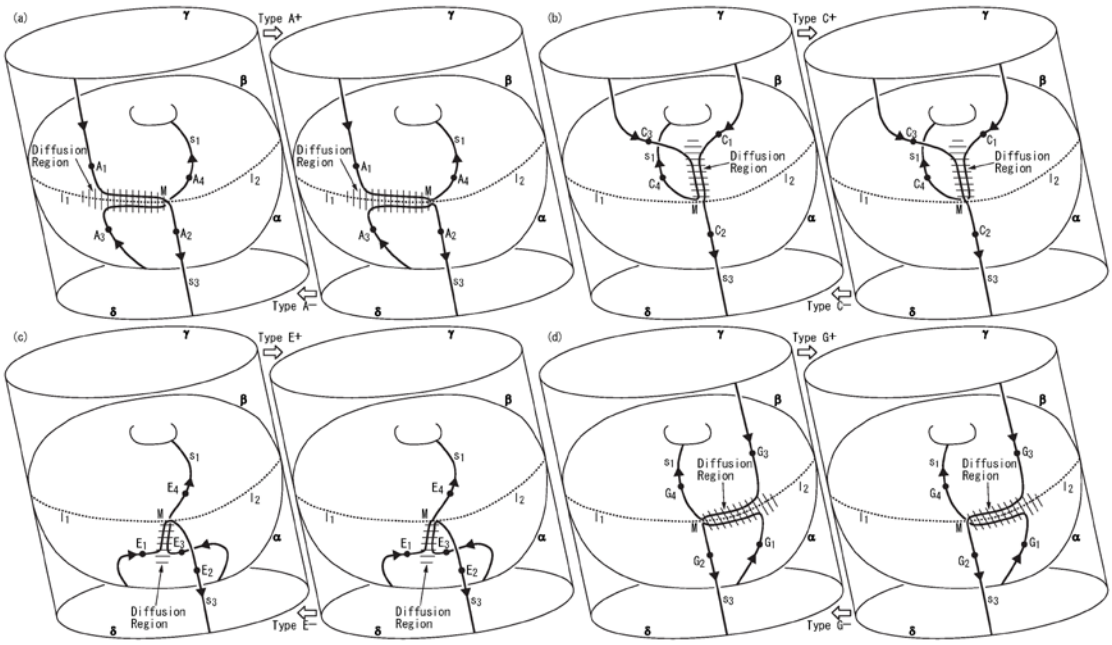

Figure 1.22. (a-d) Topological representation of complete reconnection types associated with the null point M. The magnetic field lines are not only on the separatrix surfaces, but on their immediate neighborhood. Field lines are shown by arrowed lines, with the dots showing the plasma elements frozen to the field lines. The 3 dimensional diffusion region where field lines merge is shown by the hatched pattern. In figure (a) and (d), the diffusion region is around the separator line, while in figure (b) and (c), the diffusion region is around the "center-of-merging" line on the separatrix surface. The topology changes between the left and right panels are indicated by wide arrows. The arrows towards left (right) indicate "+" ("-") types of reconnection (adapted from Figure 4 of *Watanabe et al.* [2007]).

Figure 1.23 shows topologically the eight types of reconnections associated with Null N, and is similar to Figure 1.22. The eight types can be divided into four groups by the location of merging, type B merging on Separator l_1 shown in Figure 1.23(a), type F merging on Separatrix δ shown in Figure 1.23(b), type D merging on Separatrix β shown in Figure 1.23(c) and type H merging on separator l_2 shown in Figure 1.23(d). At each merging location, the two types of merging are labeled plus or minus, depending on whether the electric field is toward or away from Null N. However, in Figure 1.23(a-d), the plus (minus) types of merging are from right panel to left panel (left panel to right panel), opposite to Figure 1.22(a-d).

For example, in Figure 1.20, if field lines 2 and 4 are singular lines, the end of the guide field at +x is the null point M. The current and electric field are toward –x, out of the null

point, so it is a minus type reconnection. On the other hand, if field lines 1 and 3 are singular lines, the end of the guide field at the origin is the null point N. The current and electric field are toward –x, into the null point, so it is a plus type reconnection.

However, for the 2D view in Figure 1.20 (a2) and (b2), there is another possibility that the ends of lines 1 and 3 are at positive x, and the ends of lines 2 and 4 are at the origin (not shown), so the guide field is toward –x, parallel to the current and electric field. The reconnection is plus type reconnection with null point M if field lines 2 and 4 are singular lines. The reconnection is minus type reconnection with null point N if field lines 1 and 3 are singular lines.

We thus can determine the direction of the current and electric field and the plus or minus type of reconnection by the 3D topological representation of the reconnection.

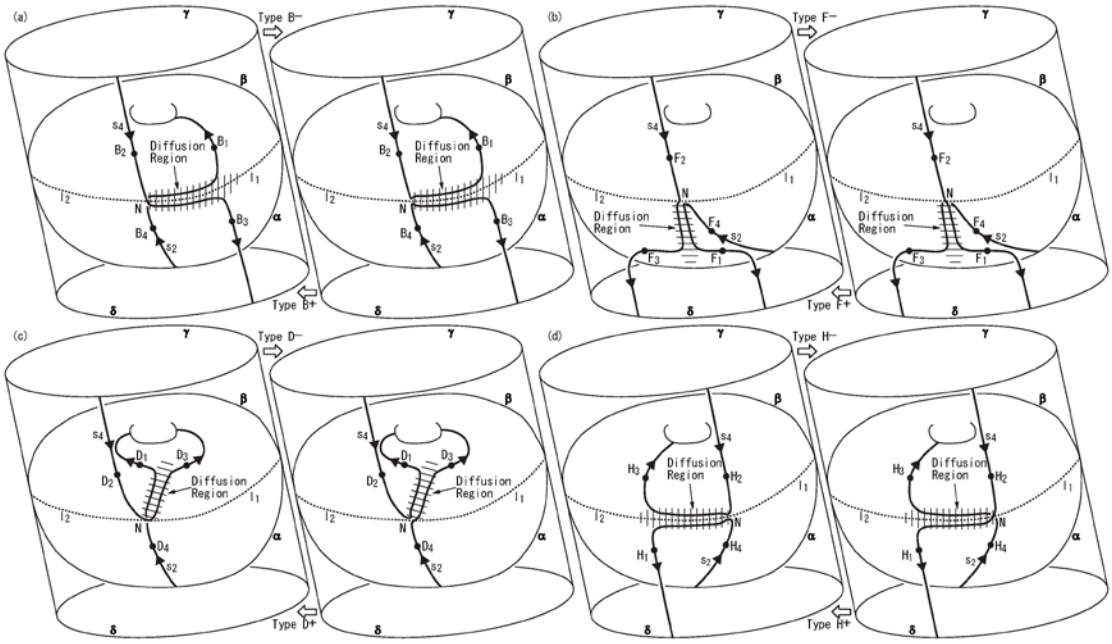

Figure 1.23. (a–d) Topological representation of complete reconnection types associated with the null point N, corresponding to those of Figure 1.22 (a-d), respectively. The difference is that the wide arrows towards left (right) indicate "-" ("+") types of reconnection (taken from Figure 3 of *Watanabe and Sofko* [2008]).

In Figures 1.22 and 1.23, we label each field line with a pair of dots representing plasma elements attached to reconnecting or reconnected field line portions outside the diffusion region. The label for each dot consists of the type of reconnection and a number, which has a subscript "4" for a plasma element on the stemline, and subscript "2" for a plasma element on the singular line. For example, in type A+ reconnection in Figure 1.22 (a), the field lines before reconnection (left panel) are the A_1-A_2 IMF line and the A_3-A_4 line closed field line, and the field lines after the reconnection (right panel) are the A_1-A_4 line North Lobe line and the A_2-A_3 South Lobe line. The plasma elements sometimes belong

to different types of field line before and after “reconnection” but not always, as for example the elements C_2 (IMF before and after), C_4 (north lobe before and after), E_2 (south lobe before and after), E_4 (closed line before and after) in Figure 1.22. By putting the double quotes on “reconnection”, we confine its meaning to the discontinuous breaking and rejoining at a null point (the reconnection lasts from the time when a pair of field lines enters the diffusion region to the time when they emerge from the diffusion region). The labeling is for the field lines just before and just after the “reconnection”.

Figure 1.22 and 1.23 show the complete reconnection types for merging topologies, type A+/A- in Figure 1.22 a, type C+/C- in Figure 1.22 b, type E+/E- in Figure 1.22 c, type G+/G- in Figure 1.22 d, type B+/B- in Figure 1.23 a, type F+/F- in Figure 1.23 b, type D+/D- in Figure 1.23 c, type H+/H- in Figure 1.23 d [*Watanabe et al.*, 2007; *Watanabe and Sofko*, 2008].

In Chapter 4, the above 3D null-separator model is applied to the actual convection signatures expected from combinations of the reconnection types.

2. INSTRUMENTS

This thesis makes use of ground-based and satellite instruments. Ground-based instruments include the SuperDARN HF radars, particularly the two PolarDARN radars at Rankin Inlet and Inuvik. Satellite instruments include the particle (ion and electron) spectrometers on the NOAA POES satellites and the DMSP satellites.

2.1 The PolarDARN Radars

2.1.1 Introduction to SuperDARN

Table 2.1. SuperDARN radar names, locations and boresight directions (normal to the transmitting antenna array lines).

Radar Station	Geog. Lat. (°N)	Geog. Long. (°E)	AACGM Lat. (°N)	AACGM Long. (°E)	Boresight Direction (°E of N)
Rankin Inlet	62.83	-92.11	73.17	-28.20	5.71
Inuvik	68.41	-133.77	71.15	-86.5	29.47
King Salmon	58.68	-156.65	57.43	-100.51	-20
Kodiak	57.61	-152.19	57.17	-96.28	30
Prince George	53.98	-122.59	59.88	-65.67	-5
Saskatoon	52.16	-106.53	61.34	-45.26	23.1
Kapuskasing	49.39	-82.32	60.06	-9.22	-12
Goose Bay	53.32	-60.46	61.94	23.02	5
Stokkseyri	63.86	-22.02	65.04	67.33	-59
Pykkvibaer	63.77	-20.54	64.48	68.48	30
Hankasalmi	62.32	26.61	59.78	105.53	-12
Wallops Island	37.93	-75.47	49.21	-0.03	26.14
Hokkaido	43.53	143.61	36.46	-145.34	30
Blackstone	37.10	-77.95	48.59	-3.63	-32
Halley	-75.52	-26.63	-61.68	28.92	165
Sanae	-71.68	-2.85	-63.80	42.95	173.2
Syowa South	-69	39.58	-66.08	71.65	165
Syowa East	-69.01	39.61	-66.21	71.70	106.5
Kerguelen	-49.35	70.26	-58.73	122.14	168
Bruny Island	-43.38	147.23	-55.31	-133.36	180
Unwin	-46.51	-168.38	-49.18	-81.74	227.9

The SuperDARN radar project is an international system of coherent high frequency (HF) radars which are used to study high-latitude and mid-latitude ionospheric plasma convection [*Greenwald et al.*, 1995; *Chisham et al.*, 2008]. Table 2.1 shows the locations of the SuperDARN radar sites. There are currently 20 SuperDARN radars in operation (the Halley Bay radar is not operating until 2012 pending changes to the station by the British Antarctic Survey), 14 in the Northern Hemisphere and 6 in the Southern Hemisphere. In the Northern Hemisphere, 9 radars can be classified as auroral zone radars because they are located in the equatorward portion of the auroral zone and look northward through the auroral zone, with the radar beams sometimes reaching the polar cap region, poleward of the boundary between the closed and open magnetic field lines. The PolarDARN radars at Rankin Inlet and Inuvik are located in the poleward portion of the auroral zone and are primarily meant for studying the polar cap at high magnetic latitudes surrounding the magnetic north (dipole) pole. The other three northern hemisphere radars, namely the Wallops Island, Hokkaido and Blackstone radars, are mid-latitude radars. In March 2009, a US project to expand SuperDARN has been funded. Eight new radars, consisting of four radar pairs, will be installed in Kansas (2009), Oregon (2010), the Aleutian Islands (2011), and the Azores (2012), the brackets indicating the years the radars will be constructed, with the project scheduled for completion by 2012. In addition, a new Australian radar has been funded for installation near Adelaide. These 9 new radars will be an extension of mid-latitude radar work. Finally, two more Antarctic radars have been funded. One is being built at the US base McMurdo, and will be essentially a PolarDARN South radar beamed toward the south magnetic dipole pole (which is near the base called Concordia or Dome C), and the other (an Italian-French effort) will be installed at Concordia base itself. There are thus 11 new fully funded radars. By 2012, including Halley again, the number of operating radars will be 32. Ten additional radars have been proposed – Baffin Island (Canada), Falkland Islands (Britain), Maitri (Indian Antarctic base), four radars for Russia (Arti, Magadan and two at Bratsk), South Pole (US Antarctic station), Hokkaido West (Japan) and Hermanus (South Africa), but these have not yet been funded.

Each SuperDARN radar sweeps over a 16-beam (beams 0-15) scan in 1 or 2 minutes. The beams are separated by 3.24°, so the total azimuthal range covered by the 16 beams is about 52°. Each beam originally scanned 75 range cells, starting from 180 km, with 45 km range extent for each cell, but 100 or more range cells now can be used. SuperDARN radars are monostatic, i.e. they transmit and receive pulses at the same site, and employ a coherent detection. The radars now typically transmit an 8-pulse sequence which has 23 useful lags that can be used to evaluate the autocorrelation function of the received signal. The original multipulse sequence employed only 7 pulses [*Baker et al.*, 1995].

2.1.2 The PolarDARN Component of SuperDARN

2.1.2.1 Introduction to PolarDARN

PolarDARN is a pair of HF radars looking into the northern polar cap, which is the region of open magnetic field lines poleward of the closed field lines in the auroral zone. The PolarDARN radar locations were chosen so that the pattern of the convection streamlines (which are equipotentials) could be measured at high magnetic latitudes within about 15°

of the magnetic pole. Also, the open-closed field line boundary (OCFLB) dividing the open (polar cap) and closed (auroral zone) field lines tends to be at those higher latitudes when the Bz component of the interplanetary magnetic field (IMF) is northward. Magnetic flux tubes in the vicinity of the OCFLB can undergo magnetic reconnection at altitudes near the magnetopause, and it is the energy transferred from the magnetic field to the magnetospheric particles during magnetic reconnection that plays an important role in driving the magnetospheric convection pattern, although coupling between the magnetosphere and the ionosphere by Alfven waves is essential for the ionospheric convection that is measured by the radars. The ionospheric convection pattern consists of three types of convection cells, namely merging cells, lobe cells and reciprocal cells. The merging cells have streamlines that cross the OCFLB twice. The lobe cells have closed convection streamlines which are entirely within the polar cap open-field line region. The reciprocal cells have streamlines that lie entirely on closed field lines equatorward of the OCFLB, which is within the auroral zone. There is another type of convection cell on closed field lines, namely the viscous cell, but that is not reconnection-driven and will not be treated here.

2.1.2.2 The PolarDARN Radar Configuration

Figure 2.1 shows the PolarDARN radars (in red) in relation to the other North American SuperDARN radars (in grey) (not including the new midlatitude radar in Blackstone, VA). The nominal auroral oval (for the relatively disturbed Q-level 3) is also shown [*Feldstein and Starkov*, 1967]. The PolarDARN radars are SuperDARN radars, but differ from the Saskatoon (1993) and Prince George (2000) Canadian radars in the antenna type, which was the log-periodic type for these two sites. The PolarDARN radars use TTFD (twin-terminated folded dipole) wire antennas with a 21-wire reflecting fence that reduces echoes from the back direction (where strong auroral-zone echoes could originate during magnetically disturbed conditions).

The PolarDARN radar locations are particularly favourable for the measurement of convection for IMF Bz+ conditions, unlike the nine SuperDARN northern hemisphere auroral zone radars stretching from King Salmon, Alaska, in the west to Prince George and Saskatoon in Canada, and to Hankasalmi, Finland, in the east. These radars were primarily designed to study convection during magnetic storms and auroral substorm conditions that are most likely driven by IMF Bz- conditions. It is of interest to note, however, that when the IMF is dominated by the IMF By component, even when there is a Bz+ IMF component, there will be a large “round” convection merging cell, within which there is a lobe cell whose structure is ideally measured by PolarDARN. The first PolarDARN radar that was built is located at Rankin Inlet, Canada, and became operational on May 11, 2006. Its Geographic Coordinates are 62°49’41”N, 92°06’46”W, the boresight is 5.71°E of N, and the magnetic (AACGM, for Altitude Adjusted Corrected GeoMagnetic) Coordinates are 73.17°N, 28.20°W. The second PolarDARN radar is located at Inuvik, Canada, and became operational on December 15, 2007. Its Geographic Coordinates are 68°24’46”N, 133°46’10”W, the boresight is 29.47°E of N, and the AACGM Coordinates are 71.15°N, 86.5°W. The sites were chosen so that the fields-of-view of the two radars cover much of the region surrounding the nominal AACGM north magnetic pole (NMP). Also, both radars look at the ionosphere above

Resolute Bay, which is on beam 4.6 of the Rankin Inlet radar, and beam 12.4 of the Inuvik radar and which is the site of two new AMISR incoherent scatter radars, one of which is Canadian. In the high-speed normal scan mode, the radar sweeps over a full 16-beam scan in 1 minute, with 3 s dwell time for each beam, and then 12 "dead" seconds at the end of the sweep. During this "dead" time, the radar goes into sounding mode, with transmissions at varying frequencies, so that the optimal frequency can be evaluated every 15 minutes. On each beam, there were originally 75 range cells, each 45 km in extent, but now extended sweeps of 100 range cells or more can be used. The radars employ coherent detection and use a multi-pulse sequence (N = 7 or 8 pulses, so that the number of lags is equal to N(N-1)/2+1 = 22 for 7 pulses and 29 for 8 pulses, which includes 0 lag, to measure the real (I) and quadrature (Q) parts of the autocorrelation function (ACF) versus the lag in each range cell. The mean Doppler frequency is the slope of the best fit line to the graph of the ACF phase, given by arctan (Q/I), versus lag.

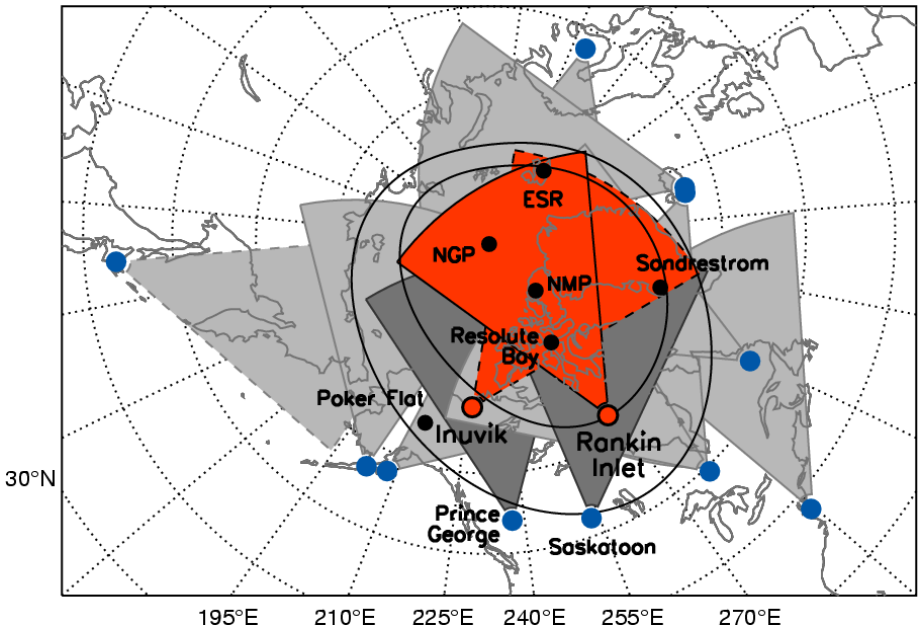

Figure 2.1. North hemisphere plot in geographic coordinates of PolarDARN radars, shown in red, and SuperDARN radars, shown in grey. The geographic (NGP) and AACGM magnetic (NMP) poles are labeled. Also shown on the map are: (a) the poleward and equatorward contours bounding the Q=3 auroral oval; (b) the ISR radar sites at Poker Flat (PFISR), Resolute Bay (AMISR), Sondrestrom, and Svalbard (ESR).

2.1.3 ACF Determination

The SuperDARN radars can be used to determine the Doppler velocity, power spectrum, and spectral width of echoes by the measurement of the autocorrelation function (ACF) [*Baker et al.*, 1995] of the received signals.

2.1.3.1 8-Pulse Sequence

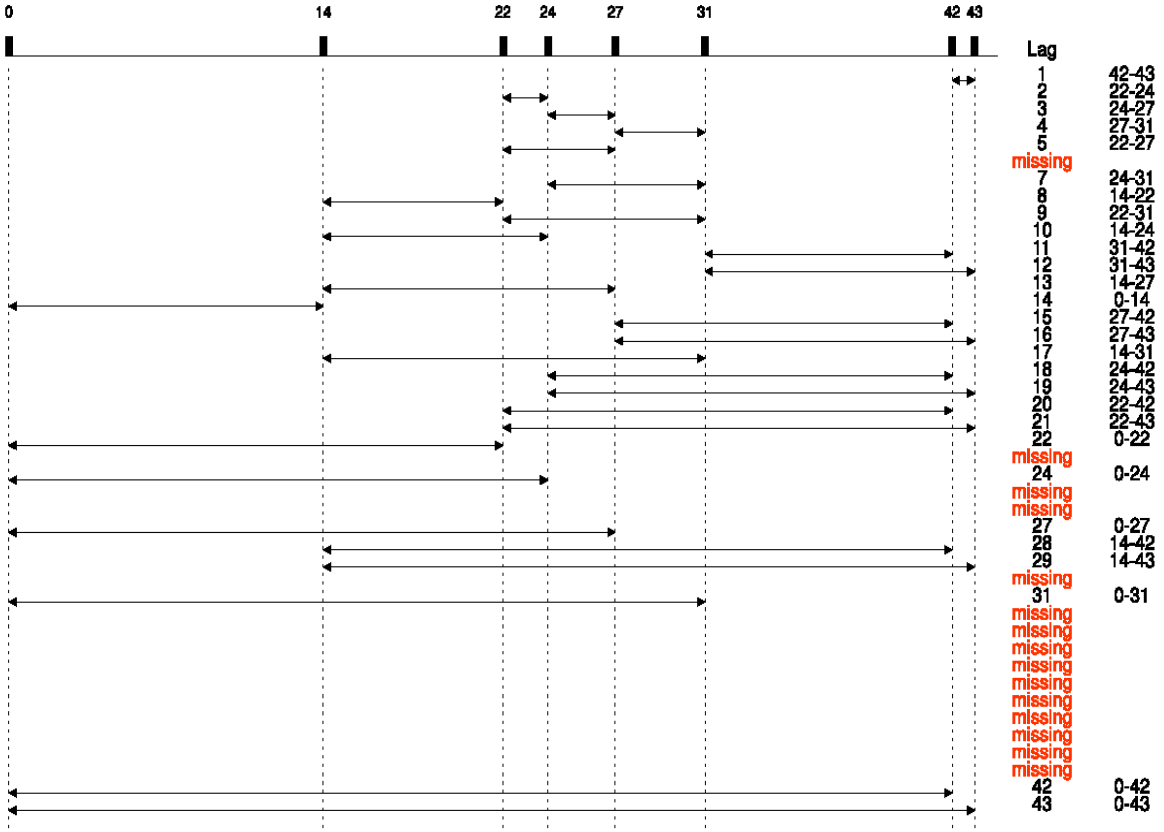

Figure 2.2. Current SuperDARN 8 pulse sequence. The top axis shows the pulse times in units of the fundamental lag time. The right axis shows the pulse pairs that give the different lags (taken from *Drayton* [2006]).

SuperDARN radars emit a multipulse transmission sequence. As shown in Figure 2.2, currently an 8-pulse sequence is used with a 300 μs length of each pulse at multipulse lags of 0, 14, 22, 24, 27, 42, 43 units, where the unit of lag time is 1.5 ms. The radar cannot transmit and receive pulses at the same time, so it cannot receive pulses at some ranges, which are called bad lag ranges. The current pulse sequence contains 29 lags (including the zero lag), but as can been seen on the right side of Fig. 2.2, the ACF will in practice have only 23 lags, namely lags from 0 to 24, with lags 6 and 23 not possible with that particular pulse pattern. Note that zero lag is evaluated on the basis of the pulse at time 0 because there is a long gap of 14 lags (21 ms) to the next pulse, which corresponds to a distance of 3150 km in range, so there is no contamination of the zero lag power except when signals come from beyond that range.

The multipulse sequence is repeated roughly 70 times for each beam position. For each multipulse transmission, the ACF is evaluated and averaging of all the roughly 70 ACFs

is done to form the mean ACF for that beam position. From the ACF, the velocity can be determined.

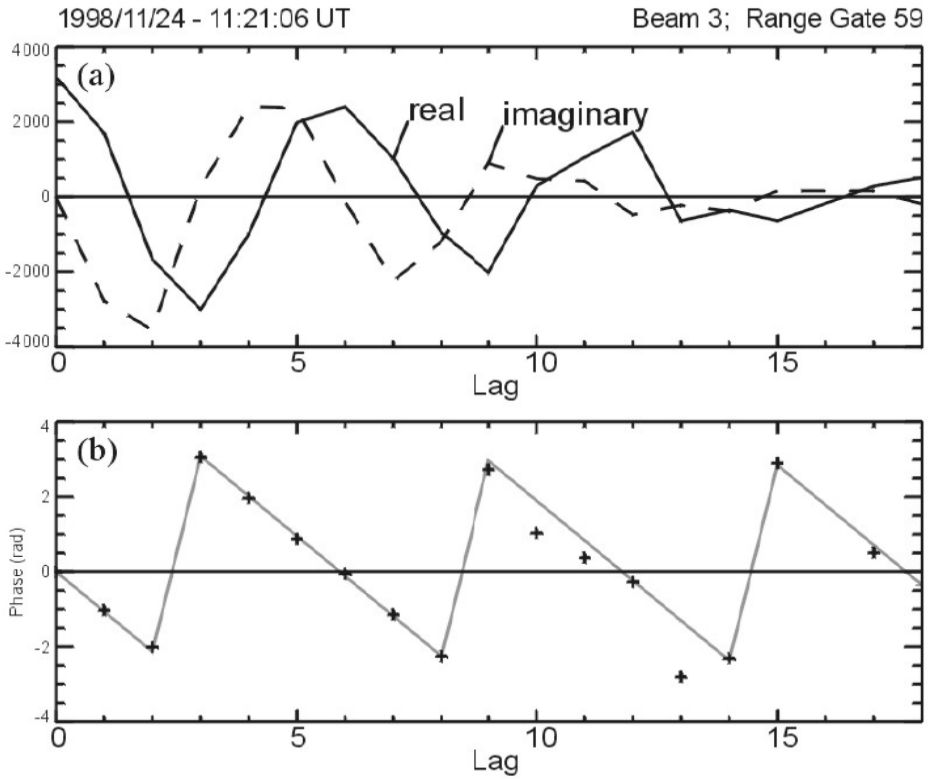

Figure 2.3. The top panel shows the real part and imaginary part of the ACF versus lag in a 7-pulse sequence. The bottom panel is the phase versus lag for the ACF from a 7-pulse sequence (taken from *McWilliams* [2002]).

The line-of-sight (LOS) Doppler velocity can be derived from ACF. The mean Doppler shift frequency is the slope of the best fit line to the graph of the phase versus the lag, where the phase is given by arctan (Q/I), in which Q and I refer respectively to the quadrature and in-phase parts of the ACF, as is shown in Figure 2.3 of *Villain et al.* [1987]. The key equations are given below.

$$\tan^{-1}\left(\frac{Q}{I}\right) = \omega_{D_S}\tau_n = \phi \tag{2.1}$$

$$\omega_{D_S} = \frac{\partial\phi}{\partial\tau} \tag{2.2}$$

in which ω_{D_S} is LOS Doppler frequency shift, τ_n is the lag time, and ϕ is the phase of the ACF.

2.1.3.2 ACF at Lag τ

The SuperDARN radars employ a multipulse sequence, and this allows the evaluation of many lags in the ACF. This, however, is simply the evolution of the most basic radar, which is a radar that transmits only a single pair of pulses separated by lag τ. We thus first consider such a basic radar.

Figure 2.4 shows 2-pulse sequence at lag τ. The radar sends out 2 pulses, pulse p_1 at time t_0, pulse p_2 at time $t_0 + \tau$. The radar subsequently receives 4 pulses, p_1 from distance d_0 at time t_1, p_1 from distance d_+ at time $t_1 + \tau$, p_2 from distance d_0 at time $t_1 + \tau$, p_2 from distance d_- at time t_1.

The amplitude received at t_1 is given by

$$A(t_1) = A_1(d_0) + A_2(d_-) \tag{2.3}$$

in which $A_1(d_0)$ is the amplitude of p_1 scatter from d_0, $and\ A_2(d_-)$ is the amplitude of p_2 scatter from d_-.

The amplitude at $t_1 + \tau$ is

$$A(t_1 + \tau) = A_1(d_+) + A_2(d_0) \tag{2.4}$$

In which, $A_1(d_+)$ is the amplitude of p_1 scatter from d_+, and $A_2(d_0)$ is the amplitude of p_2 scatter from d_0.

The ACF is the product of (2.3) and the complex conjugate of (2.4)

$$A(t_1)A(t_1 + \tau)^* = [A_1(d_0) + A_2(d_-)][A_1(d_+)^* + A_2(d_0)^*] \tag{2.5}$$

By averaging over the total number of multipulse sequences transmitted during the beam dwell time (about 70 patterns for the two-minute dwell time), the three terms on the right which involve the product of the received signals from different ranges will disappear because different ranges are not correlated. Finally, only one term remains, i.e. the ACF equals the product of the signals at t_1 and $t_1 + \tau$ from the "desired" range d_0 only. As Appendix 1 (which provides a complete derivation of the ACF method for obtaining the Doppler velocity) shows, this term has a phase which equals the product of the Doppler frequency ω_D and the lag τ, as given by:

$$\langle A(t_1)A(t_1 + \tau)^* \rangle \sim \langle A_1(d_0)A_2(d_0)^* \rangle \sim Ae^{i\omega_D \tau} \tag{2.6}$$

in which, the bracket ($\langle\ \rangle$) means the time average over all the multipulse sequences transmitted during the beam dwell time. Equation (2.6) is equivalent to equation (25) in the Appendix. By measurement of the multipulse-sequence averaged ACF at many lags τ, the slope of the plot of the phase $\omega_D\tau$ versus τ is the Doppler frequency ω_D.

Figure 2.5 shows a 3-pulse sequence. The 3 pulses are emitted at time t_0, $t_0 + \tau$ and $t_0 + 3\tau$. Any pair of pulses acts like a two-pulse sequence. From the 3-pulse sequence,

we thus can evaluate three ACF values, at lag τ (pulses p_1 and p_2), lag 2τ(pulses p_2 and p_3), and lag 3τ (pulses p_1 and p_3).

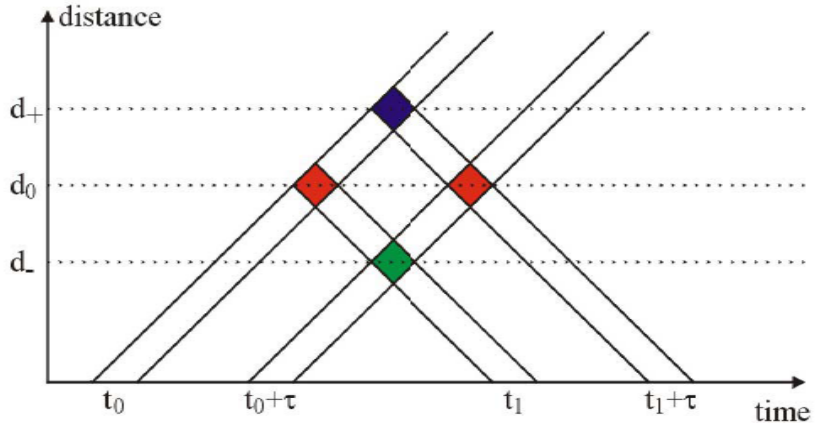

Figure 2.4. 2-pulse sequence at lag τ (taken from *McWilliams* [2002]).

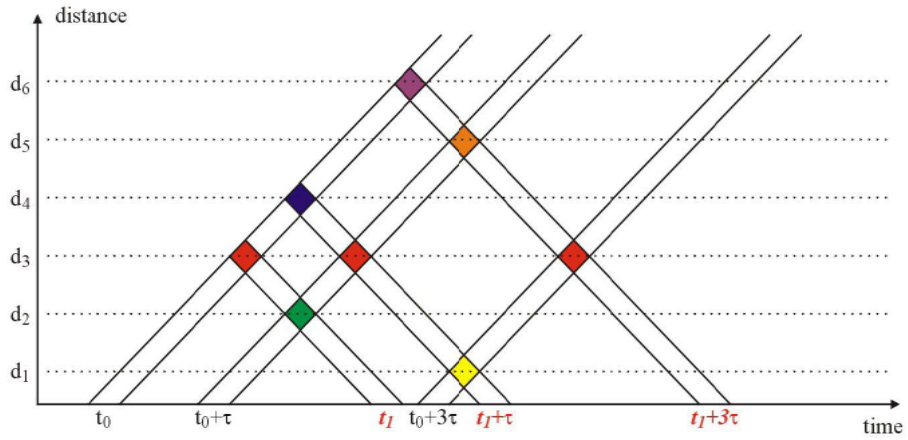

Figure 2.5. 3-pulse sequence (taken from *McWilliams* [2002]).

2.1.3.3 Determination of Velocity, Electric Field and Electric Potential

The Doppler frequency ω_D, determined by ACF in equation (2.2), can be converted to v_{conv}, which is the line-of-sight velocity of the plasma at the distance d_0, by using the equation

$$\frac{\omega_D}{\omega} = \frac{2v_{conv}}{c/n} \tag{2.7}$$

where ω is the frequency transmitted by the radar, c is the speed of light, and n is the refractive index in the scattering region. The Doppler velocity corresponds to the phase velocity of the plasma irregularity from which the coherent back-scattering occurs.

To obtain (2.7), we use the time derivation of the signal phase, which is given by

$$\Phi(t) = \omega t - \int \vec{k} \cdot d\vec{r} \tag{2.8}$$

in which ω is the frequency transmitted by the radar, t is time, $\vec{k}$ is the propagation vector, and $\vec{r}$ is the position vector.

The equation of $\vec{k}$ is given by

$$\vec{k} = k_0 n \hat{k} \tag{2.9}$$

where k_0 is the wavenumber in the vacuum, n is the refractive index, and $\hat{k}$ is the unit propagation vector.

We can also have the relationship as the following equation.

$$\hat{k} \cdot d\vec{r} = ds \tag{2.10}$$

where ds is the differential path element of the wave.

Substituting (2.9) and (2.10) into (2.8) results in

$$\Phi(t) = \omega t - k_0 \int_{S_A(t)}^{S_B(t)} n(t,s) ds \tag{2.11}$$

We should notice that there are two variables t and s. We will use the following equation to solve the derivation. If a function F(x) is the integral of f(x,y),

$$F(x) = \int_{\alpha(x)}^{\beta(x)} f(x,y) dy \tag{2.12}$$

the derivative of F(x) with respect to x is given by

$$F'(x) = \beta'(x) f[x, \beta(x)] - \alpha'(x) f[x, \alpha(x)] + \int_{\alpha(x)}^{\beta(x)} \frac{\partial f(x,y)}{\partial x} dy \tag{2.13}$$

By applying (2.10), we obtain the derivative of $\Phi(t)$ with respect to t

$$\Phi'(t) = \omega - k_0 n_B[t, s_B(t)] \frac{\partial s_B}{\partial t} + k_0 n_A[t, s_A(t)] \frac{\partial s_A}{\partial t} - k_0 \int_{S_A(t)}^{S_B(t)} \frac{\partial n(t,s)}{\partial t} ds \tag{2.14}$$

The first term in (2.14) is the transmitted frequency, and the last three terms are contributions to the total Doppler shift. We notice that the speed along the ray trajectory at B will be the speed of the scatterer located at B, namely

$$\frac{\partial s_B}{\partial t} = v_B \tag{2.15}$$

and the speed at A, which is the fixed location of the radar, is 0.

The equation thus reduces to

$$\Phi'(t) = \omega - \omega_D \tag{2.16}$$

In which, the Doppler shift is given by

$$\omega_D = k_0 n_B[t, s_B(t)] \frac{\partial s_B}{\partial t} + k_0 \int_{S_A(t)}^{S_B(t)} \frac{\partial n(t,s)}{\partial t} ds = \omega_{D1} + \omega_{D2} \tag{2.17}$$

In this thesis work, we only consider the first term ω_{D1} (the "Gillies" or "Ginzburg" term) [*Ginzburg*, 1964; *Gillies et al.*, 2009].

By substituting the following equation, in which c is the speed of light,

$$k_0 = \frac{\omega}{c} \tag{2.18}$$

we obtain the equation

$$\omega_{D1} = \frac{\omega}{c} n_B[t, s_B(t)] v_B \tag{2.19}$$

or

$$\frac{\omega_{D1}}{\omega} = \frac{v_B}{c/n_B[t, s_B(t)]} \tag{2.20}$$

where the speed given in the right denominator is the phase velocity in the scattering medium. Equation (2.20) is for the one-way path from the radar to scatterer, and for the two-way backscatter case, the result should be multiplied by a factor of 2, which gives the final result

$$\frac{\omega_{D1}}{\omega} = \frac{2v_B}{c/n_B[t, s_B(t)]} \tag{2.21}$$

in which ω_{D1} is ω_D, and v_B is v_{conv} in (2.7), so equation (2.7) is obtained.

By obtaining v_{conv} in (2.7), we can then use v_{conv} to calculate the electric field **E** and electric potential Φ by means of the equation

$$\boldsymbol{E} = -\boldsymbol{v}_{conv} \times \boldsymbol{B} \tag{2.22}$$

In which, B is the magnetic field. Finally, the electric potential pattern Φ can be obtained from the electric field pattern by

$$\boldsymbol{E} = -\nabla\Phi \tag{2.23}$$

2.1.4 The Convection Mapping

2.1.4.1 Merging of Radar LOS Velocities

The original method to measure the velocity at the scattering site v_R is merging of two radar LOS velocities v_1, v_2. Since they are the components of the resultant v_R, we take lines perpendicular to v_1, v_2 to obtain v_R, as shown in Figure 2.6. We consider v_R is the magnitude of the velocity, which is positive.

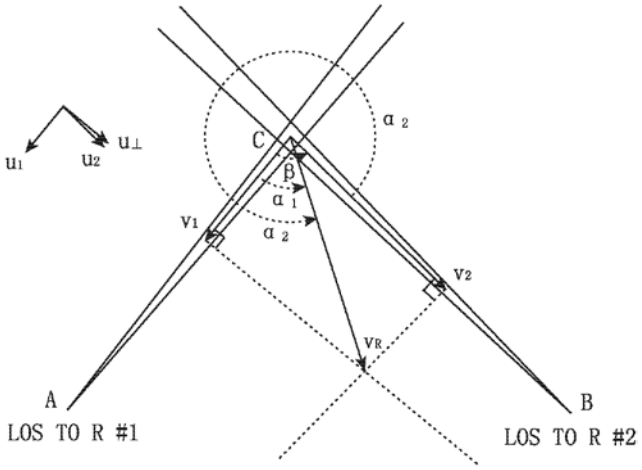

Figure 2.6. Merging of radar LOS velocities v_1, v_2. The angles α_1, α_2 are shown in the positive traditional sense. The angle β is the known angle between the beam directions.

The angles between v_1, v_2 and v_R are α_1, α_2 respectively. We use the angles α_1, α_2 in the positive traditional sense. i.e. both angles are positive when measured counterclockwise.

The angle β is always the angle between the beam (LOS) directions such that $\beta < 180°$.

LOS velocities v_1, v_2 are positive when they are toward the radar, because then the Doppler shift is also positive.

We apply two unit vectors for v_1 and v_2

$$\hat{u}_1 = \frac{\overrightarrow{CA}}{|\overrightarrow{CA}|} \tag{2.24}$$

$$\hat{u}_2 = \frac{\overrightarrow{CB}}{|\overrightarrow{CB}|} \tag{2.25}$$

The $\vec{v}_R$ can be decomposed to two perpendicular directions $\hat{u}_1$ and $\hat{u}_\perp$

$$\vec{v}_R = |v_R| \cos\alpha_1 \, \hat{u}_1 + |v_R| \sin\alpha_1 \hat{u}_\perp \tag{2.26}$$

where $\vec{v}_1$, $\vec{v}_2$ are in the $\hat{u}_1$, $\hat{u}_2$ directions respectively, as given by

$$\vec{v}_1 = v_1 \hat{u}_1 \tag{2.27}$$

$$\vec{v}_2 = v_2 \hat{u}_2 \tag{2.28}$$

In which, v_1, v_2 are projections of $\vec{v}_R$ on $\hat{u}_1$, $\hat{u}_2$ directions respectively, and v_1, v_2 can be positive (toward radar) or negative (away from the radar).

$$v_1 = \vec{v}_R \cdot \hat{u}_1 = |v_R| \cos\alpha_1 \, \hat{u}_1 \cdot \hat{u}_1 + |v_R| \sin\alpha_1 \hat{u}_\perp \cdot \hat{u}_1 = |v_R| \cos\alpha_1 \tag{2.29}$$

$$v_2 = \vec{v}_R \cdot \hat{u}_2 = |v_R| \cos\alpha_1 \, \hat{u}_1 \cdot \hat{u}_2 + |v_R| \sin\alpha_1 \hat{u}_\perp \cdot \hat{u}_2$$

$$= |v_R| \cos\alpha_1 \cos\beta + |v_R| \sin\alpha_1 \sin\beta \ . \quad (2.30)$$

Solving (2.29) and (2.30) for the magnitude of $\vec{v}_R$ gives

$$|v_R| = \frac{v_1}{\cos\alpha_1} = \frac{v_2}{\cos\alpha_1 \cos\beta + \sin\alpha_1 \sin\beta} \quad (2.31)$$

and $$v_1 \cos\alpha_1 \cos\beta + v_1 \sin\alpha_1 \sin\beta = v_2 \cos\alpha_1 \quad (2.32)$$

Grouping the terms in $\cos\alpha_1$ gives

$$(v_1 \sin\beta) \sin\alpha_1 = v_2 \cos\alpha_1 - v_1 \cos\alpha_1 \cos\beta = (v_2 - v_1 \cos\beta) \cos\alpha_1 \quad (2.33)$$

$$\tan\alpha_1 = \frac{\sin\alpha_1}{\cos\alpha_1} = \frac{v_2 - v_1 \cos\beta}{v_1 \sin\beta} \quad (2.34)$$

From (2.34), we get the angle α_1

$$\alpha_1 = \text{atan2}(v_2 - v_1\cos\beta, v_1 \sin\beta), \quad \text{if } \text{atan2}(v_2 - v_1\cos\beta, v_1 \sin\beta) \geq 0$$

$$\alpha_1 = \text{atan2}(v_2 - v_1\cos\beta, v_1 \sin\beta) + 360°, \text{ if } \text{atan2}(v_2 - v_1\cos\beta, v_1 \sin\beta) < 0 \quad (2.35)$$

The magnitude of $\vec{v}_R$ can be obtained by

$$|v_R| = \frac{v_1}{\cos\alpha_1} = v_1 \sec\alpha_1 = \left| v_1 \sqrt{\tan^2\alpha_1 + 1} \right| = |v_1| \sqrt{\left(\frac{v_2 - v_1\cos\beta}{v_1 \sin\beta} \right)^2 + 1}$$

$$= \left| \frac{v_1}{v_1 \sin\beta} \right| \sqrt{v_2^2 - 2v_1 v_2 \cos\beta + v_1^2 \cos^2\beta + v_1^2 \sin^2\beta}$$

$$= \frac{\sqrt{v_1^2 + v_2^2 - 2v_1 v_2 \cos\beta}}{\sin\beta} \quad \text{(in which, } \sin\beta > 0) \quad (2.36)$$

Thus, $\vec{v}_R$ is determined by (2.35) and (2.36).

The angle α_2 can be obtained easily by

$$\alpha_2 = \alpha_1 - \beta, \quad \text{if } \alpha_1 > \beta$$

$$\text{or } \alpha_2 = \alpha_1 + 360° - \beta, \text{ if } \alpha_1 < \beta \quad (2.37)$$

2.1.4.2 The Convection Mapping by SVD Matrix Technique

For many conditions, only one velocity is available at the scattering site, and the method of merging radar LOS velocities is not applicable, so the SVD matrix technique [*Press et al.*, 1986] is applied for the convection mapping [*Ruohoniemi and Baker*, 1998; *Chisham et al.*, 2007].

The initial step required in using the measured SuperDARN line-of-sight (LOS) velocity data is to average that data in such a way as to eliminate the presence of a few rather large spurious values that may occur due to external signal interference such as that caused by short industrial noise bursts. The smoothing is accomplished by "boxcar" filtering in which the data are arranged sequentially and the median value is used. For the scan at time t_k, we estimate the velocity of a desired range cell of beam b and range gate g by using a 3×3 beam/gate template centered at (b, g). However, it was found found by *Ruohoniemi and Baker* [1998] that not only was the above spatial averaging useful, but also that it was useful to include time averaging over 3 successive radar sweeps, including the one before t_k at t_{k-1} and the one after at t_{k+1}. As a result, there are 27 potential data points in the successive 3 scans. Of course, not all 27 will contain data, but the chances of getting a useful smoothed velocity are much enhanced by this technique. Before obtaining the median value, the velocities are assigned weighting factors that decrease away in space and time from the desired cell (b,g). Because some of the data are absent, the assignment of the velocity relies on the sum of the weights. If the sum is too small, the value of velocity is not determined for the cell, while if it is high enough, the value of velocity is determined for the cell by finding the median value.

For producing the convection map, it has been found useful to use a grid consisting of cells that are roughly squares whose sides have the length of about 1° in magnetic latitude. We expand the electric potential Φ in Legendre functions

$$\Phi(\theta,\phi) = \sum_{l=0}^{L} A_{l0}\, P_l^0(\cos\theta) + \sum_{m=1}^{l} (A_{lm}\cos m\phi + B_{lm}\sin m\phi)\, P_l^m(\cos\theta) \qquad (2.38)$$

In which (θ, ϕ) are the usual spherical coordinates, P_l^m are associated Legendre functions and the coefficients A_{lm} and B_{lm} are real-valued.

Then we can obtain the electric field $\boldsymbol{E}$ and the velocity $\boldsymbol{v}$ by using the usual equations, namely

$$\boldsymbol{E} = -\nabla\Phi \qquad (2.39)$$

and

$$\boldsymbol{v} = \frac{\boldsymbol{E}\times\boldsymbol{B}}{B^2} \ . \qquad (2.40)$$

We convert the filtered line-of-sight velocity values to the mapping grid of N values, in which the velocity values and their uncertainties are expressed as W_i and σ_i. The SVD (singular value decomposition) matrix technique is used to give the best possible least squares fit. This ultimately is checked by evaluating the chi-squared value for the fit, namely

$$\chi^2 = \sum_{i=1}^{N} \frac{1}{\sigma_i^2} \left[\mathbf{v}[\mathrm{i}] \cdot \hat{\mathbf{k}}[\mathrm{i}] - W_i\right]^2 , \qquad (2.41)$$

in which $\mathbf{v}[\mathrm{i}]$ is the result of (2.40) for the grid cell i and its projection onto the line-of-sight direction is its dot product with the unit propagation vector $\hat{\mathbf{k}}[\mathrm{i}]$. The set of coefficients (A_{lm}, B_{lm}) are determined by the best possible least squares fit using the

powerful SVD technique, so the electric field and electric potential are determined by (2.39) and (2.38). The convection map is thus obtained.

When there is not sufficient data for the use of the SVD technique, the measured data is supplemented by putting into the data gaps convection vectors arising from averaged statistical convection models that characterize the different IMF conditions. The only problem with this technique is that the real-time radar data is combined with long-term statistically averaged values, and the latter may not be appropriate for the real-time short interval being studied. A possible new approach to address this issue is mentioned in Chapter 5 in the suggestions for future research.

2.1.5 The Wire Antennas - Theory

2.1.5.1 The Half-Wave Dipole

The basic antenna upon which the SuperDARN antennas were based is the half-wave dipole. It is the basic element of the original log-periodic antennas used for all radars erected before 2005. A log-periodic antenna consists of a series of interconnected half-wave dipoles of decreasing length. A signal of a given frequency fed to this series of antennas is mainly radiated by the half-wave dipoles (usually about 3 or 4 antennas) whose lengths are closest to the half-wavelength of the signal at the given frequency. Such an antenna has a frequency range determined by the lengths of the shortest and longest half-wave dipole antennas. The original SABRE log-periodic antennas had 10 half-wave dipoles which gave a frequency range from 8 to 20 MHz. Such log-periodic antennas were large, cumbersome and expensive (about US$16,000 each). As a result, Dr. Greenwald, the former head of the international SuperDARN science team, led the effort to design a new, less-expensive antenna that had good forward gain and a reflecting fence that prevented signal from being radiated or received from the back-directions. Again, the new design is simply a version of a folded dipole, which is essentially a half-wave dipole whose ends are joined by a second wire parallel to the original dipole, the two elements being separated by a small distance. The new design is in fact a double-folded or twin-folded dipole, in which the central half-wave dipole is symmetrically separated from two parallel wires, one on each side of the dipole. A new feature is that the parallel wires each have a resistor at their center. This arrangement, shown in the next section in Figures 2.9 and 2.10, is called a twin-terminated folded dipole (TTFD). The use of TTFD antennas for the 16-antenna main transmitting array and the 4-antenna "interferometer" array resulted in a savings of more than US$250,000 for each radar, since 20 log-periodic antennas would have cost US$320,00, while the TTFD design resulted in a total cost of less than US$70,000. To summarize, both antenna types used by SuperDARN are based upon the half-wave dipole, so we first briefly discuss the radiation pattern of that basic antenna.

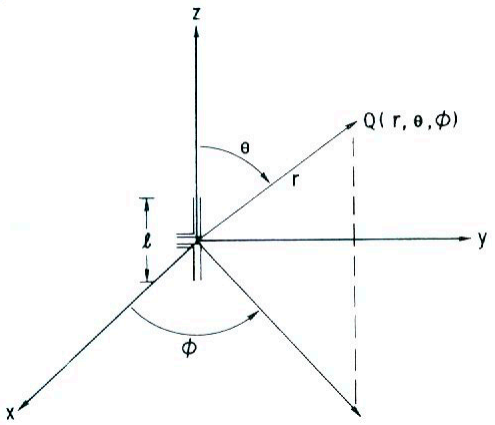

Figure 2.7. Half-wave dipole placed at the origin of the spherical coordinate system (taken from *Ulaby*, [1981]).

The Poynting vector in the direction r, θ has magnitude given by

$$S_r = \frac{15\, I_0^2}{\pi\, r^2}\left[\frac{\cos\left(\frac{1}{2}\pi\cos\theta\right)}{\sin\theta}\right]^2 \tag{2.42}$$

In which, r and θ are shown in the coordinate system in Figure 2.7, and I_0 is the peak value of the current [*Ulaby*, 1981] .

The Poynting flux S_r is maximum at $\theta = \pi/2$, at right angles to the line of the dipole. The normalized radiation pattern $F_n(\theta)$ is then given by

$$F_n(\theta) = \frac{S_r(\theta)}{S_r\left(\frac{\pi}{2}\right)} = \left[\frac{\cos\left(\frac{1}{2}\pi\cos\theta\right)}{\sin\theta}\right]^2 \tag{2.43}$$

As shown in Fig. 2.8, no energy is radiated in the direction of the dipole axis ($\theta = 0$ and $180°$), and maximum radiation is in the broadside direction ($\theta = 90°$). Since F_n is independent of φ, as would be expected from symmetry considerations, the pattern is doughnut-shaped.

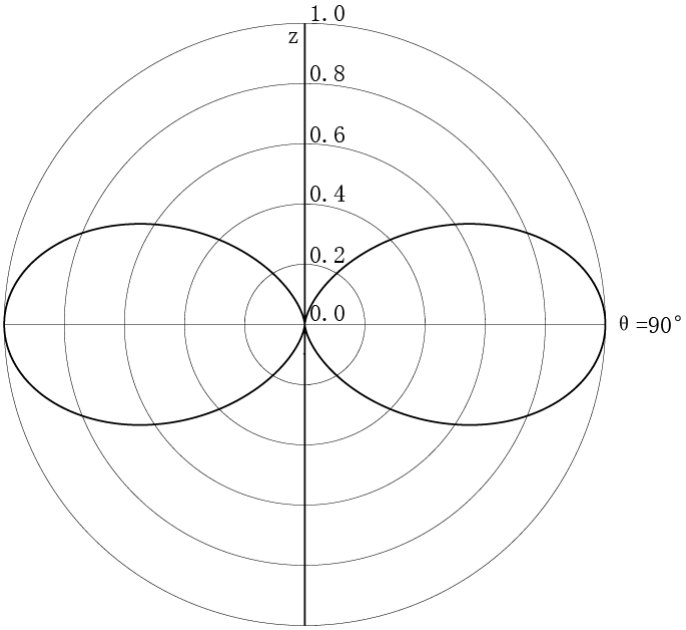

Figure 2.8. Polar plot of the normalized radiation pattern of a half-wave dipole antenna.

2.1.5.2 The Twin-Terminated Folded Dipole Antenna (TTFD)

The PolarDARN radars use TTFD (twin-terminated folded dipole) wire antennas with a 21-wire reflecting fence to prevent echoes from the back direction (where strong auroral-zone echoes could originate during magnetically disturbed conditions). Figure 2.9 shows a folded dipole antenna element.

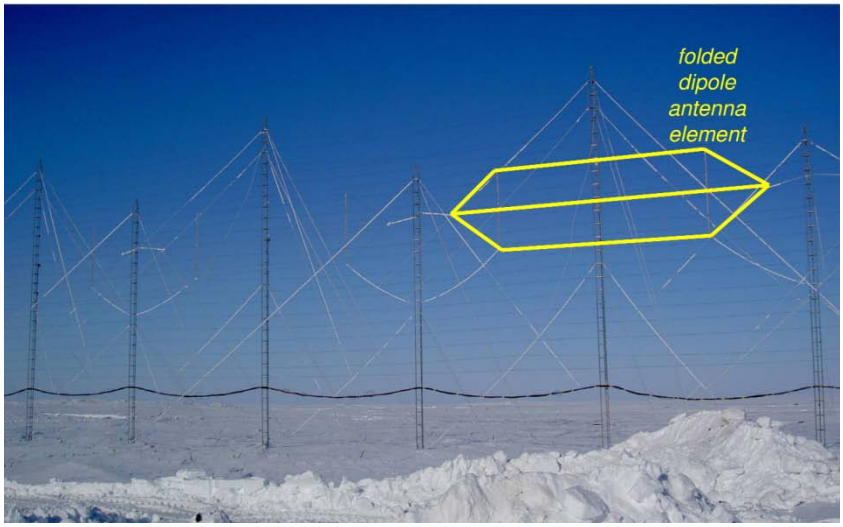

Figure 2.9. A folded dipole antenna element.

The basic element of a TTFD is a half-wave dipole, whose impedance is 73 Ω. If we add one wire to the antenna, it is called a folded dipole, the impedance of which is 300 Ω. Similarly, the impedance of the three-wire folded dipole or double-folded dipole is 600 Ω [see, for example, the Radio Amateur's Handbook, *American Radio Relay League*, 38th edition, 1961]. A twin-terminated folded dipole (TTFD), as shown in Figure 2.10, is a little different from the twin folded dipole because the twin folded wires are terminated in the middle with a 100 Ω resistor each, and are a little shorter than the half-wave dipole. However, the impedance of a TTFD is still about 600 Ω.

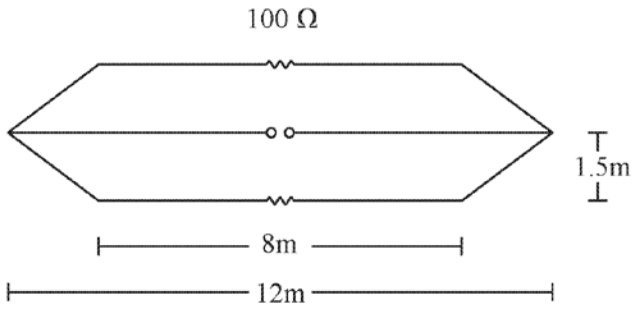

Figure 2.10. A portrait of a TTFD.

Since the impedance of a TTFD is about 600 Ω, a balun (balanced to unbalanced transformer) should be installed so that its balanced output terminals have an impedance of 600 Ω shown to the antenna, while its unbalanced input terminals present a 50 Ω impedance to the RG58 50-ohm coaxial cable carrying signal from to the transmitter output or to the receiver input, both of which have 50 Ω impedance. The type of balun used actually is a compromise match to the antenna, which must operate over a range from about 10 to 15 MHz. The balun output impedance is about 1200 Ω, which is a little high and causes a standing wave pattern due to reflections from the antenna. However, the two resistors in the "folded dipole arms" of the TTFD absorb some of the energy that is reflected, and the overall performance of the antennas appears to be acceptable. For the TTFD shown in Figure 2.10, the length of the half-wave dipole is 12 m, so the "resonant" wavelength is about $2 \times 12\ \mathrm{m} = 24\ \mathrm{m}$. The frequency is the quotient of the speed of light ($3 \times 10^8\ \mathrm{m/s}$) over the wavelength 24 m, namely 12.5 MHz. This is the central frequency for PolarDARN which, as stated above, generally operates in the frequency range within about 2.5 MHz of that central frequency.

Figure 2.11 shows the radiation pattern of a single TTFD antenna operating at 10MHz and 30° elevation angle (near the maximum power elevation angle). In the figure, the irradiance is given in dB, defined by

$$\mathrm{I_{dB}}(\theta) = 10\log_{10}\left(\frac{\mathrm{I}(\theta)}{\mathrm{I}(0)}\right) + \mathrm{I_{dB}}(0) \qquad (2.44)$$

where $\mathrm{I_{dB}}(\theta)$, $\mathrm{I}(\theta)$ are the irradiances at the angle θ, and $\mathrm{I_{dB}}(0)$, $\mathrm{I}(0)$ are the reference values at the angle 0. $\mathrm{I_{dB}}(0)$ varies with frequency, but is 4.94 dB for 10 MHz and 30° elevation angle. $\mathrm{I_{dB}} = 0$ is the irradiance of the isotropic pattern for the same total power.

The Max Gain is 4.94 dB in the broadside direction. The half-power points can be obtained by substituting $\frac{I(\theta)}{I(0)} = \frac{1}{2}$ into (2.44), giving the angles where the intensity is 3 dB down with respect to $I_{dB}(0)$. In Figure 2.11, the red lines show that the intensity is -3dB down at about 35° either side of the maximum, giving a 70° 3dB BeamWidth.

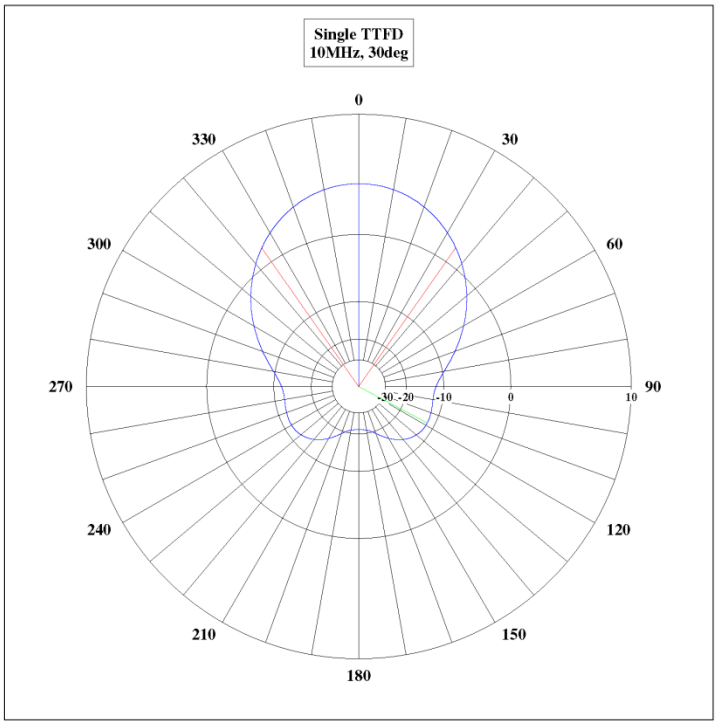

Pattern Analysis			
Max Gain (Front):	Gain = 4.94 dB Phi = 0 Deg	Max Gain (Back):	Gain = -11.55 dB Phi = 118 Deg
-3dB (Left of Max):	Gain = 1.82 dB Phi = 325 Deg	-3dB (Right of Max):	Gain = 1.82 dB Phi = 35 Deg
3dB BeamWidth:	70 Deg	Front/Back Ratio:	16.49 dB

Figure 2.11. This figure shows the single TTFD pattern at 10MHz frequency and 30° elevation angle in polar coordinates. The Max Gain is 4.94 dB in the broadside direction. The red lines indicate the half-power directions where the intensity is 3 dB down, so there is a 70° 3 dB BeamWidth. The green line shows that the maximum backward intensity is about -11.55 dB, down about 16.49 dB from the maximum forward intensity (courtesy of Jan Wiid, University of Saskatchewan SuperDARN engineer).

2.1.5.3 The Transmitting Antenna Array

The linear transmitting array consists of 16 TTFD antennas, equal spaced and fed with equal amplitude. The interference pattern for an array of N TTFD antennas all fed in phase is given by

$$I_N(\phi) = I_1(\phi)\left[\frac{\sin\left(\frac{N\,\pi\,d\,\sin\,\phi}{\lambda}\right)}{\sin\left(\frac{\pi\,d\,\sin\,\phi}{\lambda}\right)}\right]^2 \qquad (2.45)$$

where $I_1(\phi)$ is the pattern of a single TTFD antenna, which includes the vertical two-source interference pattern between the actual antenna and its image an equal distance below the ground (assumed to be highly conducting), given by $\sin^2\left(\frac{2\,\pi\,H\cos\,\theta}{\lambda}\right)$, where H=10m is the height of the antenna above ground, N=16 is the number of antennas, d=15m is the spacing between adjacent antennas, and the angles ϕ, θ correspond to the coordinate system in Figure 2.7. The power at $\phi = 0$ will be $N^2 = 256$ times of that of a single TTFD. However, SuperDARN radars are phased-array radars, in which a constant phase gradient is applied across the 16 antennas, with each antenna differing in phase by a fixed phase α from the neighbouring antenna. The usual way to apply the phase α is simply by means of a length L of coaxial cable of refractive index n. The phase difference between antennas is then given by

$$\gamma = k_0\, d \sin\phi - k_0\, n\, L \tag{2.46}$$

and the principal maxima occur where

$$\gamma = m\, 2\pi = k_0\, d \sin\phi - k_0\, n\, L \tag{2.47}$$

where m is the order of the principal maximum. The resulting irradiance equation for the array of antennas in which each individual antenna has the pattern $I_1(\theta,\varphi)$ would be

$$I(\theta,\phi) = I_1(\theta,\phi)\left[\frac{\sin\,(N\gamma/2)}{\sin\,(\gamma/2)}\right]^2 \tag{2.48}$$

In this equation, the θ-dependence is simply for an antenna of pattern $I_1(\phi)$ at a height H above a flat perfectly reflecting ground. The "vertical" radiation pattern is then given by $\sin^2\left(\frac{2\,\pi\,H\cos\,\theta}{\lambda_0}\right)$,

so that

$$I_1(\theta,\phi) = I_1(\phi)\,\sin^2\left(\frac{2\,\pi\,H\cos\,\theta}{\lambda}\right) \tag{2.49}$$

The above vertical pattern would give a minimum at θ= 90°(elevation angle is 0°) and a maximum at θ= 41.41°(elevation angle is 48.59°), for the usual height H = 10.0 m of the antennas, and for an operating frequency of 10 MHz (λ_0 = 30.0 m). In practice, the danger of such an arrangement is that incoming signals can reach the radar from both the forward and backward directions. To eliminate echoes from the back-directions, a 45° inclination reflecting fence consisting of 21 horizontal wires is placed directly behind the 16-antenna array. The top of the fence is at height 15.0 m and located just above the center of the antennas (at height H = 10.0 m). The 45° fence thus extends to the ground at a distance of 15.0 m behind the main array. This reflecting fence greatly reduces the irradiance from the back directions (a 44 dB two-way reduction is achieved, i.e 22 dB from antenna to scatterer and 22 dB along the return path from scatterer to antenna). However, it also has the effect of altering the vertical pattern of the antenna. Instead of a peak at an elevation angle of θ= 41.41°, the actual array has a peak at θ= 54° (elevation angle is 36°), and about 12° of this difference can be attributed to the reflecting fence (the remaining small part of the difference is due to the use of the 3-wire TTFD antennas).

In radar work, it is usual to operate in zeroth order, so m = 0, and the phase equation thus becomes simply

$$\gamma = 0 \tag{2.50}$$

As a result, we see that

$$d \sin \phi = n L \tag{2.51}$$

which simply means that the applied phase difference k_0 n L must equal the natural phase difference k_0 d sin ϕ between antennas. In order to ensure that all antennas radiate in phase in direction ϕ, the applied phase must be greatest where the natural phase is smallest, and vice versa. For example, the boresight for an east-west array of antennas would be northward. If one looks at an angle ϕ to the west of north, the natural path lengths would go from 0 to 15 d sin ϕ across the array from the westernmost antenna #1 to the easternmost antenna #16 (the path coming in to the westernmost antenna is shortest, which we set to 0, while that to the easternmost antenna is longest). Therefore, the applied coaxial line lengths would go from 16 L on the west to L on the east, and the total phase, the sum of the natural and applied phases, at each antenna would be 16 d sin ϕ (for example, antenna #3 would have a natural phase length of k_0 2 d sin ϕ and an applied phase of k_0 n 14 L = k_0 14 d sin ϕ).

The only difficulty with the above scheme is that, for high enough frequencies (using the antenna separation of 50.00 ft = 15.24 m, the frequencies affected are those above 13.95 MHz), there will be another principal maximum in order m = -1. Let us write the phase equation (noting that the line length L has already been employed for the m = 0 order in which the radar is designed to operate), i.e. in direction ϕ, the length L is given by

$$d \sin \phi_{m=0} = n L \tag{2.52}$$

The phase equation for order m = -1 then becomes

$$k_0 d \sin \phi_{m=-1} - k_0 d \sin \phi_{m=0} = -2\pi \tag{2.53}$$

which can be written as

$$\sin \phi_{m=-1} = -\frac{\lambda_0}{d} + \sin \phi_{m=0} \tag{2.54}$$

Suppose the frequency is 18.0 MHz (λ_0 = 50/3 m) and the desired beam direction is the beam 0 direction given by ϕ = 24.30°. The preceding equation then shows that

$$\sin \phi_{m=-1} = -1.0936 + \sin 24.30° \tag{2.55}$$

which gives the solution $\phi_{m=-1} = -43.10°$. This means that the "desired" zeroth order beam at $\phi_{m=0} = 24.30°$ is "contaminated" with an undesired m = -1 principal maximum beam at $\phi_{m=-1} = -43.10°$. Of course, if there is strong scatter coming from the latter undesired direction and only weak scatter from the desired direction, the signal received will interpreted as having come from the usual m = 0 direction but this will be incorrect since it will have come mainly from the m = -1 direction instead.

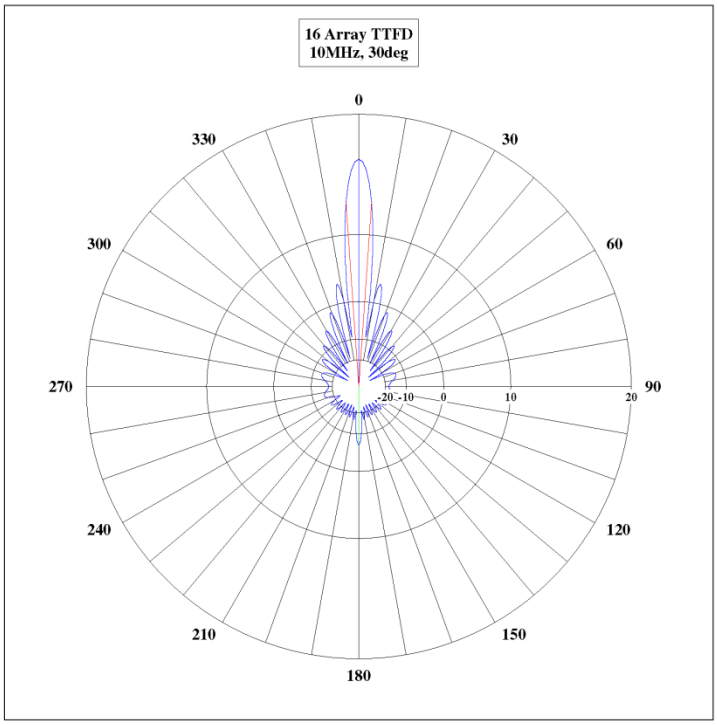

Pattern Analysis			
Max Gain (Front):	Gain = 16.9 dB Phi = 0 Deg	Max Gain (Back):	Gain = -6.47 dB Phi = 180 Deg
-3dB (Left of Max):	Gain = 13.32 dB Phi = 356 Deg	-3dB (Right of Max):	Gain = 13.32 dB Phi = 4 Deg
3dB BeamWidth:	8 Deg	Front/Back Ratio:	23.37 dB

Figure 2.12. This figure shows the 16-antenna Array pattern at 10 MHz and 30° elevation angle in a polar plot. The Max Gain is 16.9 dB in the broadside direction. The red lines indicate an 8° 3 dB beamwidth. The green line shows that the maximum intensity in the backward radiation pattern is some 23.37 dB below the forward maximum (courtesy of Jan Wiid, University of Saskatchewan SuperDARN engineer).

Figure 2.12 shows the 16-antenna array pattern at 10MHz frequency and 30° elevation angle. The Max Gain is 16.9 dB in the broadside direction. The red lines indicate the half-power directions and they show that there is an 8° 3dB BeamWidth, which is much sharper than the 70° 3-dB beamwidth of a single TTFD.

We can fit a curve to $I_1(\phi)$ (ϕ < .10 rad) to get more accurate result of the 3-dB beamwidth. For Figure 2.12, the fitted curve is

$$I_1(\phi) = I_0\,(1 - 7.9870 \times 10^{-6}\phi - 5.7101 \times 10^{-4}\phi^2) \qquad (2.56)$$

in which, $I_1(\phi)$ is the power of a single TTFD, and I_0 is the power at $\phi = 0$. For the small angles ϕ < .10 rad, $I_1(\phi)$ is essentially constant at I_0.

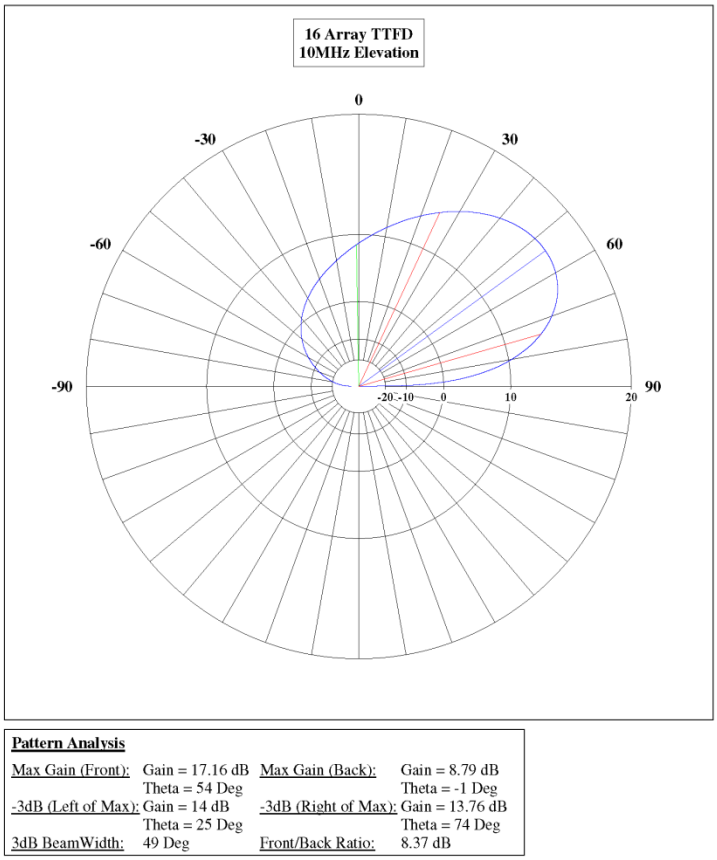

Figure 2.13. A plot of the 16-antenna array TTFD elevation pattern at 10MHz. The NEC-Win software package plotted the angles measured from the zenith, so the angles shown are the complement of the elevation angle (courtesy of Jan Wiid, University of Saskatchewan SuperDARN engineer).

Substituting (2.56) into (2.45), we find that the half power points are at 356.8° and 3.2°, so the 3 dB beamwidth is 6.4°. This is smaller than the 3 dB beamwidth of 8° obtained from the NEC-Win software package. The phasing matrix used to shift the beams of the PolarDARN radars gives a shift of 3.24° between successive beams. This is only about half the actual 6.4° half-power beamwidth, so it is clear that adjacent beams of PolarDARN are not independent because their half-power beam patterns have a substantial overlap. It is more correct to say that the beams separated by two beam positions are independent.

In this way, we can calculate 3 dB beamwidth for different frequencies. The results show that 3 dB beamwidth decreases when the frequency increases.

Figure 2.13 shows the 16 antenna array TTFD elevation pattern at 10MHz (angles shown are from the zenith). The Max Gain is 17.16 dB at 36° elevation angle. The red lines at the -3dB positions show that there is a 49° vertical beamwidth.

A prototype of the TTFD antenna system was built at Saskatoon by Dr. Andre and Mr. Marshall in the fall of 2003 and tested during the SuperDARN Workshop in 2004. The antenna has both halved the cost of the PolarDARN system and worked well in practice.

2.2 DMSP particle precipitation detector

The Defense Meteorological Satellite Program (DMSP) (*Greenspan et al.*, 1986; *Rich and Hairston*, 1994) is operated by the US Air Force. The DMSP satellites are in circular orbits at an altitude of about 848 km and an inclination of about 98.8°, which causes the orbit to be "sun-synchronous". A sun-synchronous satellite orbit ensures that the orbital meridian plane is roughly fixed in local time throughout the year. Two DMSP satellites are supposed to be in high-inclination near-polar orbits at all times, one in the dawn-dusk meridian plane and one in the 10:30 – 22:30 meridian plane.

The space environment sensors for the DMSP spacecraft include a low-light-level imager (OLS), precipitating particle spectrometers (SSJ/3 and SSJ/4), a thermal plasma monitor (SSIES) and a flux-gate magnetometer (SSM). In this research, we utilized precipitating particle data obtained from these satellites to determine the polar cap boundary.

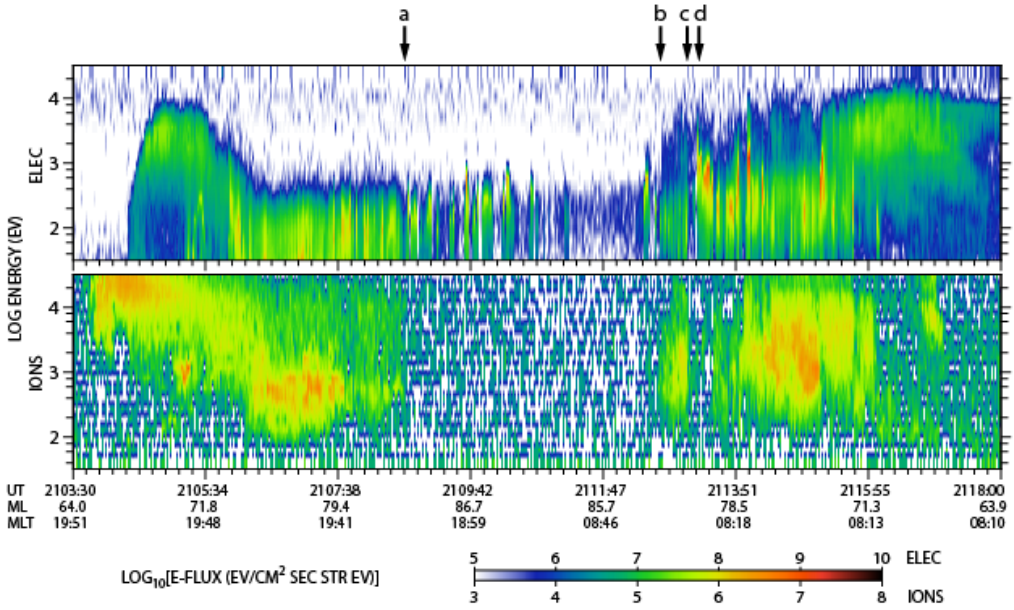

Figure 2.14. DMSP F16 satellite results on March 8, 2008. Top panel: electron energy spectrum. Bottom panel: ion energy spectrum. Arrow "a" shows the duskside polar cap boundary; arrow "b" shows the dawnside polar cap boundary. The space between "c" and "d" is also in a displaced open field line region (from *Watanabe et al.*, [2009]).

The SSJ/4 sensors measure the fluxes of electrons and ions in 20 energy channels in the range of 0.03–30 keV, by using a set of four cylindrical curved plate electrostatic analyzers arranged in two pairs. Each pair of analyzers contains one set of cylindrical plates with radius of curvature of 60°, and one set with radius of curvature of 127°, which

measures the electrons and ions in ten equally logarithmically spaced energy channels in the range of 1-30 keV and ten more in the range 30-1000eV. The two analyzers measure at the same time, and return a 20 point ion spectrum and a 20 point electron spectrum once per second [*Hardy et al.*, 1984].

Figure 2.14 shows a DMSP electron and an ion energy spectrum taken during a period of time that included an interval when the DMSP satellite flew over the polar cap. The bright data points indicate high energy flux. The 1 – 30 keV ion data is particularly useful, since these are auroral energies, too high for the polar cap, so the poleward boundary of these ions is a very good indicator of the transition from the closed field line geometry of the auroral zone to the open field line region of the polar cap. Figure 2.14 shows clear boundaries of 1 – 30 keV ion data at "a" at time 21:08:36 UT and "b" at time 21:12:41 UT, between which is the polar cap boundary. The space between "c" at time 21:13:05 UT and "d" at time 21:13:15 UT is also in the open field line region.

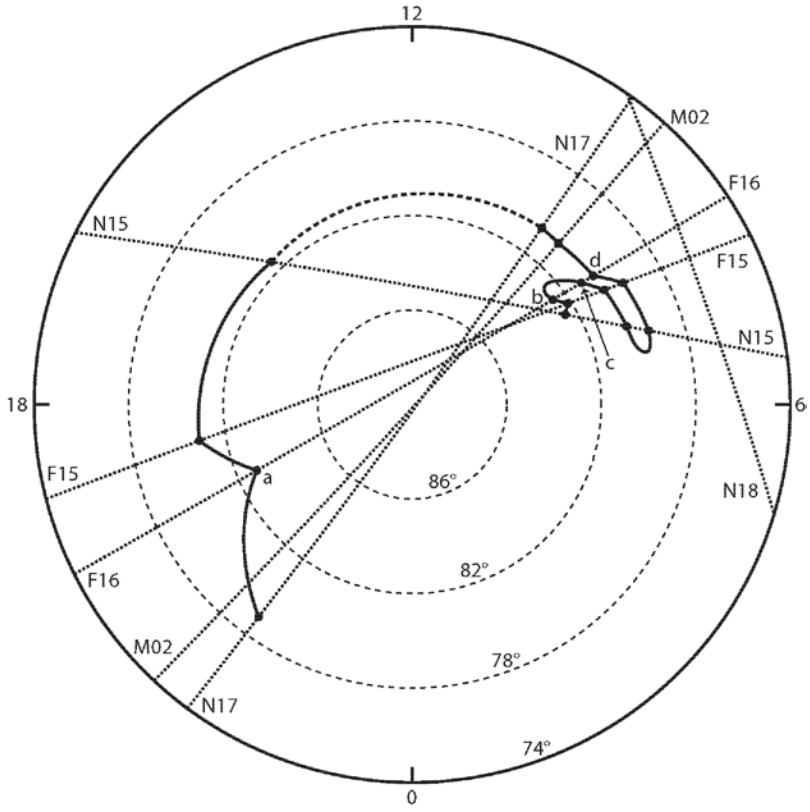

Figure 2.15. The paths of six satellites in the Northern Hemisphere on March 8, 2008. The solid line inside the circle shows the OCFLB. The dashed lines show the paths of each satellite with dots indicating where the OCFLB is located. Satellites F15 and F16 are DMSP satellites, while N15, N17, N18 are NOAA POES satellites, and M02 is the METOP satellite (from *Watanabe et al.*, [2009]).

By putting the dots of the time points “a”, “b”, “c” and “d” on the satellite’s path, we can obtain the polar cap boundary. Figure 2.15 shows the polar cap boundary obtained by 6 satellites which flew over the polar cap in the time interval 20:42-21:30 UT. The dotted line with “F16” on it indicates the path of the DMSP F16 satellite, on which the dots “a”, “b”, “c” and “d” are the dots in Figure 2.14.

2.3 POES Space Environment Monitor

The National Oceanic and Atmospheric Administration Polar Orbiting Environmental Satellites (POES) are operated by the National Oceanic and Atmospheric Administration (NOAA) and carry a suite of instruments which have a broad range of applications in detecting and monitoring the environment.

Since NOAA-15, an upgraded version of the Space Environment Monitor (SEM-2) is onboard. It contains two components, namely a Total Energy Detector (TED) and a Medium Energy Proton and Electron Detector (MEPED) [*Evans*, 2000, 2006].

The Total Energy Detector measures the energy flux of precipitating electrons and ions.

There are eight individual cylindrical curved-plate, electrostatic-analyzer, Channeltron charged-particle detector systems in the TED, which are divided into two sets of four systems measuring particles from different directions. The center of the field-of-view of each detector in one set is outward along local zenith, parallel to the Earth-center-to-satellite radial vector. This set is called the 0° detector set. The other set, in which the center of field of view of each detector is pointed at 30° to the Earth-center-to-satellite radial vector, is called the 30° detector set.

Two detectors in each set of four measure integral flux of precipitating electrons in the energy ranges of 50 - 1000 eV and 1000 - 20,000 eV respectively. The other two detectors in each set measure integral flux of precipitating ions in the energy ranges of 50 - 1000 eV and 1000 - 20,000 eV respectively.

All eight detectors sweep over eight contiguous energy bands, energy bands 1-8 for low energy detectors that sweep through 50 - 1000 eV, and energy bands 9-16 for high energy detectors that sweep through 1000 - 20,000 eV.

A full sweep for each detector is 2.0 s, with 0.2 s in each energy band, which makes 1.6 s for eight energy bands, 0.2 s reset and 0.2 s background accumulation.

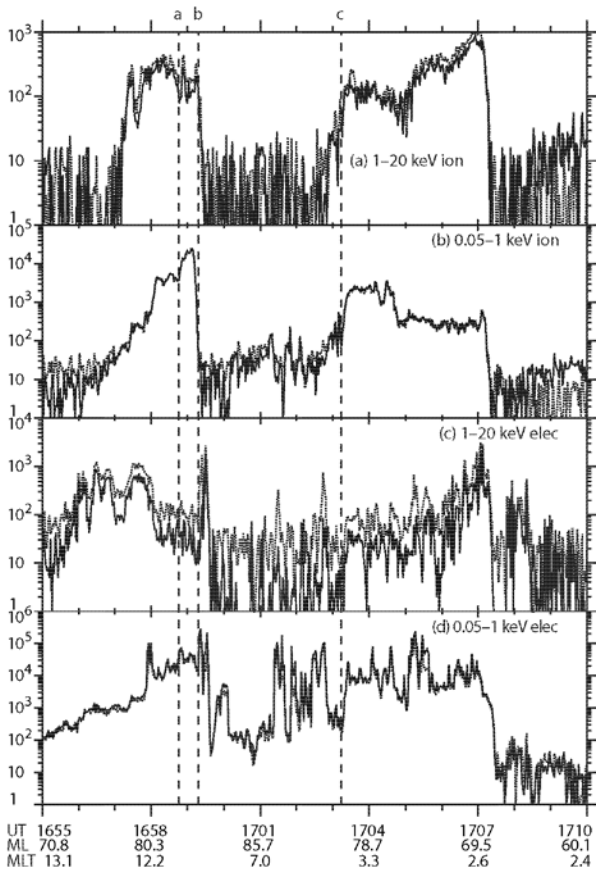

Figure 2.16. NOAA POES 18 satellite results on March 22, 2008. Panels 1 to 4 (from top to bottom) give integral flux data: protons 1000-20,000 eV; protons 50 eV-1000; electrons 1000 – 20,000 eV; electrons 50 eV-1000 eV. The solid line denotes 0° pitch angle, dashed line 30° pitch angle. The x axis shows the universal time (UT), magnetic latitude (ML), and magnetic local time (MLT) (from *Watanabe et al.*, [2009]).

Similar to the DMSP data, the POES 1000 - 20,000 eV ion data is particularly useful for identifying the polar cap boundary. Figure 2.16 shows the POES energy flux of electrons and ions when the satellite flew over the polar cap, in which clear boundaries of 1 – 20 keV ion data are shown at “b” at time 16:59:18 UT and “c” at time 17:03:14 UT, between which is the polar cap. The space between “a” at time 16:58:46 UT and “b” is the cusp [*Newell and Meng*, 1988, 1992], which is also in the open field line region.

Figure 2.17 shows the polar cap boundary obtained by 5 satellites which flew over the polar cap in the time interval 16:52-17:34 UT. The dotted line with “N18” on it indicates the path of the POES N18 satellite, on which the dots “a”, “b” and “c” are the dots in Figure 2.16.

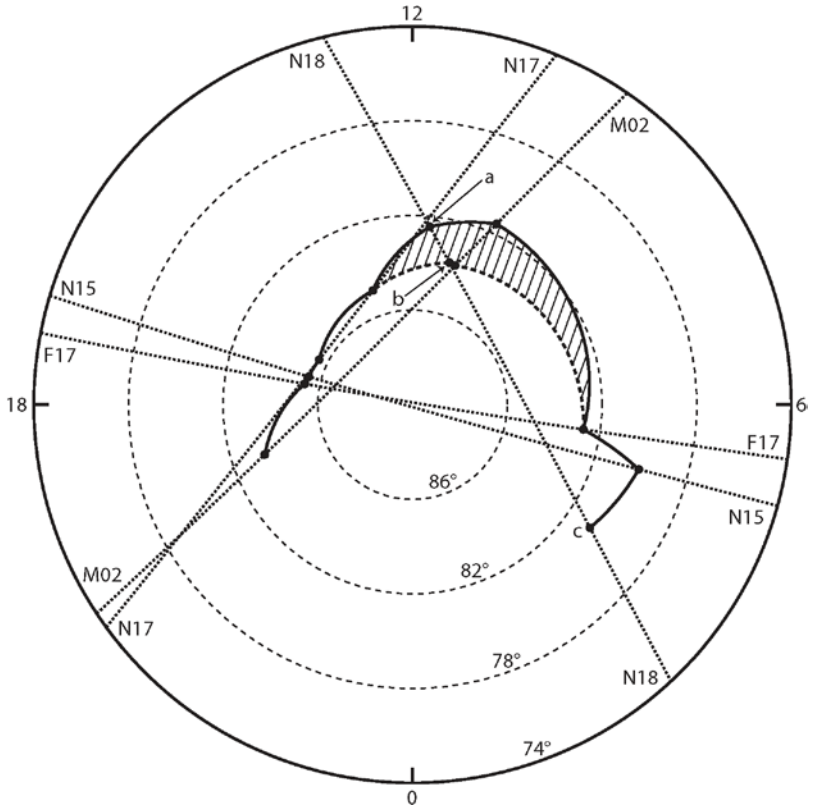

Figure 2.17. The satellite paths in Northern Hemisphere on March 22, 2008. The solid line inside the circle shows the OCFLB. The dashed lines show the paths of each satellite with dots on it where the OCFLB locate. F17 is a DMSP satellite, while N15, N17, N18 are NOAA POES satellites, and M02 is the METOP satellite (from *Watanabe et al.*, [2009]).

3. SOLAR MAGNETIC POLARITY AND SECTOR STRUCTURE

3.1 Magnetic Structure of the Sun during 11-year and 22-year Solar Cycle

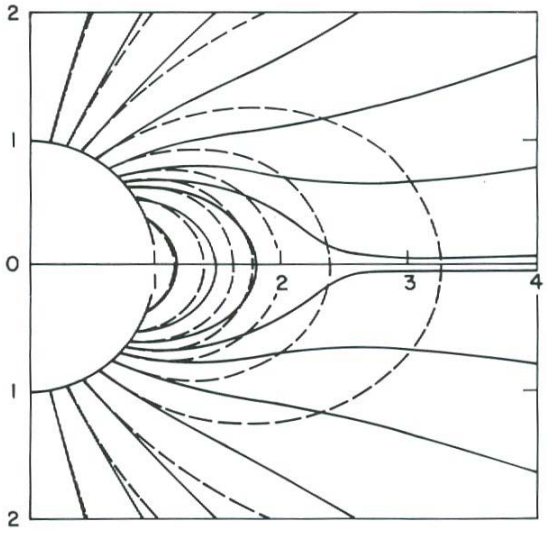

Figure 3.1. Magnetic field lines deduced from an MHD model for isothermal conditions are shown in solid lines, compared with the dipole field lines shown by the dashed lines, for a common coronal base (taken from *Pneuman and Kopp* [1971]).

In Figure 3.1, solid lines show MHD-modeled magnetic field lines in the solar meridian plane, and are compared with pure dipole field lines from the same footprints at the base of corona. Near the equator, the MHD model field lines are stretched away from the Sun much more than the pure dipole field lines. At high latitudes, the field lines are "open" (i.e. they close far from the Sun), and near solar minimum the solar wind originates from these open field line regions in the corona. The field lines originating at about ±45° latitude eventually become antiparallel lines on either side of the equatorial plane. The different polarity of these field lines signifies a rapid change of magnetic field at the equator, and is consistent with a thin current sheet of high density $\mathbf{j} = \left(1/\mu_0\right)\boldsymbol{\nabla} \times \mathbf{B}$, normal to the paper. The current is called the heliospheric current sheet [*Crooker et al.*, 2004] and is analogous to the magnetospheric current sheet in the magnetotail.

The solar magnetic activity has about an 11-year cycle. At the start of a solar cycle, the solar magnetic field is a fairly well-defined dipole. For example, at the start (~1997) of Solar Cycle 23, the North Pole was of positive polarity, while the South Pole was of negative polarity. During Solar Cycle 23, the polarity of the bipolar sunspots in the northern solar hemisphere was positive for the leading sunspots and negative for the

following sunspots. When sunspots decay, they break into magnetic fragments, with the leading spot fragments going equatorward and the following spot fragments poleward. Thus, during Solar Cycle 23, in the northern solar hemisphere, the positive leading spot fragments went to the equator, while the negative following spot fragments went to the North Pole, where they progressively cancelled the initial positive polarity during the increase of sunspot activity up to the time of the solar maximum. The magnetic polarity at the poles became weaker and weaker until it was very small in the solar maximum years. After that, the magnetic polarity reversed, and the dipole grew in strength. By the end of the Solar Cycle, in the solar minimum years between Cycles 23 and 24, the Sun formed a very well defined dipole field with reversed polarity compared to the start of the cycle. Thus, Solar Cycle 23 ended with a dipole field that was negative in the north polar region and positive in the south polar region. The magnetic polarity changes sign over an 11-year solar cycle, and returns to its original polarity after two 11-year solar cycles. The result is a 22-year solar magnetic cycle called the Hale cycle [*Hale et al.*, 1919].

In the solar minimum years, when the global magnetic field is nearly dipolar, there are two types of solar wind. Slow solar wind comes from the corona at low latitudes where the field lines are closed. Also, solar coronal holes occur at high latitudes due to the dipole field. The fast solar wind appears to originate from solar coronal holes where the field lines are open [*Krieger et al.*, 1973; *Sheeley et al.*, 1976]. The ionized oxygen ratio $\frac{O^{7+}}{O^{6+}}$ is low, which reflects a low value of coronal temperature [*Hundhausen et al.*, 1968].

In the solar maximum years, however, the polar field is weak. Only slow solar wind exists. Solar wind arises in the low-latitude sunspot region and streamer on closed field lines, which act to restrain the speed to slow values. But the low-latitude corona is hot, since the $\frac{O^{7+}}{O^{6+}}$ ratio is high. The comparison between the solar wind speeds and the oxygen ionization ratio during solar maximum and minimum years reveals that there is an anticorrelation between coronal temperature and the solar wind speed.

Figure 3.2 shows the solar wind velocity and the $\frac{O^{7+}}{O^{6+}}$ ratio between the solar minimum year 1995 and solar maximum year 2000 using the Ulysses SWICS data [*Zurbuchen et al.*, 2002]. Every data point is for a 6 hour interval. The x axis is the heliographic latitude from -80° to 80°, with dashed vertical lines inserted between adjacent years. In the solar minimum years, the solar wind speed is high and the $\frac{O^{7+}}{O^{6+}}$ ratio is low, and both the speed and ionization ratio exhibit low variability, presumably reflecting stable, low-temperature conditions in coronal holes. In the solar maximum years, the solar wind associated with the low-latitude source region has a higher $\frac{O^{7+}}{O^{6+}}$ ratio, indicating higher coronal temperature, but the solar wind speed is slow. The coronal-hole-associated fast solar wind is characterized by an oxygen ionization ratio $\frac{O^{7+}}{O^{6+}} < 0.1$ [*Von Steiger et al.*, 2001]. It is not clear if the origin of the fast solar wind is from the polar plumes, inter-plume regions or both. The above low ratio implies that the "frozen-in temperature" was $\sim 8 \times 10^5$ K. On the assumption that the coronal temperature increases with height above the polar

holes and is not contaminated by Quiet Sun emissions, one can infer that the fast solar wind plasma very likely arises at low altitudes, less than $1.2R_{sun}$ [*Feldman et al.*, 2005].

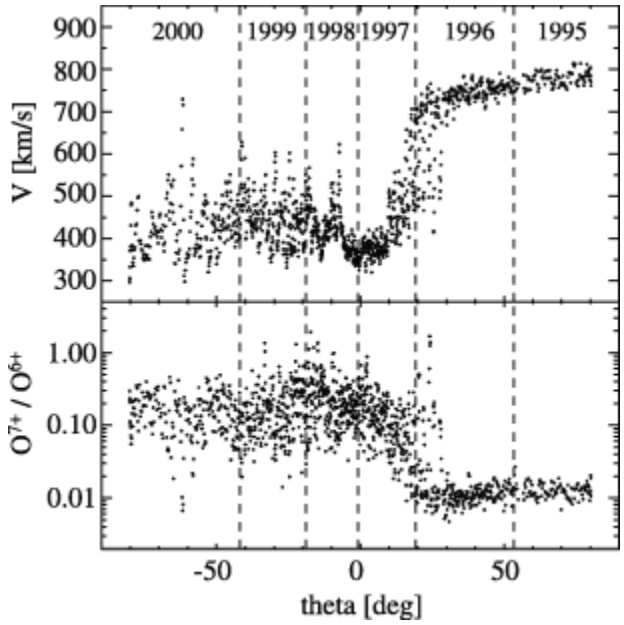

Figure 3.2. Solar wind speed and the oxygen charge state ratio O^{7+}/O^{6+} from SWICS-Ulysses between 1995 at highest northern latitude and solar maximum year 2000 at highest southern latitude. The data is more variable in solar maximum years than in solar minimum years (taken from *Zurbuchen* [2002]).

The slow solar wind appears to be associated with the streamer belt near the solar equator. This closed field region of high coronal temperature is the main source in the solar maximum years and leads to higher ionization ratios in the range $0.1 < \frac{O^{7+}}{O^{6+}} < 1.0$, with the ratio $\frac{O^{7+}}{O^{6+}}$ being highly variable [*Zurbuchen et al.*, 2000]. The data points where $\frac{O^{7+}}{O^{6+}} > 1.0$ indicate unusually hot charge states typically related to the more extreme conditions during coronal mass ejection (CME) events [*Lepri et al.*, 2001; *Henke et al.*, 2001]. The slow solar wind is presumed to arise from plasma in the so-called Quiet Sun group 3 [*Feldman et al.*, 2005], which are 1.2-1.6 K plasmas that are normally confined within large loops whose tops reach out to about 1.5 R_{sun} and in some cases even beyond 2 R_{sun} [*Schwenn et al.*, 1997]. Most of that plasma is confined within the loops only for one day or two, and is released with no significant changes in composition or ionic fraction when the loop disintegrates. This conclusion is drawn because the temperature and the composition are similar in QS group 3 plasma and that measured by in-situ solar wind instruments on satellites. In the solar wind, the heliospheric current sheet (HCS) is formed at the top of the streamer belt and advected out into the heliosphere by the solar wind. Thus, the closed-field line region of the inner HCS is the source of the streamer-associated solar wind, and this is slow solar wind [*Suess et al.*, 2009]. The Fe/Mg abundance ratio in slow solar wind is photospheric, which indicates that the slow solar

wind consists of plasma originally originating from a height less than 1.2 R_{sun} [*Feldman et al.*, 2005].

Figure 3.3 compares histograms of solar wind speed and the $\frac{O^{7+}}{O^{6+}}$ ratio in two time periods of two years each, with solar minimum years shown on the top and solar maximum years on the bottom. In solar minimum years, there are bimodal distributions in both solar wind speed and the $\frac{O^{7+}}{O^{6+}}$ ratio.

In solar maximum years, the distribution of solar wind speeds does not have a high speed peak. The histograms of solar wind speed and the $\frac{O^{7+}}{O^{6+}}$ ratio are broad because of the varying conditions within the streamer belt, and the possibility of admixture of streamer-belt plasma with higher latitude coronal-hole-associated plasma at latitudes neighbouring the streamer belt [*Zurbuchen et al.*, 2002].

In both solar maximum and minimum years, there is an anticorrelation between the solar wind speed and the $\frac{O^{7+}}{O^{6+}}$ ratio, or coronal temperature.

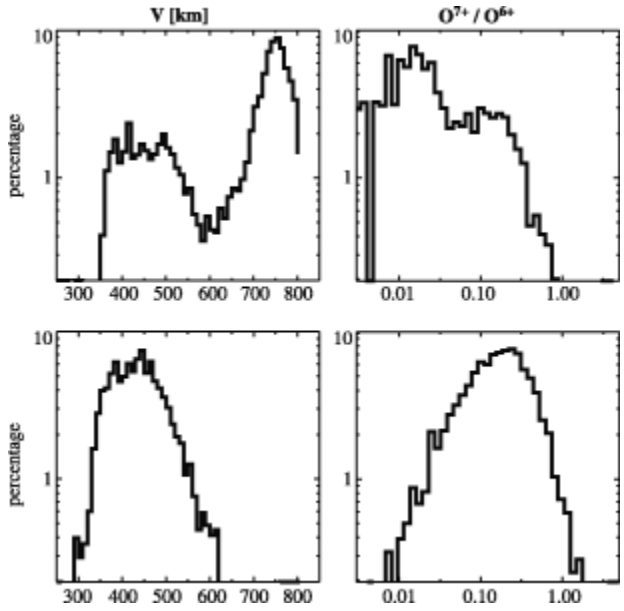

Figure 3.3. Histograms of solar wind speed V and the $\frac{O^{7+}}{O^{6+}}$ ratio. The top panels are for solar minimum years, and shows bimodal character in speed V and O^{7+}/O^{6+}. The bottom panels indicate the solar wind conditions in solar maximum years, and show only broader distributions with low peak velocity and high peak temperature (taken from *Zurbuchen* [2002]).

The plasma is poorly contained at the top of the HCS core in the sharply cusped streamers [*Suess and Nerney*, 2004]. The confinement of the core by the magnetic pressure from the external regions of the streamer belt on the sides of the HCS core is

weaker in the sharper cusps, so it is from these cusps that the plasma has a tendency to escape. The mass will episodically release from the cusp if there are small pressure pulses from "streamer puffs" [*Bemporad et al.*, 2005].

From Figure 3.4, we should notice a speed difference should occur between the outflow from the two legs of the HCS streamers, since the two legs are rooted in different locations on the Sun.

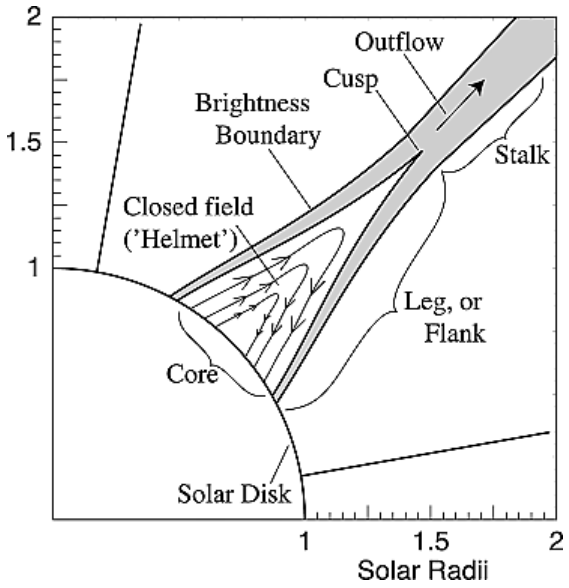

Figure 3.4. A streamer model [*Suess and Nerney*, 2006] with its internal magnetic loops based on empirical results [*Uzzo et al.*, 2006]. A quasi-steady process is depicted in which the stretching and opening by reconnection of the HCS magnetic loops causes open lines that merge into a stalk which appears to form from two outer HCS legs closer to the Sun. The outflow of the slow solar wind occurs in the stalk (taken from *Suess and Nerney* [2006], after *Uzzo et al.* [2006]).

Figure 3.5 shows a hypothetical solar wind source based on all observational results. A solar plasma blob escapes from the top of the core or helmet, with a loop of magnetic flux in it. The shear between such blobs in the two legs of the streamers causes the displacement of two opposite halves of blob, and the blob is seen as two blobs at 1AU. The loop of flux will also be sheared, and is embedded in the HCS and heliospheric plasma sheet. The points A and B show the ends of sheared flux. The HCS would lie just inside the boundary of the blob because of the shear. However, the HCS would lie in the middle of the depletion in the 5-10% of cases when there is negligible shear between the outflows of the two legs [*Suess et al.*, 2009].

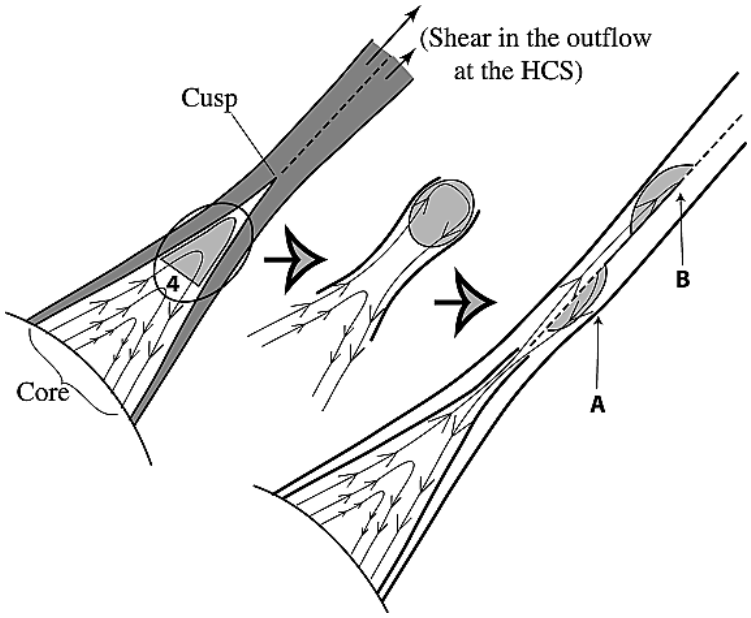

Figure 3.5. Low He/H blob of plasma is halved and displaced when it escapes from the streamer core, carrying loops of magnetic flux. The HCS is located at the edge of the blob (taken from *Suess et al.* [2009]).

The electron temperature T at the source of the solar wind can be obtained from the $\frac{O^{7+}}{O^{6+}}$ ratio [*Ko et al.*, 1997]. The solar wind speed V_{sw} and 1/T have a strong correlation as shown in Figure 3.6. The data points were measured during a period of 6 solar rotations between Aug 27, 1996 and Feb 9, 1997 when Ulysses remained at about the same solar latitude of $(+30° \pm 5°)$ and periodically crossed the boundary between the fast solar wind from the northern polar coronal hole and the slow solar wind from outside the coronal hole. The 1/T curve and the solar wind speed curve match remarkably well in this period, even in the fast transition period between fast solar wind and slow solar wind, except two periods indicated by shaded regions when a CME occurs. Except for these two periods, the deviation of 1/T from the solar wind speed is within a limited range of 10-15%, which is surprising because the electron temperature reflects the conditions close to the solar surface while the solar wind speed changes in transit from the inner heliosphere to several AU because of processes such as stream-stream interactions. We should also notice that the deviations of 1/T from V_{sw} are not greater in the leading edges of fast streams that originated in coronal holes or in the low speed solar wind. A least-squares fit to the data (excluding the two shaded regions corresponding to CME events), assuming a linear relation of the form $V_{sw} = \frac{\langle B^* \rangle}{T} - V_0$, gives

$$V_{sw} = \frac{844}{T} - 88, \tag{3.1}$$

where the units are km/s for V_{sw} and 10^6 K for T [*Gloeckler*, 2003].

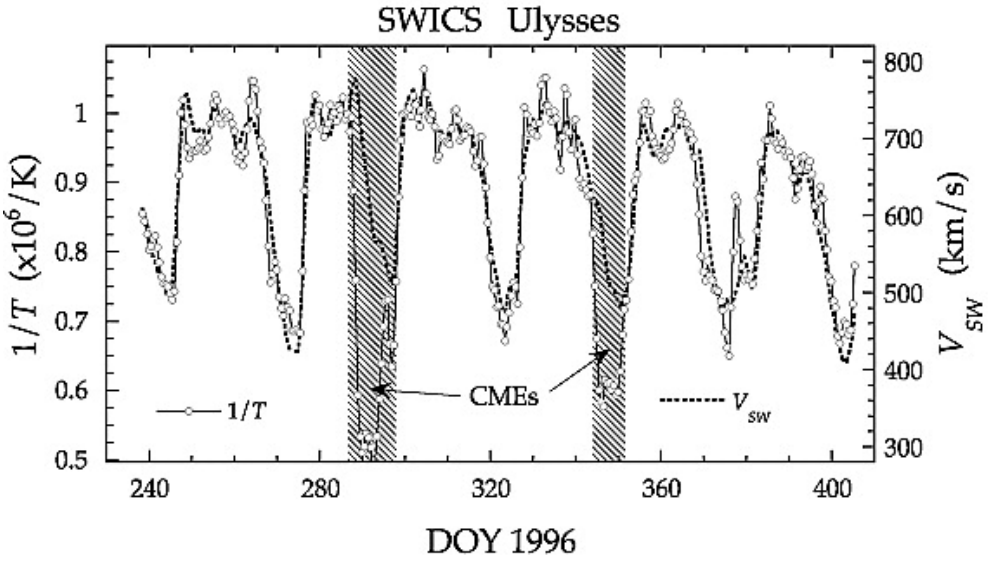

Figure 3.6. The solar wind speed V_{sw} (dotted line) and inverse of the electron temperature 1/T (solid line) in the time period Aug 27, 1996 to Feb 9, 1997, seen by Solar Wind Ion Composition Spectrometer (SWICS) on Ulysses. The data are three point averages of the basic 12-hour averages [*Gloeckler*, 2003].

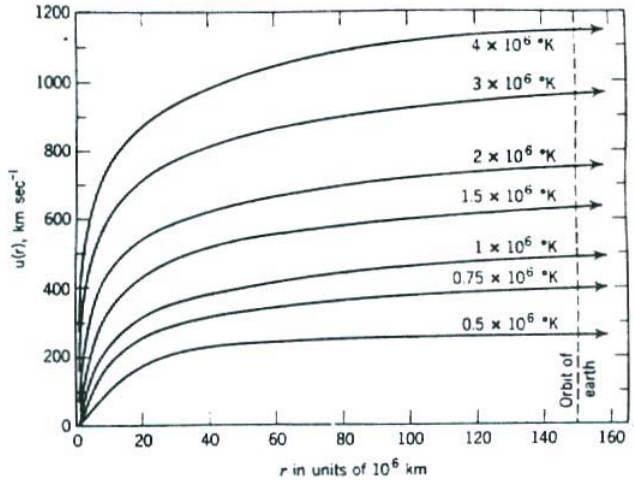

Figure 3.7. Coronal expansion speeds in isothermal corona for different coronal temperatures as a function of heliocentric distance (*Parker* [1963]).

Figure 3.7 shows the coronal expansion speed u(r) as the heliocentric distance r varies for different coronal temperature and with the reference $r_0 = 10^{11}$cm (about 1.4 solar radii), which undergoes an acceleration when the coronal expends. The continuous, supersonic expansion of the corona is what constitutes the solar wind [*Parker*, 1963].

The high temperature corona is characterized by high conductivity, which results in "frozen-in" streamlines. The coronal material streams outward along the streamlines, which also are the magnetic field lines. If the Sun were stationary, the field lines would go radially outward from the Sun. However, the Sun rotates in a period of about 27 days [*Broun*, 1876; *Maunder*, 1905], which causes the field lines to form a spiral curve. In a spherical coordinate system (r, φ, θ), the solar wind components are

$$U_r = u \quad \text{the expansion speed} \tag{3.2}$$

$$U_\varphi = -\omega r \sin\theta \tag{3.3}$$

$$U_\theta = 0\,, \tag{3.4}$$

as shown in Figure 3.8, for which the value $\omega = 2.7 \times 10^{-6}$ radians $\cdot\, s^{-1}$ was adopted for the angular velocity of solar rotation.

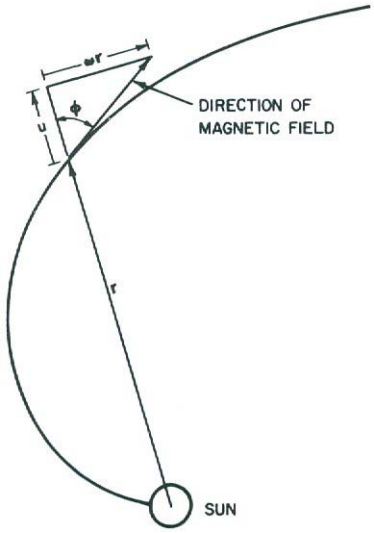

Figure 3.8. A streamline or magnetic field line in a frame of reference rotating with the Sun (taken from *Hundhausen* [1972]).

The extension of the solar magnetic field into interplanetary space is then given simply in terms of the differential relationship between the radial and azimuthal components, namely

$$\frac{1}{r}\frac{dr}{d\varphi} = \frac{U_r}{U_\varphi} = \frac{u}{-\omega r \sin\theta}\,, \tag{3.5}$$

which can be readily integrated.

At some distance away from the Sun, Figure 3.7 shows that the value of u(r) becomes nearly constant, which we can represent as u_s. By integrating (3.5), we get the explicit form of the magnetic field lines, given by

$$r - r_0 = \frac{-u_s}{\omega \sin\theta}(\varphi - \varphi_0) \tag{3.6}$$

where φ_0 is at the reference position with the distance r_0. The explicit magnetic field components are obtained from Maxwell's equation $\nabla \cdot \mathbf{B} = 0$ for a spherically symmetric geometry.

$$B_r(r, \varphi, \theta) = B(r_0, \varphi_0, \theta)\left(\frac{r_0}{r}\right)^2 \tag{3.7}$$

$$B_\varphi(r, \varphi, \theta) = -B(r_0, \varphi_0, \theta)\frac{\omega r_0}{u_s}\frac{r_0}{r}\sin\theta \tag{3.8}$$

$$B_\theta = 0 \tag{3.9}$$

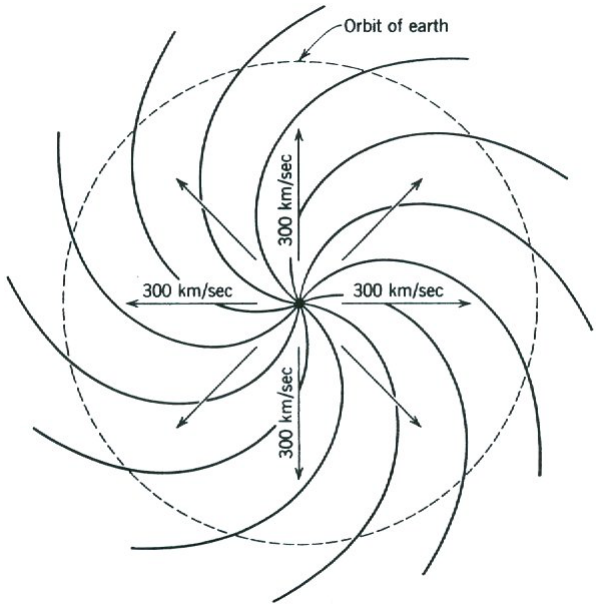

Figure 3.9. The configuration of the interplanetary magnetic field in a solar wind speed of 300 km/sec in the equatorial plane (taken from *Parker* [1963]).

Figure 3.9 shows that the magnetic field lines are Archimedes spirals in the solar equatorial plane and that they reach the earth at about 45° to the Sun-Earth line.

3.2 Solar Magnetic Field Sector Structure

A sector boundary is the transition region where the polarity of the IMF makes a persistent change from "away" to "toward", with respect to the Sun, or vice versa [*Ness and Wilcox*, 1965]. The heliospheric plasma sheet (HPS) is a sheath encompassing the heliospheric current sheet (HCS), much like the magnetospheric tail contains a central "neutral current sheet" and the surrounding central plasma sheet. Recent work shows that

about half of the sector boundaries lack a high-beta HPS, and that, for sector boundaries that are associated with a HPS, the latter often occurs away from the sector boundary [*Crooker et al.*, 2004].

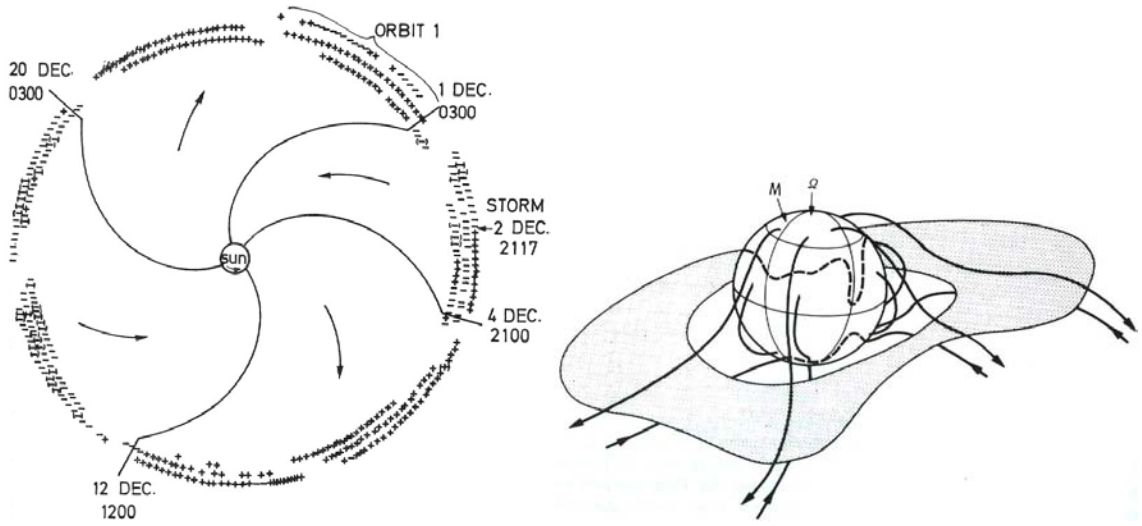

(a) (b)

Fig 3.10. (a) This shows a four-sector structure in the interplanetary magnetic field during November 1963 to February 1964. The "+" ("-") sign indicates that the interplanetary magnetic field is away from the Sun (toward the Sun), as measured in 3-hour intervals by IMP-1 (taken from *Ness and Wilcox* [1965]). (b) A model of the warping of the heliospheric current sheet. The plane of the current sheet is approximately the solar equatorial plane normal to the dipole axis M, which is separated from the rotation axis Ω. The current sheet separates the "away" and "toward" interplanetary magnetic fields, shown as solid lines (taken from *Sturrock* [1986]; based on *Smith et al.* [1978]).

The "away" and "toward" fields can show a very clear annual period [*Rosenberg and Coleman*, 1969], especially during solar minimum conditions when the global solar field is nearly dipolar. The solar rotation axis has about a 7.2° tilt from the normal to the ecliptic plane. In fall, around September 6, the solar northern hemisphere rotation axis has its maximum tilt toward the Earth, and away from the Earth in southern hemisphere. Similarly, around March 5, the southern solar hemisphere rotation axis has its maximum tilt toward the Earth, and the northern hemisphere had maximum tilt away from the Earth. In the present minimum between Solar Cycles 23and 24, the magnetic polarity of the solar north polar region is negative, so the magnetic field lines of the roughly dipolar solar field point toward the solar north pole. Therefore, the polarity of the field in the six-month period centered on September 6 is mainly "toward". However, in the six-month period centered on March 5, the southern hemisphere, which has positive magnetic polarity, tilts toward the Earth so the solar magnetic field is mainly "away" from the Sun.

In Figure 3.11, the polarity observed by several spacecraft which have the Earth's heliographic latitude is positive in March and negative in September in solar minimum

years 1964-1968. The annual period of the magnetic sector structure is very clear. This solar minimum period between Solar Cycles 19 and 20 had the same dipolar polarity as the present minimum between Solar Cycles 23 and 24.

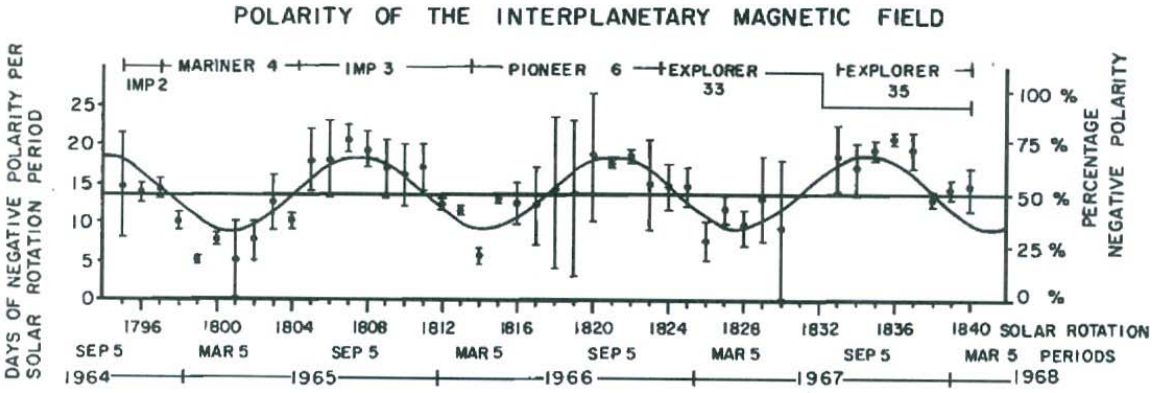

Figure 3.11. The annual period of the polarity observed by the spacecraft which have the Earth's heliographic latitude. Every data point is for a solar rotation period. The curve is the least-squares best-fit sinewave, which shows clearly the expected one year period (taken from *Rosenberg and Coleman* [1969]).

In addition to the annual variation of the magnetic sector polarity in the years around solar minimum, there are also annual variations in both the solar wind speed and geomagnetic activity for the solar minimum years of the four solar cycles since the mid 1960's, as seen by direct satellite solar wind observations. Since geomagnetic activity (GA) is closely associated with solar wind speed, analysis of magnetic indices such as Kp or aa also reveal an annual variation of GA. The phase of this annual variation reverses when the Sun's polarity reverses, making a 22 year Hale period. The annual variation is due to a north-south asymmetry in solar wind speed distribution. The minimum speed region is shifted to the hemisphere with northern (positive) magnetic polarity. Since 1964, the solar wind speed on average has been about 50 – 60 km/s faster when the solar hemisphere that tilts more toward the Earth has been the negative magnetic polarity hemisphere, which is associated with toward (T) magnetic field in the ecliptic plane. The reason for this variation is not known but it has been suggested that polar coronal holes (from which fast solar winds flow) may extend further toward the equator in the solar hemisphere with negative magnetic polarity than in the hemisphere of positive magnetic polarity [*Zieger and Mursula*, 1998a, 1998b; *Musula et al.*, 2002]. This is quite a different effect from the semiannual variation in magnetic activity explained by *Russell and McPherron* [1973], due in part to the fact that the solar wind is perpendicular to the Earth's magnetic axes in spring and fall, when the activity peaks. It is interesting that the increased solar wind speed has been associated with toward solar sectors during the past 40 years or so. By using older magnetic indices like aa to study geomagnetic activity, *Mursula and Zieger* [2001] found that the annual asymmetry was also present, but that the phase was reversed from that of recent years. They therefore inferred that the solar wind speed annual variation also was reversed in phase, such that the solar hemisphere of

positive magnetic polarity was strongest in those earlier records. On this basis, they suggested that there was the possibility of a century-scale solar oscillation.

In the years since ~1960, the effective latitudinal gradient of solar wind has been different on the two sides of the heliographic equator. A gradient of 10 km/s/deg is found at heliographic latitudes in the hemisphere with southern magnetic, while no gradient is found in the hemisphere with northern magnetic polarity, for solar minimum years. If coronal holes extend closer to the equator in the hemisphere of southern magnetic polarity, they could cause the gradient difference. The minimum speed region, associated with the streamer belt, is shifted to the hemisphere with northern magnetic polarity. At least during one solar minimum (1994-1995), the streamer belt and the HCS were shifted to opposite directions. The average solar wind speeds are equal in Northern and Southern Hemispheres, so the annual variation of solar wind speed is consistent with a shift of the streamer belt toward the hemisphere of northern magnetic polarity [*Mursula et al.*, 2002].

3.3 Studies of the solar wind and IMF

3.3.1 Comparison of 36-month IMF absolute values

Because both reconnection and the resulting convection patterns are closely dependent upon the solar wind and particularly the IMF, it is of considerable interest to study the IMF conditions since 2006 (Rankin Inlet began operating in mid-May of 2006). In particular, because of the installation of the high-latitude PolarDARN radars, the emphasis for the convection studies reported here has been on Bz+ conditions at small clock angles where Bz is less than about 30° (where Bz dominates). However, convection has also been studied at clock angles where Bz<|By|, namely $45° < \theta_c < 90°$ (where By dominates). To show the relative importance of the Bz and By components, we have performed a study of the monthly averaged values of the absolute values of the IMF components during the 2006 – 2008 period, during which solar minimum conditions of Solar Sunspot Cycle 23 have taken place (that minimum has continued well into 2009).

Our statistical study of the IMF components shows that Bz+ is usually accompanied a By component (By+, By-) and that normally |By|>|Bz+|. This is to be expected because, to a first approximation, the magnetic field from the Sun is an Archimedes spiral in the solar equatorial plane, which is very nearly the ecliptic plane. The clock angle θ_c, defined by the equation $\theta_c = \mathrm{atan2}(B_y, B_z)$, is thus often in the range +45° to +90° (By+), or -45° to -90° (By-). At the location of the Earth, the spiral angle is about 45°, so that Bx and By are roughly the same magnitude, but when Bx is negative (away from the Sun, so the IMF is an "away" (A) field), By is positive, and vice versa (in which case Bx is toward the Sun and the IMF is a "toward" (T) field). The Bz component comes from 3D warping of the IMF due to current systems near the solar equatorial plane [*Parker*, 1958; *Ness and Wilcox*, 1964, 1965], as shown in Figure 3.10 (b).

The IMF data at about 0.99 AU from the Sun is listed in the OMNI database provided by the National Aeronautics and Space Administration (NASA) (J. King and N. Papitashvili, 2006, http://omniweb.gsfc.nasa.gov/html/omni_min_data.html). We have time-shifted the

IMF data observed by the ACE satellite at the Lagrangian point L1 (~240 R_E) to match the time expected for the solar wind to affect SuperDARN/PolarDARN measurements.

Figure 3.12 shows a statistical study of the monthly averaged values of the magnitudes of the IMF components starting in January, 2006. The average from Jan. 2006 to Dec. 2008 of <|Bz|> is lower by 21.5% than that of <|By|>, and <|Bz+|> is lower by 20.1% than that of <|By|>. The By component thus is expected to play an important role in reconnection.

<|Bz-|> is lower by 3.7% than <|Bz+|> in this period, and the proportion of Bz+ is 52.0%, which favors our study of Bz+ conditions.

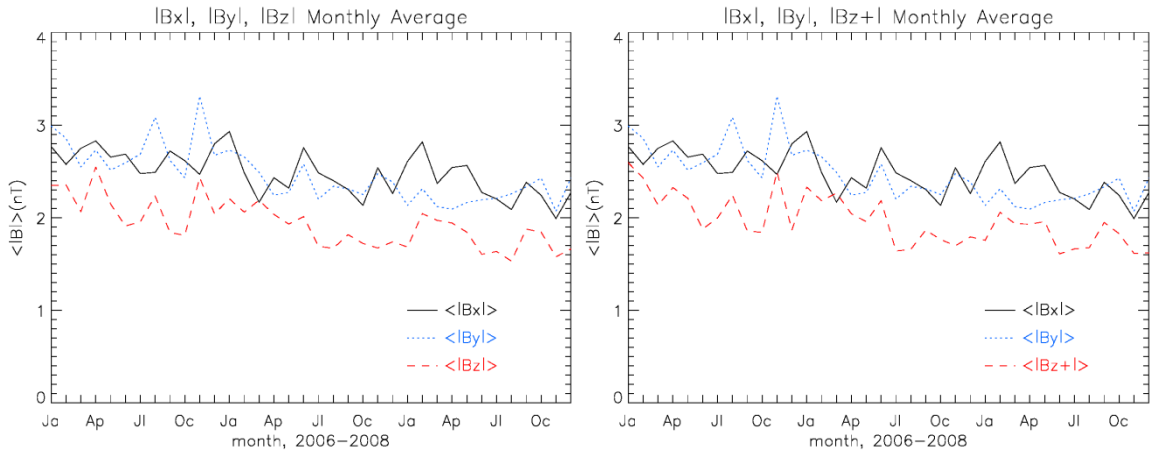

(a) (b)

Figure 3.12. This figure shows, for the solar minimum period Jan. 2006 – Dec. 2008, 36 monthly average values of Bx, By and Bz absolute value. In Figure 3.12(a), all values of the IMF Bz component are included, while in Figure 3.12(b), only the positive IMF Bz values are included. Both figures show clearly show that <|By|>, the blue line, is greater than <|Bz|> and <|Bz+|>, the red line.

The linear regression lines that best fit the three components are given by:

$<|Bx|> = 2.727 - 0.0140x \quad x=0, 1, 2, \ldots, 35 \quad <|By|> = 2.807 - 0.0196x \quad x=0, 1, 2, \ldots, 35$

$<|Bz|> = 2.239 - 0.0174x \quad x=0, 1, 2, \ldots, 35 \quad <|Bz+|> = 2.276 - 0.0177x \quad x=0, 1, 2, \ldots, 35$

where x is the integer value of the month, starting from x=0 in Jan, 2006.

The results show that the IMF has been getting weaker during the solar minimum conditions, and that <|By|> decreases most and <|Bx|> decreases least.

For comparison, the linear regression line (not shown) that best fits the monthly averages of the Penticton DRAO 10.7 cm solar adjusted flux taken from the website ftp://ftp.geolab.nrcan.gc.ca/data/solar_flux/monthly_averages/maver.txt in the period Jan. 2006 – Dec. 2008 is given by (again note the decreasing value):

Flux = 82.18 – 0.457x x=0, 1, 2, …, 35, where x is the same as above.

In the linear regression equations above, the percentage monthly change in a parameter is simply 100 times the ratio of the slope to the y-intercept. For the four parameters <|Bx|>, <|By|>, <|Bz|> and the 10.7 cm flux, the monthly percentage changes are -0.513, -0.699, -0.779, and -0.556. Because a measure of the spiral angle is given by arctan2 (<|By|>, <|Bx|>), it is clear that the spiral angle has been decreasing because <|By|> has had a monthly percentage decrease that is about 1.36 times that of <|Bx|>. Because of the z-component of the IMF, the IMF is not a pure spiral in the xy plane, so a measure of the "warping" of that plane is given by the angle $\mathrm{atan2}(\langle|B_z|\rangle, \sqrt{\langle|B_x|\rangle^2 + \langle|B_y|\rangle^2})$. The percentage monthly change in $\sqrt{\langle|B_x|\rangle^2 + \langle|B_y|\rangle^2}$ is -0.608. Because <|Bz|> has been decreasing at a monthly rate more than $\sqrt{\langle|B_x|\rangle^2 + \langle|B_y|\rangle^2}$, the amount of warping has actually decreased slightly during the 36-month period. Finally, the percentage monthly change of the total magnetic IMF, namely $\sqrt{\langle|B_x|\rangle^2 + \langle|B_y|\rangle^2 + \langle|B_z|\rangle^2}$ is -0.650. Since the 10.7 flux monthly percentage decrease is only about 0.855 of the monthly percentage decrease of the total magnitude of the IMF, it is clear that the decrease in IMF is a more sensitive measure of the solar minimum than is the decrease in 10.7 flux, although both quantities are useful monitors of the solar minimum conditions. For comparison, the IMF component absolute values are shown in Figure 3 for the solar maximum years 2000 and 2001. Figure 3 shows that the average in 2000 and 2001 of <|Bz|> is lower by 19.1% than that of <|By|>, comparable to 21.5% lower value in the period January, 2006 to December, 2008.

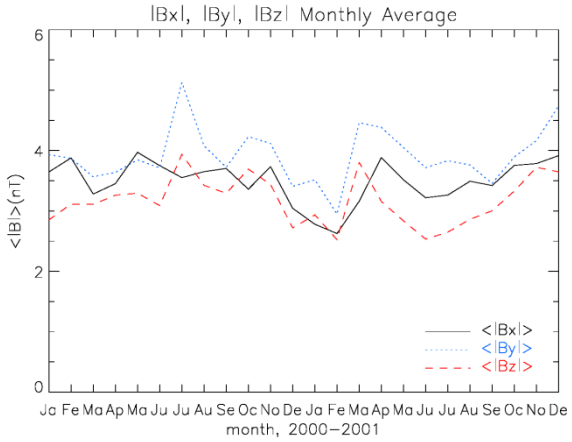

Figure 3.13. IMF data taken during Solar Cycle 23 maximum years 2000 and 2001 shows that <|By|>, the blue line, is greater than <|Bz|>, the red line.

3.3.2 Statistical studies of the IMF azimuth, latitude angle and clock angle

The IMF data points from the Jan 1, 2007 – Dec 31, 2008, interval during the minimum years between Solar Cycles 23 and 24 are averaged values over 5 min 20 s intervals, and are given in GSM coordinates.

The azimuth and latitude angles specify the direction of the IMF.

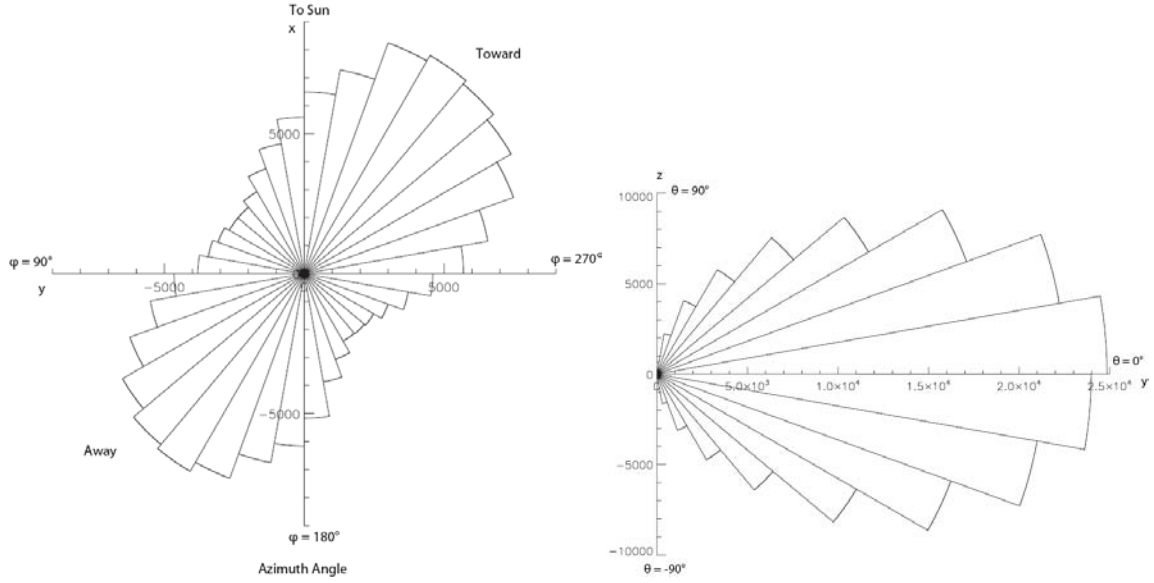

(a) (b)

Figure 3.14. (a) A histogram of the distribution of the IMF azimuth angle ϕ values from Jan. 1, 2007 to Dec. 31, 2008, solar minimum period, in 10° intervals. (b) The histogram of the IMF latitude angle distribution, again in 10° intervals.

The first statistical study was of the azimuth angle, defined by $\phi = \text{atan2}(B_y, B_x)$. The azimuth angle is related to the spiral angle ψ. Because at the Earth, ψ is about 45°, the azimuth angle is expected to peak at -45° (+315°) for "toward" field and +135° for "away" field. Figure 3.14(a) shows a statistical frequency-of-occurrence diagram which illustrates the number of data points in each 10° azimuth angle interval. The 270° < ϕ < 360° quadrant is the typical "toward" field sector, with B_x+, B_y-; that sector has a maximum in the 320°-330° interval. The mean value of the azimuth in this quadrant is 316°. The 90° < ϕ < 180° quadrant is the typical "away" field, and Fig. 3.14(a) shows a maximum in the 140° – 150° interval. However, the mean value in this quadrant is 137°. The included angle δ between these two means is 179°, shows an asymmetry that is expected [*Svalgaard and Wilcox*, 1974; *King*, 1976]. A more detailed analysis using 5°-intervals shows that the "toward" maximum lies in the 310°–315° interval, and the "away" maximum is in the 145°–150° interval. The difference in angle between two maxima is about 165°. This is in approximate agreement with the results expected from the Archimedes spiral geometry. Going counter–clockwise from ϕ = 270°, the percent in each quadrant of the total number of points is: 35.1%, 17.4%, 31.0% and 16.4%. However, if we take all the points between 45° and 225° as "away" field (positive

polarity), and vise versa, as in the work by *King* [1976] and *Sabbah* [1995], the mean value in "away" field is 137°, and the mean value in "toward" field is 318°. The included angle δ is 181°. The percent of "away" field and "toward" field of the total number of points is 47.15% and 52.85%.

Figure 3.14(b) shows the distribution of the IMF latitude angles $\theta = \mathrm{atan2}(B_z, \sqrt{B_x^2 + B_y^2})$. The maximum number is near 0°, and the minimum number is near ±90°. Clearly, the majority of IMF latitudes are near 0°, and the likelihood of a pure Bz field (either + or -) is very small.

We now move on to the study of the clock angle θ_c, which is defined by the equation $\theta_c = \mathrm{atan2}(B_y, B_z)$.

Figure 3.15 is a statistical frequency-of-occurrence diagram which shows the number of data points in each 10° clock angle interval. The maximum numbers are in the 70° – 80° interval and in the 270° – 280° interval. The difference in angle between the two maxima is about 200°. Going counter-clockwise from θ_c = 270°, the percent in each quadrant of the total number of points is: 26.2%, 25.9%, 22.5% and 25.4%.

From the clock angle distributions, the number of Bz- points is lower by 8.1% than that of Bz+, which favors our interest in high-latitude convection, because Bz+ reconnection occurs at high latitudes, poleward of the cusp. We are especially interested in θ_c within the range $-30° < \theta_c < +30°$. From the clock angle statistics, the latter conditions occur only 12.4% of the time.

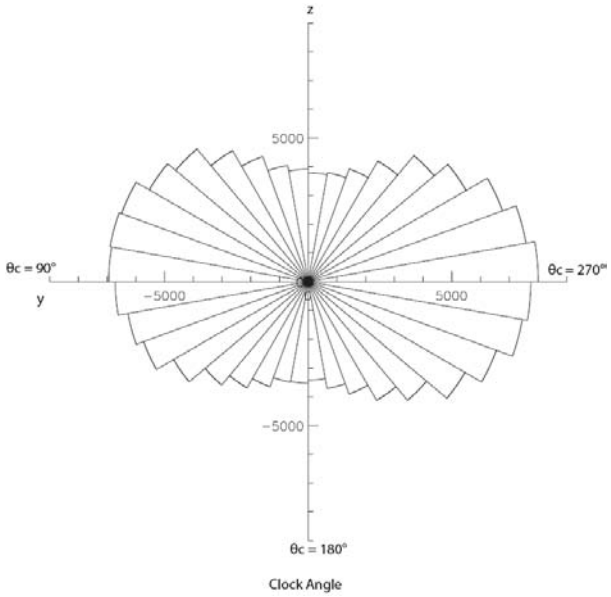

Figure 3.15. A histogram of the clock angle values in 10° intervals during the Jan. 1, 2007, to Dec. 31, 2008 solar minimum period.

For comparison, with the solar minimum period 2007-2008, we studied the IMF azimuth, latitude angle and clock angle from the Jan 1, 2000 – Dec 31, 2001 interval during the maximum years of Solar Cycle 23. Again, the azimuth and latitude angles specify the direction of the IMF.

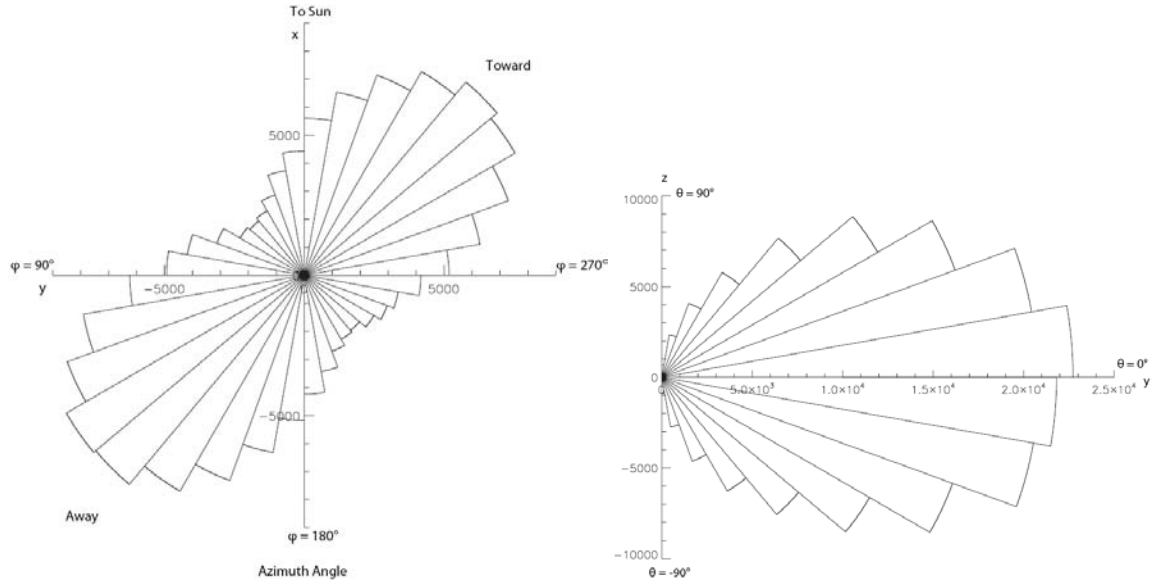

(a) (b)

Figure 3.16. (a) A histogram (10° intervals) of the distribution of the IMF azimuth angle ϕ values during the Jan. 1, 2000, to Dec. 31, 2001, solar maximum period. (b) The histogram of IMF latitude angle distribution, also in 10° intervals.

The first statistical study was of the azimuth angle, defined by $\phi = \text{atan2}(B_y, B_x)$. Figure 3.16(a) shows a statistical frequency-of-occurrence diagram which illustrates the number of data points in each 10° azimuth angle interval. The 270° < ϕ < 360° quadrant is in the typical "toward" field sector, with B_x+, B_y-; that sector has a maximum in the 310°-320° interval. The mean value of the azimuth in this quadrant is 315°. The 90° < ϕ < 180° quadrant is the typical "away" field with a maximum in the 120° – 130° interval. However, the mean value in this quadrant is 133°. The included angle δ between these two means is 182°, and shows an asymmetry that is expected [*Svalgaard and Wilcox*, 1974; *King*, 1976]. A more detailed analysis using 5°-intervals shows that the "toward" maximum lies in the 315° – 320° interval, and the "away" maximum is in the 120° – 125° interval. The difference in angle between the two maxima is about 195°. This is in approximate agreement with the results expected from the Archimedes spiral geometry. Going counter–clockwise from ϕ = 270°, the percent in each quadrant of the total number of points is: 33.0%, 16.0%, 36.0% and 14.9%. However, if we take all the points between 45° and 225° as "away" field (positive polarity), and vise versa, the definition used by *King* [1976] and *Sabbah* [1995], the mean value of "away" field is 133°, and the mean value in "toward" field is 315°. The included angle δ is 182°. The percent of "away" field and "toward" field of the total number of points is 51.69% and 48.31%.

Figure 3.16(b) shows the distribution of the IMF latitude angle defined by the equation $\theta = \mathrm{atan2}(B_z, \sqrt{B_x^2 + B_y^2})$. The maximum number is near 0°, and the minimum number is near ±90°. Clearly, the majority of IMF latitudes are near 0°, and the likelihood of a pure Bz field (either + or -) is very small.

We now move on to the study of the clock angle θ_c, which is defined by the equation $\theta_c = \mathrm{atan2}(B_y, B_z)$.

Figure 3.17 is a statistical frequency-of-occurrence diagram which shows the number of data points in each 10° clock angle interval. The maximum number is in the 80° – 90° interval and in the 250° – 260° interval. The difference in angle between the two maxima is about 170°. Going counter-clockwise from θ_c = 270°, the percent in each quadrant of the total number of points is: 23.3%, 26.7%, 25.4% and 24.7%.

From the clock angle distributions, the number of Bz+ is lower by only 0.17% than that of Bz-, so the proportion of Bz+ and Bz- is about the same. We are especially interested in θ_c within the range -30°<θ_c<+30°. From the clock angle statistics, the latter conditions occur only 12.4% of the time.

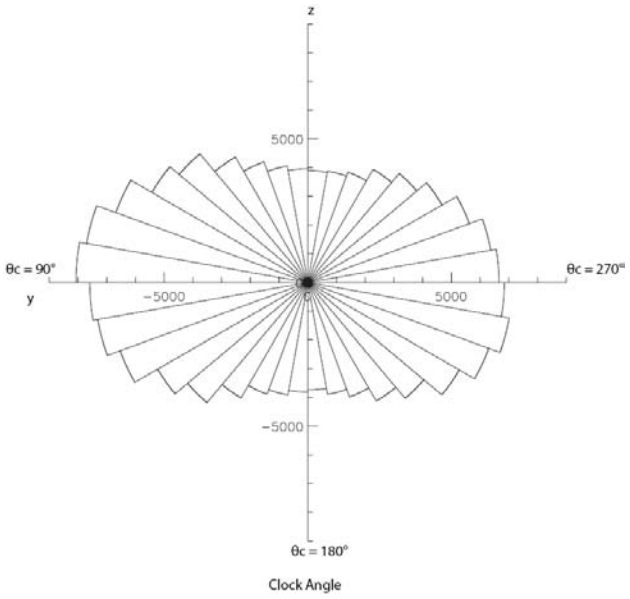

Figure 3.17. A histogram of the clock angle values in 10° intervals during the Jan. 1, 2000, to Dec. 31, 2001, solar maximum period.

3.3.3 Studies of Sector Boundaries

A sector boundary is the transition region where the polarity of IMF makes a persistent change from “away” to “toward”, or vice versa, and the transition marks passage from

one side of the heliospheric current sheet (HCS) to the other. The heliospheric plasma sheet (HPS) is a sheath encompassing the heliospheric current sheet (HCS), much like the magnetospheric tail contains a central “neutral current sheet” and the surrounding central plasma sheet. Recent work shows that about half of the sector boundaries lack high-beta HPS’s, and that HPS’s often occur away from the sector boundaries [*Crooker et al.*, 2004].

The onset of Solar Cycle 24 has been long delayed; the minimum at the end of Solar Cycle 23 has continued into early 2009 and sunspot activity belonging to Cycle 24 has been very weak. There may be something unusual happening to the Sun now. The longer the Cycle 23 minimum persists, the more likely it is that Cycle 24 will be weak. Because we are now in a period when the sunspot number is persistently low, there are fewer auroras, and the auroral oval is seen at higher latitudes than during solar maximum conditions. The OCFLB now can be located at latitudes higher than 80°. Consequently, our PolarDARN radars provide a view of high-latitudes which is very favourable for studying polar cap and high-latitude auroral convection in this solar minimum period.

Because the Rankin Inlet radar began operating in 2006, while the Inuvik radar began operating in Dec. 15, 2007, both during the deep minimum years at the end of Solar Cycle 23, we have focused on the IMF data from Jan 1, 2007 – Dec 31, 2008. We have studied the sector boundary to see if there were any special structures in this period which might have affected reconnection and convection, and to relate this work to our convection studies.

Like the preceding IMF statistical studies, we also studied the sector structure in the period Jan 1, 2007 – Dec 31, 2008 during the minimum years of Solar Cycle 23. The data were averaged over 3 h intervals, and given in GSM coordinates.

Figure 3.18 shows Bx as the blue line, and By as the red line. As expected from the Archimedes spiral geometry, they have opposite polarities most of the time (Bx+, By- is normal “toward” field, and Bx-, By+ is normal “away” field). Usually, the sector boundary is obvious, in that Bx and By change their signs at the same time and reach maximum values after the sector boundary crossing. Mostly, but not always, the crossing is dramatic in that the values of Bx and By undergo, within one three-hour interval, a discontinuous change at the crossing. In the 2007 January to August period, there are four sectors every approximately 27 days, which is the mean synodic solar rotation period. The first sector has a “toward” field. The number of days in the first sector increases from about 6 days to 10.5 days and then decreases to about 7.5 days. The second sector has an “away” field. The number of days in the second sector decreases from about 11 days to 2.5 days. The third sector has a “toward” field. The number of days in the third sector fluctuates and has an increasing trend from about 2.5 days to 8 days. The fourth sector has an “away” field. The number of days in the fourth sector fluctuates and has a decreasing trend from about 7 days to 3.5 days and then increases to about 9 days. The total number of days in the second and the third sectors is about 14 days in the first 4 panels of (a) and about 11 days in the last 4 panels of (a).

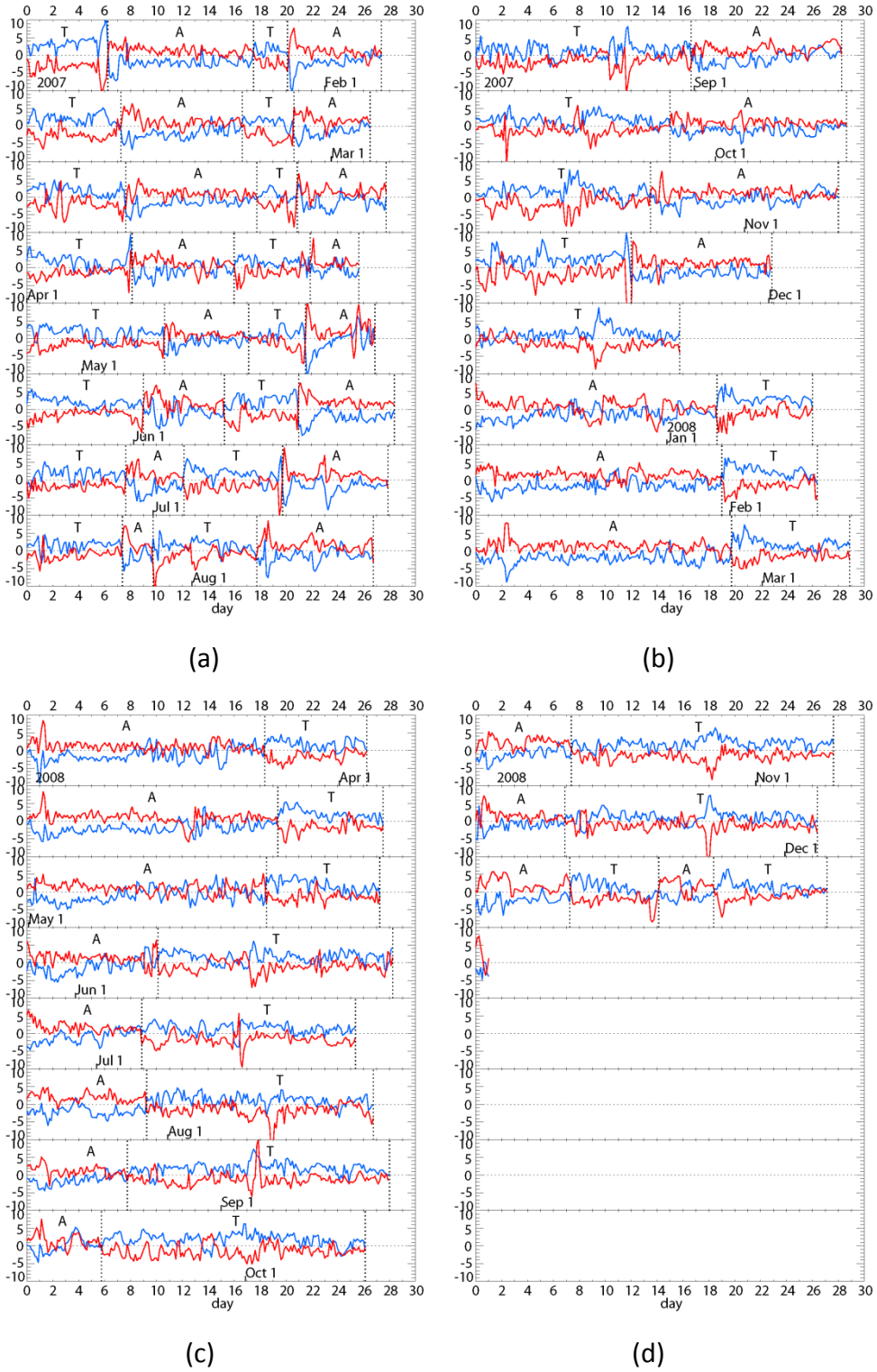

Figure 3.18. A plot of Bx (blue) and By (red). The sector boundary crossings are shown by vertical dashed lines. “A” and “T” refer to “away” and “toward” field. (a) Interval from Jan/07 to Aug/07. (b) Interval from Aug/07 to Mar/08. (c) Interval from Mar/ 08 to Oct/08. (d) Interval from Oct/08 to Dec/08.

However, there are only two sectors during the interval Aug, 2007–Nov, 2008. The transition from four sectors to two sectors is sudden, in that there is a four-sector 27-day interval centered about Aug. 1, and the very next 27-day interval has only two sectors. The nature of the transition is that the number of days in the short second sector (the inner sector) decreased to 0, and the number of days in the fourth sector (the outer sector) increased.

In the two-sector interval that begins in the panel labeled Sept. 1 in Figure 3.18(b), there is a change from number of days of "away" field larger to "toward" field larger, which we will discuss in the section 3.1.4. In the first three panels of (b), the first sector has a "toward" field. The number of days in the first sector decreases from about 16.5 days to 13.5 days. The second sector has an "away" field. The number of days in the second sector increases from about 12 days to 14.5 days. In the fourth and fifth panels of (b), the sectors do not fit the 27-day synodic solar rotation period. This may be a transition period when sector structures change. After that, in the next 6 panels showing two-sector structure, the first sector has an "away" field. The number of days in the first sector is about 18.5 - 19.5 days. The second sector has a "toward" field and lasts about 7.5 - 9 days. In the fourth to eighth panels of (c) and first two panels of (d), the number of days in the second sector is larger, which is quite different from previous 6 panels. The number of days in the first sector is only about 7 - 10, while the number of days in the second sector is about 16 - 20.

In the third panel of (d), there are four sectors. The first sector stays almost the same. The third sector comes out from the second sector. The number of days in the four sectors is respectively about 7, 7, 4, 9.

For comparison, we looked at the sector structure in Jan. 2000–Dec. 2001 interval during solar maximum years. As seen in Figure 3.19 above, the IMF is stronger than during solar minimum years. There were two or four sectors in approximately 27 days, no more sectors than during solar minimum years. There are more periods of ambiguous polarity, so it is harder to identify the sector boundaries. This is because, in solar maximum years, the dipole field is weak so quadrupole and octupole fields dominate, while in the solar minimum years, the magnetic field is dominantly a dipole field.

In the first panel of (a), there are four sectors in approximately 27 days, which is the mean synodic solar rotation period. The first sector has a "toward" field. The number of days in the four sectors is respectively about 10, 3, 5, 9. In the 2000 February to October period, there are two sectors in approximately 27 days. The first sector has a "toward" field. In the second panel to fifth panel of (a), the number of days of the first sector increases from 10 days to 15 days. The number of days of the second sector decreases from 19 days to 11.5 days. There is a change from number of days of "away" field larger to "toward" field larger. However, in the sixth panel of (a), the number of days of "away" field is larger. In the five panels starting from the sixth panel of (a), the number of days of the first sector increases from 12 days to 16 days. The number of days of the second sector decreases from 17 days to 10 days. The number of days of "toward" field becomes larger.

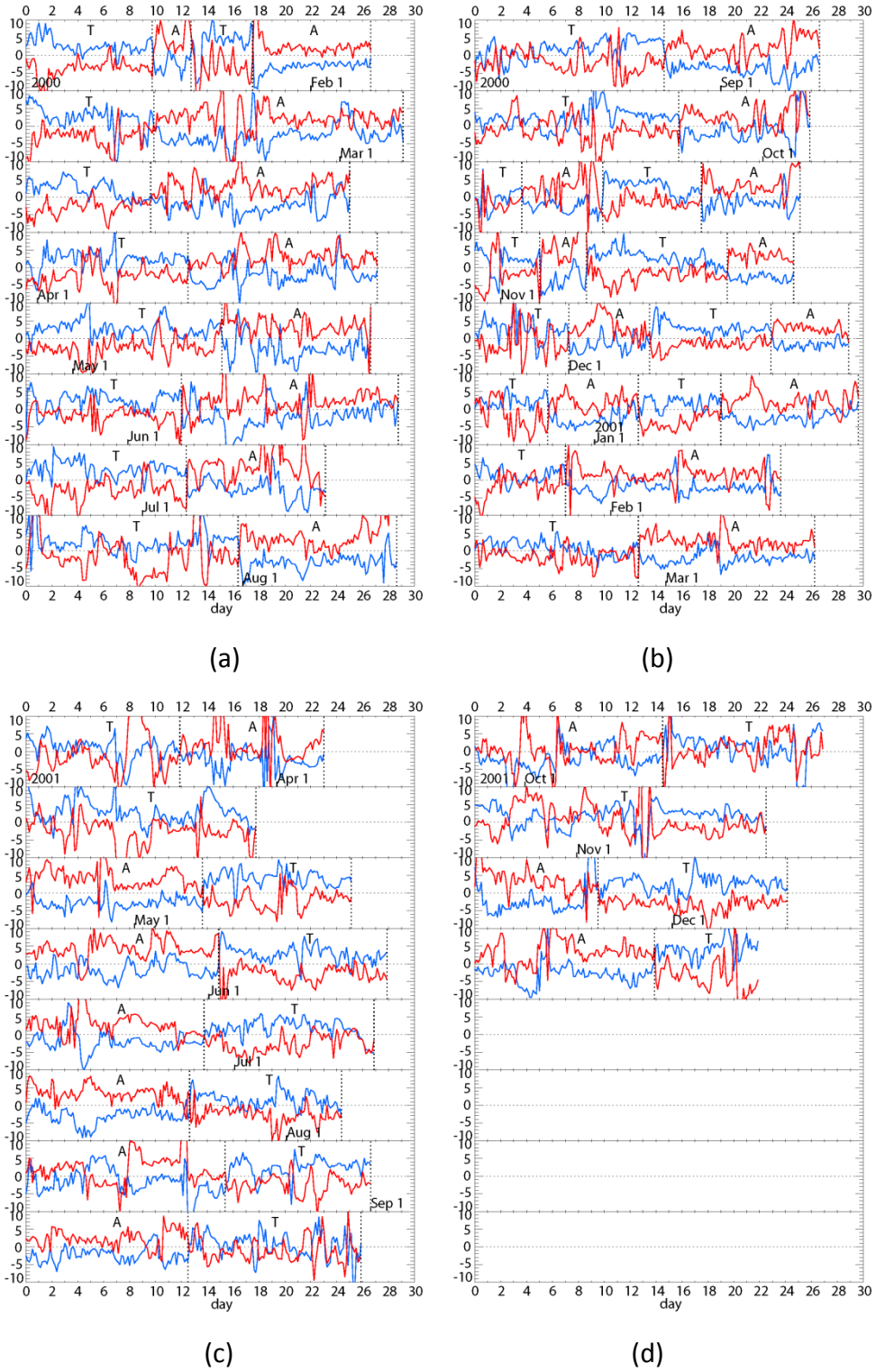

Figure 3.19. A plot of Bx (blue) and By (red). The sector boundary crossings are shown by vertical dashed lines. “A” and “T” refer to “away” and “toward” field. (a) Interval (Jan 2000 to Aug 2000). (b) Interval (Aug 2000 to Mar 2001). (c) Interval (Mar 2001 to Sep 2001). (d) Interval (Sep 2001 to Dec 2001).

In the third and sixth panels of (b), there are four sectors. The first sector has a “toward” field. The number of days in the first sector increases from about 3.5 days to 7 days and then decreases to about 5.5 days. The second sector has an “away” field. The number of days in the second sector decreases from about 6.5 days to 3.5 days, and then increases to about 7 days. The third sector has a “toward” field. The number of days in the third increases from about 6.5 days to 11 days, and then decreases to about 7.5 days. The fourth sector has an “away” field. The number of days in the fourth sector decreases from about 7.5 days to 5 days and then increases to about 11 days.

In the last two panels of (b) and first panel of (c), there are two sectors. The first sector has a “toward” field. The number of days in the first sector increases from about 7 days to 12 days. The number of days in the second sector decreases from about 17.5 days to 11 days. In the second panel of (c), the number of days in the “toward” sector increases to about 18 days, but doesn’t fit in a 27-day period. This appears to be a transition period when the sector structure is changing.

After that, there are two sectors in the rest of the panels of (c). The first sector has an “away” field. The number of days in the first sector is about 12.5 days to 15 days. The number of days in the second sector is about 12 days to 13.5 days.

In the first two panels of (d), the first sector is has a 14.5 day “away” field. The second sector is mainly “toward” but has some periods of ambiguous polarities. The “T” field extends into the second panel and lasts about 35 days. This again seems to be a transition period when the sector structure is changing.

In the third and fourth panels of (d), there are two sectors. The first sector has an “away” field. The number of days in the first sector increase from about 9.5 days to 14 days. The number of days in the second sector in the third panel of (d) is 14.5 days.

For the sector boundaries above, we analyzed the solar wind velocity at sector boundaries. Figure 3.20 (a) shows a superposed epoch analysis of solar wind speed near sector boundary crossings in the time interval Jan. 2007 to Dec. 2008. The solar wind velocity reaches a minimum about half a day before the sector boundary crossing, and then reaches a maximum about two days after the sector boundary crossing. Figure 3.20 (b) shows that the standard deviation reaches the minimum at about the same time as the velocity.

For comparison, a study was made of the solar wind speed near sector boundary crossings in the period 2000–2001 during the maximum years of Solar Cycle 23. As shown in Figure 3.21, the velocity also shows the same type of change, but the amplitude is not as great as it was during the minimum years.

This is expected because the solar wind velocity distribution is slow and single-peaked (peak at about 400 km/s) at solar maximum but at solar minimum is double-peaked with the high-speed portion of the distribution peaking at 750 km/s (see Figure 2 of *Zurbuchen et al.* [2002]). The standard deviation reaches a minimum about 1 day before the velocity reaches the minimum, which is different from the solar minimum years, when both the standard deviation and the velocity reached minimum at about the same time.

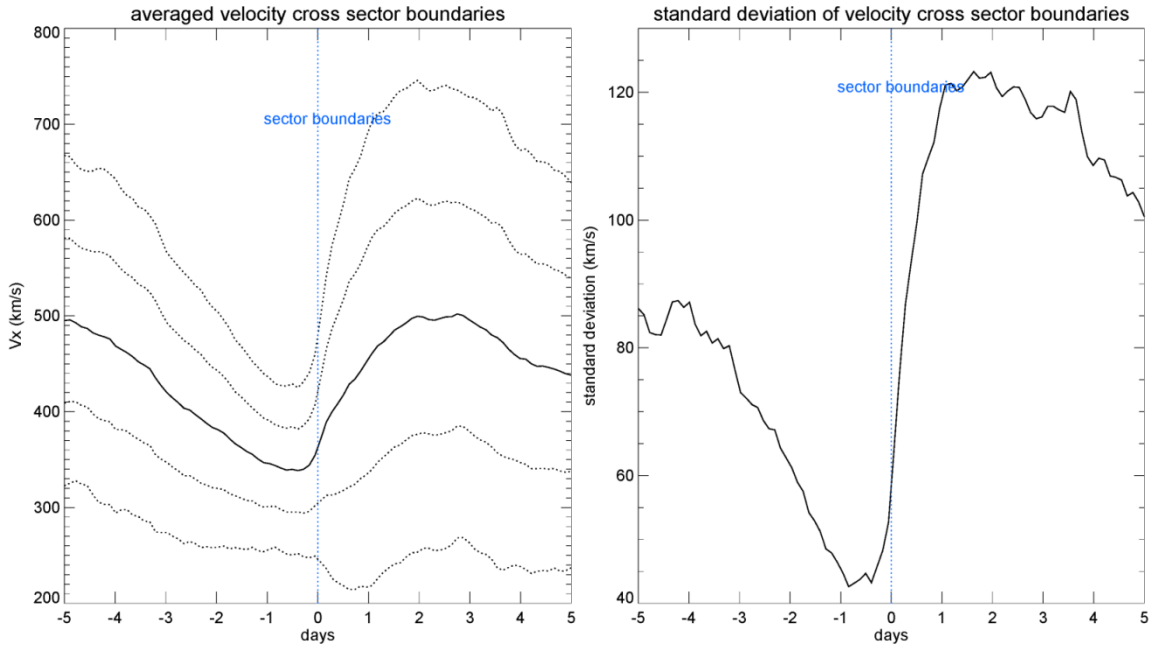

Figure 3.20. (a) The averaged solar wind velocity at sector boundaries in the interval Jan. 2007 to Dec. 2008. The dashed lines show 1 and 2 standard deviations from the mean velocity. (b) The standard deviation of the velocity at sector boundaries in the interval Jan. 2007 to Dec. 2008.

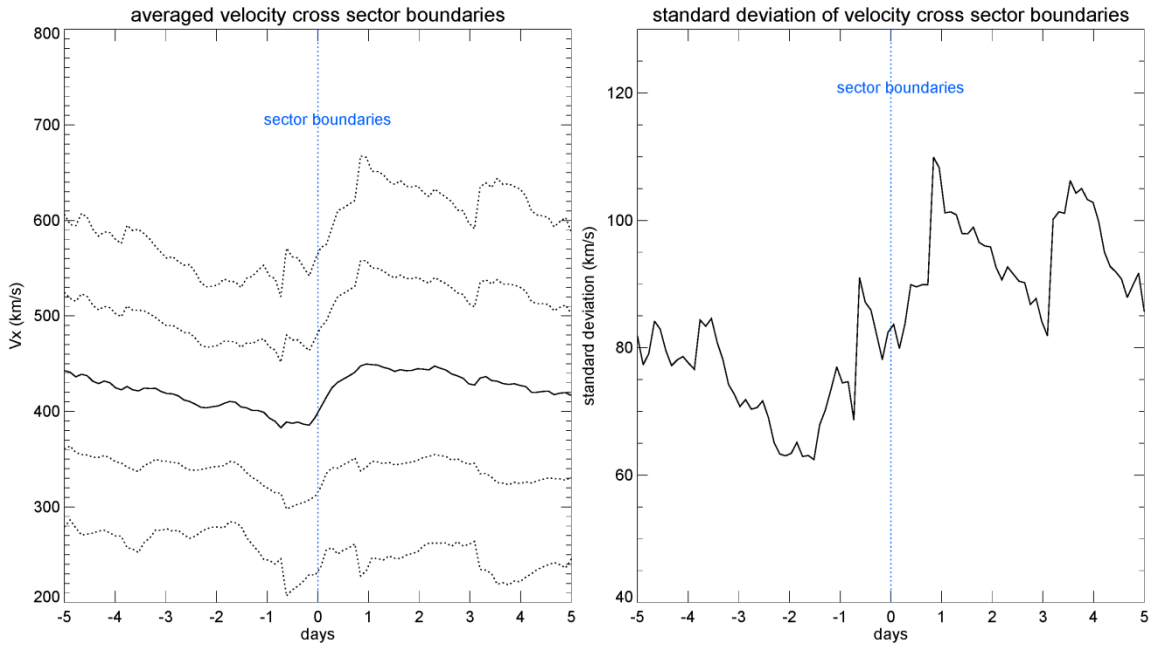

Figure 3.21. (a) The averaged solar wind velocity at sector boundaries in the interval Jan. 2000 to Dec. 2001. The dashed lines are drawn at 1 and 2 standard deviations from the mean velocity. (b) The standard deviation of the velocity at sector boundaries in the interval Jan. 2000 to Dec. 2001.

3.4 The Correlation between SSC Occurrence, IMF Sector Polarity and ENSO Climate Cycles

Recently, Khachikjan et al. (2009) studied the sequence of Storm Sudden Commencement (SSC) onset times. At each onset time, the longitude of the geographic meridian at the sub-solar point (MSP) was found. The sequence of these MSP longitudes was then plotted, subject only to the condition that the difference between successive MSP longitudes be less than 180°. By subtracting the general westward progression linear trend of the MSP, the remaining MSP longitude series showed a very clear long-term (~ 22 year) variation that correlates well with the sunspot number variation. This is not unexpected because it indicates a good correlation between long-term variations of the solar activity (as characterized by the sunspot numbers) and the occurrence of SSCs. Also, the long-term variation of MSP interval has a good correlation with the long-term variation of IMF sector polarity.

After next subtracting the long-term 22-year variation of the MSP longitudes, the remaining curve shows irregular cycles of 3-6 years duration. Remarkably, these irregular cycles correlate very well with similar cycles in the El Niño-Southern Oscillation (ENSO). On average, the warm phase of ENSO (El Niño) starts about 15-16 months after an extreme point of the MSP progression. The next solar cycle is predicted to start in March-April of 2010.

The top panel a of Figure 3.22 shows that, in solar minimum years, there are regular annual variations [*Rosenberg and Coleman*, 1969] of the sector polarity lasting for about a 3-year interval, as shown in the red boxes, while in solar maximum years, there are irregular variations. This is because, in solar maximum years, the solar dipole field becomes rather weak, while in the solar minimum years, the dipole character of the magnetic field is well defined. The bottom panel b shows the southern oscillation index (SOI) variations. On the SOI curve of panel b, strong El Niño events occur where there are deep minima. It is to be noted that a strong El Nino occurred in each of the solar minima in 1977-78, 1986-87 and 1997-98, and that the end of each El Niño event is roughly coincident with the end of the regular annual variations. Even more important, the beginning of the following solar cycle began at or a little before the end of the El Nino SOI minimum. It is particularly to be noted that the present extended minimum between Cycles 23 and 24 has also been marked by an El Nino event, which is predicted not to end before about April, 2010. The remarkable coincidence in the end times of the El Niño events and the nearly sinusoidal annual magnetic sector polarity oscillations provides further evidence of another link between the solar cycle conditions and the Earth's weather.

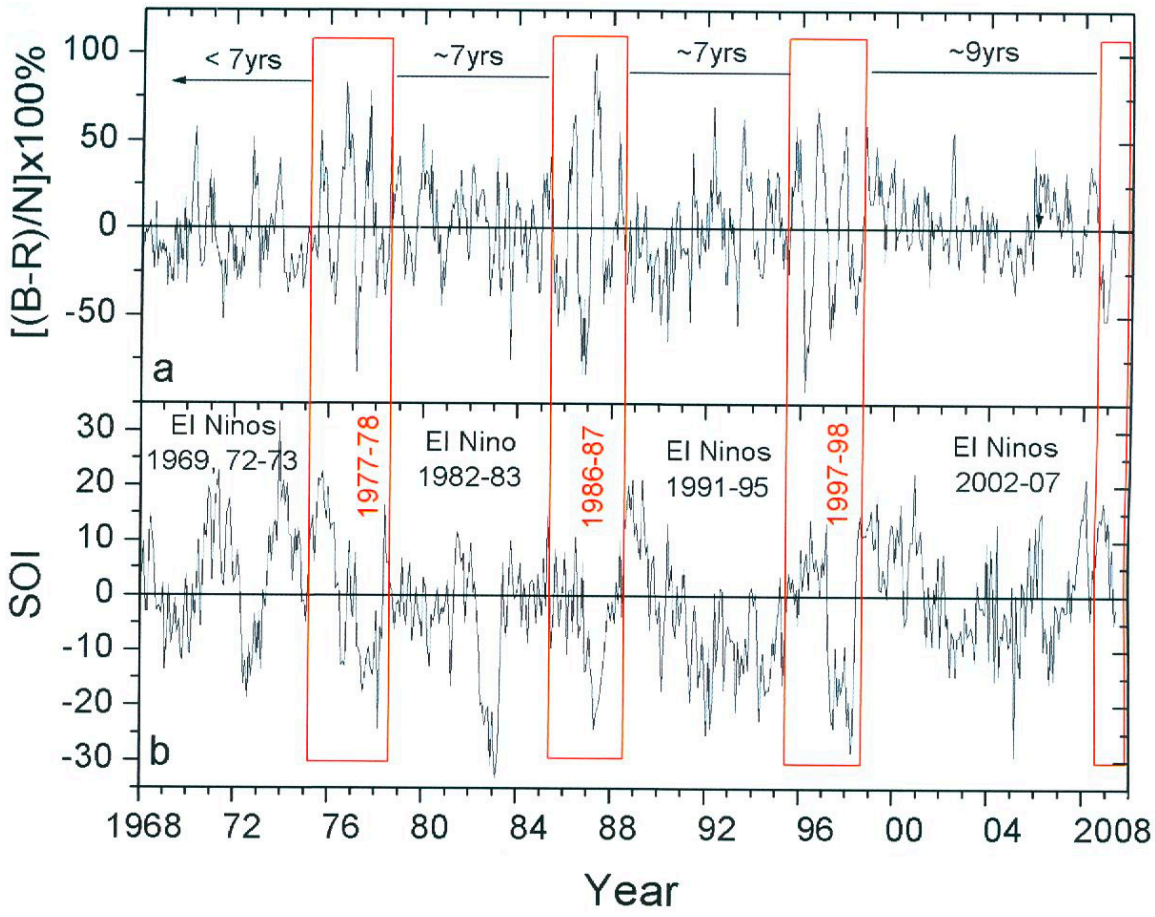

Figure 3.22. The top panel shows IMF sector polarity <SP> data, expressed by [(B-R)/N]*100% for 27-day cycle, in which, "B" is the number of days of "away" (A) field, "R" is the number of days of "toward" (T) field, and "N" is the number of days in the 27-day cycle for which the IMF polarity data are available. The bottom panel shows the monthly average southern oscillation index SOI in the January, 1968, to June, 2009, interval. The red boxes indicate the periods around solar minimum years for which the <SP> time series shows regular annual variations. Each of the last four (including recent 2009 data that are not shown) of these annual oscillation periods, usually lasting about 3 years, include a single strong El Niño event (taken from *Khachikjan et al.* [2009]).

Our sector boundary study shows in Figure 3.18 that, since Dec. 2007, there were 6 roughly 27-day synodic solar rotation cycles near spring equinox when "away" field dominated, and that the following seven 27-day cycles close to the autumnal equinox were dominated by "toward" field. The transition is sudden. However, the sector structures did not show a dominant polarity in the present solar minimum until near the end of 2007. There were no regular variations in the solar maximum years 2000-2001 shown in Figure 3.19. This agrees with Khachikjan's work, shown in Figure 3.22, that in solar minimum years, there are regular annual variations of the sector polarity lasting for about a 3-year interval, while in solar maximum years, there are only irregular variations.

Before the 6 “away” field dominated cycles beginning in December, 2007, there was a single sector which did not appear to fit the 27-day synodic cycle, so that sector may have marked the transition from the irregular variation period to the 3-year regular annual variation period. Therefore, the 3-year oscillation for this minimum appeared to begin in Dec. 2007. Although the present solar minimum has lasted for a long time (since 2005), the regular annual variations of the magnetic sector polarity began late, in Dec. 2007, and will probably not terminate until the second half of 2010. This may reflect an about 3 year period on the Sun, corresponding to the IMF phase reversal period of 3.2 years [*Takalo and Mursula*, 2002]. The El Niño event which is taking place now (end of November 2009), may extend to Jul. or Aug. 2010, which roughly agrees with the 3.2-year oscillation period above. The new cycle is expected to start a little before the end of the regular annual variations and the El Niño event. By this method, we can tentatively predict that Solar Cycle 24 may not start until the spring or summer of 2010.

4. DETAILED STUDIES OF CONVECTION EVENTS

4.1 Introduction

The main purpose of the thesis work is to incorporate the new PolarDARN radar data into studies of high-latitude convection within and just equatorward of the open closed field line boundary (OCFLB). In this section, we will make specific applications of the reconnection work introduced in Chapter 1, based upon the recent 3D topological formulation of reconnection in a series of papers led by Watanabe [*Watanabe et al.*, 2004, 2005, 2006, 2007; *Watanabe and Sofko*, 2008, 2009a, 2009b, 2009c].

We will stress a new type of convection pattern – the reciprocal cell - which is driven by reconnection and which results from Tanaka-type interchange reconnection.

One purpose of PolarDARN is to study IMF Bz+ conditions, when interchange reconnection happens. Prior to 1999, only one type of interchange reconnection had been proposed [*Russell*, 1972], namely

$$\text{IMF (Bz+)} + \text{lobe} \rightarrow \text{lobe} + \text{IMF}.$$

The resulting polar cap convection pattern was predicted to show only one or two lobe cells, which are high-latitude convection cells whose streamlines are completely within the region of open magnetic field lines.

The PolarDARN radars permit a more extensive view of the high latitude and polar cap convection patterns including not only lobe cell convection streamlines but also several varieties of merging cells and even the new type of closed-field reciprocal cell outside the polar cap. PolarDARN thus not only provides a great deal of complementary information to that obtained by auroral zone or midlatitude SuperDARN radars, but also allows for these auroral zone streamlines to be completed and/or supplemented by the more complex flows which occur at high latitudes and in the polar cap.

Our study of the IMF in Chapter 3 shows that Bz+ is usually accompanied a By component (By+, By-) and that the magnitude of the By component exceeds the Bz+ value, i.e. |By|>Bz+. Clock angles are thus often in the range +45° to +90° (By+), or -45° to -90° (By-), and also in the range +30° to +45° (By+), or -30° to -45° (By-). Less frequently, the clock angle is between 0° and +30°, or between -30° and 0° (Bz+ dominant), and the occurrence rate of pure Bz+ clock angles near 0° is even smaller.

We study the convection that occurs for IMF with a Bz+ component, for three sets of clock angle conditions, with expectations as follows. (a) When the By component dominates, with a clock angle in the range +45° to +90° (By+), or -45° to -90° (By-), the convection pattern is expected to show: (i) a round cell consisting of a merging cell

containing an interior lobe cell, (ii) a crescent merging cell [*Burch et al.*, 1985 and *Reiff and Burch*, 1985]. (b) For Bz+ dominant conditions, with the clock angle in the range 0° to +30° (By+), or -30° to 0° (By-), *Watanabe and Sofko* [2009a] suggested that Dungey type reconnection cannot occur and that, when there is no dipole tilt, the convection pattern is driven entirely by interchange reconnection, resulting in a larger cell consisting of an outer interchange merging cell and an inner lobe cell, and a smaller reciprocal cell. (c) When Bz+ dominates, with a clock angle near 0°, in June solstice months, the convection pattern should show two cells consisting of inner lobe cells and outer interchange type merging cells and Dungey type merging cells, while in December solstice months, the convection pattern should show two cells consisting of inner reciprocal cells and outer Dungey type merging cells [*Watanabe and Sofko*, 2009a].

4.2 The Event of March 22, 2008 – the influence of interchange reconnection as a convection driver

Figure 4.1 below illustrates both types of interchange reconnection, namely: (a) Type C- for merging of northward IMF with north lobe field lines in the northern hemisphere; (b) Type D- showing merging of north lobe draped-over lines with closed lines, with the merging occurring in the southern hemisphere; (c) Type F+ merging of northward IMF to south lobe merging in the southern hemisphere: (d) Type E+ merging of draped-over south lobe field lines with closed field lines in the northern hemisphere. Note that the diagrams show reconnection from the left side to the right side, as indicated by the wide arrows (the labeling of the reconnection types is taken from *Watanabe and Sofko* [2008]).

Figure 4.1(e) shows the expected convection pattern in the northern hemisphere that results from reconnection Types C-, D- and E+. In Figure 4.1 (a-d), there are two plasma elements on each reconnection field line, whose labels are adapted from Figures 1.22 and 1.23. The footprints of the plasma elements are shown in the convection pattern in Figure 4.1(e).

Prior to the type D- reconnection shown in Figure 4.1(b), the plasma elements D_1 and D_4 are on a closed field line, and the plasma elements D_2 and D_3 are on a north lobe line. After reconnection, the plasma elements D_1 and D_2 are on a north lobe line, and the plasma elements D_3 and D_4 are on a closed field line. The plasma element D_1 moves from the open north lobe line to the closed field line, and thus crosses the OCFLB as shown in the convection pattern in Figure 4.1 (e). The plasma element D_3 moves from the closed field line to the open north lobe line, and also crosses the OCFLB. In the convection pattern in Figure 4.1 (e), the motion of plasma elements D_1 and D_3 is consistent with a clockwise prenoon cell which crosses the OCFLB twice, namely an interchange merging cell M_I driven by the Type D- reconnection.

In type C- reconnection shown in Figure 4.1(a), the plasma elements C_1 and C_4 are on a north lobe line, and the plasma elements C_2 and C_3 are on a northward IMF line before reconnection. After reconnection, the plasma elements C_1 and C_2 are on an IMF line, and the plasma elements C_3 and C_4 are on a draped-over north lobe line. The plasma element C_4 stays on the open north lobe line both before and after the reconnection, thus poleward

of the OCFLB as shown in the convection pattern in Figure 4.1 (e). This result is consistent with a clockwise prenoon cell in the open field line region, which is a lobe cell L driven by Type C- reconnection.

Prior to the Type E+ reconnection shown in Figure 4.1(d), the plasma elements E_1 and E_2 are on a south lobe line, and the plasma elements E_3 and E_4 are on a closed field line before reconnection. After reconnection, the plasma elements E_1 and E_4 are on a closed line, and the plasma elements E_2 and E_3 are on a south lobe line. The plasma element E_4 stays on the closed field line before and after the reconnection, thus equatorward to the OCFLB as shown in the convection pattern in Figure 4.1 (e). This is consistent with a counter-clockwise postnoon cell in the closed field line region, which is a reciprocal cell R driven by Type E+ reconnection.

As a result, the pattern in Figure 4.1 (e) shows a round cell made up of both an interchange merging cell M_I driven by Type D- reconnection and an interior lobe cell driven by Type C- reconnection in the prenoon section. The OCFLB is shown by the dashed line. On the postnoon dayside lies a reciprocal cell which is driven by type E+ reconnection and which has streamlines that lie completely in the closed field line region.

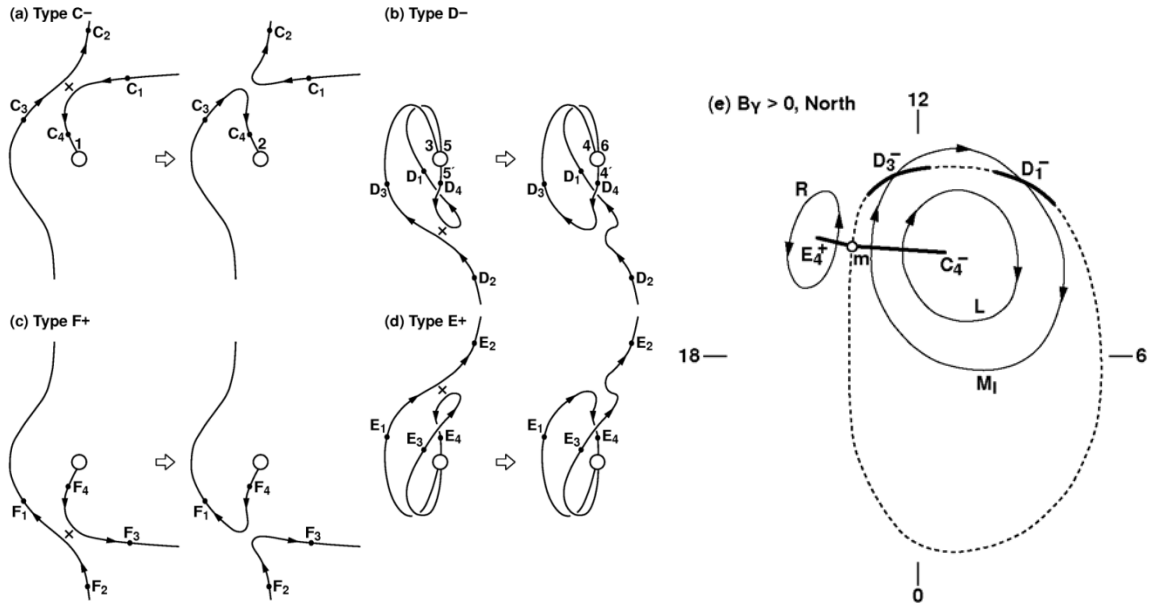

Figure 4.1. The left four panels (a) to (d) show interchange reconnection, namely northward IMF to north (south) lobe in Fig. 4.1 (a) (Fig. 4.1 (c)), and north lobe (south lobe) to closed field line reconnection in Fig. 4.1 (b) (Fig. 4.1 (d)). Fig. 4.1 (e) shows the convection pattern arising in the northern hemisphere from Types C-, D- and E+. The dashed line denotes the OCFLB, showing that the reciprocal cell R lies in a closed field line region, while the lobe cell L is in an open field line region and lies inside the interchange merging cell M_I, which crosses the OCFLB twice on the dayside (from *Watanabe et al.* [2009] and *Watanabe and Sofko* [2009a]).

For Mar 22/08, at the ACE satellite at times near 16 UT, the solar wind speed v_{SW} was about 445 km/s, so the delay time from ACE (located at the Lagrangian point about 240 R_E toward the Sun from the Earth) to the ionosphere was estimated to be about 62 min. This time delay is based on an assumed bow shock at 15 R_E (Earth radius 6378 km), and a magnetopause at 12 R_E. The total delay takes into account a drop by a factor of 3 of the solar wind speed as it crosses the bow shock and then slows to essentially zero at the "stagnation point", which is the magnetopause at the equator at noon. The average speed in the magnetosheath between the bow shock and the magnetopause is thus $v_{SW}/6$. Another 5 minutes (300 s) is allowed for the time for the signal to travel from the magnetopause down to the ionosphere (at about the Alfven speed). The total time is thus 3225 seconds from satellite to bow shock, 218 s from bow shock to magnetopause, and 300 s from magnetopause to ionosphere, for a total of 3743 s, which is roughly 62 minutes. In comparing the convection times shown in Figure 4.3 with the ACE satellite times in Figure 4.2, one must remember to correct for the 62 minute difference.

On March 22, there was, at the ACE satellite at times near 16 UT, a period of IMF with clock angles close to +30°, as shown in Figure 4.2. About 62 minutes later than the ACE satellite times, the solar wind effect was felt in the ionosphere. Figure 4.3 shows four examples of the convective pattern, from 1656-1658, 1712-1714, 1716-1718 and 1730-1732 respectively. The small cell mostly on the postnoon side is the reciprocal cell, while the prenoon side shows a nearly circular contour indicating the lobe cell and an outer portion with high speed flows that is part of the merging cell. To justify this interpretation, we need to establish that the polar cap boundary is in the vicinity of the noon meridian so that the reciprocal cell is not in the polar cap but is on closed field lines outside the cap, and that on the morning side, there is an open field line region within which the circular lobe cell is located.

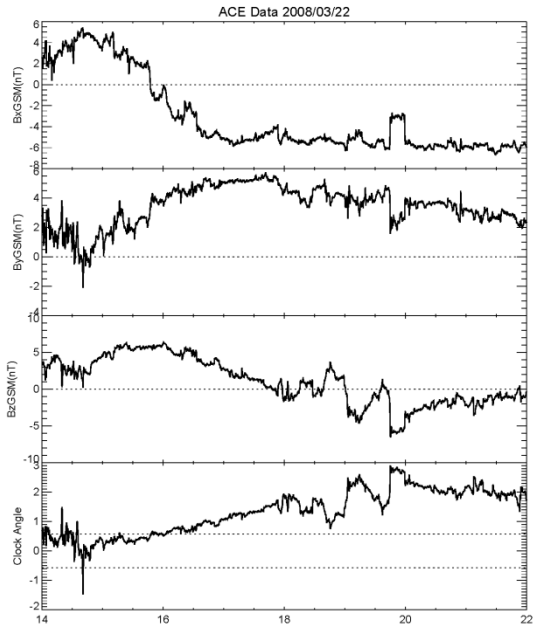

Figure 4.2. IMF and clock angle of Mar 22, 2008. The dashed lines in the fourth panel show ±30°. At about 16:00, the clock angle is near +30°.

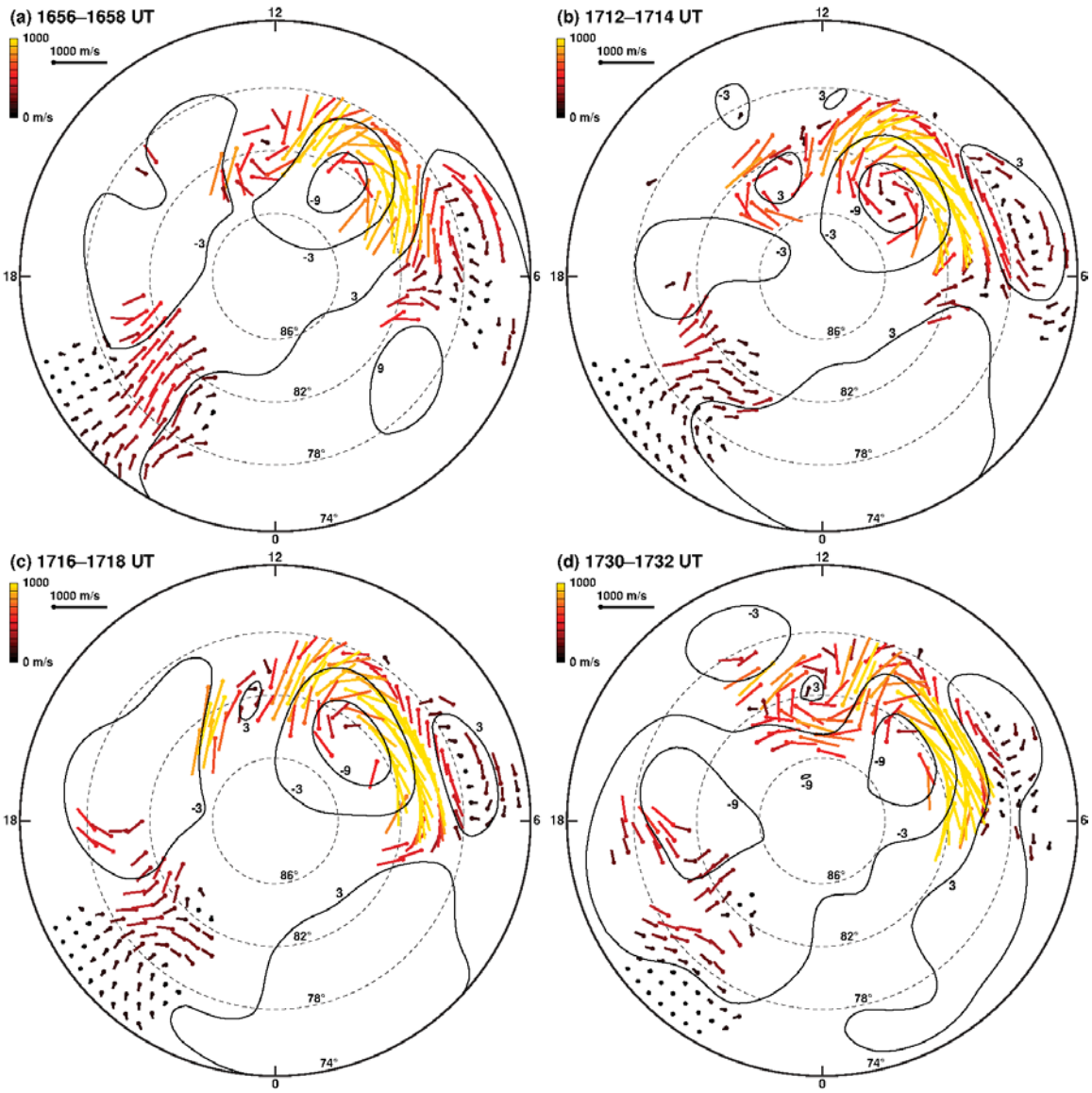

Figure 4.3. Four examples on March 22, 2008 of flow for IMF clock angle θ_C near 30°. The noon is at the top, and the dusk is on the left. The inner circle is for MLAT 86°. The dots with lines show the velocity vectors (from *Watanabe et al.* [2009]).

Figure 4.3 shows the advantage of PolarDARN in revealing details of high-latitude convection. There are two dayside convection cells of opposite rotational sense on either side of noon. The counterclockwise postnoon cell is the reciprocal cell, the prenoon cell is a combination of lobe cell (inner roughly circular streamline) and a larger merging cell. The latter shows fairly fast flows (yellow vectors), typical of By+ conditions in the prenoon. At lower latitudes on the dawnside, particularly evident during the 1712-1714 UT interval, there appears to be evidence of a viscous cell on the closed field lines. In fact, the identification of the OCFLB is one of the major problems for this research. It

should be stated that there are observations on March 8 of convection for a small clock angle event, but with By- IMF. For that event, there is supporting DMSP data that shows the reciprocal cell to be on closed lines in the prenoon sector, with the OCFLB between the reciprocal cell and the counterclockwise lobe cell, but the reciprocal cell is not quite as clear as in the March 22 data below, so we concentrate on the latter here.

We have used data observed by NOAA POES, DMSP and METOP satellites to identify the OCFLB. POES satellites are operated by the National Oceanic and Atmospheric Administration (NOAA) and carry energy detectors which measure integral flux of precipitating electrons and ions in the energy ranges of 50 - 1000 eV and 1000 - 20,000 eV. DMSP satellites are operated by the US Air Force, and carry electrostatic analyzers that measure the energy spectrum of precipitating electrons and ions in 19 logarithmically separated energy ranges from 30–30,000 eV.

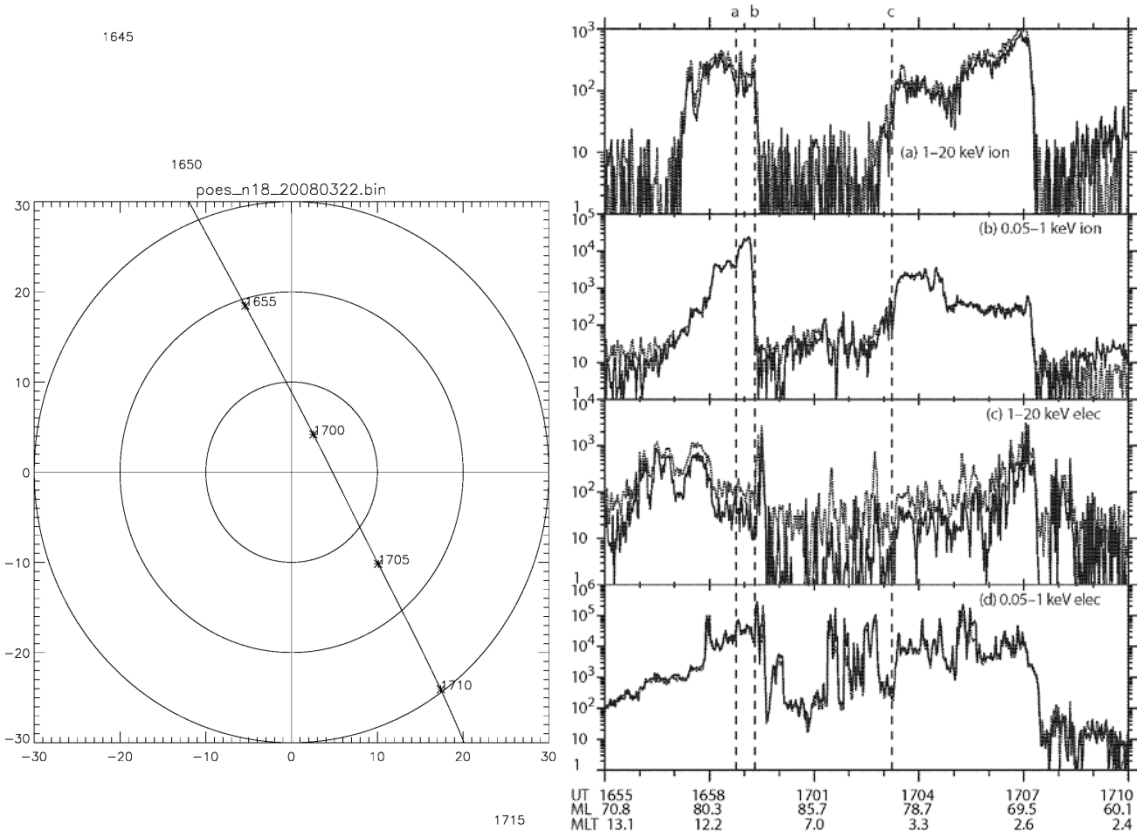

Figure 4.4. NOAA 18 (POES) satellite results. Left panel: orbit of relevance on March 22/08. Right panels (from top to bottom): Integral flux data (protons 1000-20,000 eV; protons 50 eV-1000; electrons 1000 – 20,000 eV; electrons 50 eV-1000 eV). The solid line denotes 0° pitch angle, dashed line 30° pitch angle (from *Watanabe et al.* [2009]).

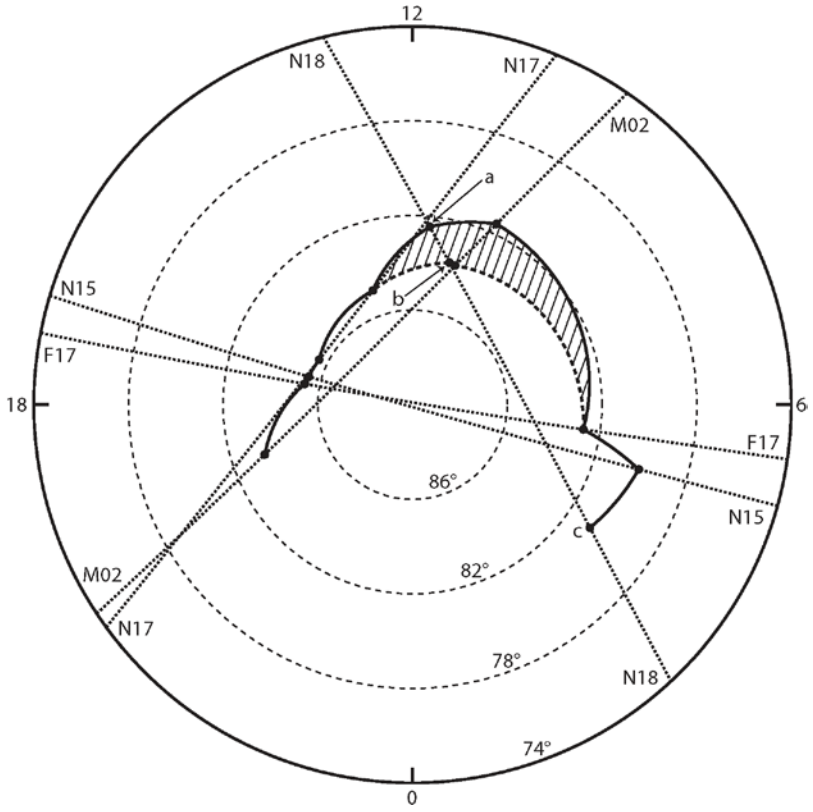

Figure 4.5. The satellite paths in the Northern Hemisphere on March 22, 2008. The solid line inside the circle shows the OCFLB. The dashed lines show the paths of each satellite with dots indicating where the OCFLB is located. F17 is a DMSP satellite, while N15, N17, N18 are NOAA POES satellites, and M02 is a METOP satellite (from *Watanabe et al.* [2009]).

Because there is By+ IMF for the March 22 event, the reciprocal cell is predicted to lie in the postnoon sector where the DMSP orbits are not particularly helpful. Fortunately, the NOAA POES 18 satellite is in a geosynchronous orbit roughly from 1330 solar time on the dayside to 0200 solar time on the nightside. This is an ideal orbit for checking the polar cap boundary location through the use of the POES integral flux data. The 1 – 20 keV ion data (top panel) are particularly useful, since these are auroral energies, but too high for the polar cap. The polar cap is the region of low-energy ion precipitation or is void of precipitation. The sharp decrease in energetic ions (1-20 keV) can thus be used as a proxy for the OCFLB. The poleward boundary of these ions is a very good indicator of the transition from the closed field line geometry of the auroral zone to the open field line region of the polar cap. As shown in Figure 4.4, the integral flux drops dramatically at "b" at time 16:59:18 UT, and increases dramatically at "c" at time 17:03:14 UT. The polar cap boundary is between "b" and "c". The $<$ 1 keV ions are abundant between "a" at time 16:58:46 UT and "b", which characterized the cusp [*Newell and Meng*, 1988, 1992], and the $<$ 1 keV electrons are also abundant between "a" and "b". We suggest that the region between "a" and "b" lies in the cusp, which is also in the open field line region.

Figure 4.4 indicates that the OCFLB was almost on the noon-midnight meridian, between the reciprocal and merging cells, thereby confirming the closed field line zone for the former and the open field line zone for the lobe cell. Also, the METOP 02 satellite data shows that the OCFLB is at about 82° latitude in the prenoon side, so that the equatoprward portion of the merging cell is outside the polar cap.

To obtain the polar cap boundary, we connect the polar cap boundary locations obtained by the 5 satellites which flew over the polar cap in the time interval 16:52-17:34 UT, as shown in Figure 4.5. The dotted line with "N18" on it indicates the path of the POES N18 satellite, on which the dots "a", "b" and "c" are the same dots in Figure 4.4. The hatched area in Figure 5 is the cusp region.

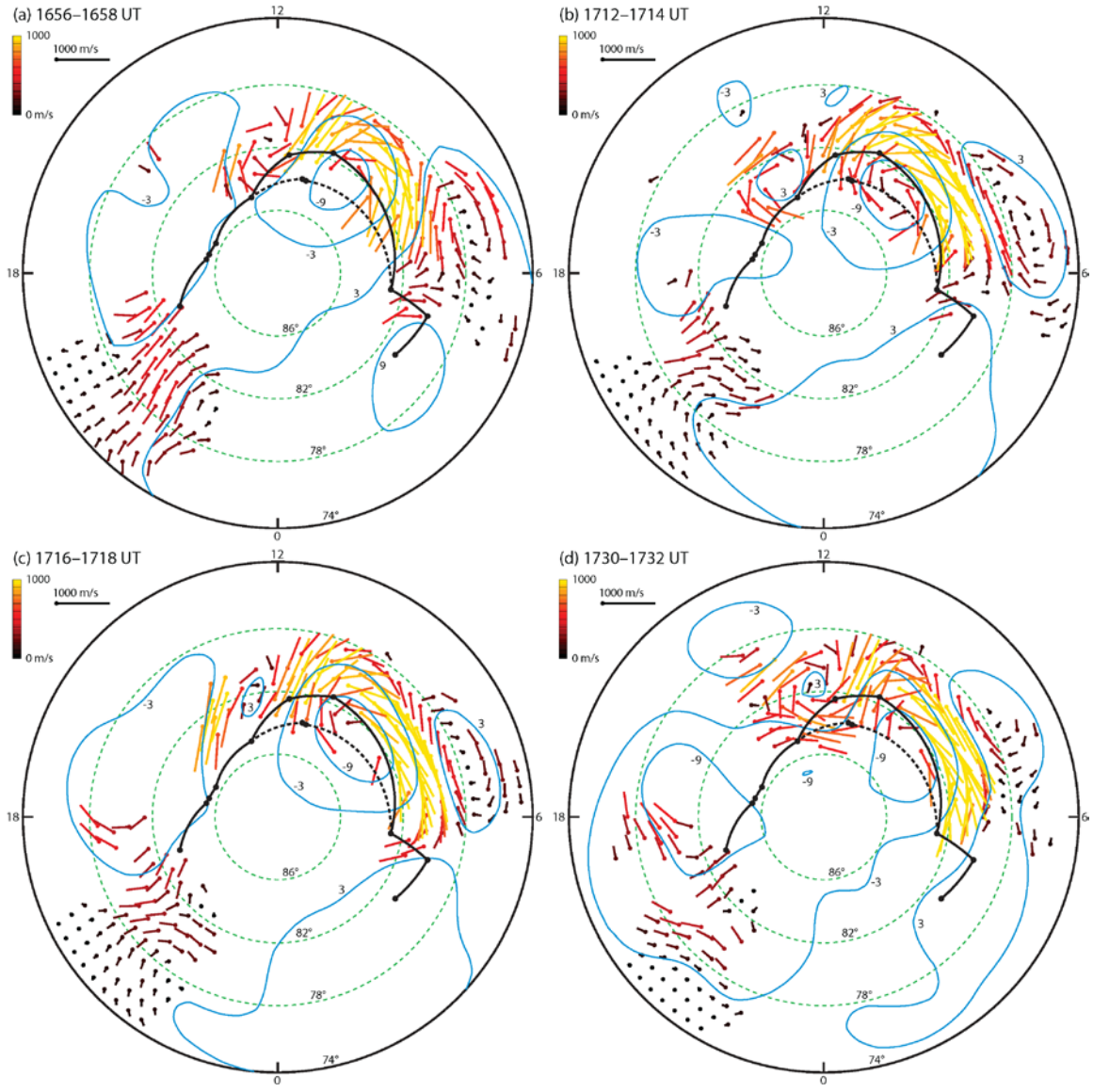

Figure 4.6. The superposition of the polar cap boundary in Figure 4.5 and the convection maps in Figure 4.3 (from *Watanabe et al.* [2009]).

Figure 4.6 shows the superposition of the polar cap boundary in Figure 4.5 and the convection maps in Figure 4.3. It is consistent with Figure 4.1 (e). The postnoon counterclockwise cell is equatorward of the polar cap boundary, which is recognized as a reciprocal cell exclusively in the closed field line region. The prenoon clockwise cell is located both poleward and equatorward of the polar cap boundary. We expect that the inner potion is a lobe cell exclusively in the open field line region, and the outer potion is a merging cell which crosses the OCFLB twice. For IMF $0° < |\theta_c| \lesssim 30°$, it was shown the Dungey-type reconnection is dormant [*Watanabe and Sofko*, 2009a], so the merging cell must be driven by interchange reconnection.

The Mar 22/08 event is an example of Bz+ dominant conditions, with a clock angle in the range of 0° to +30° (By+), and no dipole tilt. It is predicted that Dungey type reconnection cannot occur, so the convection pattern is driven entirely by interchange reconnection, resulting in a larger cell consisting of an outer interchange merging cell and an inner lobe cell, and a smaller reciprocal cell [*Watanabe and Sofko*, 2009a].

One of the most important results of this study is the occurrence of the small reciprocal cell on the postnoon side in the closed field line region. The reason for the importance of the reciprocal cell is that it is one of the predictions unique to the closed-open interchange type of reconnection in the comprehensive 3D null-separator reconnection theory. In the past, the only type of convection cell that had been observed completely on closed field lines was called a “viscous cell” [*Axford and Hines*, 1961], and it tended to originate in the magnetospheric equatorial flanks near dawn or dusk within one of the merging cells in the two-cell pattern normally expected for Bz- IMF conditions. The viscosity itself was attributed to the shear between the antisunward flow in the magnetosheath and sunward flow inside the magnetosphere. The observation of a near-noon small convection cell which occurs during Bz+ conditions and which is driven at high latitudes by interchange open-closed reconnection provides considerable support for the 3D topological null-separator theory.

4.3 The Event of September 3, 2008

On September 3, at a little before 17:00 UT, the clock angle was near 0°, as shown in the solar wind data of Figure 4.7. About 1 hour later, the solar wind effect reached the ionosphere. Figure 4.8 shows two examples of convection maps in the 1746-1748 and 1748-1750 intervals. The pattern shows asymmetry in the two cells near noon, with a small cell near postnoon and a large cell on the prenoon side. To interpret the results, we again need to identify the OCFLB to see if it is located equatorward or poleward of the cells.

In the interval 1700-1830 UT, the northern polar cap is observed by three NOAA satellites - NOAA 16, NOAA 17, and NOAA 18, one METOP satellite - METOP 02, and four DMSP satellites - DMSP F13, DMSP F15, DMSP F16, and DMSP F17. Using the energetic ion drop off between the auroral zone and polar cap, we located the points on the OCFLB, and connected each point to make a map of the OCFLB as shown in Figure 4.9 below.

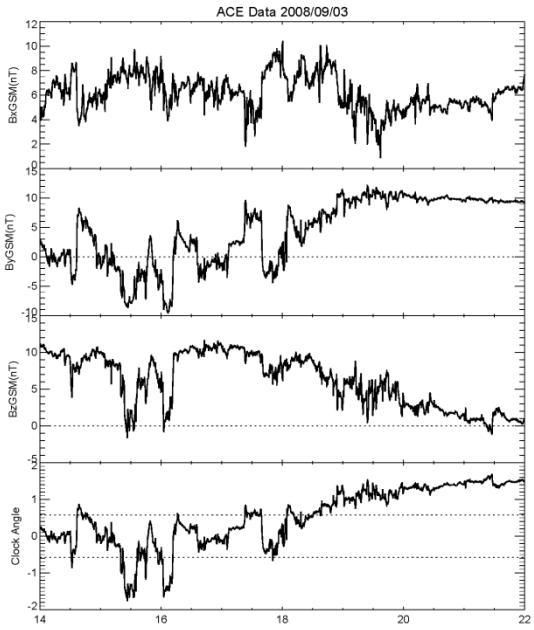

Figure 4.7. The IMF and clock angle of Sep 3, 2008, observed by the ACE satellite during the interval 16-24 UT. The dashed lines in the fourth panel show clock angles ±30°. At a little before 17:00 UT, the clock angle is near 0°.

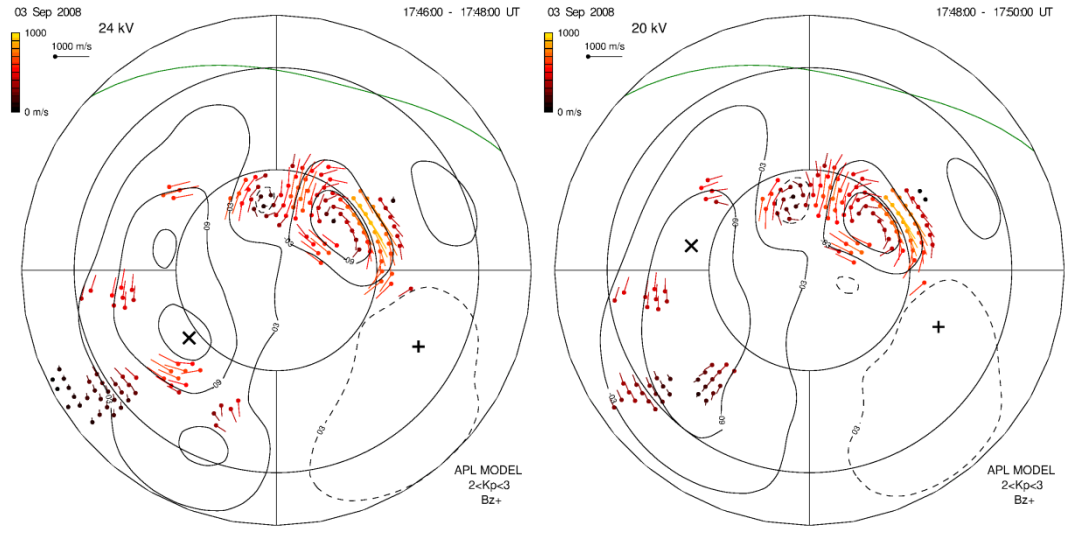

Figure 4.8. Two two-minute convection patterns on Sep 3, 2008. The noon-midnight meridian is the central vertical line, with noon at the top. The horizontal line is the dawn-dusk meridian, with dusk on the left. The inner circle is for MLAT 80°. Dayside convection cells of opposite rotational sense appear on either side of noon.

Figure 4.9 shows that the polar cap boundary near noon is at about 85° latitude. The small enclosed region is the cusp, which is in the open field line region. The OCFLB

frequently is located at 70° - 80° latitude for Bz- conditions, but is higher in latitude for Bz+ conditions. It is very remarkable to see here that the OCFLB can go to as high as 85° latitude, which may due to the combination of the Bz+ conditions and the weak solar wind during this unusual deep solar minimum at the end of Solar Cycle 23.

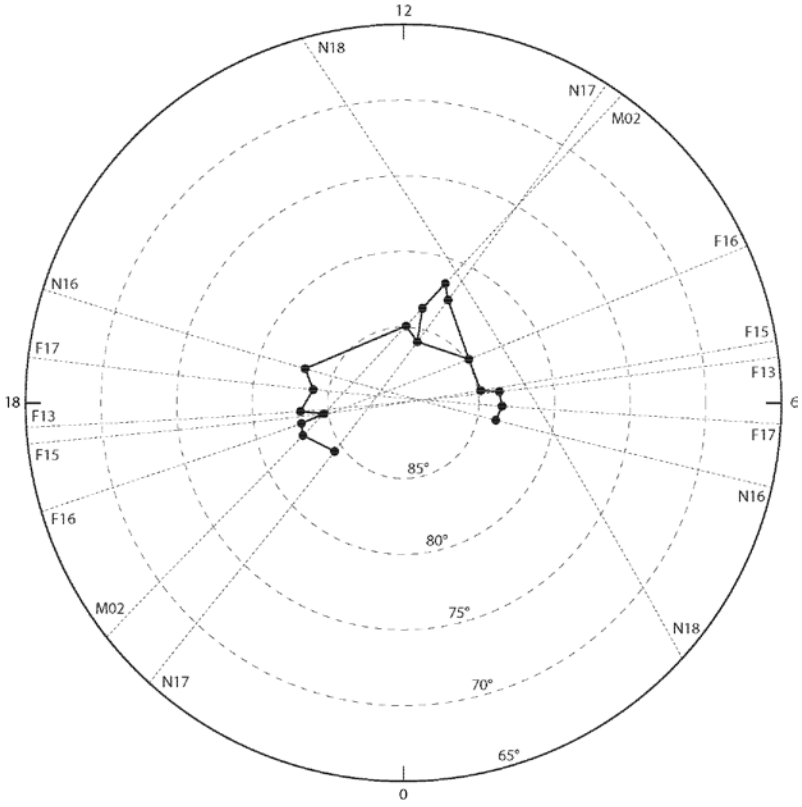

Figure 4.9. The solid line inside the circle shows the OCFLB. The dashed lines show the paths of each satellite with dots where the OCFLB is located. Symbols F13, F15, F16 and F17 denote DMSP satellites, while N16, N17, N18 denote NOAA POES satellites, and M02 is the METOP satellite.

Figure 4.10 shows the superposition of the polar cap boundary in Figure 4.9 and the convection map in the 1746-1748 UT interval in Figure 4.8. In Figure 4.10, the cell on the postnoon side is in the closed field line region and thus is a reciprocal cell, while the outer portion of the cell on the prenoon side has streamlines which cross the OCFLB twice and thus is a merging cell. The center of the prenoon cell is equatorward of the OCFLB. The MLAT of the OCFLB identified by the satellite data has an error of about 1°, so it is difficult to tell whether there is an inner portion of the prenoon cell exclusively in the closed field line region. This uncertainty leads to two possible interpretations.

First, if there is no inner portion of the prenoon cell, the prenoon cell is a merging cell. These are also examples of convection pattern in the northern hemisphere that results from Type D- and E+ reconnection for clock angle $0° < \theta_c < 30°$ near vernal equinox, as shown in Figure 4.1. However, in this case, the clock angle is near 0. Usually, when

the clock angle is near 0, the prenoon cell is a little larger than the postnoon cell, which is consistent with the convection pattern for clock angle $0° < \theta_c < 30°$. The merging cell is driven by interchange type of reconnection. However, the OCFLB is so high that there is no lobe cell within it, so the cell on the prenoon side is a merging cell only.

Secondly, if there is an inner portion of the prenoon cell, the prenoon cell consists of an outer portion of a merging cell and an inner portion of a reciprocal cell. This event applies the convection pattern for the clock angle $\theta_c = 0°$ and December solstice months, as shown in Figure 4.11 (g). The two reciprocal cells are driven by type E+ and E- reconnection. The prenoon merging cell is driven by Dungey type reconnection A- and B-, and thus is a Dungey type merging cell. We should notice the flow is toward the sun at noon, in the opposite direction to the typical Dungey cells, so it is a reversed Dungey cell [*Crooker*, 1992; *Watanabe and Sofko*, 2009a]. In this event, Bx is strongly positive, as shown in Figure 4.7, which can be equivalent to the dipole tilt in December solstice months, so the convection pattern for the clock angle $\theta_c = 0°$ and December solstice months can occur.

The convection pattern for the clock angle $\theta_c = 0°$ and December solstice months in Figure 4.11 (g) can be interpreted by reconnection types in Figure 4.11 (a-f). Figure 4.11 (a-f) are in the yx-plane. The left panel is before the reconnection, while the right panel is after the reconnection.

In type A- Dungey lobe-to-lobe reconnection shown in Figure 4.11 (a), the plasma elements A_1 and A_4 are on a north lobe line, and the plasma elements A_2 and A_3 are on a south lobe line before reconnection. After reconnection, the plasma elements A_1 and A_2 are on a southward IMF line, and the plasma elements A_3 and A_4 are on a closed field line. The plasma element A_4 moves from the open north lobe line to the closed field line, and thus crosses the OCFLB on the morning-side Dungey reversed merging cell M_D as shown in the convection pattern in Figure 4.11 (g). In the type B- reconnection shown in Figure 4.11 (b), the plasma elements B_1 and B_4 are on a closed field line, and the plasma elements B_2 and B_3 are on a southward IMF line before reconnection. After reconnection, the plasma elements B_1 and B_2 are on a north lobe line, and the plasma elements B_3 and B_4 are on a south lobe line. The plasma element B_1, which is attached to the north ionosphere end of the field line, moves from the closed field line to the open north lobe line, and thus crosses the OCFLB, again on the morningside reversed merging cell M_D. To summarize, in the convection pattern in Figure 4.11 (g), the motion of the plasma elements A_4 and B_1 is consistent with a clockwise prenoon cell which has streamlines that cross the OCFLB twice and which is a reverse Dungey cell M_D driven by Dungey reconnection Types A- and B-.

The plasma element E_4 in Type E+ reconnection shown in Figure 4.11 (f) results in a reciprocal cell R in the postnoon section, as discussed in the Mar 22/08 event in section 4.2. Similarly, the plasma element E_4 in Type E- reconnection shown in Figure 4.11 (c) results a reciprocal cell R inside the reversed Dungey cell M_D in the prenoon section.

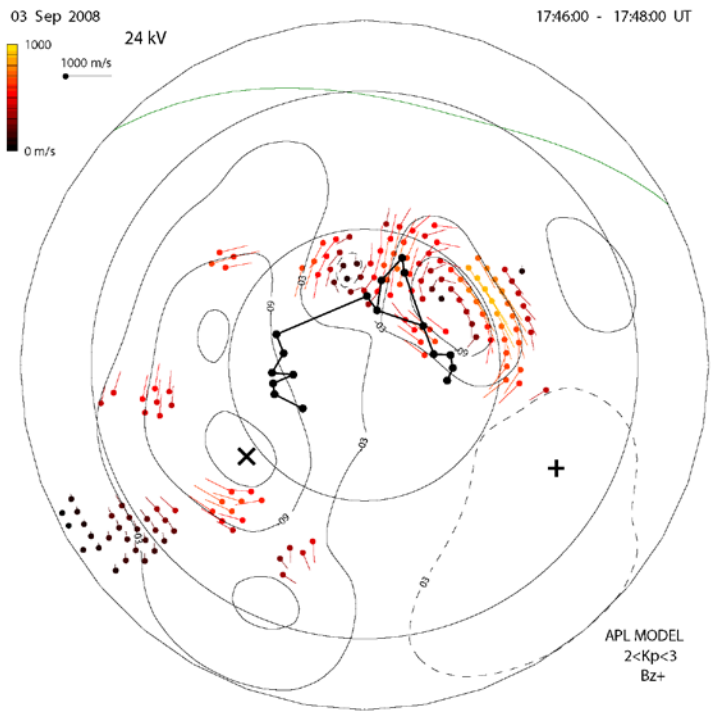

Figure 4.10. The superposition of the polar cap boundary in Figure 4.9 and the convection map in 1746-1748 interval in Figure 4.8.

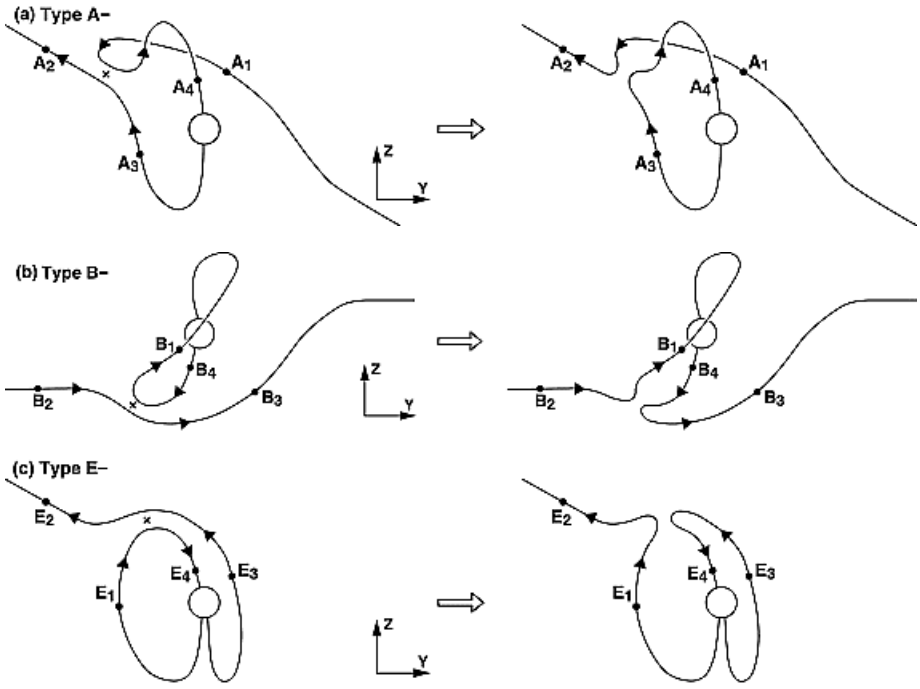

Figure 4.11, part 1. (See caption given below in Fig. 4.11, part 2.)

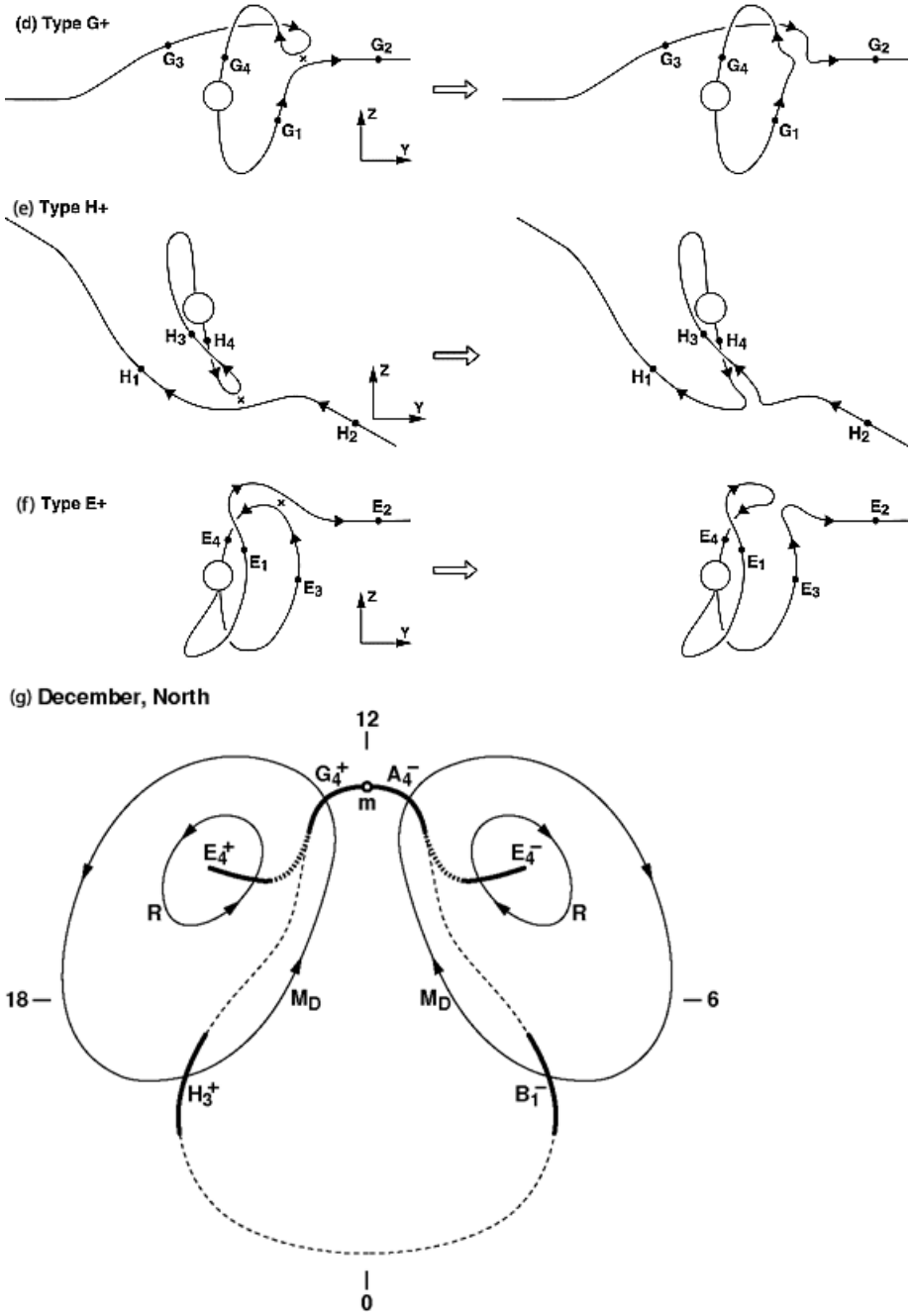

Figure 4.11, part 2. Reconnection-driven ionospheric convection for $\theta_c = 0°$ and December solstice months in the Northern Hemisphere. The convection pattern (g) arises from Type A- (a), B- (b), E- (c), G+ (d), H+ (e) and E+ (f) reconnection. The dashed line denotes the OCFLB, showing that the reciprocal cell R is on closed field lines region, and the Dungey-type merging cell M_D crosses the OCFLB twice (taken from *Watanabe and Sofko* [2008, 2009a, 2009b]).

Figure 4.11(g) also shows the presence of a postnoon reverse Dungey merging cell M_D surrounding the postnoon reciprocal cell R. Although there are enough PolarDARN measurements to define the latter reciprocal cell, there are insufficient experimental data points to determine the existence of the postnoon reverse Dungey cell. For completeness in explaining the presence of the latter in Fig. 4.11(g), we have included the reconnection scenarios shown in panels Fig. 11(d) and (e). In the G+ Dungey reconnection (d), plasma element G_4 connected to the northern ionosphere goes from a northern lobe line to a closed line, while in the H+ Dungey reconnection of 11(e), element H_3 that is attached to the northern ionosphere goes from closed line to a northern lobe line. The resulting postnoon side reversed Dungey merging cell thus behaves in a similar fashion to that on the prenoon side that was described above as the result of the A- and B- Dungey reconnections in panels 11(a) and 11(b).

4.4 The Event of January 22, 2008

The following winter event is chosen to illustrate the following point. In the winter hemisphere, when the clock angle θ_c is near 0°, there are no lobe cells, but reversed Dungey cells instead [*Crooker*, 1992; *Watanabe and Sofko*, 2009a], as shown in Figure 4.11 (g).

At about 19:00 UT, as shown in Figure 4.12, the IMF By component is about +0.4nT, and the IMF Bz component is about +3.6nT, with the clock angle near zero. There is about a one-hour delay from ACE to the ionosphere.

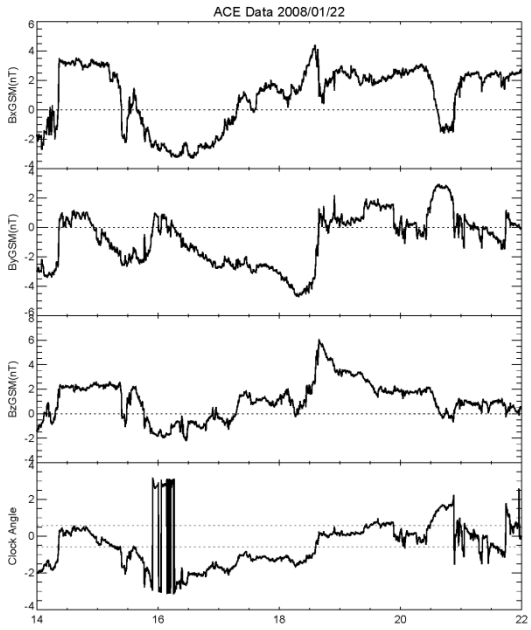

Figure 4.12. The panels show the IMF (top 3 panels) and clock angle (bottom panel) of Jan 22, 2008, during the interval 16-24 UT, as observed by ACE satellite. The dashed lines in the fourth panel show ±30°. At about 19:00, the clock angle is near zero.

Figure 4.13 shows two small cells at high latitude: a C-CWSE cell in the post noon sector and a CWSE cell in the prenoon sector, with sunward flows in the middle. They are both reversed Dungey cells (streamlines cross the OCFLB twice). The two cells turned on and off from 20:00 to 20:52. Compared to the previous examples of $|\theta_C|$ within 30°, when By component has an effect, these examples of θ_C near 0° and December solstice show much more symmetric cells.

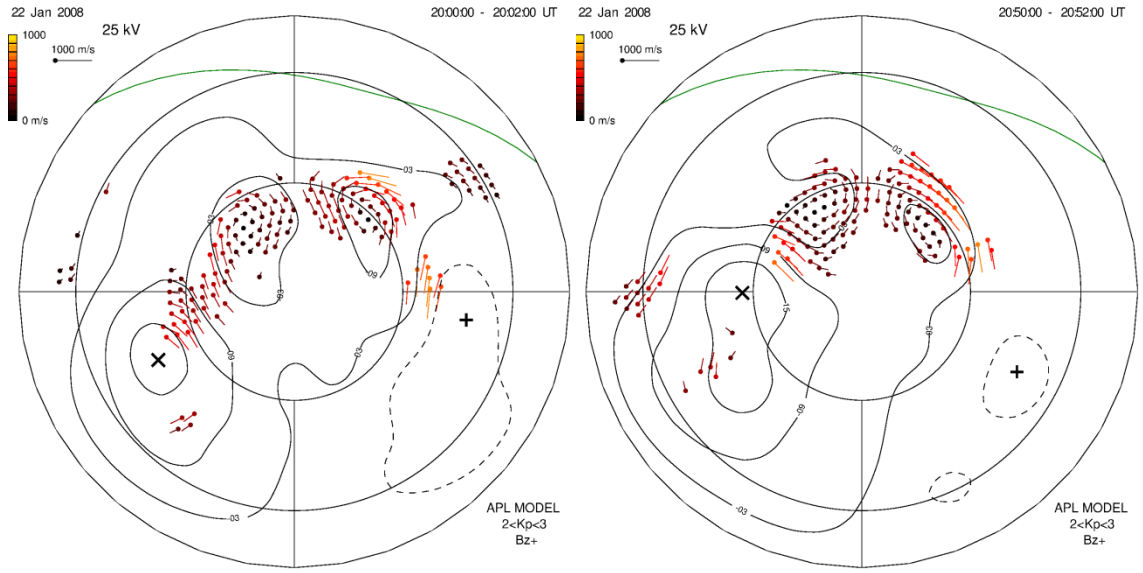

Figure 4.13. Examples of flow for IMF clock angle θ_C near 0°. It is clear that there are two dayside convection cells of opposite rotational sense on either side of noon.

Figure 4.14 is a plot of the NOAA POES N17 satellite data, which shows that the satellite crossed the polar cap boundary at about 20:20:30 UT. It is about MLAT 80° in the left panel of Figure 4.14. The satellite data indicates that the OCFLB is in the middle of the cell, so the cell streamlines cross the OCFLB twice, consistent with a merging cell. Since they are in the winter hemisphere when the IMF is due northward and there is a dipole tilt, reversed Dungey cells driven by Dungey types of reconnection should be formed in Northern hemisphere.

Another similar example was studied on Jan 26, 2008 (not shown), and it also showed two reversed Dungey cells at 18:34 UT.

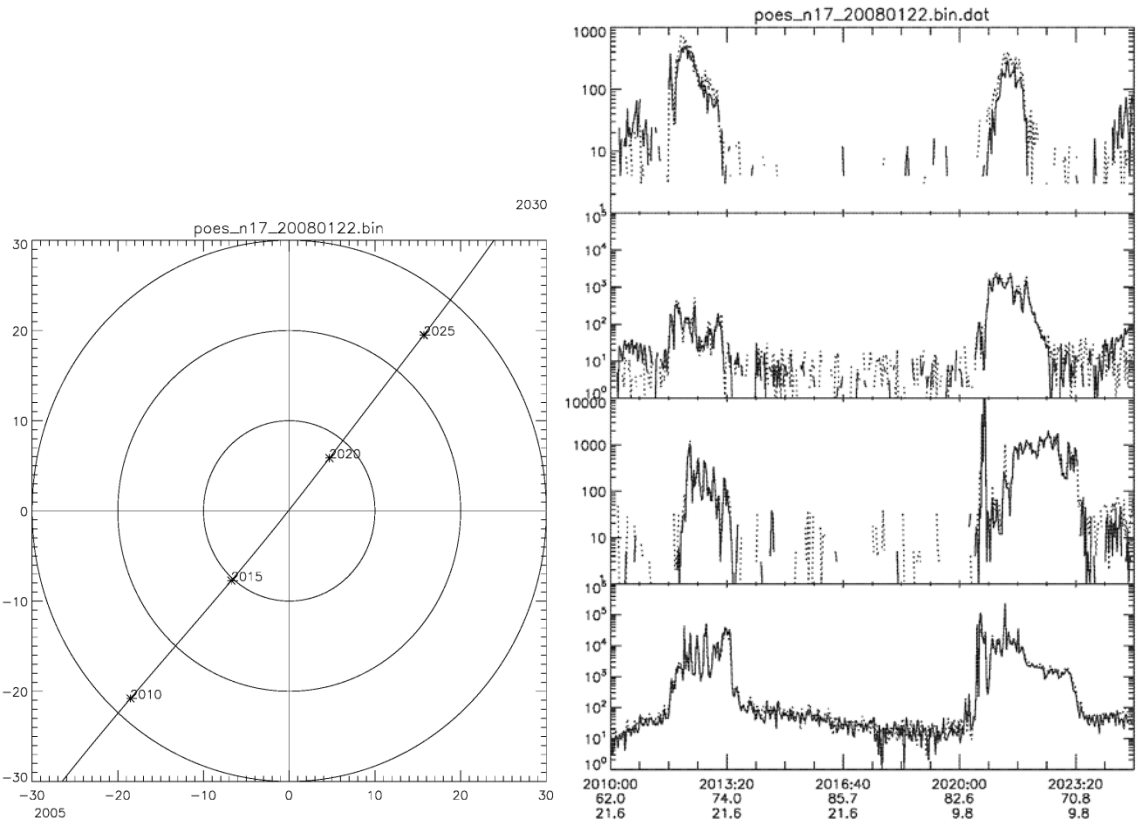

Figure 4.14. NOAA 17 (POES) satellite results. Left panel: orbit of relevance on Jan 22/08. Right panels 2 to 5 (from top to bottom): Integral flux data (protons 1000-20,000 eV; protons 50 eV-1000; electrons 1000 – 20,000 eV; electrons 50 eV-1000 eV). The solid line denotes 0° pitch angle, dashed line 30° pitch angle.

4.5 The Event of April 3, 2008

On April 3, at about 16:00 - 18:00 UT, the clock angle was near 0° and a little positive, as shown in the solar wind data of Figure 4.15. About 1 hour later, the solar wind effect reached the ionosphere. Figure 4.16 shows two examples of convection maps in the 1814-1816 and 1830-1832 intervals. The pattern shows two cells of approximately the same size near noon, a clockwise cell in the prenoon sector and a counter clockwise cell in the postnoon sector.

This event occurs closer to summer solstice, and Bx is negative, which can be equivalent to the dipole tilt in June solstice months. As shown in Figure 4.17 (i), in this condition, two lobe cells appear in Northern Hemisphere, and the outer merging cells may coexist. The lobe cells L arise from Types C+ and C- reconnection, and are in open field line regions. The plasma element C_4 in Type C- reconnection shown in Figure 4.17 (g) results a lobe cell L in the prenoon section as discussed in the Mar 22/08 event in section 4.2.

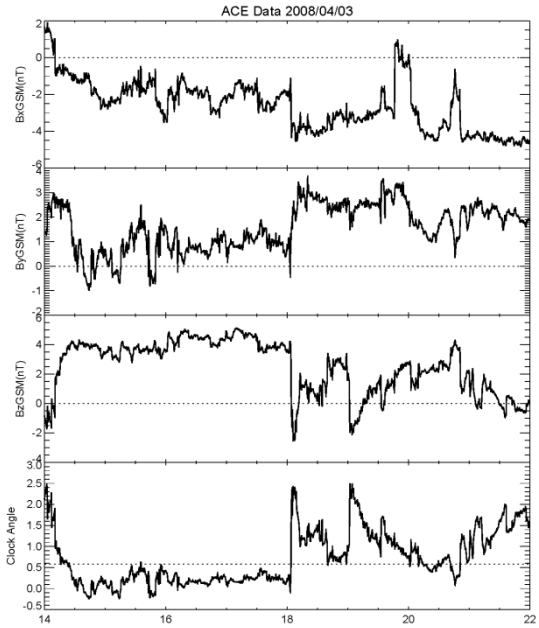

Figure 4.15. The IMF and clock angle of Apr 3, 2008 during the interval 16-24 UT observed by ACE satellite. The dashed line in the fourth panel shows +30°. At about 16:00 - 18:00 UT, the clock angle is near 0.

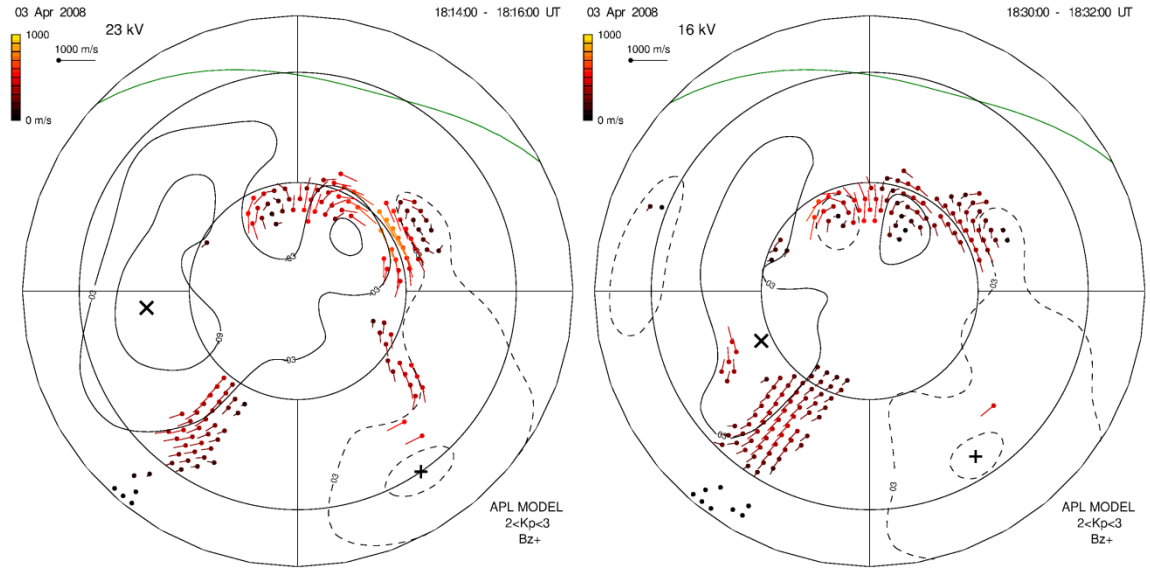

Figure 4.16. Two examples of Apr 3, 2008. The noon-midnight meridian is the central vertical line, with noon at the top; the horizontal line is the dawn-dusk meridian, with dusk on the left. The inner circle is for MLAT 80°. Dayside convection cells of opposite rotational sense appear on either side of noon.

Similarly, the plasma element C_4 in Type C+ reconnection shown in Figure 4.17 (c) results a lobe cell L in the postnoon section. The interchange type merging cells M_I arise

from Types D+ and D- interchange reconnection, and cross the OCFLB twice. Themotion of plasma elements D_1 and D_3 in Type D- reconnection shown in Figure 4.17 (h) is consistent with an interchange merging cell M_I in the prenoon section as discussed in the Mar 22/08 event in section 4.2. Similarly, the plasma elements D_1 and D_3 in Type D+ reconnection shown in Figure 4.17 (d) results an interchange merging cell M_I in the postnoon section. The Dungey-type merging cells M_D arise from Type A+, B+, G- and H- reconnection, and also cross the OCFLB twice. The motion of plasma elements A_4 and B_1 in Types A+ and B+ reconnection shown in Figure 4.17 (a), (b) is consistent with a reversed Dungey cell M_D in the postnoon section, and the motion of plasma elements G_4 and H_3 in Types G- and H- reconnection shown in Figure 4.17 (e), (f) is consistent with a reversed Dungey cell M_D in the prenoon section, similar to the plasma elements on the reversed Dungey cell discussed in the Sep 3/08 event in section 4.3.

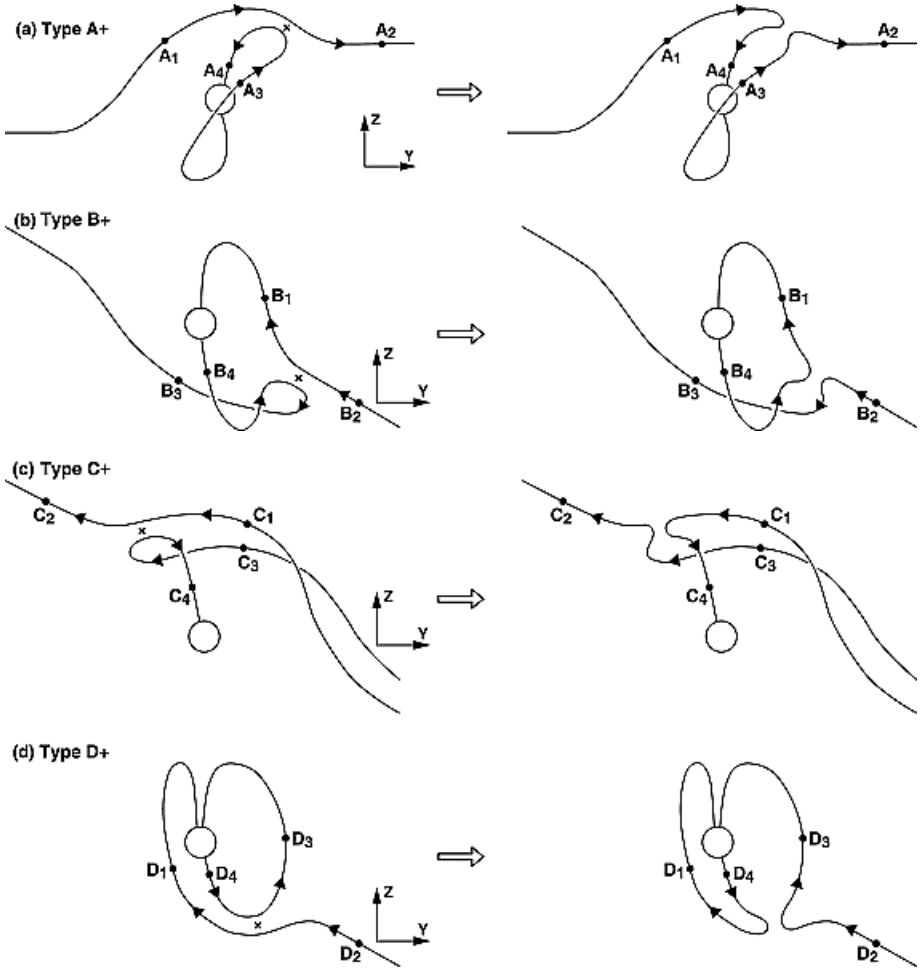

Figure 4.17, part 1. (See caption given below in Fig. 4.17, part 2.)

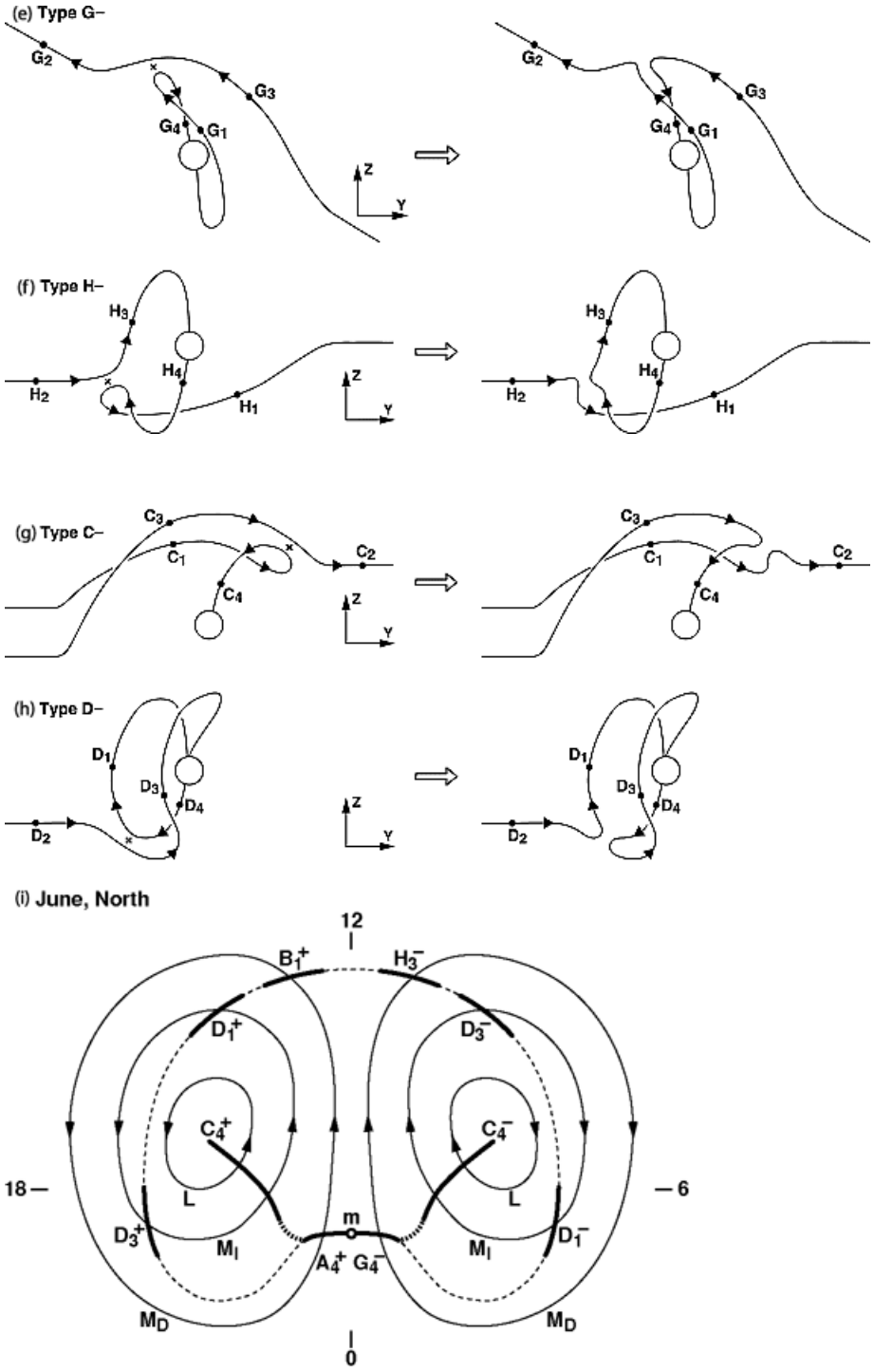

Figure 4.17, part 2. Reconnection-driven ionospheric convection for $\theta_c = 0°$ and June solstice months in the Northern Hemisphere. The convection pattern (i) arises from Type A+ (a), B+ (b), C+ (c), D+ (d), G- (e), H- (f), C- (g) and D- (h) reconnection. The dashed line denotes the OCFLB, showing that the lobe cells L are in open field line regions. The interchange type merging cells M_I and Dungey-type merging cells M_D crosses the OCFLB twice (taken from *Watanabe and Sofko* [2008, 2009a, 2009b]).

To justify if the examples apply the pattern in Figure 4.17 (i), we need to establish the polar cap boundary. In this period, DMSP orbits are near the dawn-dusk meridian, and thus are not very useful. We use NOAA POES satellites to identify the polar cap boundary. Figure 4.18 is a plot of the NOAA POES N18 satellite data, which shows that the integral flux drops dramatically at about 18:15:50 UT, when the satellite is at about MLAT 81° in the left panel of Figure 4.18, so the polar cap boundary may be located at about MLAT 81°. The prenoon cell has an inner portion exclusively poleward of the polar cap boundary, which is a lobe cell, and an outer portion cross the polar cap boundary twice, which is a merging cell. The interchange type merging cell and Dungey type merging cell may coexist. However, we cannot separate the two types of merging cells on the convection map because both of them cross the polar cap boundary twice. Since the two cells are about symmetric, we expect the postnoon cell also consists of a lobe cell and a merging cell. The convection maps are consistent with the pattern in Figure 4.17 (i).

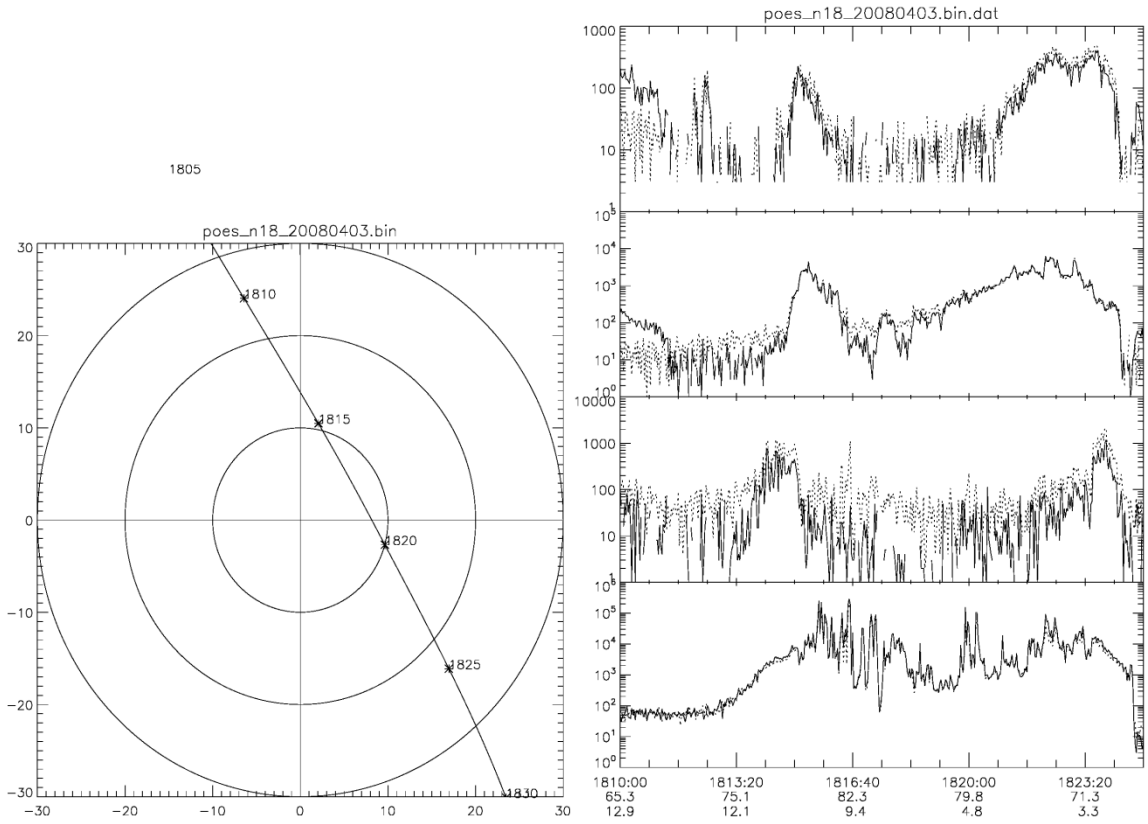

Figure 4.18. NOAA 18 (POES) satellite results. Left panel: orbit of relevance on Apr 3, 2008. Right panels 2 to 5 (from top to bottom): Integral flux data (protons 1000-20,000 eV; protons 50 eV-1000; electrons 1000 – 20,000 eV; electrons 50 eV-1000 eV). The solid line denotes 0° pitch angle, dashed line 30° pitch angle.

4.6 The Event of January 9, 2008

For Jan 09/08, the ACE satellite data in Figure 4.19 show that the By+ component dominated the IMF from about 1800 – 2045 UT and again from 2135 – 2400 UT. Bz was weak and mostly positive (Bz+). The solar wind speed was about 530 km/s, so the delay time from ACE to the ionosphere was estimated to be about 54 min. Figures 4.20(a) and 4.20(b) show the convection velocity pattern versus time for Rankin Inlet beam 5 and Inuvik beam 10, respectively. Positive values (blue) indicate motion toward the radar, and negative values (red, orange, yellow) indicate motion away from the radar (these colours near the red end of the light spectrum are chosen to reflect the Doppler red shift in astronomy, in which celestial objects are moving away from each other).

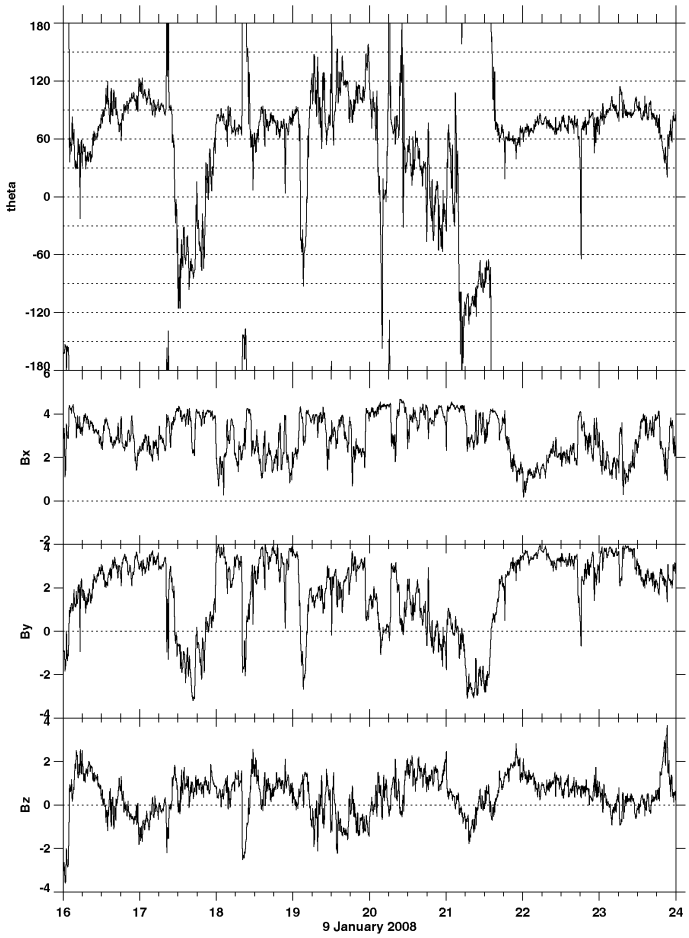

Figure 4.19. IMF results from the ACE satellite for 9 Jan, 2008. The panels from top to bottom show the clock angle $\text{atan2}(B_y, B_z)$, the Bx component, the By component and the Bz component, during the interval 16-24 UT.

During a period in which By is changing rapidly from near zero values while Bz is weakly positive, the flows in general decrease in magnitude and the lobe cell evolution becomes more complex. In the steady state, when the IMF is dominated by By, the pattern is expected to contain a smaller crescent cell and a large round cell [*Crooker et al.*,

1998], with the round cell having an outer portion that is a merging cell and an inner portion that is a lobe cell, the latter being poleward of the OCFLB. In steady-state conditions, a lobe cell can only exist inside the round cell in the winter hemisphere. However, this example is in a period when the IMF is changing [*Watanabe and Sofko,*

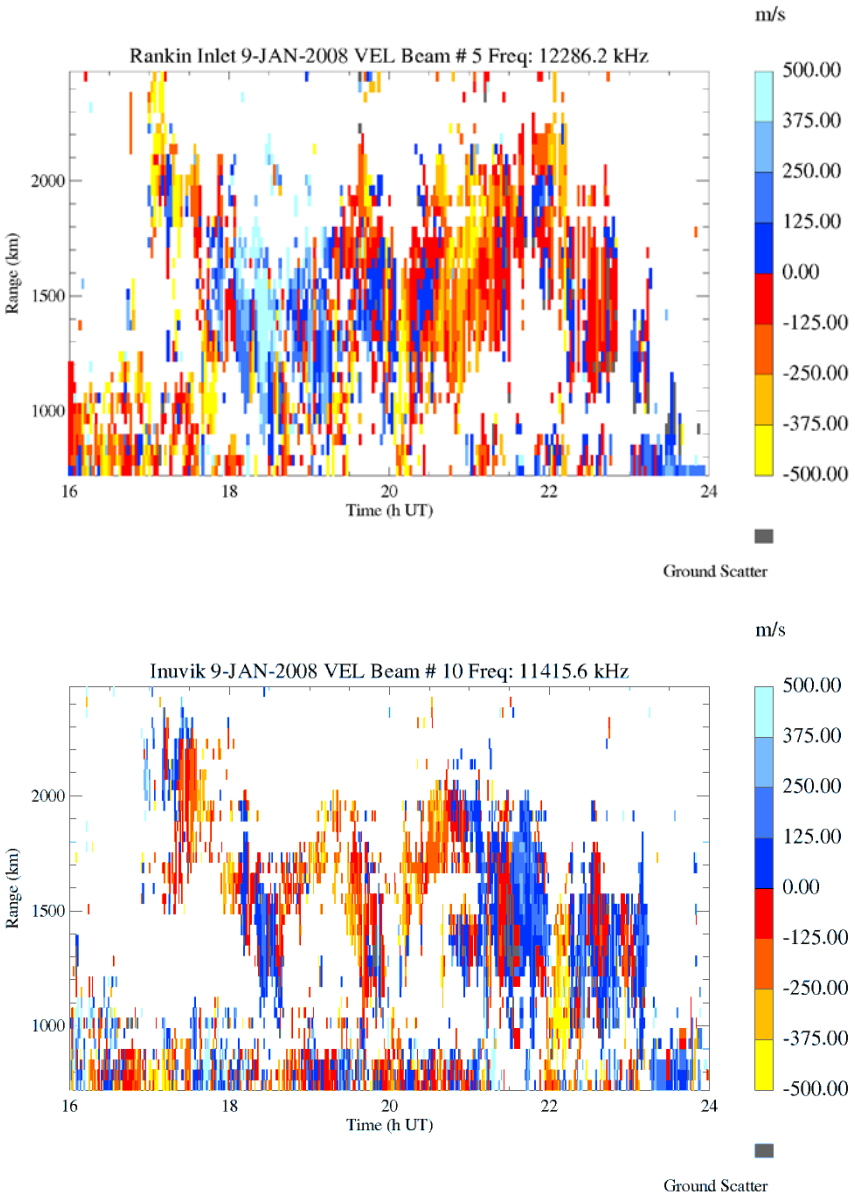

Figure 4.20. The velocity versus range measured by the Rankin Inlet radar on Beam 5 (top panel) and by the Inuvik radar on Beam 10 (bottom panel), on January 9, 2008, from 16 – 24 UT.

2009a]. We do not have a theory for such a period of variability, and we can only suggest a possible interpretation for this example. As the IMF changes from dominant

By+ to dominant By- conditions, the large round cell should shift from being a dusk-centered cell with a clockwise lobe cell that may be located on the portion of the round cell that intrudes into the prenoon sector to a dawn-centered cell with a counterclockwise lobe cell on the dusk side. As By goes through zero, the clockwise cell and the counterclockwise cell exist at the same time. The interpretation of the two cells is the result of the unsteady IMF conditions in which By is going from positive to negative. In the steady-state theory, these two lobe cells should not appear. However, we think that,

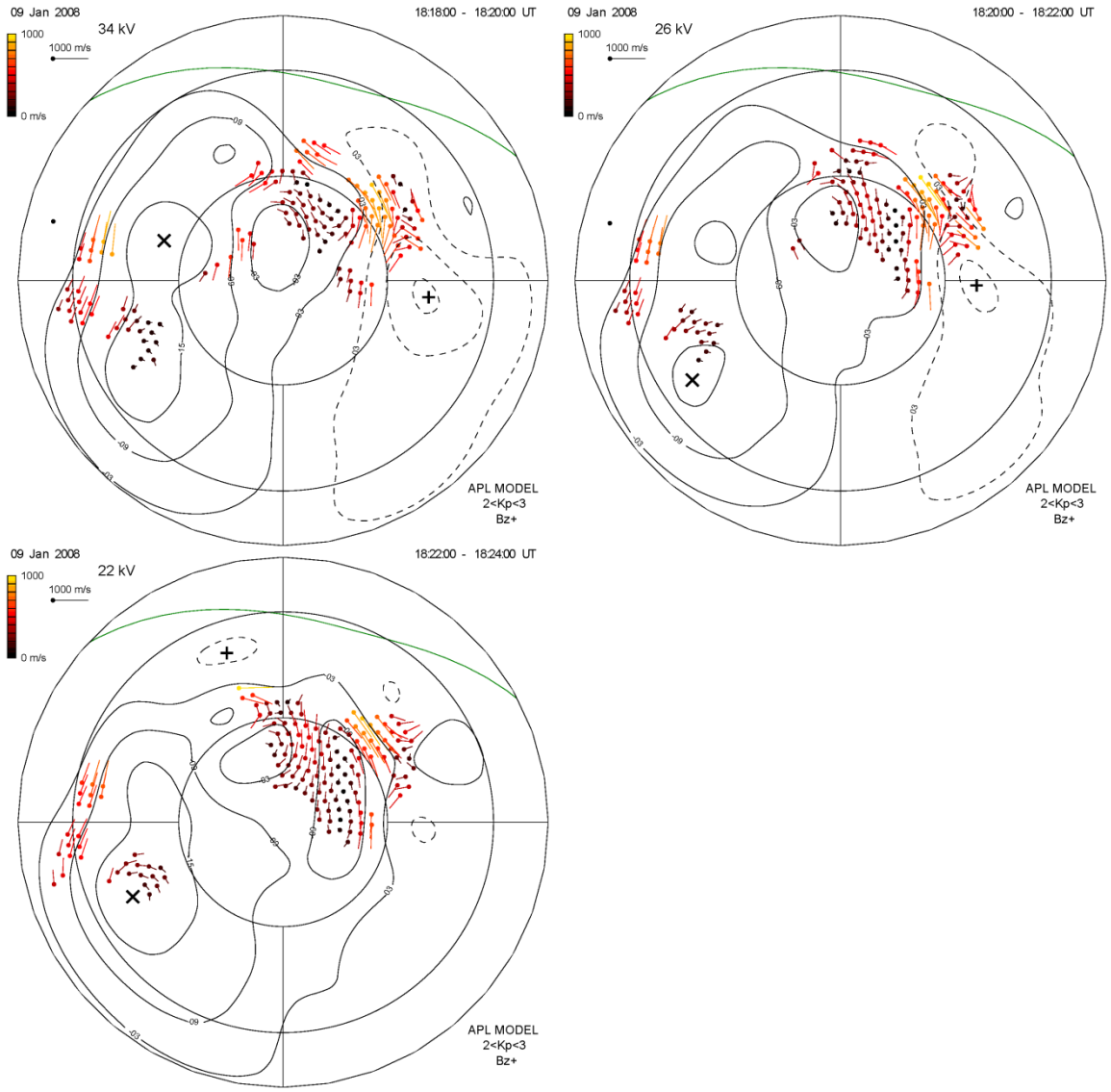

Figure 4.21. Three examples on January 9, 2008. The noon-midnight meridian is the central vertical line, with noon at the top; the horizontal line is the dawn-dusk meridian, with dusk on the left. The inner circle is for MLAT 80°. During the initial period 1818-1820 and 1820-1822 UT, By is positive. There is a large round cell centered on the postnoon side. There is also a lobe cell on the prenoon side, seen more clearly at 1822-1824 UT. By 1822-24 UT, there is also evidence of a postnoon lobe cell starting to form, and of strong sunward flow just before noon, between the two lobe cells.

because the rotational sense of these high-latitude near-noon cells is consistent with that expected for northern hemisphere lobe cells when they are allowed in summer conditions, they very likely are two lobe cells that exist temporarily during the transition period for the IMF By component. Consider the observations shown below in Figure 4.21 to Figure 4.23. In comparing with the ACE satellite times shown in Figure 4.19, remember to account for a 54 minute satellite-to-ionosphere delay. The radar convection shown in Fig. 4.21 begins at 18:18 UT, so the appropriate time in Figure 4.19 is 17:24 UT, which is about the time the By component begins a sharp decrease in value.

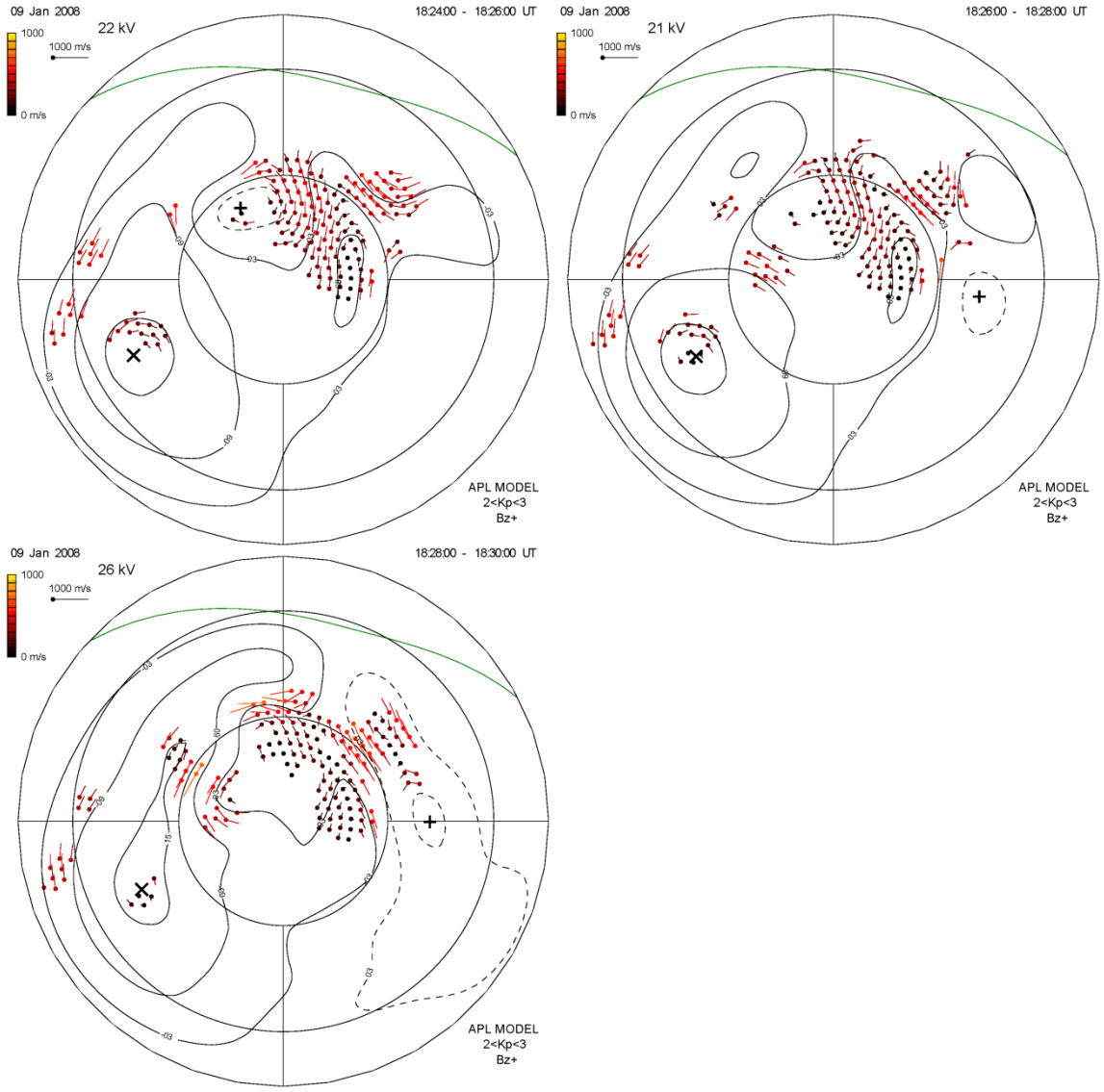

Figure 4.22. During the intervals 1824-26 and 1826-28 UT, there is reasonably good evidence for the co-existence of the two lobe cells, with well-defined sunward flow between them. By 1828-1830 UT, there is only a weak counter-clockwise prenoon cell.

There is evidence of evolution from a single CWSE cell to two lobe cells – both CWSE and C-CWSE cells – and finally to a C-CWSE cell only, as the IMF By changes to minus sense. These are the first experimental observations we know for such a transformation.

As Figure 4.21 shows, during the initial By+ period, there is clear evidence of the prenoon CWSE lobe cell. By 1822-24 UT, there is evidence of the onset of a C-CWSE cell in the noon-postnoon sector, with clear sunward flow between the two cells.

As seen in Figure 4.22, the appearance of two lobe cells is clear in the 1824-26 and 1826-28 UT periods. However, by 1828-1830 UT, when By was negative, there is only faint evidence of the C-CWSE cell. Note the eastward flow sunward of the latter lobe cell. Both the cell sense and the eastward flow are consistent with the change to By- IMF.

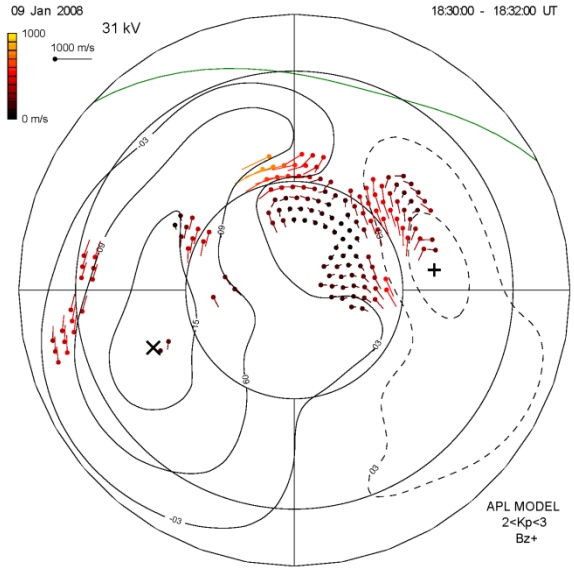

Figure 4.23. Convection plot showing that there is little remaining evidence of the postnoon lobe cell by 1830-1832 UT.

By 1830, as shown in Figure 4.23, the lobe cell structure has gone, ending the rapid 12-minute evolution from single CWSE cell to double cells to a single C-CWSE cell. This example shows that the polar cap is quite dynamic.

To verify our interpretation, we have used data observed by NOAA POES satellites to identify the OCFLB. The POES satellites are operated by the National Oceanic and Atmospheric Administration (NOAA) and carry energy detectors which measure the integral flux of precipitating electrons and ions in the energy ranges of 50 - 1000 eV and 1000 - 20,000 eV. The 1 – 20 keV ion data (top panel) is particularly useful. The poleward boundary of these ions is a very good indicator of the OCFLB. However, because the polar cap is very dynamic in a very short time period, it is difficult to find satellite data which provides an exact match in time with this IMF transition period.

Figure 4.24 is a plot of the NOAA POES N17 satellite data, which shows that the integral flux increases dramatically at about 18:42:05, when the satellite is at about MLAT 77.7° in the left panel of Figure 4.24. Although this time is a little later than the above convection changes, it is the only set of satellite data that is close enough in time. From the N17 orbit, one can see that the OCFLB is located in the prenoon sector at about MLAT 77.7°. If we compare the locations of the two lobe cells during the transition period shown in Figures 4.21 and 4.22, it is clear that the lobe cells, as expected, occur mainly at higher magnetic latitude than 77.7° MLAT.

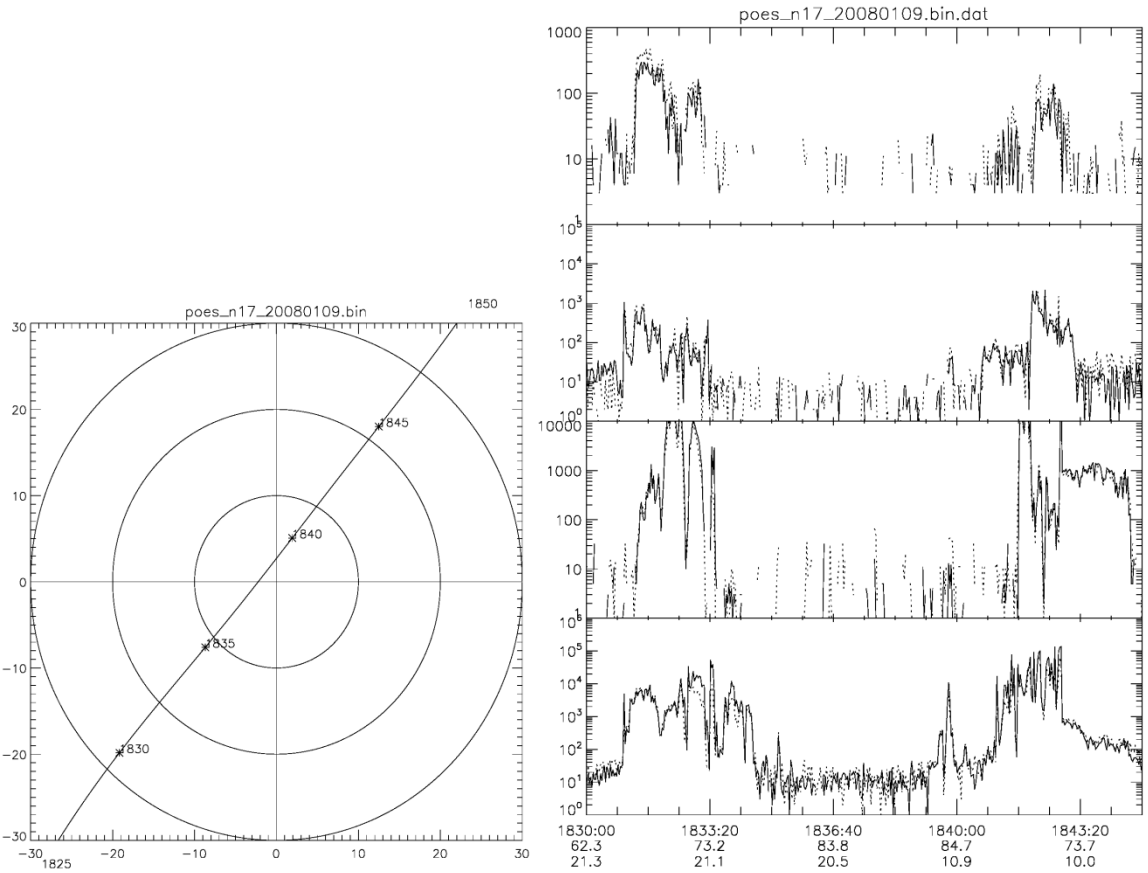

Figure 4.24. NOAA 17 (POES) satellite results. Left panel: orbit of relevance on Jan 9/08. Right panels 2 to 5 (from top to bottom): Integral flux data (protons 1000-20,000 eV; protons 50 eV-1000; electrons 1000 – 20,000 eV; electrons 50 eV-1000 eV). The solid line denotes 0° pitch angle, dashed line 30° pitch angle.

5. CONCLUSION

5.1 Summary of the solar-terrestrial conditions for this thesis work – solar cycle, solar wind, solar magnetic structure, solar effects on weather

In this thesis, the original objective was to study dayside reconnection-driven convection seen by PolarDARN. However, the PolarDARN radars became operational during an exceptionally quiet and extended solar minimum period between Solar Cycles 23 and 24. In order to provide the context for the reconnection study, it was relevant to first study the conditions in the solar wind and IMF that influence the types of reconnection which can occur. This section summarizes these conditions and the results of Chapter 3.

Because both reconnection and the resulting convection patterns are closely dependent upon the solar wind and particularly the IMF, it is of considerable interest to study the IMF conditions since 2006 (Rankin Inlet was operational in mid-May of 2006). The period since then has been unusual due to the deep Cycle 23/24 solar minimum. The current solar minimum is unusually long. There have been 750 days without sunspots through Nov. 10, 2009. The solar wind is in a uniquely low energy state [*Fisk and Zhao*, 2009]. As a result, the normal location of the auroral zone has shifted to higher latitudes, where the recently built PolarDARN radars are in optimum locations to study the polar cap and the poleward portion of the auroral oval during such solar minimum conditions.

Penn and Livingston [2006] reported that, in the period 1998 – 2005, the mean magnetic field strength in sunspot umbral regions has been decreasing at 52 G per year, while the umbral temperatures have been increasing about 73 K per year. The bipolar sunspots exist only when the umbral magnetic field strength is greater than about 1500 gauss. A linear fit of the magnetic field data of umbras suggests that, if the decrease with time continues, we may experience a dearth of bipolar sunspots after about 2015 [*Penn and Livingston*, 2006; *Livingston and Penn*, 2009]. The question is now whether we are approaching a period like the Spörer Minimum from 1450 to 1540 or the Maunder Minimum from 1645 to 1715, when the sun was in a period of low activity with few sunspots.

In addition, the solar wind and IMF also appear to play a role in influencing meteorological weather near the Earth's surface (troposphere, stratosphere). The energy output carried by solar wind is in two forms: the kinetic energy of fast-moving (~400 – 2000 km/s) charged particles (mostly H+, He++ and electrons e-) and the magnetic field energy in the Interplanetary Magnetic Field (IMF). This energy output in the solar wind and IMF is much more variable than the TSI over the solar cycle, and is very bursty during intense solar activity accompanying the occurrence of strong magnetic regions, sunspots and solar flares. There can even be solar cosmic radiation and some nuclear energy released from the solar flare activity. Effects on the climate due to the changing

solar wind conditions are expected to be associated with the strong solar variability during the solar cycles.

In this current solar cycle minimum, the solar wind IMF has decreased, the solar wind has become weak and the heliospheric current sheet has become less warped. As a result, the cosmic ray intensities are higher by 19% in 2009 than the previous space age record [*Phillips*, 2009]. The increased cosmic ray intensity provides another important link between the IMF in space and the weather at the ground. Recent work by *Chen et al.* [2008] involving the use of the ISUAL (Imager of Sprites and Upper Atmospheric Lightning) on the FORMOSAT-2 satellite from July 2004 to June 2007 has determined the occurrence statistics of TLEs (Transient Luminous Events). The results show that the dominant TLEs, by nearly an order of magnitude, are the "elves", which are doughnut-shaped luminosity patches that occur in the lower ionosphere as a result of the electromagnetic pulses (EMP) emitted in lightning discharges [*Inan et al.*, 1991; *Fukunishi et al.*, 1996]. The elves have a far higher occurrence rate by nearly an order of magnitude than the other types of TLE events known as sprites, halos, blue jets and gigantic jets. The important point about elves is that they occur over warm water whose temperature exceeds 26 ° C. The enhanced evaporation rate from the warm ocean produces the thunderclouds that preferably result in elves. The electron density change in the ionosphere in the vicinity of the elves is significant – about 5 %. This chain of events is a clear connection between the ocean (warm water), the atmosphere (thunderclouds) and the ionosphere (elves). Of course, the recent period of enhanced elf activity is also one in which the GCRs have been frequent and not only have increased the conductivity and current in the overall global electric circuit but also the formation of charged nucleation centers required for thundercloud growth [*Feynman et al.*, 1964; *Tinsley*, 2008; *Ram et al.*, 2009]. *Girish and Eapen* [2008] have also shown that the lightning occurrence rate near the dip equator at Trivandrum, India, has an inverse relationship with sunspot number.

Tree rings are thin in cold years when growth is slower and thick in warm years when growth is faster. The study of tree rings indeed shows that a significant 22-year cycle in tree ring thickness [*Stockton and Meko*, 1975] is closely in phase with the solar cycle [*Mitchell et al.*, 1979. Tree rings also contain valuable information about historical solar activity because of the presence of ^{14}C. The levels of C^{14} increase as the result of the enhanced GCR when the solar wind and hence the IMF and heliospheric magnetic field are weak. Similarly, C^{14} levels decrease when the solar wind and IMF are strong. The study of ^{14}C in tree rings appears to show that solar activity has influenced the global climate in long-term [*Eddy*, 1977a]. The Maunder and Spörer Minima are amongst the two coldest periods of the past 1000 years, and their combination is simultaneous with "The Little Ice Age" [*Gates and Mintz*, 1975]. During these periods, the tree rings were thin and contained much C^{14}. During the Medieval Maximum when temperatures were warm, the tree rings were thick and contained little C^{14}. The modern distinctively high solar activity may be one of the reasons for the global warming [*Eddy*, 1978]. It should be noted that the last six solar cycles numbered 18-23 have been on average the strongest continuous set of six since sunspots reappeared around 1715.

Both the short-term temperatures and the solar flare events statistically are characterized by Levy distributions with about the same power index α, which indicates that the global temperature appears to respond to the Sun's variability as reflected in the incidence of solar flares during solar cycles. Solar flares result in a very large amount of energy (~10^{25} J in large flares) being fed to particles and hence to stronger solar wind and its accompanying effects such as stronger IMF and magnetic storms [*Noyes*, 1982]. It is therefore not surprising that not only the 22-year Hale cycle [*Hale et al.*, 1919] fluctuations appear in the temperatures inferred from tree rings but also that the short-term temperature fluctuations on the Earth may be related to the solar cycle/solar wind/IMF variability. Also, from 1950 to 2010, the 11-year and 22-year cycles are seen in the smoothed global temperature, consistent with 11-year and 22-year cycles in the phenomenological solar signature (PSS) of climate [*Scafetta and West*, 2008].

During the recent decades, the global temperature variation appears to be affected by two factors of comparable magnitude: the anthropogenic factor (pollution by greenhouse gases) and the solar variability factor. The greenhouse gases heat the earth, but the weak solar activity during this solar minimum period may be exerting a cooling influence, the result being a stoppage of the global temperature rise or even a temperature decrease since about 2004. The next solar cycles 24 and particularly 25 are predicted to be weak, which could prevent the global temperature from rising as rapidly as during the decade before 2002, or perhaps even lead to a decline. Particularly interesting would be the effect of another extended solar minimum period, which could well occur if the trend from 1992 – 2009 shown by Zeeman splitting of the Fe I 1564.8 nm line continues (Penn and Livingston, 2006). With solar umbral magnetic fields decreasing at 52 G per year and the umbra temperatures rising by 73 K per year, the magnetic field in umbral regions would fall below the threshold value of 1500 G for solar sunspots by about 2015, in which case a new solar minimum could commence and last for an unknown period.

We have studied the averaged values of the magnitudes of IMF components during the period of Jan. 2006 – Dec. 2008. <|Bz|> is lower by 21.5% than that of <|By|>, and <|Bz+|> is lower by 20.1% than that of <|By|>. The By component thus is expected to play an important role in reconnection. <|Bz-|> is slightly lower by 3.7% than <|Bz+|> in this period, and the Bz+ occurrence frequency is larger than that of Bz-, with the Bz+ proportion being 52.0%. The significance of By component is also shown in solar maximum years in 2000 and 2001 when <|Bz|> is lower by 19.1% than that of <|By|>.

The linear regression lines that best fit the temporal behavior of the three components show that the IMF has been getting weaker during the solar minimum conditions, and show that <|By|> decreases most and <|Bx|> decreases least. As a result, the spiral angle of the solar magnetic field in interplanetary space has been decreasing because <|By|> has had a monthly percentage decrease that is about 1.36 times that of <|Bx|>. Also, the amount of warping of the heliospheric current sheet has decreased slightly during the 36-month period. Finally, since the 10.7 cm solar microwave flux monthly percentage decrease of -0.556 is only about 0.855 of the monthly percentage decrease of the total magnitude of the IMF of -0.650, it is clear that the decrease in IMF is a more sensitive measure of the solar minimum than is the decrease in the 10.7 cm flux, although both quantities are useful monitors of the solar minimum conditions.

The statistical study of the IMF from the Jan 1, 2007 – Dec 31, 2008 interval shows that the azimuth angle, $\phi = \mathrm{atan2}(B_y, B_x)$, mainly falls into the "toward" (270° - 360°) and "away" (90° - 180°) quadrants. It has a maximum in the 320°-330° interval for "toward" field, and the mean value of the azimuth in this quadrant is 316°, and a maximum in the 140° – 150° interval for "away" field, and the mean value in this quadrant is 137°. This is in approximate agreement with the results expected from the Archimedes spiral geometry that the azimuth angle peaks at -45° (+315°) for "toward" field and +135° for "away" field.

The distribution of the IMF latitude angles $\theta = \mathrm{atan2}(B_z, \sqrt{B_x^2 + B_y^2})$ from the Jan., 2007 – Dec., 2008 interval shows that the maximum number is near 0°, and the minimum number is near ±90°. Clearly, the majority of IMF latitudes are near 0°, and the likelihood of a pure Bz field (either + or -) is very small.

Finally, the statistical study of IMF clock angle $\theta_c = \mathrm{atan2}(B_y, B_z)$ in the Jan., 2007 – Dec., 2008 interval shows that the maximum number is in the 70° – 80° interval and in the 270° – 280° interval. The difference in angle between the two maxima is about 200°. The number of Bz- points is lower by 8.1% than that of Bz+, which favors our interest in high-latitude convection, because Bz+ reconnection occurs at high latitudes, poleward of the cusp. We are especially interested in θ_c within the range $-30° < \theta_c < +30°$. From the clock angle statistics, the latter conditions occur only 12.4% of the time.

For comparison, the study of the IMF azimuth and latitude angles from the Jan 1, 2000 – Dec 31, 2001 interval during the maximum years of Solar Cycle 23 shows results similar to the solar minimum years from the Jan., 2007 – Dec., 2008 interval. However, the study of IMF clock angle from the Jan., 2000 – Dec., 2001 interval shows that the two maximum intervals (80° – 90°and 250° – 260°) are more symmetric about the z axis than that of the Jan., 2007 – Dec., 2008 interval. Also, the Bz+ and Bz- occurrences were about the same, compared to Bz+ being slightly higher than Bz- in the Jan., 2007 – Dec., 2008 interval. However, the occurrence of θ_c within the range $-30° < \theta_c < +30°$ is about the same.

The sector boundary study from the Jan 1, 2007 – Dec 31, 2008 interval shows either four or two sectors in a synodic solar rotation cycle. The sector boundary crossings are usually obvious if 3-hour values are used, because the transition can happen in less than 3 hours, resulting in a discontinuity in the By and Bx "before" and "after" values. The transition from four sectors to two sectors is surprisingly smooth, in that no interruption in the 27-day synodic periodicity occurs. It is interesting to note that the very quiet recent solar minimum of Solar Cycle 23 has been characterized by the two-sector structure.

For comparison, the sector boundary study from the Jan 1, 2000 – Dec 31, 2001 interval shows that the IMF is stronger than during solar minimum years. There were two or four sectors in approximately 27 days, no more sectors than during solar minimum years. There are more periods of ambiguous polarity, so it is harder to identify the sector boundaries. This is because in solar maximum years, the dipole field is very weak, while

in the solar minimum years, the magnetic field is dominantly a fairly well defined dipole field.

We have also analyzed the solar wind velocity at sector boundaries. The superposed epoch analysis of solar wind speed near sector boundary crossings in the time interval Jan. 2007 to Dec. 2008 shows that the solar wind velocity reaches a minimum about half a day before the sector boundary crossing, and then reaches a maximum about two days after the sector boundary crossing. The standard deviation reaches a minimum at about the same time as the velocity.

For comparison, the velocity also shows the same type of change near sector boundary crossings in the period 2000 – 2001, but the amplitude is not as great as it was during the minimum years. This is expected because the solar wind velocity distribution is slow and single-peaked (peak at about 400 km/s) at solar maximum but at solar minimum is double-peaked with the high-speed portion of the distribution peaking at 750 km/s (see Figure 2 of *Zurbuchen et al.* [2002]). The standard deviation reaches a minimum about 1 day before the velocity reaches the minimum, which is different from the solar minimum years, when the standard deviation and the velocity reached minimum at about the same time.

The sector boundary study also shows that, since Dec. 2007, there were six roughly 27-day synodic solar rotation cycles near spring equinox when “away” field dominated, and that the following seven 27-day cycles close to the autumnal equinox were dominated by “toward” field. The transition is sudden. However, the sector structures did not show a dominant polarity in the present solar minimum until near the end of 2007; there were also no regular variations in the solar maximum years 2000-2001. This is expected because in solar minimum years, there are regular annual variations [*Rosenberg and Coleman*, 1969] of the sector polarity lasting for about a 3-year interval, while in solar maximum years, there are only irregular variations. This is because in solar maximum years, the dipole field is very weak, while in the solar minimum years, the magnetic field is a very well defined dipole. Before the 6 “away” field dominated cycles beginning in December, 2007, there was a single sector which did not appear to fit the 27-day synodic cycle, so that sector may have marked a transition from the irregular variation period to the 3-year regular annual variation period. Therefore, the 3-year oscillation for this minimum appeared to begin in Dec. 2007. Although the present solar minimum has lasted for a long time (since 2005), the regular annual variations of the magnetic sector polarity began late, in Dec. 2007, and will probably not terminate until the second half of 2010. This may reflect a roughly 3 year period on the sun, corresponding to the IMF phase reversal period of 3.2 years found by *Takalo and Mursula* (2002). Also, a strong El Niño event occurs in each solar minimum, and the end of each El Niño event is roughly coincident with the end of the regular annual variations [*Khachikjan et al.*, 2009]. An El Niño event is undergoing now, and may last to the summer or fall of 2010, which is in agreement with the annual oscillation period of about three years. The coincidence of the end of the El Niño event and the regular annual solar magnetic polarity variations is another link between the solar conditions and the Earth’s weather. The new solar cycle – Cycle 24 - is expected to start a little before the end of the regular annual variations and

the El Niño event. By this method, we can tentatively predict that Solar Cycle 24 may not show a definite increase of sunspot activity until the spring or summer of 2010.

5.2 PolarDARN and its measurements of reconnection-driven convection

The main part of this thesis study is dayside reconnection-driven convection seen by PolarDARN. PolarDARN is a pair of HF radars (at Rankin Inlet and Inuvik) looking into the northern polar cap, which is the region of open magnetic field lines poleward of the closed field lines in the auroral zone. The PolarDARN radar locations were chosen so that the pattern of the convection streamlines (which are equipotentials) could be measured at high magnetic latitudes within about 15° of the magnetic pole. The radars employ coherent detection and use a multi-pulse sequence to measure the real (I) and quadrature (Q) parts of the autocorrelation function (ACF) versus the lag in each range cell. The mean Doppler frequency is the slope of the best fit line to the graph of the ACF phase, given by arctan (Q/I), versus lag. The PolarDARN radars use unique TTFD (twin-terminated folded dipole) wire antennas with a 21-wire reflecting fence to prevent echoes from the back direction. In this thesis, we have used the PolarDARN data to study the convection patterns at high latitude.

We used a new comprehensive three-dimensional topological formulation of reconnection to explain specific patterns measured by PolarDARN [*Watanabe et al.*, 2004, 2005, 2006, 2007; *Watanabe and Sofko*, 2008, 2009a, 2009b, 2009c].

We were primarily interested in IMF Bz+ conditions, when convection occurs at high latitudes, which favors PolarDARN measurements. Since our study of the IMF components shows that Bz+ is usually accompanied a By component (By+, By-) and that |By|>Bz+, we have studied convection during three IMF conditions characterized by several different ranges of the clock angle: (a) clock angles in the range of +45° to +90° (By+), or -45° to -90° (By-); (b) clock angles in the range of 0° to +30° (By+), or -30° to 0° (By-); (c) clock angles near 0°.

We emphasized the interchange types of reconnection-driven convection for clock angles in the range 0° to +30° (By+), or -30° to 0° (By-). The Mar. 22/08 Bz+ dominant example (clock angle near 30°) showed clear evidence of interchange reconnection-driven convection patterns, with a lobe cell completely in the region of open field lines, an interchange merging cell in which the streamlines cross the OCFLB twice, and a reciprocal cell which was equatorward of the polar cap, completely in the region of closed field lines. The observed smaller cell on the postnoon side is a reciprocal cell. The larger cell on the prenoon side consists of an interchange merging cell and a lobe cell, and the fast flows are on merging cell streamlines. The identification of the cells depends critically on the use of satellite observations to locate the OCFLB, and this has been accomplished mainly using the drop in the flux of energetic ions which occurs when the satellite passes from the auroral zone to the polar cap. The use of the particle measurements from the NOAA POES satellites, the ESA Metop satellites, and the often-used DMSP satellites, at times nearly simultaneous with the radar convection observations, has given OCFLB profiles that appear to be consistent with the predictions

of the 3D null-separator reconnection topology formulation. Furthermore, one can infer from the results that, when there are no satellite particle energy spectrum data, the radar can be used as a proxy to estimate the OCFLB location. For example, it lies between the interchange merging cell and the reciprocal cell when the IMF clock angle is small.

One of the most important results was the occurrence of the small reciprocal cell on the postnoon side in the closed field line region. The reason for the importance of the reciprocal cell is that it is one of the predictions unique to the closed-open interchange type of reconnection in the comprehensive 3D null-separator reconnection theory. In the past, the only type of convection cell that had been observed completely on closed field lines was called a "viscous cell" [*Axford and Hines*, 1961], and it tended to originate in the magnetospheric equatorial flanks near dawn or dusk within one of the merging cells in the two-cell pattern normally expected for Bz- IMF conditions. The viscosity itself was attributed to the shear between the antisunward flow in the magnetosheath and sunward flow inside the magnetosphere. The observation of a near-noon small convection cell which occurs during Bz+ conditions and which is driven at high latitudes by interchange open-closed reconnection provides considerable support for the 3D topological null-separator theory.

For the example of convection measured on Sept. 3/08, the clock angle was near 0°. It was interesting to see that the OCFLB was located at latitudes as high as 85°, due to a combination of both the Bz+ conditions and the weak solar wind during this unusual deep solar minimum period.

The small cell on the postnoon side is in the closed field line region and thus is a reciprocal cell, while the outer portion of the cell on the prenoon side has streamlines which cross the OCFLB twice and thus defines a merging cell. The center of the prenoon cell is equatorward of the OCFLB. The magnetic latitude (MLAT) of the OCFLB identified by satellite data has an error of 1°, so it is hard to tell if there is an inner portion of the prenoon cell exclusively in the closed field line region, which leads to two possible interpretations. If there is no inner portion of the prenoon cell, the prenoon cell is an interchange merging cell. These are also examples of interchange type reconnection - driven convection patterns for the Mar. 22/08 event. However, the OCFLB is so high that there is no lobe cell within it, so the cell on the prenoon side is a merging cell only. On the other hand, if there is an inner portion of the prenoon cell, the prenoon cell consists of an outer portion of a reversed Dungey type merging cell and an inner portion of a reciprocal cell. This event is an example of convection pattern which shows two cells consist of inner reciprocal cells and outer Dungey type merging cells for the clock angle $\theta_c = 0°$ and December solstice months.

The Jan. 22/08 example for clock angle near 0° at about December solstice shows two reversed Dungey cells, in each of which the streamlines cross the OCFLB twice. This example illustrates that there are no lobe cells unless one occurs inside the round cell in the winter hemisphere.

For the Apr. 3/08 example for clock angles near 0° (roughly approaching the summer solstice), the convection pattern shows two cells consist of inner lobe cells and outer interchange type merging cells and Dungey type merging cells.

The Jan. 9/08 example shows that as the IMF changes from dominant By+ to dominant By- conditions, the large round cell shifted from being a dusk-centered cell with a clockwise lobe cell that may be located on the portion of the round cell that intrudes into the prenoon sector to a dawn-centered cell with a counterclockwise lobe cell on the dusk side. As By goes through zero, the clockwise cell and the counterclockwise cell exist at the same time. The interpretation of the two cells is not in agreement with the steady state theory, for which the two lobe cells should not appear. However, this is clearly an example which shows that, during transient conditions, the steady-state theory simply does not always apply.

5.3 Suggestions for Future Work

We use spherical harmonic analysis with associated Legendre polynomials to fit the data by the least squares method to the computed convection maps for PolarDARN and SuperDARN, where the SVD (singular value decomposition) matrix technique is used to give the best possible least squares fit. When the data coverage by the radars is not sufficient for the SVD technique, we can supplement the measured data by putting into the data gaps convection vectors arising from averaged statistical convection models that characterize the different IMF conditions. However, the convection pattern is quite dynamic, and is different for each event. The averaged convection values from the statistical model do not reflect the real time dynamics of the convection pattern. Therefore, it would seem more appropriate to employ data which are taken at the same time as the radar data and which provide reasonable proxy values for the convection. The most obvious data which fulfills these criteria is magnetometer data. The magnetometers measure the magnetic field perturbations caused by the ionospheric Hall current to estimate the electric field, which we can use in supplement of the SuperDARN data. They are real time data, and thus are better than the averaged models in reflecting the real time convection. One problem with this approach is that the magnetic Hall perturbations are due to the product of the height-integrated Hall conductivity and the electric field. It is thus important that the conductivity not be subject to variations that overwhelm the electric field variations. This is often the case on the dayside, where photoconductivity dominates, or in the polar cap, where the conductivity is generally small. The weak point is that the magnetometer measures a rather large area above it, at least about 150 km in radius, and if it detects a current density, the location would be attributed to the region directly above the magnetometer, which might not be close to where the current actually is. However, the application of the real-time data from the magnetometers with the real-time data from the radars could provide more accurate convection maps.

Also, a digital phase generator is being developed to replace the present phasing matrix. The new digital version will generate much more accurate phases for pointing of the beams of the antenna array. SuperDARN radars are phased-array radars, in which a

constant phase gradient is applied across the 16 antennas, with each antenna differing in phase by a fixed phase α from the neighbouring antenna. The usual way to apply the phase α is simply by means of a length L of coaxial cable of refractive index n. For each beam, we have to cut 16 cables for 16 antenna array, and there are 16 beams, so we need 256 cables. However, the east and west beams are symmetric. If we use a switch for the symmetric beams, we only have to cut 128 cables. The phase α is slightly different for different frequencies, which may cause some error. The application of the digital phase generator can save us from cutting many cables and generate more accurate phases for different frequencies.

Furthermore, we should track the IMF and sector structures to see what they will be like at the start of Solar Cycle 24, and during Solar Cycles 24 and 25, which are predicted to be weak. This could provide valuable information not only about the magnetosphere and ionosphere, but could be important for the study of the global temperature variations that result from the weaker solar wind conditions. If another extended solar minimum period occurs after 2015, an answer could be provided as to just how much the solar variability affects the weather, compared to the anthropogenic greenhouse gas effect.

We want to find more examples of lobe cells. Because the IMF has been very weak since both PolarDARN radars began to operate in Dec. 2007, there was not much data in the convection maps in summer, and not many good examples of lobe cells. We are supposed to see lobe cells in Bz+ dominant condition in summer, and PolarDARN is favorably located for measuring lobe cells at high latitudes. We want to perform a statistical study on the lifetime, position of the center, and the area of the lobe cells.

We stressed on events for small clock angles within |30°|. We would like to find more examples for small clock angles, especially for interchange reconnection events. However, our statistical study of IMF shows the significance of By component in reconnection. We should also study more By dominant examples.

The Jan 9/08 transition event shows some contradiction with the steady state theory. However, the IMF is quite variable, and not at steady state most of the time. We should also study the transition events, and develop theories for transition conditions. By comparing the transition time in the IMF and convection patterns, we might be able to more accurately calculate the time delay from the satellites to the magnetopause, and from the magnetopause to the ionospheric polar cap region.

Finally, it will be a considerable interest to study the high-latitude convection patterns during solar maximum years and to compare them with those we have found during the present solar minimum years.

LIST OF REFERENCES

Allegrini, P., M. Bologna, P. Grigolini, and B. J. West (2007), Fluctuation-Dissipation Theorem for Event-Dominated Processes, *Phys. Rev. Lett.*, 99, 010603.

Aquino, G., P. Grigolini, and B. J. West (2007), Linear response and Fluctuation-Dissipation Theorem for non-Poissonian renewal processes, *Europhys. Lett.*, 80, 10002 (1-6).

Axford, W. I., and C. O. Hines (1961), A unifying theory of high-latitude geophysical phenomena and geomagnetic storms, *Can. J. Phys.*, 39, 1433.

Baker, K. B., J. R. Dudeney, R. A. Greenwald, M. Pinnock, P. T. Newell, A. S. Rodger, N. Mattin, and C. .-I. Meng (1995), HF Radar Signatures of the Cusp and Low-Latitude Boundary Layer, *J. Geophys. Res.*, 100(A5), 7671–7695.

Bemporad, A., A. C. Sterling, R. L. Moore, and G. Poletto (2005), A new variety of coronal mass ejection: Streamer puffs from compact ejective flares, *Astrophys J.*, 635, L189–L192.

Brohan, P., J. J. Kennedy, I. Harris, S. F. B. Tett, and P. D. Jones (2006), Uncertainty estimates in regional and global observed temperature changes: A new data set from 1850, *J. Geophys. Res.*, 111, D12106, doi:10.1029/2005JD006548.

Broun, J. A. (1876), On the variations of the daily mean horizontal force of the Earth's magnetism produced by the sun's rotation and the moon's synodical and tropical revolutions, *Philos. Trans. R. Soc.*, London, 166, 387.

Chen, A. B., C.-L. Kuo, Y.-J. Lee, H.-T. Su, R.-R. Hsu, J.-L. Chern, H. U. Frey, S. B. Mende, Y. Takahashi, H. Fukunishi, Y.-S. Chang, T.-Y. Liu and L.-C. Lee (2008), Global distributions and occurrence rates of transient luminous events, *J. Geophys. Res.*, 113, A08306, doi:10.1029/2008JA013101.

Chisham, G., T. K. Yeoman, and G. J. Sofko (2008), Mapping ionospheric backscatter measured by the SuperDARN HF radars – Part 1: A new empirical virtual height model, *Ann. Geophys.*, 26, 823–841, http://www.ann-geophys.net/26/823/2008/.

Chisham, G., M. Lester, S. E. Milan, M. P. Freeman, W. A. Bristow, A. Grocott, K. A. McWilliams, J. M. Ruohoniemi, T. K. Yeoman, P. L. Dyson, R. A. Greenwald, T. Kikuchi, M. Pinnock, J. P. S. Rash, N. Sato, G. J. Sofko, J.-P. Villain and A. D. M. Walker (2007), A decade of the Super Dual Auroral Radar Network (SuperDARN): scientific achievements, new techniques and future directions, *Surv. Geophys.*, 28, 33-109.

Cowley, S. W. H. (1973), A qualitative study of the reconnection between the Earth's magnetic field and an interplanetary field of arbitrary orientation, *Radio Sci., 8*(11), 903–913.

Crooker, N. U., J. T. Gosling, and S. W. Kahler (2002), Reducing heliospheric magnetic flux from coronal mass ejections without disconnection, *J. Geophys. Res., 107*(A2), 1028, doi:10.1029/2001JA000236.

Crooker, N. U. (1992), Reverse Convection, *J. Geophys. Res., 97*(A12), 19,363–19,372.

Crooker, N. U., J. G. Lyon, and J. A. Fedder (1998), MHD model merging with IMF B_Y: Lobe cells, sunward polar cap convection, and overdraped lobes, *J. Geophys. Res., 103*(A5), 9143–9151.

Crooker, N. U., C.-L. Huang, S. M. Lamassa, D. E. Larson, S. W. Kahler, and H. E. Spence (2004), Heliospheric plasma sheets, *J. Geophys. Res.*, 109, A03107, doi:10.1029/2003JA010170.

de Vries, H. L. (1958), Variation in Concentration of Radiocarbon with Time and Location on Earth, *Proceedings Koninlijke Nederlandse Akademie Wetenschappen* B, 61: 94-102.

Dorelli, J. C., A. Bhattacharjee, and J. Raeder (2007), Separator reconnection at Earth's dayside magnetopause under generic northward interplanetary magnetic field conditions, *J. Geophys. Res., 112*, A02202, doi:10.1029/2006JA011877.

Drayton, R. (2006), Study of SAPS-like flows with the King Salmon SuperDARN radar, M.Sc. thesis, Saskatoon, Canada, University of Saskatchewan.

Duffy, P. B., B. D. Santer, and T. M. L. Wigley (2009), Solar variability does not explain late-20th-century warming, *Physics Today*, 62(1):48–49.

Dungey, J. W. (1963), The structure of the exosphere or adventures in velocity space, in *Geophysics, The Earth's Environment*, edited by C. DeWitt, J. Hieblot, and A. LeBeau, pp. 503–550, Gordon and Breach, New York.

Dungey, J. W. (1961), Interplanetary magnetic field and the auroral zones, *Phys. Rev. Lett., 6*, 47–48.

Dungey, J. W. (1953), Conditions for the occurrence of electrical discharges in astrophysical systems, *Phil. Mag.*, 44, 725.

Dungey, J. W. (1958), *Cosmic Electrodynamics*, P. 98, Cambridge University Press, New York.

Eddy, J. A. (1978), *The New Solar Physics*, Westview Press, Boulder Colorado, USA.

Eddy, J. A. (1977a), Climate and the changing sun, *Climatic Change*, Volume 1, Number 2, 173-190, DOI: 10.1007/BF01884410.

Eddy, J. A. (1977b), Historical Evidence for the Existence of the Solar Cycle, in *The Solar Output and its Variation*, Edited by Oran R. White. Boulder: Colorado Associated University Press, p.51.

Eddy, J. A. (1976), The Maunder minimum, *Science*, Vol. 192. no. 4245, pp. 1189 – 1202.

Evans, D. S., and M. S. Greer (2006), Polar Orbiting Environmental Satellite Space Environment Monitor - 2 Instrument Descriptions and Archive Data Documentation, http://poes.ngdc.noaa.gov/docs/sem2_docs/2006/SEM2v2.0.pdf.

Evans, D. S., and M. S. Greer (2000), Polar orbiting environmental satellite space environment monitor: 2, Instrument description and archive data documentation, *NOAA Tech. Memo. OAR SEC-93*, Natl. Oceanic and Atmos. Admin., Boulder, Colo. M.

Feldman, U., E. Landi, and N. A. Schwadron (2005), On the sources of fast and slow solar wind, *J. Geophys. Res.*, 110, A07109, doi:10.1029/2004JA010918.

Feldstein, Y. I., and G. V. Starkov (1967), Dynamics of auroral belt and polar geomagnetic disturbances, *Planet. Space Sci.* 15:209-29.

Feynman, R. P., R. B. Leighton, M. Sands (1964), Electricity in the Atmosphere, in *the Feynman Lectures on Physics*, volume II, Addison-Wesley publishing company, inc., Massachusetts, Palo Alto, London.

Fisk, L. A., and L. Zhao (2009), The heliospheric magnetic field and the solar wind during the solar cycle, in *Universal Heliophysical Processes: Proceedings of the International Astronomical Union*, vol. 257, edited by N. Gopalswamy and D. F. Webb, pp. 109–120, Cambridge Univ. Press, New York.

Forbes, T. G. (2007), Classical theory of two-dimensional reconnection, in *Reconnection of Magnetic Fields, Magnetohydrodynamics and Collisionless Theory and Observations*, edited by J. Birn and E. R. Priest, 16-25, Cambridge University Press, Cambridge, UK.

Fukunishi, H., Y. Takahashi, M. Kubota, K. Sakanoi, U. S. Inan, and W. A. Lyons (1996), Elves: Lightning-induced transient luminous events in the lower ionosphere, *Geophys. Res. Lett.*, 23(16), 2157–2160.

Gates, W. L. and Y. Mintz (1975), *Understanding Climate Change*, National Acad. Of Science, Washington D. C..

Gillies, R. G., G. C. Hussey, G. J. Sofko, K. A. McWilliams, R. A. D. Fiori, P. Ponomarenko, and J.-P. St.-Maurice (2009), Improvement of SuperDARN velocity measurements by estimating the index of refraction in the scattering region using interferometry, *J. Geophys. Res.*, 114, A07305, doi:10.1029/2008JA013967.

Ginzburg, V. L. (1964), *The Propagation of Electromagnetic Waves in Plasmas*, Pergamon, New York.

Giovanelli, R. G. (1947), Magnetic and electric phenomena in the sun's Atmosphere associated with Sunspots, *Mon. Not. Roy. Astron. Soc.*, 107, 338.

Girish, T. E., P. E. Eapen (2008), Geomagnetic and sunspot activity associations and ionospheric effects of lightning phenomena at Trivandrum near dip equator, *Journal of atmospheric and solar-terrestrial physics*, Volume 70, Issue 17, 2222-2232.

Gloeckler, G., T. H. Zurbuchen, and J. Geiss (2003), Implications of the observed anticorrelation between solar wind speed and coronal electron temperature, *J. Geophys. Res.*, 108(A4), 1158, doi:10.1029/2002JA009286.

Greenspan, M. E., P. B. Anderson, and J. M. Pelagatti (1986), Characteristics of the thermal plasma monitor (SSIES) for the Defense Meteorological Satellite Program (DMSP spacecraft S8 through F10), Tech. Rep. AFGL-TR-86-0227, Hanscom AFB, Mass.

Greenwald, R. A., K. B. Baker, J. R. Dudeney, M. Pinnock, T. B. Jones, E. C. Thomas, J.-P. Villain, J.-C. Cerisier, C. Senior, C. Hanuise, R. D. Hunsuker, G. Sofko, J. Koehler, E. Nielsen, R. Pellinen, A. D. M. Walker, N. Sato, and H. Yamagishi (1995), DARN/SuperDARN: A global view of the dynamics of high-latitude convection, *Space Sci. Rev.*, 71, 763–796.

Hardy, D. A., L. K. Schmitt, M. S. Gussenhoven, F. J. Marshall, H. C. Yeh, AIR FORCE GEOPHYSICS LAB HANSCOM AFB MA (1984), Precipitating electron and ion detectors (SSJ/4) for the Block 5D/Flights 6-10 DMSP satellites: Calibration and data presentation, Air Force Geophysics Lab Report #AFGL-TR-84-0317, Hanscom AFB, MA,.

Hale, G. E., F. Ellerman, S. B. Nicholson, and A. H. Joy (1919), The magnetic polarity of sunspots, *Astrophys. J.*, 49, 153.

Headquarters Staff of the American Radio Relay League (1961), The radio amateur's handbook, Thirty-eight Edition, West Hartford, CONN., U.S.A.

Henke, T., J. Woch, R. Schwenn, U. Mall, G. Gloeckler, R. von Steiger, R. J. Forsyth, and A. Balogh (2001), Ionization state and magnetic topology of coronal mass ejections, *J. Geophys. Res.*, 106, 10, 597.

Hosokawa, K., K. Shiokawa, Y. Otsuka, T. Ogawa, J. P. St-Maurice, G. J. Sofko and D. A. Andre (2009), Relationship between polar cap patches and field-aligned irregularities as observed with an all-sky airglow imager at Resolute Bay and the PolarDARN radar at Rankin Inlet, *J. Geophys. Res.*, 114, A03306, doi:10.1029/2008JA013707.

Hoyle, F. (1949), *Some Recent Researches in Solar Physics*, Cambridge Univ. Rress, Cambridge.

Hundhausen, A. J. (1972), Coronal Expansion and Solar Wind, Springer-Verlag Berlin Heidelberg New York.

Hundhausen, A. J., H. E. Gilbert, and S. J. Bame (1968), Ionization State of the Interplanetary Plasma, *J. Geophys. Res.*, 73(17), 5485–5493.

Inan, U. S., T. F. Bell, and J. V. Rodriguez (1991), Heating and ionization of the lower ionosphere by lightning, *Geophys. Res. Lett.*, 18(4), 705–708.

Kennel, C. F. (1995), Convection and Substorms: Paradigms of Magnetospheric Phenomenology, Oxford University Press. 10.

Khachikjan, G. Y., G. J. Sofko, and A. V. Koustov (2009), Times of SSC Occurrence and Their Correlation with IMF Sector Polarity and ENSO Climate Cycles. Submitted to Annales Geophysicae.

King, J. H. (1976), A Survey of Long-Term Interplanetary Magnetic Field Variations, *J. Geophys. Res.* 81, 653-660.

Kivelson, M. G., and C. T. Russell (1995), *Introduction to Space Physics*, Cambridge University Press, Cambridge UK.

Ko, Y.-K., L. A. Fisk, J. Geiss, G. Gloeckler, and M. Guhathakurta (1997), An empirical study of the electron temperature and heavy ion velocities in the south polar coronal hole, *Sol. Phys.*, 171, 345.

Koustov, A. V., J.-P. St.-Maurice, G. J. Sofko, D. Andre, J. W. MacDougall, M. R. Hairston, R. A. Fiori, and E. E. Kadochnikov (2009), Three-way validation of the Rankin Inlet PolarDARN radar velocity measurements, *Radio Science*, 44, RS4003, doi:10/1029/2008RS004045.

Krieger, A. S., A. F. Timothy, and E. C. Roelof (1973), A coronal hole and its identification as the source of a high velocity solar wind stream, *Solar Phys.*, 29, 505.

Lau, Y.-T., and J. M. Finn (1990), Three-dimensional kinematic reconnection in the presence of field nulls and closed field lines, *Astrophys. J., 350*, 672–691.

Lepri, S., T. H. Zurbuchen, L. A. Fisk, I. G. Richardson, H. V. Cane, and G. Gloeckler (2001), Ion charge distribution as an identifier of interplanetary coronal mass ejections, *J. Geophys. Res.*, 106, 29,231.

Livingston, W., and M. Penn (2009), Are Sunspots Different During This Solar Minimum?, *Eos Trans. AGU*, 90(30), doi:10.1029/2009EO300001.

Maunder, E. W. (1905), Magnetic disturbances, 1882 to 1903, as recorded at the Royal Observatory, Greenwich, and their association with sunspots, *Mon. Not. Roy. Astronom. Soc.*, 65, 2.

McWilliams, K. A. (2002), Ionospheric Signatures of Dayside Reconnection Processes, Ph.D. thesis, Leicester, UK, University of Leicester.

Mitchell, J. M., Jr., C. W. Stockton, and D. M. Meko (1979), Evidence of a 22-year rhythm of drought in the western United States related to the Hale solar cycle since the 17th century, *Solar–Terrestrial Influences on Weather and Climate,* B. M. McCormac and T. A. Seliga, Eds., D. Reidel, 125–144.

Mursula, K., and B. Zieger (2001), Long-term north-south asymmetry in solar wind speed inferred from geomagnetic activity: A new type of century-scale solar oscillation?, *Geophys. Res. Lett.*, 28(1), 95–98.

Mursula, K., T. Hiltula, and B. Zieger (2002), Latitudinal gradients of solar wind speed around the ecliptic: Systematic displacement of the streamer belt, *Geophys. Res. Lett.*, 29(15), 1738, doi:10.1029/2002GL015318.

Ness, N. F. and J. M. Wilcox (1965), Sector Structure of the Quiet Interplanetary Magnetic Field, *Science* 148, 1592-1594.

Ness, N. F. and J. M. Wilcox (1964), Solar Origin of the Interplanetary Magnetic Field, *Phys. Rev. Lett.* 13, 461 - 464.

Newell, P. T., and C.-I. Meng (1988), The cusp and the cleft/boundary layer: Low-altitude identification and statistical local time variation, *J. Geophys. Res.*, *93*(A12), 14,549–14,556.

Newell, P. T., and C.-I. Meng (1992), Mapping the dayside ionosphere to the magnetosphere according to particle precipitation characteristics, *Geophys. Res. Lett.*, *19*(6), 609–612.

Noyes, R. W. (1982), *The Sun, Our Star*, Harvard University Press, Cambridge, Massachusetts, and London England.

Parker, E. N. (1957), Sweet's mechanism for merging magnetic fields in conducting fluids, *J. Geophys. Res.*, 62, 509-520.

Parker, E. N. (1958), Dynamics of the interplanetary gas and magnetic fields, *Astrophys, J., 128,* 664-676.

Parker, E. N. (1963), *Interplanetary Dynamical Processes*, Interscience Publishers, New York.

Penn, M. J., S. Walton, G. Chapman, J. Ceja and W. Plick (2003), Temperature Dependence of Molecular Line Strengths and Fe I 1565 nm Zeeman Splitting in a Sunspot, *Solar Phys.*, 213, 55-67.

Penn, M. J., and W. Livingston (2006), Temporal changes in sunspot umbral magnetic fields and temperatures, *Astrophys. J., 649,* L45–L48.

Petschek, H. E. (1964), Magnetic field annihilation, p. 425, in *The Physics of Solar Flares, NASA Spec. Publ., SP-50,* edited by W. N. Hess, NASA, Washington, DC.

Petschek, H. E. (1966), The mechanism for reconnection of geomagnetic and interplanetary field lines, in *The Solar Wind*, edited by R. J. Mackin and M. Neugebauer, p. 257, Pergamon, New York.

Phillips, T. (2009), Cosmic Rays Hit Space Age High, http://science.nasa.gov/ headlines/y2009/29sep_cosmicrays.htm.

Pneuman, G. W., and R. A. Kopp (1971), Gas-Magnetic Field Interactions in the Solar Corona, *Solar Physics*, Volume 18, Issue 2, pp.258-270.

Press, W. H., B. P. Flannery, S. A. Teukolsky, W. T. Vetterling (1986), General linear least squares, in *Numerical Recipes, the Art of Scientific Computing*, Cambridge University Press, Cambridge, 509-520.

Ram, M., M. R. Stolz, and B. A. Tinsley (2009), The Terrestrial Cosmic Ray Flux: Its Importance for Climate, *Eos Trans. AGU*, 90(44), doi:10.1029/2009EO440001.

Rich, F. J., and M. Hairston (1994), Large-scale convection patterns observed by DMSP, J. Geophys. Res., 99 (A3), 3827–3844.

Rosenberg, R. L., and P. J. Coleman (1969), Heliographic latitude dependence of the dominant polarity of the interplanetary magnetic field, *J. Geophys. Res.*, 74, 5611.

Russell, C. T. and R. L. McPherron (1973), Semiannual variation of geomagnetic activity, *J. Geophys. Res.*, 78 (1) , 92–108.

Russell, C. T. (1972), The configuration of the magnetosphere, in *Critical Problems of Magnetospheric Physics*, edited by E. R. Dyer, pp.1–16, Inter-Union Comm. on Sol.-Terr. Phys. Secretariat, Natl. Acad. of Sci., Washington, D. C.

Ruohoniemi, J. M., and K. B. Baker (1998), Large-scale imaging of high-latitude convection with Super Dual Auroral Radar Network HF radar observations, J. Geophys. Res., 103(A9), 20,797–20,811.

Sabbah, I. (1995), North-South asymmetry of the daily interplanetary magnetic field spiral during the period: 1965–1990, *Earth, Moon and Planets*, v. 70, UN/ESA Workshops Vol. 5, p. 173-178.

Scafetta, N., and B. J. West (2008), Is climate sensitive to solar variability?, *Physics Today*, vol. 61, issue 3, p. 50, DOI: 10.1063/1.2897951.

Scafetta, N., and B. J. West (2007), Phenomenological reconstructions of the solar signature in the Northern Hemisphere surface temperature records since 1600, *J. Geophys. Res.*, 112, D24S03, doi:10.1029/2007JD008437.

Schwabe, H. (1843), Excerpts from Solar Observations during 1843, *Astronomische Nachrichten*, 20, 495.

Schwenn, R., et al. (1997), First view of the extended green-line emission corona at solar activity minimum using the Lasco-C1 coronagraph on SOHO, *Sol. Phys.*, 175, 667–684.

Sheeley, N. R., J. W. Harvey, and W. C. Feldman (1976), Coronal holes, solar wind streams, and recurrent geomagnetic disturbances 1973–1976, *Solar Phys.*, 49, 271.

Siscoe, G. L., G. M. Erickson, B. U. Ö. Sonnerup, N. C. Maynard, K. D. Siebert, D. R. Weimer, and W. W. White (2001a), Magnetospheric sash dependence on IMF direction, *Geophys. Res. Lett., 28*(10), 1921–1924.

Siscoe, G. L., G. M. Erickson, B. U. Ö. Sonnerup, N. C. Maynard, K. D. Siebert, D. R. Weimer, and W. W. White (2001b), Global role of E∥ in magnetopause reconnection: An explicit demonstration, *J. Geophys. Res., 106*(A7), 13,015–13,022.

Smith, E. J. , B. T. Tsurutani, and R. L. Rosenberg (1978), Observations of the Interplanetary Sector Structure up to Heliographic Latitudes of 16°: Pioneer 11, *J. Geophys. Res. Lett.* 83(A2), 717-724.

Solanki, S. K. (2003), Sunspots: An overview, *Astron. Astrophys. Rev., 11*(2- 3), 153–286.

Stockton, C. W. and D. M. Meko (1975), A long-term history of drought occurrence in western United States as inferred from tree rings, *Weatherwise*, v. 28, no. 6, p. 245-249.

Sturrock, P. A. (1986), Physics of the Sun: Volume III - Astrophysics and Solar-Terrestrial Relations, D. Reidel Publishing Company. 196.

Suess, S. T., and S. F. Nerney (2004), Flow in streamer boundaries and streamer stability, *Adv. Space Res.*, 33, 668–675.

Suess, S. T., and S. F. Nerney (2006), Flow inside the brightness boundary of coronal streamers, *Geophys. Res. Lett.*, 33, L10104, doi:10.1029/2006GL026182.

Suess, S. T., Y.-K. Ko, R. von Steiger, and R. L. Moore (2009), Quiescent current sheets in the solar wind and origins of slow wind, *J. Geophys. Res.*, 114, A04103, doi:10.1029/2008JA013704.

Svalgaard, L. and J. M. Wilcox (1974), The Spiral Interplanetary Magnetic Field: A Polarity and Sunspot Cycle Variation, *Science* 186, 51-53.

Sweet, P. A. (1958), The Neutral Point Theory of Solar Flares, pp.123-140, in *Electromagnetic Phenomena in Cosmical Physics, Proceedings from IAU Symposium no. 6. Stockholm, 1956*, edited by B. Lehnert, Cambridge University Press, New York.

Takalo, J., and K. Mursula (2002), Annual and solar rotation periodicities in IMF components: Evidence for phase/frequency modulation, *Geophys. Res. Lett.*, 29(9), 1317, doi:10.1029/2002GL014658.

Tanaka, T. (1999), Configuration of the magnetosphere-ionosphere convection system under northward IMF conditions with nonzero IMF *BY, J. Geophys. Res., 104*(A7), 14683–14690.

Tinsley, B. A (2008), The global atmospheric electric circuit and its effects on cloud microphysics, *Rep. Prog. Phys.*, 71, 066801, 31pp, doi:10.1088/0034-4885/71/6/066801.

Ulaby, F. T., R. K. Moore, A. K. Fung (1981), Microwave Remote Sensing Active and Passive, Volume I, Microwave Remote Sensing Fundamentals and Radiometry, Addison-Wesley Publishing Company.

Uzzo, M., L. Strachan, A. Vourlidas, Y.-K. Ko, and J. C. Raymond (2006), Physical properties of a 2003 April quiescent streamer, *Astrophys. J.*, 645, 720–731.

Vasyliunas, V. M. (1975), Theoretical models of magnetic field line merging, 1, *Rev. Geophys. Space Phys.*, 13, 303-336.

Villain, J. P., R. A. Greenwald, K. B. Baker, and J. M. Ruohoniemi (1987), HF Radar Observations of *E* Region Plasma Irregularities Produced by Oblique Electron Streaming, *J. Geophys. Res.*, 92(A11), 12,327–12,342.

Von Steiger, R., T. H. Zurbuchen, J. Geiss, G. Gloeckler, L. A. Fisk, and N. A. Schwadron (2001), The 3-D heliosphere from the Ulysses and ACE solar wind composition experiments, *Space Sci. Rev.*, 94, 123.

Wallace, L., and W. Livingston (1992), The effect of the Pinatubo cloud on hydrogen chloride and hydrogen fluoride, *Geophys. Res. Lett.*, 19(12), 1209.

Watanabe M., G. J. Sofko (2008), Synthesis of various ionospheric convection patterns for IMF *BY*-dominated periods: Split crescent cells, exchange cells, and theta aurora formation, *J. Geophys. Res.*, *113*, A09218, doi:10.1029/2007JA012868.

Watanabe, M., and G. J. Sofko (2009a), Role of interchange reconnection in convection at small interplanetary magnetic field clock angles and in transpolar arc motion, *J. Geophys. Res.*, *114*, A01209, doi:10.1029/2008JA013426.

Watanabe, M., and G. J. Sofko (2009b), Dayside four-sheet field-aligned current system during IMF B_Y-dominated periods, *J. Geophys. Res.*, 114, A03208, doi:10.1029/2008JA013815.

Watanabe, M., and G. J. Sofko (2009c), The interchange cycle: A fundamental mode of magnetic flux circulation for northward interplanetary magnetic field, *Geophys. Res. Lett.*, 36, L03107, doi:10.1029/2008GL036682.

Watanabe, M., G. J. Sofko, X. Yan, K. A. McWilliams, J.-P. St.-Maurice, A. V. Koustov, G. C. Hussey, and M. R. Hairston (2009), Ionospheric signatures of the interchange cycle at small IMF clock angles, submitted to *J. Geophys. Res.*, October, 2009, final acceptance pending.

Watanabe, M., G. J. Sofko, D. A. André, T. Tanaka, and M. R. Hairston (2004), Polar cap bifurcation during steady-state northward interplanetary magnetic field with $|BY| \sim BZ$, *J. Geophys. Res.*, *109*, A01215, doi:10.1029/2003JA009944.

Watanabe, M., K. Kabin, G. J. Sofko, R. Rankin, T. I. Gombosi, A. J. Ridley, and C. R. Clauer (2005), Internal reconnection for northward interplanetary magnetic field, *J. Geophys. Res.*, *110*, A06210, doi:10.1029/2004JA010832.

Watanabe, M., G. J. Sofko, D. A. André, J. M. Ruohoniemi, M. R. Hairston, and K. Kabin (2006), Ionospheric signatures of internal reconnection for northward interplanetary magnetic field: Observation of "reciprocal cells" and magnetosheath ion precipitation, *J. Geophys. Res.*, *111*, A06201, doi:10.1029/2005JA011446.

Watanabe, M., G. J. Sofko, K. Kabin, R. Rankin, A. J. Ridley, C. R. Clauer, and T. I. Gombosi (2007), Origin of the interhemispheric potential mismatch of merging cells for interplanetary magnetic field *BY*-dominated periods, *J. Geophys. Res.*, *112*, A10205, doi:10.1029/2006JA012179.

White, W. W., G. L. Siscoe, G. M. Erickson, Z. Kaymaz, N. C. Maynard, K. D. Siebert, B. U. Ö. Sonnerup, and D. R. Weimer (1998), The magnetospheric sash and the cross-tail S, *Geophys. Res. Lett., 25*(10), 1605–1608.

Zieger, B. and K. Mursula (1998a), Annual variation in near-Earth solar wind speed: Evidence for persistent north-south asymmetry related to solar magnetic polarity, *Geophys. Res. Lett.* 25, 841.

Zieger, B., and K. Mursula (1998b), Correction to "Annual variation in near‐Earth solar wind speed: Evidence for persistent north‐south asymmetry related to solar magnetic polarity", *Geophys. Res. Lett.*, 25(14), 2653.

Zurbuchen, T. H., S. Hefti, L. A. Fisk, G. Gloeckler, and N. A. Schwadron (2000), The magnetic structure of the slow solar wind: Constraints from composition data, *J. Geophys. Res.*, 105, 18,327.

Zurbuchen, T. H., L. A. Fisk, G. Gloeckler, and R. von Steiger (2002), The solar wind composition throughout the solar cycle: A continuum of dynamic states, *Geophys. Res. Lett.*, 29(9), 1352, doi:10.1029/2001GL013946.

APPENDIX: The Evaluation of the Doppler Shift Frequency

Using the ACF Technique

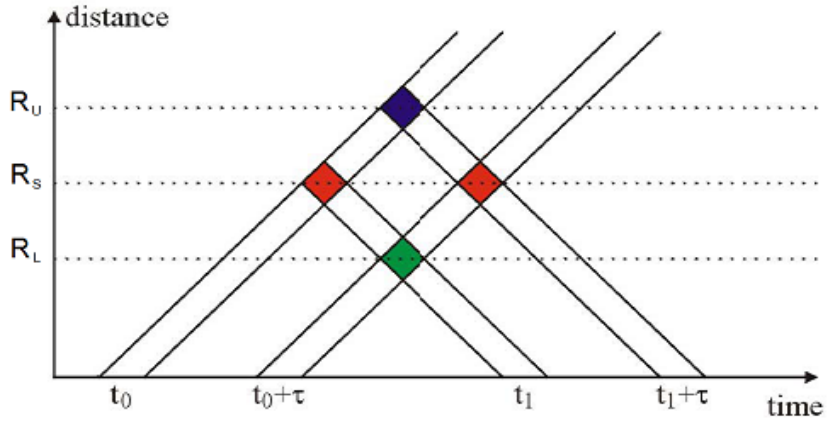

Figure 1. Two-pulse sequence at lag τ.

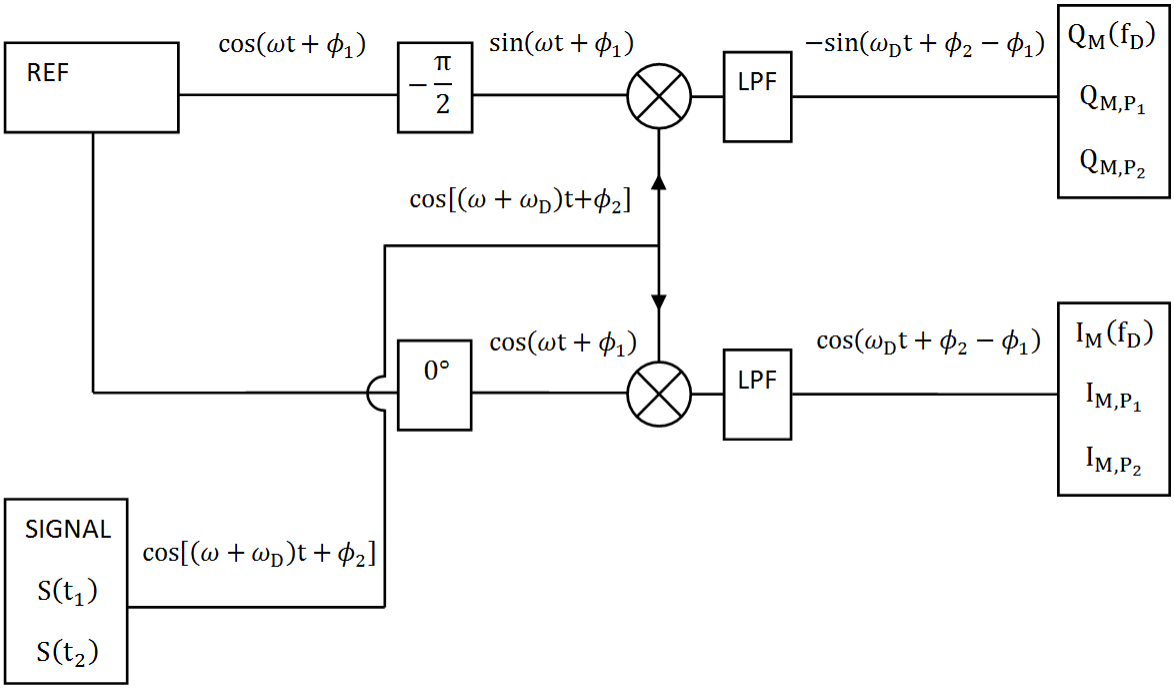

Figure 2. Conditioning of the signal by: (i) mixing with the reference signal phased with $-\frac{\pi}{2}$ and $0°$ respectively; (ii) low-pass-filtering the resultant cosine and sine components.

Figure 1 shows how the ACF at lag τ is formed from a pair of pulses. Two pulses are sent out, pulse p_1 at time t_0, and pulse p_2 at time $t_0 + \tau$. Four scattered signals are received, as follows: from p_1 at desired range R_S at time t_1, from p_1 at the undesired far range R_U at time $t_1 + \tau$, from p_2 at desired range R_S at time $t_1 + \tau$, and finally from p_2 at undesired near range R_L at time t_1. We express this mathematically as follows. At time t_1, the received signal is $S(t_1)$, which includes two parts: $S_{P_1}(t_1)$ is the signal from pulse p_1 received at time t_1, with an amplitude $A_{P_1}(t_1)$; $S_{P_2}(t_1)$ is the signal from pulse p_2 received at time t_1, with an amplitude $A_{P_2}(t_1)$. Similarly, the received signal at time $t_2 = t_1 + \tau$ is $S(t_2)$ and it includes two parts: $S_{P_1}(t_2)$ is the signal from pulse p_1 received at time t_2, with an amplitude $A_{P_1}(t_2)$; $S_{P_2}(t_2)$ is the signal from pulse p_2 received at time t_2, with an amplitude $A_{P_2}(t_2)$. We thus can write

$$S(t_1) = S_{P_1}\left(t_0 + \frac{2R_S}{c}\right) + S_{P_2}\left(t_0 + \tau + \frac{2R_L}{c}\right) \tag{1}$$

where c is the speed of light. Equation (1) can be written more fully as

$$S(t_1) = S_{P_1}(t_1) + S_{P_2}(t_1)$$

$$= A_{P_1}(t_1)\ \cos[(\omega + \omega_{D_S})t_1 + \phi_S] + A_{P_2}(t_1)\ \cos[(\omega + \omega_{D_L})t_1 + \phi_L] \tag{2}$$

where

$$S_{P_1}(t_1) = A_{P_1}(t_1)\ \cos[(\omega + \omega_{D_S})t_1 + \phi_S] \tag{3}$$

and

$$S_{P_2}(t_1) = A_{P_2}(t_1)\ \cos[(\omega + \omega_{D_L})t_1 + \phi_L] \tag{4}$$

In equations (2) to (4), ω is the transmitted frequency, ω_{D_S}, and ϕ_S are respectively the Doppler shift and initial phase at distance R_S, while ω_{D_L} and ϕ_L are respectively the Doppler shift and initial phase at distance R_L.

As shown in Figure 2, the reference $\cos(\omega t + \phi_1)$ is at the same frequency ω as the transmitted signal and ϕ_1 is the phase of the reference. By phasing the reference with $-\frac{\pi}{2}$ and $0°$ respectively, reference outputs $\sin(\omega t + \phi_1)$ and $\cos(\omega t + \phi_1)$ are produced. Through the quadrature detector, they mix with the signal respectively, so (2) is multiplied by $\cos(\omega\, t_1 + \phi_1)$ to obtain the in-phase output I, and multiplied by $\sin(\omega t_1 + \phi_1)$ to obtain the quadrature output Q. In fact, since $[\cos(\omega\, t_1 + \phi_1) + j \sin(\omega t_1 + \phi_1)]$ is equivalent to $e^{j(\omega t_1 + \phi_1)}$, quadrature detection is effectively exponential detection. The outputs then go through a LPF (low pass filter), after which only the Doppler frequency part of the signal remains. We now formulate the quadrature detection process mathematically, starting with

equation (2)× $e^{j(\omega t_1+\phi_1)}$, which gives

$$S(t_1)\,[\cos(\omega\, t_1+\phi_1)+j\,\sin(\omega t_1+\phi_1)] = S_{P_1}(t_1)\,[\cos(\omega\, t_1+\phi_1)+j\,\sin(\omega t_1+ \phi 1]+SP2t1[\cos(\omega t1+\phi 1)+j\sin(\omega t1+\phi 1)] \quad (5)$$

From the above, the results are as follows.

1. The I and Q outputs of the first signal part $S_{P_1}(t_1)\,[\cos(\omega\, t_1+\phi_1)+j\,\sin(\omega t_1+\phi_1)]$ are given by

$$I_{M_0,P_1}(t_1) = S_{P_1}(t_1)\cos(\omega\, t_1+\phi_1) = A_{P_1}(t_1)\ \cos[(\omega+\omega_{D_S})t_1+\phi_S]\cos(\omega\, t_1+\phi_1)$$

$$= A_{P_1}(t_1)\ \frac{\cos[(2\omega+\omega_{D_S})t_1+\phi_S+\phi_1]+\cos(\omega_{D_S}t_1+\phi_S-\phi_1)}{2} \quad (6)$$

and

$$Q_{M_0,P_1}(t_1) = S_{P_1}(t_1)\sin(\omega\, t_1+\phi_1) = A_{P_1}(t_1)\ \cos[(\omega+\omega_{D_S})t_1+\phi_S]\sin(\omega t_1+\phi_1)$$

$$= A_{P_1}(t_1)\ \frac{\sin[(2\omega+\omega_{D_S})t_1+\phi_S+\phi_1]-\sin(\omega_{D_S}t_1+\phi_S-\phi_1)}{2} \quad (7)$$

where $I_{M_0,P_1}(t_1)$ and $Q_{M_0,P_1}(t_1)$ are respectively the in phase part and quadrature part of the signal of pulse p_1 received at time t_1 after mixing with the reference, but before passing through the low-pass filter (LPF).

After passing through the LPF, only the low frequency parts remain, as follows.

$$I_{M,P_1}(t_1) = A_{P_1}(t_1)\ \frac{\cos(\omega_{D_S}t_1+\phi_S-\phi_1)}{2} \quad (8)$$

and

$$Q_{M,P_1}(t_1) = A_{P_1}(t_1)\ \frac{-\sin(\omega_{D_S}t_1+\phi_S-\phi_1)}{2} \quad (9)$$

where $I_{M,P_1}(t_1)$ and $Q_{M,P_1}(t_1)$ are respectively the in phase part and quadrature parts of the scattered signal from pulse p_1 received at time t_1 after mixing with the reference and passing through the LPF.

2. The I and Q quadrature detector outputs arising from the scattered signal from pulse 2 are given by $S_{P_2}(t_1)\,[\cos(\omega\, t_1+\phi_1)+j\,\sin(\omega t_1+\phi_1)]$.

The calculation is the same for the signal from pulse p_2. The outputs after the LPF are given by

$$I_{M,P_2}(t_1) = A_{P_2}(t_1)\ \frac{\cos(\omega_{D_L}t_1+\phi_L-\phi_1)}{2} \quad (10)$$

and

$$Q_{M,P_2}(t_1) = A_{P_2}(t_1)\ \frac{-\sin(\omega_{D_L} t_1 + \phi_L - \phi_1)}{2} \tag{11}$$

where $I_{M,P_2}(t_1)$ and $Q_{M,P_2}(t_1)$ are respectively the in phase and quadrature outputs.

Now we consider the signal received at time t_2.

$$S(t_2) = S_{P_1}\left(t_0 + \frac{2R_U}{c}\right) + S_{P_2}\left(t_0 + \tau + \frac{2R_S}{c}\right) \tag{12}$$

$$S(t_2) = S_{P_1}(t_2) + S_{P_2}(t_2)$$

$$= A_{P_1}(t_2)\cos[(\omega + \omega_{D_U})t_2 + \phi_U] + A_{P_2}(t_2)\cos[(\omega + \omega_{D_S})t_2 + \phi_S] \tag{13}$$

where ω is the transmitted frequency, ω_{D_U}, and ϕ_U are respectively the Doppler shift and relative phase of the signal from range R_U, and ω_{D_S}, and ϕ_S are respectively the Doppler shift and initial phase of the signal from range R_S.

Because the ionosphere is assumed to remain correlated at R_S, ϕ_S at t_2 remains the same as at t_1.

Through the quadrature detector, which is equivalent to (14)$\times e^{j(\omega t_2 + \phi_1)}$, and through LPF, the same as (5-10),

3. The I and Q of the third part $S_{P_1}(t_2)$ $[\cos(\omega\, t_2 + \phi_1) + j\sin(\omega t_2 + \phi_1)]$ is shown by

$$I_{M,P_1}(t_2) = A_{P_1}(t_2)\frac{\cos(\omega_{D_U} t_2 + \phi_U - \phi_1)}{2} \tag{14}$$

$$Q_{M,P_1}(t_2) = A_{P_1}(t_2)\frac{-\sin(\omega_{D_U} t_2 + \phi_U - \phi_1)}{2} \tag{15}$$

In which, $I_{M,P_1}(t_2)$ and $Q_{M,P_1}(t_2)$ are respectively the in phase part and quadrature part of the signal of pulse p_1 received at time t_2 after mixing with the reference and passing through the LPF.

4. The I and Q of the fourth part $S_{P_2}(t_2)$ $[\cos(\omega\, t_2 + \phi_1) + j\sin(\omega t_2 + \phi_1)]$ are given by

$$I_{M,P_2}(t_2) = A_{P_2}(t_2)\frac{\cos(\omega_{D_S} t_2 + \phi_S - \phi_1)}{2} \tag{16}$$

and

$$Q_{M,P_2}(t_2) = A_{P_2}(t_2)\frac{-\sin(\omega_{D_S}t_2+\phi_S-\phi_1)}{2} \tag{17}$$

where $I_{M,P_2}(t_2)$ and $Q_{M,P_2}(t_2)$ are respectively the in phase part and quadrature part of the signal of pulse p_2 received at time t_2 after mixing with the reference and passing through the LPF.

Now we calculate the ACF averaged by the number of multipulse sequences used during the one-minute scans (~35) or two-minute scans (~70). Each multipulse sequence contains either N = 7 or N = 8 pulses. The time between two pulses is

$$t_2 - t_1 = \tau_n = n\tau_1 \tag{18}$$

where τ_1 is the unit lag (which was originally 2.4 ms, but has gone as low as 1.5 ms). The lag τ_n is simply n times the unit lag.

The time-averaged ACF at lag τ_n and R_S is given by:

$$C(n,R_S) = \langle S_M(t_1)S_M(t_2)^*\rangle = \langle S_{M,P_1}(t_1)S_{M,P_1}(t_2)^*\rangle + \langle S_{M,P_1}(t_1)S_{M,P_2}(t_2)^*\rangle + \langle S_{M,P_2}(t_1)S_{M,P_1}(t_2)^*\rangle + \langle S_{M,P_2}(t_1)S_{M,P_2}(t_2)^*\rangle \tag{19}$$

where $C(n,R_S)$ is the ACF at lag τ_n and R_S, and $S_M(t_1)$, $S_M(t_2)$, $S_{M,P_1}(t_1)$, $S_{M,P_1}(t_2)$, $S_{M,P_2}(t_1)$, $S_{M,P_2}(t_2)$ are respectively the total signal received from pulses p1 and p2 received at times t_1 and t_2, the signal from pulse p_1 received at times t_1 and t_2, and the signal from pulse p_2 received at times t_1 and t_2, after mixing with the reference and passing through the LPF. The symbol * indicates the complex conjugate.

1. First, we consider the second term $\langle S_{M,P_1}(t_1)S_{M,P_2}(t_2)^*\rangle$, given by:

$$\langle S_{M,P_1}(t_1)S_{M,P_2}(t_2)^*\rangle = \left[A_{P_1}(t_1)\frac{\cos(\omega_{D_S}t_1+\phi_S-\phi_1)}{2} - jA_{P_1}(t_1)\frac{\sin(\omega_{D_S}t_1+\phi_S-\phi_1)}{2}\right]\left[A_{P_2}(t_2)\frac{\cos(\omega_{D_S}t_2+\phi_S-\phi_1)}{2} + jAP2t2\sin(\omega DSt2+\phi S-\phi 1)2\right.$$

$$= A_{P_1}(t_1)\,A_{P_2}(t_2)\left\{\left[\frac{\cos[\omega_{D_S}(t_1+t_2)+2(\phi_S-\phi_1)]}{8} + \frac{\cos[\omega_{D_S}(t_1-t_2)]}{8}\right.\right. \qquad (I_{M,P_1}(t_1)\times I_{M,P_2}(t_2)^*)$$

$$\left.\left. - \frac{\cos[\omega_{D_S}(t_1+t_2)+2(\phi_S-\phi_1)]}{8} + \frac{\cos[\omega_{D_S}(t_1-t_2)]}{8}\right] \qquad (Q_{M,P_1}(t_1)\times Q_{M,P_2}(t_2)^*)\right.$$

$$\left. + j\left[\frac{\sin[\omega_{D_S}(t_1+t_2)+2(\phi_S-\phi_1)]}{8} - \frac{\sin[\omega_{D_S}(t_1-t_2)]}{8}\right. \qquad (I_{M,P_1}(t_1)\times Q_{M,P_2}(t_2)^*)\right.$$

$$-\frac{\sin[\omega_{D_S}(t_1+t_2)+2(\phi_S-\phi_1)]}{8}-\frac{\sin[\omega_{D_S}(t_1-t_2)]}{8}\Big]\Big\} \qquad (Q_{M,P_1}(t_1)\times I_{M,P_2}(t_2)^*)$$

$$= A_{P_1}(t_1)\,A_{P_2}(t_2)\left\{\frac{\cos[\omega_{D_S}(t_1-t_2)]}{4}-j\,\frac{\sin[\omega_{D_S}(t_1-t_2)]}{4}\right\}$$

$$= A_{P_1}(t_1)\,A_{P_2}(t_2)\left\{\frac{\cos(\omega_{D_S}\tau_n)}{4}+j\,\frac{\sin(\omega_{D_S}\tau_n)}{4}\right\} \qquad (20)$$

The same procedure is used for the other 3 terms,

2. We next consider the first term $\langle S_{M,P_1}(t_1)S_{M,P_1}(t_2)^*\rangle$, as follows:

$$\langle S_{M,P_1}(t_1)S_{M,P_1}(t_2)^*\rangle =$$
$$\left[A_{P_1}(t_1)\,\frac{\cos(\omega_{D_S}t_1+\phi_S-\phi_1)}{2}-jA_{P_1}(t_1)\,\frac{\sin(\omega_{D_S}t_1+\phi_S-\phi_1)}{2}\right]\left[A_{P_1}(t_2)\,\frac{\cos(\omega_{D_U}t_2+\phi_U-\phi_1)}{2}+\right.$$
$$jAP1t2\sin(\omega DUt2+\phi U-\phi 1)2$$

$$= A_{P_1}(t_1)\,A_{P_1}(t_2)\left\{\frac{\cos(\omega_{D_S}t_1-\omega_{D_U}t_2+\phi_S-\phi_U)}{4}-j\,\frac{\sin(\omega_{D_S}t_1-\omega_{D_U}t_2+\phi_S-\phi_U)}{4}\right\} \qquad (21)$$

3. We next consider the third term $\langle S_{M,P_2}(t_1)S_{M,P_1}(t_2)^*\rangle$, as follows:

$$\langle S_{M,P_2}(t_1)S_{M,P_1}(t_2)^*\rangle =$$
$$\left[A_{P_2}(t_1)\,\frac{\cos(\omega_{D_L}t_1+\phi_L-\phi_1)}{2}-jA_{P_2}(t_1)\,\frac{\sin(\omega_{D_L}t_1+\phi_L-\phi_1)}{2}\right]\left[A_{P_1}(t_2)\,\frac{\cos(\omega_{D_U}t_2+\phi_U-\phi_1)}{2}+\right.$$
$$jAP1t2\sin(\omega DUt2+\phi U-\phi 1)2$$

$$= A_{P_2}(t_1)\,A_{P_1}(t_2)\left\{\frac{\cos(\omega_{D_L}t_1-\omega_{D_U}t_2+\phi_L-\phi_U)}{4}-j\,\frac{\sin(\omega_{D_L}t_1-\omega_{D_U}t_2+\phi_L-\phi_U)}{4}\right\} \qquad (22)$$

4. Finally, we consider the fourth term $\langle S_{M,P_2}(t_1)S_{M,P_2}(t_2)^*\rangle$, as follows:

$$\langle S_{M,P_2}(t_1)S_{M,P_2}(t_2)^*\rangle =$$
$$\left[A_{P_2}(t_1)\,\frac{\cos(\omega_{D_L}t_1+\phi_L-\phi_1)}{2}-jA_{P_2}(t_1)\,\frac{\sin(\omega_{D_L}t_1+\phi_L-\phi_1)}{2}\right]\left[A_{P_2}(t_2)\,\frac{\cos(\omega_{D_S}t_2+\phi_S-\phi_1)}{2}+\right.$$
$$jAP2t2\sin(\omega DSt2+\phi S-\phi 1)2$$

$$= A_{P_2}(t_1)\,A_{P_2}(t_2)\left\{\frac{\cos(\omega_{D_L}t_1-\omega_{D_S}t_2+\phi_L-\phi_S)}{4}-j\,\frac{\sin(\omega_{D_L}t_1-\omega_{D_S}t_2+\phi_L-\phi_S)}{4}\right\} \qquad (23)$$

The ACF is the sum of the four terms, given by (20)=(21)+(22)+(23)+(24). Written out fully, this becomes:

$$\langle S_M(t_1)S_M(t_2)^*\rangle = \langle S_{M,P_1}(t_1)S_{M,P_1}(t_2)^*\rangle + \langle S_{M,P_1}(t_1)S_{M,P_2}(t_2)^*\rangle$$

$$+\langle S_{M,P_2}(t_1)S_{M,P_1}(t_2)^*\rangle + \langle S_{M,P_2}(t_1)S_{M,P_2}(t_2)^*\rangle$$

$$= A_{P_1}(t_1)\, A_{P_2}(t_2) \left\{ \frac{\cos\left(\omega_{D_S}\tau_n\right)}{4} + j\frac{\sin\left(\omega_{D_S}\tau_n\right)}{4} \right\}$$

$$+A_{P_1}(t_1)\, A_{P_1}(t_2)\, \left\{ \frac{\cos\left(\omega_{D_S}t_1-\omega_{D_U}t_2+\phi_S-\phi_U\right)}{4} - j\frac{\sin\left(\omega_{D_S}t_1-\omega_{D_U}t_2+\phi_S-\phi_U\right)}{4} \right\}$$

$$+A_{P_2}(t_1)\, A_{P_1}(t_2) \left\{ \frac{\cos\left(\omega_{D_L}t_1-\omega_{D_U}t_2+\phi_L-\phi_U\right)}{4} - j\frac{\sin\left(\omega_{D_L}t_1-\omega_{D_U}t_2+\phi_L-\phi_U\right)}{4} \right\}$$

$$+A_{P_2}(t_1)\, A_{P_2}(t_2)\, \left\{ \frac{\cos\left(\omega_{D_L}t_1-\omega_{D_S}t_2+\phi_L-\phi_S\right)}{4} - j\frac{\sin\left(\omega_{D_L}t_1-\omega_{D_S}t_2+\phi_L-\phi_S\right)}{4} \right\} \quad (24)$$

Because ϕ_S, ϕ_L and ϕ_U are random with respect to each other, when time-averaging over the number of multipulse sequences during a complete scan is performed, the last 6 terms average to zero. The results of the equation above are then equivalent to the following:

$$= A_{P_1}(t_1)\, A_{P_2}(t_2) \left\{ \frac{\cos\left(\omega_{D_S}\tau_n\right)}{4} + j\frac{\sin\left(\omega_{D_S}\tau_n\right)}{4} \right\}$$

$$= \frac{A_{P_1}(t_1)\, A_{P_2}(t_2)}{4} e^{j\,\omega_{D_S}\tau_n} \quad (25)$$

The phase of the ACF is obtained from

$$\tan\left(\omega_{D_S}\tau_n\right) = \frac{\sin\left(\omega_{D_S}\tau_n\right)}{\cos\left(\omega_{D_S}\tau_n\right)} = \frac{Q}{I} \quad (26)$$

where Q and I are respectively the quadrature and in phase parts of the ACF $C(n, R_S) = \langle S_M(t_1) S_M(t_2)^* \rangle$.

The phase of the ACF is then obtained readily as follows:

$$\tan^{-1}\left(\frac{Q}{I}\right) = \omega_{D_S}\tau_n = \phi \quad (27)$$

The above equation shows that the Doppler shift of the signal is obtained directly from the slope of the graph of the ACF phase versus the lag, namely

$$\omega_{D_S} = \frac{\partial\phi}{\partial\tau}. \quad (28)$$